A study of point defects in UO 2+x and their impact upon fuel properties

Yue Ma

To cite this version:

Yue Ma. A study of point defects in UO 2+x and their impact upon fuel properties. Materials Science [cond-mat.mtrl-sci]. Université d'Aix-Marseille, 2017. English. NNT : . tel-01714468v2

HAL Id: tel-01714468
https://hal.science/tel-01714468v2

Submitted on 22 Mar 2018

Université d'Aix-Marseille

Ecole Doctorale 352 : Physique et Science de la Matière

CEA Cadarache, DEN/DEC/SFER/LCU

Thèse présentée pour obtenir le grade universitaire de docteur

Discipline : Matière Condensée et Nanosciences

Yue MA

A study of point defects in UO_{2+x} and their impact upon fuel properties

Soutenue le **07/12/2017** devant le jury :

Henry Fischer	Chercheur, ILL	Président
Marie-France Barthe	Directrice de Recherche CEMHTI	Rapporteur
Jean-Marc Heintz	Professeur ICMCB	Rapporteur
Boris Dorado	Ingénieur-Chercheur, CEA	Examinateur
Jacques Lechelle	Ingénieur-Chercheur, CEA	Directeur de thèse
Philippe Garcia	Ingénieur-Chercheur, CEA	Encadrant de thèse

Numéro national de thèse/suffixe local : 2017AIXM0310/031ED352

Résumé

Les propriétés d'autodiffusion de l'uranium sont essentielles pour la compréhension de l'interaction pastille-gaine dans le réacteur. L'objectif de cette thèse est de déterminer les coefficients d'autodiffusion de l'uranium dans l'UO_2 sur-stœchiométrique qui dépendent, par l'intermédiaire des conditions thermodynamiques, des défauts ponctuels. Dans ce but trois techniques expérimentales ont été mises en œuvre. La première étude porte sur la compréhension des défauts d'oxygène et les différents réarrangements du réseau après oxydation. Pour cela, des échantillons d'UO_2 et d'UO_{2+x} ont été caractérisés par diffraction neutronique au sein de l'institut ILL à Grenoble (diffractomètre D4c). Les résultats obtenus par analyse de la « Pair Distribution Function » montrent que les anions interstitiels ont tendance à être isolés aux faibles valeurs de x mais sont regroupés aux valeurs plus élevées de x. La deuxième partie vise à étudier les défauts lacunaires d'uranium, prédominants dans les échantillons d'UO_{2+x} recuits à haute température, qui influent directement sur l'autodiffusion de l'uranium. La méthode non destructive de « Spectroscopie d'annihilation de Positrons », implémentée au laboratoire CEMHTI à Orléans, a été appliquée. Les résultats de spectroscopie d'élargissement Doppler d'annihilation de paires d'électrons-positons ont montré l'existence des lacunes d'uranium dans le matériau et leurs concentrations peuvent être estimées en fonction de la mesure de durée de vie des positons à l'aide d'un modèle de piégeage. La connaissance de la nature des défauts cationiques et anioniques ainsi que des équilibres de défauts aide à comprendre la corrélation entre les propriétés importantes du combustible (par exemple, la diffusion, le fluage) et les conditions thermodynamiques (c'est-à-dire la température et la pression partielle d'oxygène). La diffusion d'un traceur de l'uranium a été étudiée par Secondary Ion Mass Spectrometry pour caractériser la diffusion dans UO_{2+x}.

Mots clés : dioxyde d'uranium, diffraction neutronique, Spectroscopie d'annihilation de positons, Secondary Ions Mass Spectrometry

Abstract

Uranium dioxide is an oxygen excess, non-stoichiometric, fluorite material which exists over a wide range of compositions. At temperatures and oxygen activities that are relevant to its in-reactor behaviour, it has been reported that various types of point defects and clusters thereof may exist with different charge states and different compositions on both the anion and cation sublattices. These defects have a major influence on certain key engineering properties such as cation self-diffusion or creep. It is the aim of this work both to characterize the majority defects present in thermodynamically equilibrated samples and further our understanding of their impact upon uranium self-diffusion.

To this end, three types of experiments were carried out. Neutron diffraction was used, as neutrons are sensitive to oxygen ions, to characterize samples with different oxygen to metal ratios at different temperatures. This work was carried out at Institut Laüe Langevin in Grenoble on the D4c diffractometer which enables the determination of local atomic arrangements by means of the Pair Distribution Function analysis. Radial Distribution functions were modelled and compared to the experimental data. It is difficult to draw any firm conclusion about whether oxygen interstitials remain isolated or form clusters of ions in the low deviation from stoichiometry material as the system is extremely dilute. However, in samples containing much larger quantities of oxygen, results are consistent with the formation of clusters, either in a 2:2:2 type configuration or in the form of so-called cuboctahedron clusters, that are similar to those observed in U_4O_9.

Positron Annihilation Spectroscopy was also carried out at CEMHTI, Orléans on samples originally equilibrated at high temperature but under different oxygen partial pressures and subsequently quenched. At high enough oxygen partial pressures, Doppler broadening and lifetime spectroscopy prove the emergence of a specific, uranium vacancy containing defect, with characteristics similar to the ones observed in irradiated material. Our results also highlight the specific effect of the presence of oxygen interstitials alone on Doppler broadening characteristics and confirm that their life-time properties are similar to those of the lattice. Uranium and oxygen defect concentrations are tentatively derived from interpreting the data using a trapping model.

Finally, these results are complemented by uranium tracer diffusion experiments and attempt is made at interpreting changes in uranium self-diffusion coefficients based on our understanding of point defect behaviour.

Keywords : Uranium dioxide, Neutron diffraction, Positron annihilation spectroscopy, Self-diffusion, Secondary Ions Mass Spectrometry

Acknowledgement

It is a great opportunity to allow me to express my gratitude to people hereafter mentioned.

First and the most, I would like to thank my thesis supervisor, M. Philippe Garcia. Thank you for trusting me and recruiting me for this PhD position. Thanks a lot for all the patience, time, guidance and advice throughout three years. It is a great honour and pleasure to learn from you. You always encourage me when it is so hard for me. Thanks a lot for bearing all my problems and helping me correct the most of them. Also many thanks to your wife Aurore, for helping me when I just came to this country and knew nothing.

Here I would like to sincerely thank my thesis director, M. Jacques Lechelle. Thanks a lot for the time and ideas with which you contributed to this thesis work. It is always so pleasent to talk and work with you. You are such a wise and modest person. Every time we have a problem, it is always right to come to you and you can always find a proper solution.

I am really grateful for being the student of these two gentlemen. Thanks a lot again.

This research was carried out in the Laboratory of Combustible Uranium at CEA Cadarache, France. Thanks a lot for the great time working here. I have nothing but sincere gratitude for everyone and everything done that helped me here.

I would like to thank Mme Audrey Miard, for the great collaboration with her. My dear Audrey, thanks a lot for helping for those complicated lab administrative issues, for your technical support to me.

I would like to thank my laboratory director, M. Jerome Lamontagne, who has always covered me, solving every practical and administrative problems we had and supported my work in the lab.

I would like to thank Mme Xaviere Iltis, M. Nicolas Tarisien, Mme Andrea Sanchez for their great help in topological analyses. Also, many thanks to M. Pierre Matheron, M. Oliver Fiquet, M. Frank Marion, Mme Laetitia Silvestre. You were always so kind to me and helped me out of many technical difficulties. Thanks a lot Mme Nicole Buon and Mme Corine Druesne for your administrative support.

I would like to take this opportunity to thank every member of this lab again, particularly for their patience and kindness to me. Even though some of you may not be able to communicate with me well in English, you still try hard to help me and most importantly be kind to me. I will remember everyone's smile here. Thanks a lot.

During my three years, I have had opportunities to work with many intelligent and professional persons here. Firstly I would like to thank M. Lionel Desgranges. You brought me into the world of diffraction and

gave chances to this young girl who knew nothing about the experiment. Thanks a lot for your guidance and patience with me.

I also would like to thank M. David Simeone, M. Guido Baldinozzi, M. Henry Fischer, for their help in the experiment, advices and time spent with me in the neutron diffraction work. It is such an honour to work with you.

Many thanks to Mme Marie-France Barthe, M. Pierre Desgardin, and M. Chenwei He, for your help in the positron annihilation spectroscopy experiments. It was a great time in the CEMHTI, CNRS Orleans.

Thanks a lot to M. Philippe Bienvenu, Mme Ingrid Roure for your time and help in SIMS characterizations for the uranium self-diffusion experiment, and M. Herve Palancher as well for his support on this work and report.

Thanks a lot to all the other engineers and researchers I have worked with or came for help. Thanks a lot for your idea, your time, or simply a kind smile to me.

I would like to sincerely thank my jury. Thanks a lot for your presence, your comments and advices on this manuscript and in the defence.

Thanks a lot for my friends in France, who helped me for everyday life here. It's a great pleasure to have you by my side.

Finally, I would like to thank my family, my great parents in particular, for your understanding and support. You are my strength all the time. In this three years, although we are far away from each other, I know you always love me and give the best to me. I always love you.

诚挚感谢这三年身边的每一位！*Thanks a lot again!*

MA YUE

I would like to dedicate this thesis to my supervisors, my loving parents, and my husband.

Contents

Introduction

Uranium dioxide is the most commonly used nuclear fuel worldwide in Pressurized Water Reactors. Its basic engineering properties are essential to understand and predict fuel rod behaviour under all reactor operating conditions thus ensuring a safe and cost-effective use of this electricity producing technology. However, a substantial number of these properties reflect the behaviour of the material on several length scales: atomic scale, grain scale and engineering scale. For instance, thermally or radiation induced bulk atomic transport properties, which impact many engineering aspects of nuclear fuel behaviour are known to be dependent upon the complex interplay of point defects that exist on both cation and anion sublattices.

The increase in computational resources, has enabled models to be established at all length scales (Helfer et al., 2015) and it is important that experimental methods are able to provide insight into these different length scales and at best, generate experimental data which will be used to guide the modelling. Conversely, modelling can constitute a guide to interpret experimental results that would otherwise have been left pending. An example of this is oxygen self-diffusion. The oxygen diffusion mechanism has been shown experimentally to be an interstitial mechanism and this has been corroborated by *ab initio*, first principles calculations. These calculations, because of the detailed insight they provide, have indicated that the mechanism is actually of the interstitialcy type as it is associated with considerably lower migration barriers than others, bringing theory quantitatively in line with experimental estimates (Dorado et al., 2010).

Uranium dioxide and hyper-stoichiometric oxide have been extensively studied over many years, but still a great deal remains to be understood in relation to crystal imperfections and their formation and migration mechanisms. In addition, the in-pile material properties are very much dependent upon the behaviour at free surfaces or interfaces and little is known about the relationship between the bulk, grain boundary and macroscopic behaviours of our material: understanding the role of grain boundaries in regard to polycrystalline sinters, is still in its infancy. The main reason for this is the very broad variety of defects or imperfections that exist in this iono-covalent, non-stoichiometric oxide. Indeed, three distinct but coupled types of disorder are known to co-exist in uranium oxide: electronic disorder (uranium ions in different charge states), anion and cation disorder (vacancies, interstitials and clusters thereof). Defects can take on different charge states and the composition of defect clusters can change with deviation from stoichiometry (Crocombette, 2012; Crocombette et al., 2011) as formation energies are strongly dependent upon the Fermi level. Despite this rather complex picture, order of magnitude estimates of defect formation and migration energies are relatively well established. We know both from theoretical (usually density functional theory, DFT) and experimental approaches that right across the composition range, defects in UO_{2+x} come in the following order of increasing abundance: cation, anion and electronic disorder (Andersson et al., 2012; Garcia et al., 2017; Matzke, 1973).

From an experimental standpoint, there are basically two ways of deriving quantitative information about point defects. One can either measure a property that is sensitive to a particular type of defect over a given range of temperature and oxygen partial pressure (Dieckmann, 1984). The alternative is to carry out some sort of spectroscopic (RAMAN, XANES, EXAFS, PAS…) or structural (neutron or X-ray scattering) characterization of the material, preferably *in situ*, for which a defect will have a distinctive signature. Irrespective of the strategy, some sort of model, if only extremely basic, is usually necessary to correlate the presence of the defect to the experimental quantity of interest. And in most cases, the relationship is tenuous and requires additional information, usually obtained from DFT calculations, to narrow down the range of possible solutions. One reason for this can be a lack of sensitivity of the technique to the defect, another can be that several kinds of defects will usually coexist producing conflicting or, which can be as confusing, similar effects. For instance, it has been surmised since (Lidiard, 1966), that although uranium dioxide is essentially an oxygen excess oxide, its oxidation will lead to a concomitant increase in the oxygen interstitial and uranium vacancy concentrations simply as a result of Schottky and oxygen Frenkel equilibria.

As will be described in this work the fundamental drive for charged defect clustering and in particular for oxygen interstitial clustering stems from the fact that it enables the material to find lower energy configurations. This phenomenon, observed in other oxide systems, was mentioned for the first time in relation to uranium dioxide by Willis (Willis, 1978) (who carried out neutron diffraction experiments on a hyper-stoichiometric single crystal ($UO_{2.12}$). It was only natural that such results should come from neutron characterization work. Indeed, one of the difficulties inherent to the structural characterization of actinide oxides using X-Rays is that they are usually only sensitive to the actinide. Neutrons on the other hand, are actually useful for probing oxygen defects as neutron scattering cross sections for U and O atoms have similar orders of magnitude. However, Bragg diffraction only provides information relating to long range, periodic ordering of atoms. So Willis's 2:2:2 cluster was actually only inferred from an average cell model used in his refinement procedure. In recent years, people have increasingly turned to pair distribution function (PDF) analysis to characterize disordered systems such as liquids or nano-structured materials (Egami and Billinge, 2012; Fischer et al., 2002) that lack sufficient long-range order to produce sharp diffraction peaks. The information relating to disorder or defects is contained within the diffuse scattering intensities that are usually subtracted away as 'Background' in conventional Rietveld analysis but that the PDF can pick up. In recent years, this technique has been applied to the study of a number of uranium oxide compounds, mainly U_4O_9 and has revealed atomic scale details of the basic oxygen rich clusters it contains (Desgranges et al., 2016). However it has never been applied to single phase hyper-stoichiometric UO_{2+x}.

Oxygen defect behaviour may also be assessed from characterizing properties that are sensitive to oxidation such as electrical conductivity, oxygen chemical potential or oxygen activity, oxygen chemical or self-diffusion. This may provide evidence for the existence of defects of given composition or charge (Dieckmann, 1984; Garcia et al., 2010; Ruello et al., 2004). However, usually this technique will only reveal details about the most abundant type of defects, *i.e.* electronic and anion defects. In UO_{2+x} however, there are many engineering properties such as sintering or creep for which the rate limiting phenomenon is related to mobility on the cation sub-lattice and so it is important to acquire data in relation to this (Dorado et al., 2012; Matzke, 1969). It is well established in other non-stoichiometric oxide systems (Philibert, 1984) that creep rates are controlled by the slower of the two moving defect populations (in our case uranium). Also uranium self-diffusion is thought to occur via a vacancy mediated mechanism (Matzke, 1987). Such measurements have been carried out in the past and indicate that uranium self-diffusion is indeed an increasing function of non-stoichiometry. However these measurements, whether creep or self-diffusion, come with a good many caveats. In addition to this, past studies have focused on studying the problem as a function of deviation from stoichiometry, which is not a true thermodynamic quantity but a property in its own right (Dieckmann, 1984). The fact that little is known about the effect of additives or grain boundaries on these properties just adds to our interest (Dugay et al., 1998; Sabioni et al., 2000).

Spectroscopic techniques for characterizing uranium vacancies in actinide oxides are not readily available and at first glance, this aim appears to be a rather difficult task as under equilibrium conditions, uranium vacancies are present in much smaller quantities than oxygen defects. In recent years however, Positron Annihilation Spectroscopy (PAS) has proven to be a rather useful tool for characterizing such defects (Barthe et al., 2007). Further combining first principles approaches and experiment has confirmed the fact that PAS was indeed sensitive to the presence of uranium vacancy containing defects (Wiktor et al., 2014) which makes PAS a candidate for thermodynamically induced uranium vacancies.

It is the aim of this study to build on our knowledge of the U-O system to further our understanding of defect and defect related engineering properties. Because it has proven to be a promising technique in the study of disordered systems and atomic distortions in U_4O_9, we have chosen to carry out total scattering experiments and study the pair distribution function of hyper-stoichiometric UO_2. As regards the uranium sublattice, we have carried out PAS experiments on samples prepared at different levels of non-stoichiometry. Finally, since the property is important and only a limited number of experiments are available, we have set up cation diffusion experiments and attempted to derive uranium self-diffusion coefficients as a function of oxygen activity and temperature.

This exclusively experimental work is presented in this manuscript in six distinct parts. The first is devoted to a summary of what is known about point defect behavior in UO_{2+x} based on a limited number of spectroscopic or structural studies, diffusion property measurements or atomic scale modelling. Chapter 2 is devoted to the sample microstructural characteristics and their preparation details. In this chapter, we also present the experimental techniques, the theoretical principles they are based upon, how they are implemented experimentally and how the data treatment is carried out. Chapter 3 concerns our neutron scattering experiments, results and discussion thereof. It focuses primarily on oxygen clustering in UO_{2+x}. Chapter 4 concerns PAS experiments and how we have used them to separate the effect of defects on both sublattices. Chapter 5 describes self-diffusion experiments and their interpretation. In chapter 6, we summarize our results, their implications, attempt to establish links between them and highlight areas of research that should be focused on in the future.

Chapter 1 Literature review

1.1 Introduction

The aim of this chapter is by no means to cover in an exhaustive way our current understanding of point defects in UO_{2+x} or its atomic transport and mechanical properties. Rather, it is first to emphasize the practical significance of continuing to acquire basic knowledge and data in relation to point defects, be it from carrying out structural or spectroscopic characterisations, or measuring point defect dependent properties. Throughout this introductive chapter, we provide examples that establish that the data we are concerned with in this work are relevant to oxide fuel behaviour in a whole range of real-case situations: under normal and accidental reactor irradiation conditions, at the manufacturing or repository stage of the fuel cycle.

In section 1.2, we briefly present the complex U-O phase diagram. Because of its practical significance, we focus upon the iono-covalent single phase UO_{2+x} region and particularly upon the chemical potential of oxygen, i.e. the relationship between oxygen concentration and oxygen partial pressure. This fundamental property is used as an example of a macroscopic manifestation of the changing nature (composition and charge) of oxygen point defects with increasing oxygen content and changing temperature. In this section we also highlight the fundamental reasons why charged anion defects have a tendency to cluster and review the literature mainly relating to neutron scattering work and DFT approaches that reports the different atomic scale configurations of these defect clusters.

Section 1.3 is concerned with cation vacancies, their impact upon fuel behaviour and methods for characterising these defects. A particular attention is paid to Positron Annihilation Spectroscopy (PAS) and properties that are directly dependent upon cation vacancy behaviour (uranium self-diffusion and creep). In section 1.3, we also summarise the small number of characteristic features of equilibrium point defect models that determine defect concentrations.

1.2 Phase diagram and deviation-from-stoichiometry

1.2.1 A complex phase diagram

Uranium dioxide (UO_2) is the most commonly used fuel material in PWRs. Stoichiometric UO_2 has two stable crystalline structures with a phase transition at the Néel temperature T_N =30.8 K (Brandt and Walker, 1967; Frazer et al., 1965). Above this transition temperature, uranium dioxide presents as a paramagnetic order. It crystallizes in a cubic fluorite structure with a lattice parameter of 5.471Å at room temperature. The fluorite structure is described in Figure 1.1 and its space group is $Fm\overline{3}m$.

Uranium ions (U^{4+}) form a face-centred cubic lattice within which the oxygen ions (O^{2-}) (in green in Figure 1.1) define a simple cubic lattice with an O-O distance equal to half the lattice parameter. Another way of considering this crystal structure is as a three-dimensional array of oxygen cubes with the centre of every-other oxygen cube occupied by a uranium ion. As a result, the centre of one in two oxygen cubes is unoccupied and constitutes an interstitial site. These sites are often referred to as octahedral sites as they are at the centre of a regular octahedron, the vertices of which are occupied by cations.

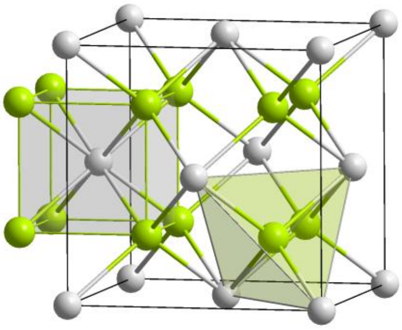

Figure 1.1: UO_2 crystal structure. The grey spheres are uranium ions and the green spheres at tetrahedral sites are oxygen ions.

At a given temperature and oxygen partial pressure, oxygen diffusion will enable UO_2 to oxidise and equilibrate with the surrounding gaseous atmosphere. The composition of uranium dioxide may deviate substantially from exact stoichiometry as the material reacts with the gas phase.

Oxidation of UO_2 is made possible in this iono-covalent system by uranium atoms taking on higher valence states than +4. As excess oxygen ions are incorporated from the gas phases at octahedral sites, uranium ions oxidise to a +5 state. This leads to the formation of UO_{2+x} (x>0) which is stable over a rather large composition range as shown in Figure 1.2 but also to the formation of non-stoichiometric higher oxide phases such as α-, β- and γ- U_4O_{9-y}, U_3O_7 which is meta-stable at relatively low temperatures, α- or β- U_3O_8 and eventually UO_3.

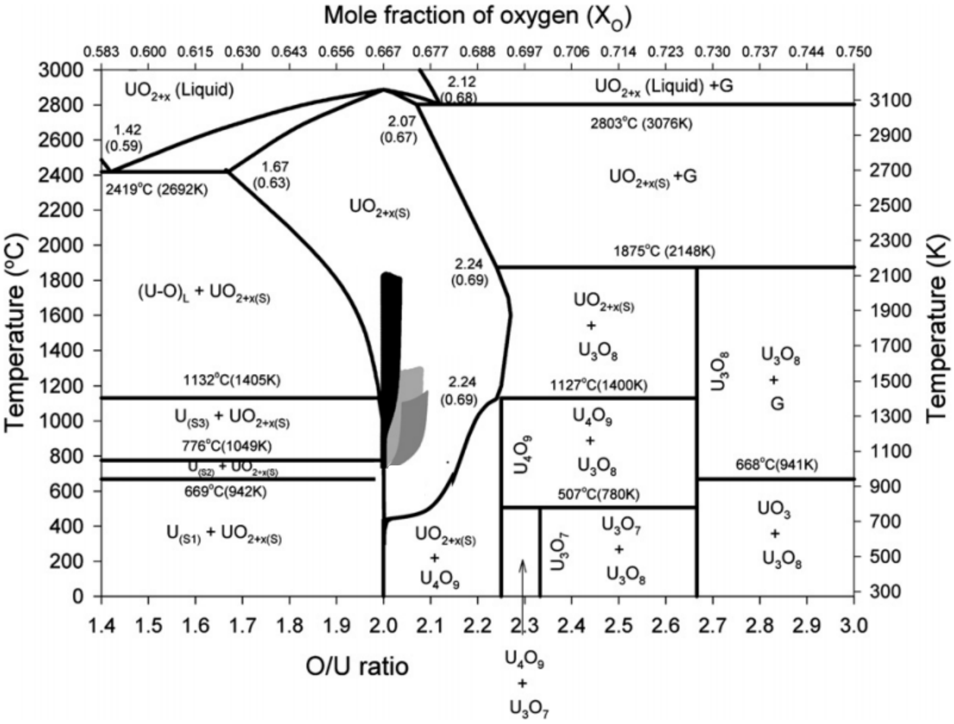

Figure 1.2: Phase diagram of uranium oxide (Higgs et al., 2007).

U_4O_9 is a cubic crystal which is an intermediate phase between UO_2 and orthorhombic U_3O_8, and has a superlattice structure based on the fluorite arrangement of UO_2 but with very weak superlattice reflexions. It is important to note that UO_{2+x} is not stable at low temperature but decomposes into a low stoichiometry fluorite phase $UO_{2+x'}$ and α- or β- U_4O_{9-y} (depending on temperature). **Studying single-phase (UO_{2+x}) is essential because of its practical significance with respect to the technological application of the material.** It is the expected phase at reactor temperatures under normal operating conditions (between 400 ℃ and 1100 ℃).

1.2.2 Deviation-from-stoichiometry

1.2.2.1 Hyper-stoichiometry

Many studies have assessed data relating to the dependence of deviation from stoichiometry upon thermodynamic conditions, i.e. oxygen partial pressure and temperature, otherwise known as the chemical potential of oxygen (Baichi et al., 2006; Guéneau et al., 2002; Higgs et al., 2007; Perron, 1968). At a given temperature, this dependence provides an insight into the underlying point defect related chemical equilibria and, as a result, in the composition or charge state of the defects involved (Kofstad, 1995).

Perron assessed the validity of chemical potential of oxygen data from various studies relating to hyper-stoichiometric material in the temperature range we are interested in (Perron, 1968). Figure 1.3 shows resulting recommendations in the temperature range 1073 K – 1573 K.

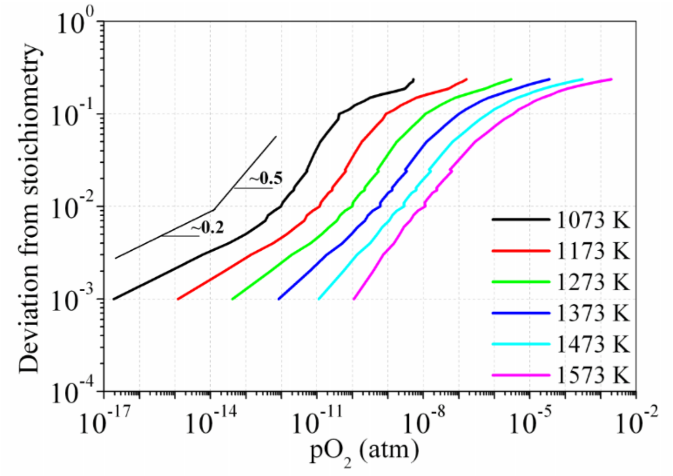

Figure 1.3: Dependence of deviation-from-stoichiometry upon oxygen partial pressure and temperature for hyper-stoichiometric UO_{2+x} (Perron, 1968).

Figure 1.3 indicates that depending on the range of oxygen partial pressure, two or three distinct regions of deviation-from-stoichiometry appear. There is a transition from $x \propto p_{O_2}^{0.2}$ to $x \propto p_{O_2}^{0.5}$ with increasing oxygen partial pressure at lower temperatures. However, this transition progressively disappears as the temperature increases. At all temperatures, the deviation from-stoichiometry levels off at higher p_{O_2}. The change of oxygen partial pressure dependency (from a power law exponent of 0.2 to 0.5) may be regarded as reflecting changes in the underlying defect equilibria. For example, a 0.5 exponent is usually associated with the presence of excess oxygen ions in the form of singly charged di-interstitial clusters (Garcia et al., 2017).

1.2.2.2 Hypo-stoichiometry

The hypo-stoichiometric or sub-stoichiometric UO_{2-x} phase is stable only at high temperature as shown in Figure 1.2 and under reducing conditions. In this region of the phase diagram, the predominant oxygen defects are oxygen vacancies and charge compensation occurs through the formation of U^{3+} ions. There are much fewer studies relating to this phase than to the hyper-stoichiometric phase. This is mainly because it is not as relevant to technological applications but also because the conditions required for stabilising UO_{2-x} are difficult to control due to the low oxygen potential and high temperatures required (Kapshukov et al., 1990; Kim and Olander, 1981).

1.2.3 UO_2 oxidation and anion defect clustering

Fresh fuel is usually required to have a near-stoichiometric composition. However, during reactor operation, fission of ^{235}U leads to the formation of a wide range of fission products which on average, have a valence state less than +4. Two oxygen ions are released in the process so that fission may generally be regarded as being an oxidising process (Brillant et al., 2011; Croff, 1980; Grimes and Catlow, 1991; Matzke, 1995; Olander, 2009; Park et al., 1997). Oxidation issues are not only relevant to in-reactor operation. Under LOCA (Loss Of Coolant Accident) conditions, fuel oxidation will occur due to the high temperatures and steam environment. Long-term repository scenarios, because of the geological time periods involved, assume the fuel will at one point be subjected to a form of oxidation (Ewing, 2015; OECD NEA/NSC, 2009).

Both kinetics of oxidation and oxidation phases (α, β, γ- U_4O_9, U_3O_7, α and β- U_3O_8) have therefore been studied extensively (McEachern and Taylor, 1998; Rousseau et al., 2006). A feature that is common to the various U_4O_9 cubic phases and UO_{2+x}, is that excess oxygen ions do not simply remain at octahedral sites but have a tendency to cluster to form larger size defects. This manifests itself through a greater degree of covalency (Bagus and Nelin, 2014; Prodan et al., 2007) but one may well wonder why anion defects have a tendency to cluster.

The answer has to be found in the basic charge compensation mechanisms related to oxidation and the mobility of electronic charge carriers (essentially U^{5+} ions in UO_{2+x} and U_4O_9). In UO_{2+x} excess oxygen ions are incorporated as doubly charged interstitials noted O_I''in Kröger-Vink notations (Kröger and Vink, 1956). Incorporation of such ions leads to the formation of two U^{5+} ions according to the following reaction:

$$\frac{1}{2}O_2 \leftrightarrow O_I'' + 2U_U^{\circ} \tag{1.1}$$

, where U_U° represents U^{5+} ions.

As mentioned in the previous section, analyses of deviation-from-stoichiometry and electrical conductivity data relative to the UO_{2+x} phase, conclude that in the temperature range we are concerned with here, doubly-charged isolated oxygen interstitials give way to singly-charged di-interstitial clusters as deviation-from-stoichiometry rises (Garcia et al., 2017; Ruello et al., 2004). It has also been concluded from the formation energy calculations of charged defect clusters that increasing non-stoichiometry favours both anion clustering and a decrease in the charge state of the most stable cluster (Crocombette, 2012; Crocombette et al., 2011). The reason has to be found in the effect of entropy. In general, having single isolated defects such as those described in equation (1.1) is favourable from the point of view of entropy, but unfavourable from the stand point of energy. However, as charged defect concentrations rise, the entropy gain of having isolated defects is lost over the energy gain that is incurred from having them in a compact clustered form with a lower overall charge. This may explain why doubly charged negative oxygen ions will tend to form structures in which they are associated with three U^{5+} ions (that are now pinned to the defect) to form one negatively charged di-interstitial cluster. One would expect therefore to see a gradual change in the majority anion defect population as deviation-from-stoichiometry increases from a single-interstitial to a di-interstitial (Andersson et al., 2009; Willis, 1978), to possibly an even more compact structure such as those encountered in U_4O_9 (Andersson et al., 2012; Cooper and Willis, 2004; Desgranges et al., 2016).

1.2.4 Structural characterisation of anion clustering from experiment and theory

It is reported that the anion defect clusters alluded to in the previous section have an influence on various engineering properties, notably the chemical diffusion of oxygen (Ruello et al., 2004). One is therefore justified in seeking to identify the atomic arrangement of these defects and the conditions under which they are stable. Such characterisations can also provide data against which the growing number of theoretical atomic-scale studies may be assessed.

Different types of defects in hyper-stoichiometric uranium dioxide have been suggested either from experimental or theoretical studies. The most obvious one is the single interstitial in which an oxygen ion occupies an octahedral site of the UO_2 fluorite structure as Figure 1.4.a illustrates. Willis (Willis, 1964) and Murray (Murray and Willis, 1990) proposed and refined an oxygen defect cluster in UO_{2+x} but at relatively high deviation-from-stoichiometry (roughly 2.12). Willis's analyses of neutron diffraction data obtained at 800 ℃ indicated the presence of what was subsequently coined a "Willis cluster". This type of 2:2:2 defect consists of two regular oxygen atoms displaced away from their original position by approximately 1 Å in the <111> direction (thus producing two unoccupied regular lattice positions and two interstitials) and two adjacent interstitial oxygen ions displaced in the <110> direction from the octahedral site. This defect is illustrated in Figure 1.4.b.

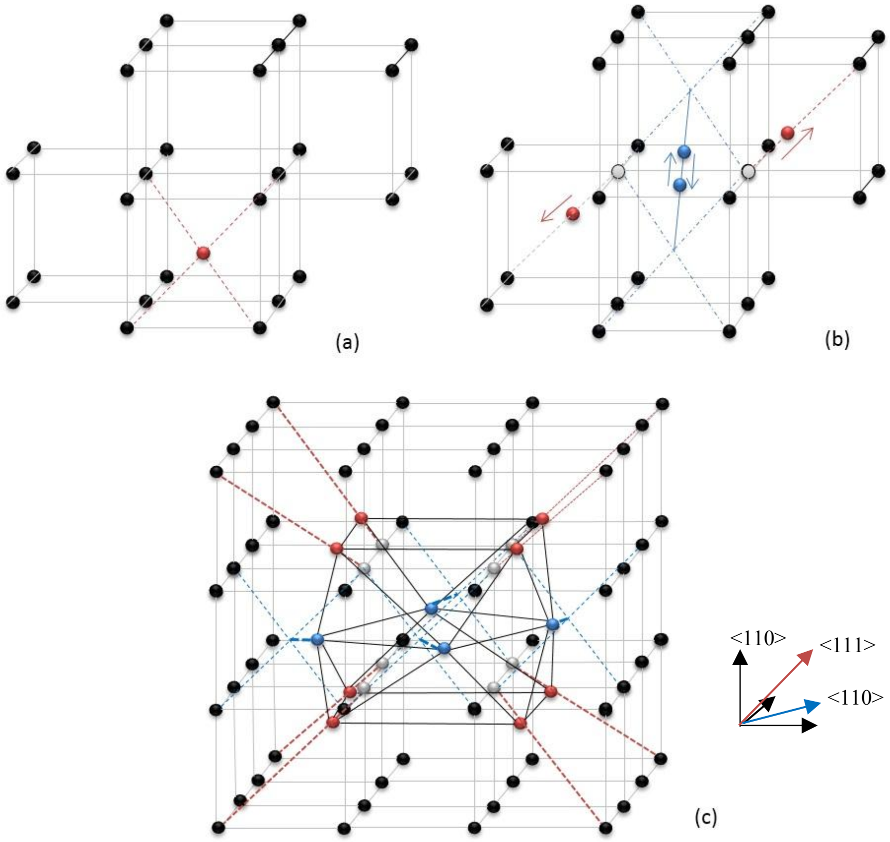

Figure 1.4: Three types of expected oxygen defects mainly based on experimental data - (a) Single-interstitial in red occupying the octahedral site; (b) Willis 2:2:2 cluster with two interstitial oxygen ions in blue moving along <110> direction (blue dashed lines), and two lattice oxygen atoms in red displaced along <111> direction (red dashed lines), grey spheres are the remaining oxygen vacancies; (c) cuboctahedron defect, the colour codes are the same as for (b) (from (Willis, 1964)). Black spheres are oxygen ions on normal lattice sites.

With the recent rise in the number of theoretical studies based on first principles and more recently *ab initio* molecular dynamics computations, yet more atomic configurations for oxygen clusters have been reported. Geng et al. (Geng et al., 2008) performed first-principles calculations and suggested that the oxygen cuboctahedron cluster would be more stable in UO_{2+x} when there is an additional oxygen at the centre of the cluster. Andersson et al. (Andersson et al., 2009) suggested that di-interstitials could relax into a split di-interstitial cluster in Figure 1.5.a). In a follow-up study relating to greater deviation-from-stoichiometry material, he suggested that cuboctahedron-type defects shown in Figure 1.4.c could transform into yet another defect type which he designated as the split quad-interstitial which is shown in Figure 1.5.b and comprises two edge-sharing split di-interstitials (Andersson et al., 2012).

In the past, Cheetham (Cheetham et al., 1971) suggested a 4:3:2 anion defect configuration for Calcium fluoride, which was further studied by Catlow (Catlow, 1976a, 1977) for highly oxidized material (e.g.$UO_{2.13}$) as Figure 1.5.c shows. He calculated the energy associated with the relaxation of interstitial and lattice oxygen ions (Catlow, 1976b). This cluster comprises four oxygen interstitials moving along <110> directions, three oxygen vacancies and two lattice oxygen ions displaced towards the octahedral site along the <111> direction. Following his work, Allen and Tempest (Allen and Tempest, 1983) suggested the distorted fluorite structure of UO_{2+x} is a mixture of chained Willis clusters and 4:3:2 clusters in proportion.

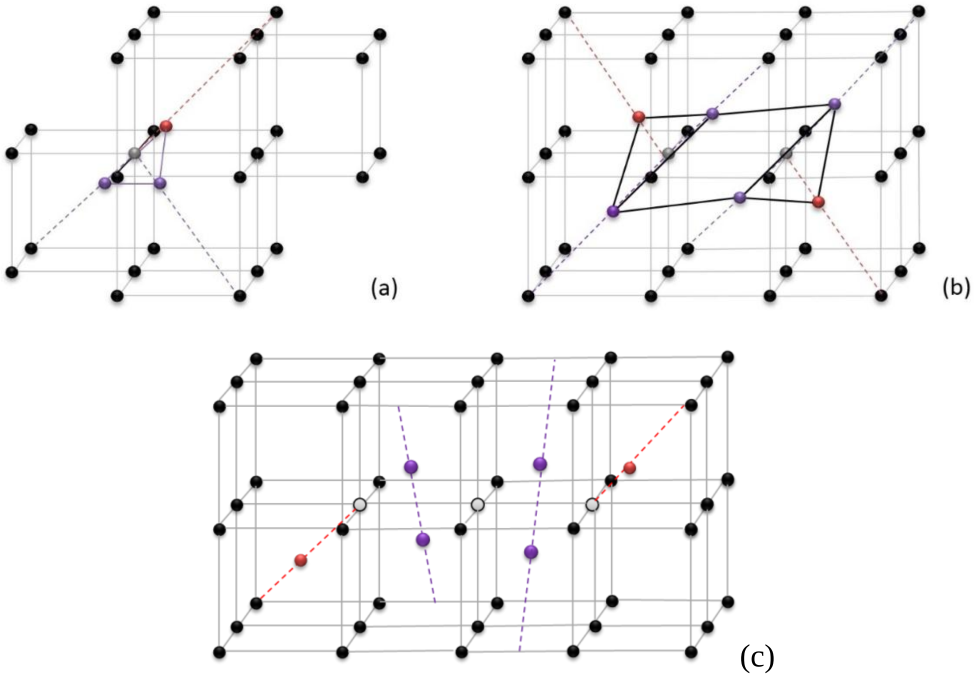

Figure 1.5: Two oxygen defect cluster structures suggested by computational methods (a) Split di-interstitial model O_X with two interstitials in purple moving towards one lattice oxygen ion in red that moves along a <111> direction and sharing an oxygen vacancy (Andersson et al., 2009); (b) Split quad-interstitial (purple spheres and red spheres) belonging to two individual split di-interstitials, colour codes are the same as in (a); (c) the 4:3:2 cluster with four interstitials in purple moving along the <110> direction, three vacancies in grey and two lattice oxygen ions displaced along a <111> direction.

Wang et al. tackled the temperature dependent problem by performing first-principles molecular dynamics calculations between 300K and 2000K. They modelled a supercell with O/M ratios of 2.06, 2.13, and 2.19. The resulting atomic density probability map showed that the split di-interstitial cluster, is the dominant defect at temperatures below 1200 K, therefore confirming Andersson's initial study at 0 K. Furthermore, his calculations show that the Willis cluster is simply a transient state between two split di-interstitial configurations which may enable oxygen migration to occur at high temperature (Wang et al., 2014). The latest DFT study in relation to this carried out by Brincat et al. (Brincat et al., 2015) suggests that at high deviation-from-stoichiometry Willis defects are stabilised into chains or may co-exist with single interstitials$_i$, and therefore constitute a genuine type of defect in UO_{2+x}. According to Brincat, below a deviation-from-stoichiometry of 0.125, the Willis defect transforms into a more stable split di-interstitial.

1.2.5 Conclusions

We have seen that anion defects in UO_{2+x} have a tendency to cluster and that this clustering process is related to the structural characteristics of higher oxide phases. This transpires from property measurements, structural and DFT studies. However, at this stage, it is difficult to draw up a clear picture of the type of oxygen clusters that exist in UO_{2+x} over the entire range of temperatures and oxygen pressures of interest. Obviously the nature of these defects will play a major role on the properties of UO_{2+x} and oxygen diffusion in particular. Our study, as laid out in Chapter 3 and 4, aims to contribute to improving the understanding of this phase and determining which if any of the above mentioned clusters predominate over others for a given oxygen content. In the next section, we focus on uranium vacancy defects as they are crucial to different set of properties.

1.3 Cation vacancy defects and their characterisation

1.3.1 Uranium vacancies and their impact on fuel behaviour

A great deal of effort has been devoted to understanding anion defect properties from certain oxidation dependent quantities such as the relation between stoichiometry (Perron, 1968), or electrical conductivity and the chemical potential of oxygen (Ruello et al., 2004). Oxygen self-diffusion has been extensively studied both experimentally (Auskern and Belle, 1961; Belle, 1969; Breitung, 1978; Contamin et al., 1972; Dorado et al., 2010; Garcia et al., 2010; Nagels et al., 1966; Sabioni et al., 2000) and by computational methods (Andersson et al., 2009; Bai et al., 2013; Dorado et al., 2010; Skomurski et al., 2013).

Characterising cation defects and properties related to them is a more complicated task because it involves much slower processes that occur at higher temperatures than for oxygen. Also, the choice of the property has to be related as directly as possible to the behaviour of cation defects (Dieckmann, 1984). As will be seen below and in section 1.4.3, uranium self-diffusion is one such property.

Although uranium diffusion involves cation defects in much smaller concentrations than those responsible for oxygen diffusion, it is essential to characterise this property because it is the rate-determining step for a variety of essential microstructural changes covering the whole range of the nuclear fuel cycle. We provide in this section a few examples that highlight the importance of cation self-diffusion and cation vacancy diffusion in UO_2.

Creep laws, i.e. strain rates observed at high temperature under high stresses, as suggested by Philibert in most binary oxides (Philibert, 1984), are usually expressed as being proportional to the diffusion coefficient of the slowest moving defect species. The fundamental reason for this is that for deformation to occur requires the movement of an entire molecule of solid, i.e. a UO_2 formula. Migration barriers calculated from first principles (Dorado et al., 2012, 2010) and derived, albeit indirectly, from self-diffusion experiments (Matzke, 1987, 1969), suggest that uranium vacancies are by far the slowest moving defect species (activation energies for U self-diffusion are higher than for O self-diffusion). In addition to which it is also suggested that uranium migration occurs via a vacancy mechanism (Dorado et al., 2012). So as regards creep laws, and essentially irrespective of the deformation mechanism, strain rates are proportional to the uranium vacancy diffusion mechanism.

Sintering is also a good example of a phenomenon that it is at some stage of the process controlled by cation volume diffusion. The so-called third stage of sintering which involves the elimination or shrinkage of large size closed pores requires that vacancies be eliminated to free surfaces at the outer boundaries of the solid (Harada, 1997). This requires the transport of vacancies from the pores to the external surfaces of the solid which shrinks as a result.

Until now, we have only illustrated the relevance of studying uranium vacancies through examples that do not involve radiation effects. However, although they do not explain by any means all the very complex phenomena induced under irradiation, cation vacancies and cation vacancy behaviour hold at least part of the answer. This is particularly true of fission product behaviour. Jackson and Catlow published results from atomistic studies (Catlow, 1978; Jackson et al., 1986) which showed that incorporation energies for xenon (i.e. the energy gain or cost of incorporating a xenon atom into a pre-existing defect) were the lowest for uranium vacancies or clusters of vacancies involving at least one uranium vacancy. Grimes and Catlow then went on to look at a host of other fission products and concluded that Cs and Rb were also most stable at tri-vacancy sites (two oxygen vacancies and one uranium vacancy) (Grimes and Catlow, 1991). Under irradiation, these defects are expected to be present as host sites in quantities much greater than predicted from thermodynamic equilibrium. The fact that defects involving uranium vacancies are favourable incorporation sites for fission products have since been confirmed for iodine (Dorado et al., 2009) and krypton (Martin et al., 2015) and xenon (Bès et al., 2015) from first principles calculations and X-ray absorption experiments. Naturally, the reported mechanisms for the diffusion of these fission products often involves vacancies. Andersson et al. recently proposed a reassessment of a number of basic xenon diffusion experiments based on a model assuming the migration of xenon bound to a di-(uranium type)-vacancy (Andersson et al., 2014). A simple kinetic model was developed and appropriate energetics (formation, migration and binding enthalpies) were derived from first principles.

Most kinetic models describing radiation induced microstructural changes in UO_2 assume, in a way similar to what is considered in metals, that the rate of change of bulk point defect concentrations can simply be described by two coupled ordinary differential equations in which only the cation vacancies and interstitials are considered (White and Tucker, 1983), or alternatively that only neutral defects need be treated under irradiation (Skorek, 2013).

1.3.2 Basic defect equilibrium representation of UO_{2+x}

It is important at this stage to discuss the defect equilibria which will be used in the course of this work to understand, if only qualitatively, the types of defects one can expect in UO_{2+x} and how their concentration changes with changing oxygen activity. We use Kröger-Vink notation (Kröger and Vink, 1956) as it is a useful way of expressing equilibria between defects with site and charge constraints. In this notation A_S^C the subscript designates the sublattice (O: oxygen sublattice, U: uranium sublattice, I: interstitial sites), the main character designates what is at the site (V is a vacancy, O: oxygen ion, U: uranium ion) and the superscript is the apparent charge of the defect: ' representing negative charges, ° positive charges and ^{X} a neutral defect.

Frenkel disorder is accounted for through the following equilibria (assuming for simplicity that the activity of the host lattice species is unity, as expected in a dilute system):

$$\emptyset \leftrightarrow U_I^{\circ\circ\circ\circ} + V_U'''' \tag{1.2}$$

$$\emptyset \leftrightarrow O_I'' + V_O^{\circ\circ} \tag{1.3}$$

,where $\emptyset$ represents the ideal material with no point defect. These equilibria are characterised in a dilute system by the following equilibrium constants:

$$K_{FP_U} = [U_I^{\circ\circ\circ\circ}][V_U''''] = exp\left(-\frac{\Delta G_{FP_U}}{k_B T}\right) \tag{1.4}$$

$$K_{FP_O} = [O_I''][V_O^{\circ\circ}] = \exp\left(-\frac{\Delta G_{FP_O}}{k_B T}\right) \tag{1.5}$$

, where ΔG represents the Gibbs free energy associated with appropriate equilibrium. Because the formation energies associated with uranium Frenkel disorder (equation 1.2) are so much higher than the other two (Dorado et al., 2012), this type of disorder is neglected.

The basic oxidation reaction for UO_2 is given by equation 1.1. and is associated with the following equilibrium constant:

$$K_{O_i} = \frac{[O_i''][U_U^\circ]^2}{\sqrt{p_{O_2}}} = \exp\left(-\frac{\Delta G_{O_i}}{k_B T}\right) \tag{1.6}$$

The fourth fundamental defect equilibrium describes Schotty disorder:

$$\emptyset \leftrightarrow 2V_O^{\circ\circ} + V_U'''' \tag{1.7}$$

and its equilibrium constant is:

$$K_S = [V_U''''][V_O^{\circ\circ}]^2 = \exp(-\frac{\Delta G_S}{k_B T}) \tag{1.8}$$

Several comments may be made at this stage:

1- These equations and notably the charges of the respective defects reflect a purely ionic behaviour. This is expected at or around exact stoichiometry. If the material deviates from stoichiometry, then the defect charges are expected to change (Crocombette, 2012; Crocombette et al., 2011; Vathonne et al., 2014).

2- This latter fourth equilibrium corresponds physically to the movement of two oxygen vacancies and one uranium vacancy from the bulk of the material to its surface. Assume it is characterised by an equilibrium constant which is a function of temperature $K_S(T)$. It has been shown that there is an energy gain for the material to form neutral Schottky trios, or in other words that the enthalpy of the following reaction is negative:

$$2V_O^{\circ\circ} + V_U'''' \leftrightarrow S \tag{1.9}$$

Where S designates a neutral Schottky trio. This equilibrium is characterised by an equilibrium constant which is a function of temperature only:

$$K_S{}'(T) = \frac{S}{[V_U''''][V_O^{\circ\circ}]^2} \tag{1.10}$$

Combining equation (1.8) and equation (1.10) shows that for **a near stoichiometric composition, the concentration in Schottky trios is a function of temperature only and so is independent of oxygen partial pressure.**

3- The final equation which is fundamental to ionic solids is the electroneutrality equation. Depending on its form the various defect concentrations have different dependencies upon oxygen partial pressure. For example, if it is given by U_U° ~ U_U'(usually the case at exact stoichiometry), then

$$[V_U''''] = \frac{K_{O_I}^2 K_S}{K_{eh}^2 K_{FP_O}^2} p_{O_2} \tag{1.11}$$

Where $K_{eh}^2 = [U_U^{\circ}][U_U']$ is the equilibrium constant of the electron-hole pair.

One can see from this that the concentration of $V_U''''$is in this case an increasing function of temperature and proportional to the equilibrium oxygen partial pressure.

It is indeed a general rule, that the uranium vacancy concentration is expected to increase in our material with increasing oxygen partial pressure. This result is important as it will guide our understanding of dependencies of uranium vacancy related properties in section 1.3.4. Andersson et al. have shown that assuming singly charged di-interstitial clusters and neutral uranium vacancies, leads to the same linear dependence of the vacancy concentration with oxygen partial pressure (Andersson et al., 2014).

In the following sections, we review the literature relating to the characterisation of cation vacancies by two methods: 1) a spectroscopic characterization using positron annihilation technique, and 2) a method involving measuring one of the essential fuel properties mentioned in the previous section, uranium self-diffusion.

1.3.3 The study of uranium vacancies in UO_2 and UO_{2+x} by positron annihilation spectroscopy

1.3.3.1 Basic concepts in relation to PAS in semiconductors

Before we examine the PAS literature in relation to UO_2, a few very basic concepts need to be introduced. Without going into the theoretical details of positron annihilation or trapping in solids, suffice it to say that once positrons have slowed down in a solid, *i.e.* once they are thermalized which takes in the region of 1 ps (R. Siegel, 1980), they are liable to annihilate from either a delocalised or a localised state. The former state, usually referring to the lattice, may have similar annihilation characteristics as for the low-binding-energy (Rydberg) states (Puska and Nieminen, 1983). Annihilation in a localised state occurs when positrons are trapped in a region where the core electron density is lower than in the bulk. This is the case of vacancies, vacancy clusters or areas around a dislocation where the solid is locally subjected to tensile stresses (Eldrup and Singh, 2003) or in precipitates when the affinity of positrons for the precipitates is greater than for the matrix (Brauer et al., 1996).

The two essential features that characterise the state in which positrons annihilate are the **positron lifetime** and the **momentum distribution** of the annihilating electron positron pair. The former characteristic can be understood as being sensitive to the concentration and size of vacancies since they constitute a potential well in which positrons may be trapped. In positron trapping models (Puska and Nieminen, 1983), each defect type is characterised by a trapping coefficient. Puska and co-workers showed that in semiconductors, the temperature dependence of this trapping coefficient is characteristic of the charge of the vacancy defect: it is a constant or slowly changing function of temperature for neutral vacancies but goes to infinity (respectively 0) in the case of negatively charged defects (respectively positively charged defects) as the temperature approaches 0 K. It is also the case that the trapping probability at positively charged vacancies, is much lower than at neutral or negative vacancies. In practise, trapping at positively charged vacancies is a negligible phenomenon at temperatures below *circa.* 200 K.

Although there are in general several possible positron electron annihilation reactions, in solids, the overwhelming majority involve the emission of two gamma photons that take away approximately 511 keV each (Dupasquier and Mills, 1997). Deviation from this 511 keV value is known as **Doppler broadening**. Because of the energy and momentum conservation principles and since annihilating positrons are thermalized (Barthe et al., 2003), this deviation reflects the momentum of the electrons with which positrons annihilate (hence the sensitivity to electronic density and to the chemical environment). Now if vacancies are present in the solid, these can constitute traps for positrons, and annihilation from this state will occur with a greater probability. Since vacancies are regions in the solid of low core electron density, the fraction of annihilating electron positron pairs of low momentum S (*resp.* high momentum W) increases (*resp*. decreases) as a result (Alatalo et al., 1996). The high and low momentum fractions of annihilating pairs (*i.e.* S, W) are therefore also sensitive to the presence of vacancies in a solid.

In order to compare samples of a same material containing different quantities or types of defects, results are usually normalised to a reference value obtained from a supposedly defect-free specimen. In certain cases when annihilation occurs for instance from two or three distinct states, it is possible to show that the (W, S) data points form a line, the slope of which is characteristic of the vacancy defect (Barthe et al., 2007) whence annihilation takes place. A commonly referred to example is that of Hakala *et al.* (Hakala et al., 1998) who compared calculated S and W parameters essentially describing annihilations with valence and core electrons to experimentally determined values. They showed that the slope of the (W, S) function was correlated to the size of vacancy clusters in silicon.

1.3.3.2 Experimental studies involving unirradiated UO_2

The main thrust of defect characterization results relative to uranium containing compounds concerns uranium dioxide. Upadhyaya *et al.* (Upadhyaya et al., 1982) performed positron lifetime measurements on poly-crystalline UO_2 powder to understand the dependence of lifetime on particle sizes. Regarding hyper-stoichiometric uranium dioxide, Howell *et al.* (Howell et al., 1984) were the first to apply PAS in an attempt to clarify the nature of complex defects in oxidized materials.

In the last decade or so however, much effort has been devoted to studying sintered uranium dioxide in various forms. The first results came from a study of sintered polished and in certain cases annealed UO_2 disks. Surface damage induced by the polishing stage of the sample preparation could be picked up using PAS (Barthe et al., 2004). The minimum value of the annihilation fraction with low momentum electrons was obtained for samples annealed at 1700 ℃ in an argon mixture containing 5% hydrogen and very slightly humidified. Both lifetime and Doppler broadening measurements were carried out (Labrim, 2006). Average lifetimes were determined for temperatures ranging between 15 K and 575 K. At temperatures below 335 K, a single lifetime component was resolved which increased slowly from 164±1 at 15 K to 169±1 ps at 335 K. In addition to this, beyond roughly 50 nm from the sample surface, the high and low momentum annihilation fractions and the effective positron diffusion length (unusually small at roughly 9 nm) were found independent of temperature up to room temperature. Both results suggested that positrons were annihilating from a unique state, characteristic of the lattice, and characterised by a lifetime component of *circa.*166 ps (Barthe et al., 2007).

Based on estimates of the trapping at negative ions and annihilation rates in the lattice, the authors conclude that positrons in un-irradiated samples are essentially annihilating from a low energy state, the so-called Rydberg state, corresponding to trapping at oxygen interstitials. It was further surmised that because these Rydberg states are rather shallow wells, the trapped positrons actually probe the electron distribution of the lattice. The annihilation characteristics reported are therefore assumed to constitute the intrinsic annihilation characteristics for UO_2.

1.3.3.3 Experimental studies involving ion or electron irradiated UO_2

Further work was reported on ion irradiated material (Barthe et al., 2007; Labrim et al., 2007, 2006). 45 MeV ^{4}He ions and electrons of both 1 MeV and 2.5 MeV were used to generate damage in pristine material. Both lifetime and Doppler broadening measurements could be carried out because the energies of all the above particles was sufficient for them to go through the thickness of the relatively thin (~300 µm) samples. Doppler broadening measurements corresponded to regions in the samples where the energy loss hence damage could be considered as uniform. In both the 2.5 MeV electron irradiation and the 45 MeV $^4He^+$ irradiation, the authors observed an increase with ion or electron fluence in the low momentum annihilation fraction and conversely a decrease in the high momentum fraction. This was interpreted as the sign of vacancy defect formation. Lifetime measurements at room temperature compounded these results. In the higher energy electron or helium irradiations, the average lifetime of the samples increased with fluence. Furthermore, two lifetime components were systematically detected, one corresponding to that of the reference sample (roughly 161 ps) and the other found at about 305 ps. In subsequent experiments (Wiktor et al., 2014), the intermediate ion-fluence sample (2×10^{16} ions/cm^2) was the object of lifetime measurements at temperatures between 15 K and 300 K. Again two lifetime components were resolved at all temperatures. A low one corresponding in principle to annihilation in the lattice (component at roughly 170 ±5 ps) and a higher one corresponding to a vacancy defect (component at roughly 310 ±5 ps). However, the authors also attempted to model these results using a positron trapping model (Puska and Nieminen, 1994; Tuomisto and Makkonen, 2013). **They found that it was necessary to use a model containing three positron traps to represent experimental results faithfully.** These traps were associated with defects present in the following decreasing order of abundance: neutral vacancies, negatively charged interstitials and negative vacancies. Defect concentrations were based on order of magnitude estimates of trapping coefficients (Tuomisto and Makkonen, 2013).

From these Doppler broadening and lifetime measurements, and since the (W, S) data points, normalised to the reference sample, lay on the same straight line, the authors concluded they were dealing with the same vacancy defect. In the case of 1 MeV-electron irradiation, S and W values were unchanged and only one short lifetime component was found at 166 ps close to that of the un-irradiated material. These results may be interpreted on the basis of Soullard's work (Soullard, 1985). He irradiated UO_2 thin foils in a high voltage electron microscope at electron energies ranging between 1 MeV and 2.5 MeV in 0.2 MeV steps. He found that below 1.6 MeV no defects could be resolved using transmission electron microscopy. However even for energies of 1 MeV, the energy transferred to oxygen ions by electrons either through direct or indirect recoil lies at about 200 eV, so far in excess of what is required to displace them. This is not the case for uranium ions. So he assumed that below 1.6 MeV only oxygen ions were displaced in his UO_2 target.

At energies in excess of 1.8 MeV however, small dislocation interstitial loops were observed, which he attributed to defects being created on the uranium sub-lattice. If we draw a parallel with the ion and electron irradiations mentioned above in relation to PAS, the conclusions which Barthe and co-workers came to was that the defect their spectroscopic technique was sensitive to, involved a single uranium vacancy possibly associated with one or more oxygen vacancies in a cluster. Because the most abundant type of defect found in the 45 MeV ^4He ions irradiated sample was neutral, they concluded that PAS was picking up Schottky defects whenever damage on the uranium sub-lattice was produced.

These results were substantiated further by Doppler broadening measurements carried out on samples irradiated with low energy (1 MeV) $^3He^+$ ions in which a defect with similar annihilation characteristics was observed (Labrim et al., 2006). Finally, to conclude this section, Roudil *et al.* (Roudil et al., 2012) found that in Pu-doped UO_2, the intermediate (one of three) lifetime component (~313 ps) detected in aged material was close to that found in the studies mentioned here.

1.3.3.4 Contribution of modelling at the atomic scale

As for many other solids, the study of UO_2 has greatly benefitted from the development of atomic scale modelling techniques. Classical Molecular Dynamics simulations (CMD) have been used widely to describe radiation effects and in particular damage cascades in UO_2 (Brutzel et al., 2003). Calculations usually span physical times in the region of 20 ps which represents an order of magnitude of the time required for the entire cascade to pass. In their study of primary defect production, Martin et al. (Martin et al., 2014) showed that irrespective of the energy of the primary uranium knock-on, between 50 and 70 % of defects end up as interstitial or vacancy defect clusters amongst which numerous Schottky defects. This result is consistent with the interpretation that the defect which PAS is sensitive to in irradiated UO_2 samples is a neutral Schottky defect, or some type of neutral vacancy cluster containing at least one uranium vacancy. One should bear in mind however that the CMD simulations implement fixed charge models which tend to favour neutral defects and reproduce the ionic character of the material.

Yet more insight was obtained with the modelling work involving Density Functional Theory (DFT). Originally, efforts in using DFT for modelling bulk properties and defect migration and formation energies were hampered by the complications associated with the treatment of uranium $5f$ electrons. A number of functionals have been tested such as hybrid functionals (Crocombette et al., 2011) or the so called DFT+U method to tackle this issue. Regarding the latter, much development has been devoted to schemes that circumvent the difficulty associated with numerous “metastable stables”. These are local energy minima that exist as a result of the presence of $5f$ electrons that can prevent computations from converging to the ground state. Dorado *et al.* (Dorado et al., 2010) proposed a scheme, coined the matrix occupation scheme, that solved this and consistent formation and migration energies were calculated for both neutral and charged defects. Wiktor *et al.* (Wiktor et al., 2014) combined this scheme with others specifically developed for self-consistently calculating positronic and electronic densities. The technical details of the methods go far beyond the scope of this review. Wiktor *et al.* selected two schemes on the grounds that they provided results relating to the lifetime of positrons in the lattice closest to experimental results at room temperature (167 and 168 ps vs. 169 ps determined experimentally). They then went on to calculate a range of lifetimes corresponding to various fully relaxed vacancy defects in charged or neutral states. For defects involving at least one uranium vacancy, from single vacancies to quadri-vacancies and irrespective of the calculation method, positron lifetimes did not span a very broad range of values. This makes the tool somewhat disappointing for discriminating *a priori* between uranium vacancy containing defects and was interpreted as resulting from the fact that as a rule, positrons tend to localise in a uranium vacancy. Consequently in calculations, positrons are in the main insensitive to the presence of other vacancies around them. However, calculated positron lifetimes for

Schottky defects (between 300 and 315 ps) appeared to be extremely close to the values corresponding to the long lifetime component, i.e. the defect identified in the experimental study of irradiated UO_2 (305 ps).

Wiktor *et al.* (Wiktor et al., 2017) further attempted to determine momentum distributions from first principles and compare them to the relevant experimental data. They calculated the momentum distributions for several uranium vacancy containing defect clusters. For all but the largest hexavacancy, they observed that although momentum distributions of annihilating positron electron pairs were dependent on the type of defect, the differences were probably not substantial enough to contribute to a definitive identification of such defects. They also investigated defect charge states and concluded that that had only a very small effect upon the calculated momentum distribution. Finally they compared normalised (W,S) curves to experimental values and concluded that finding consistency between experiment and theory with regard to an “ideal” reference probably prevented any meaningful comparisons to be made.

Two additional points are worth highlighting here in regard to momentum distribution calculations. The first, although not entirely relevant in our context, is that momentum distribution is extremely sensitive to the presence of krypton atoms in a vacancy defect. The second results from a study of the effect of doubly charged negative oxygen interstitials. They found that when the positron is localised around the negative ion, the intensity ratio (ratio of the momentum distribution of the supercell with the defect to the momentum ratio of the supercell without it) corresponding to low momentum electron-positron pairs decreases whereas the intensity ratio for high momentum pairs increases. Unfortunately these results can only be regarded as qualitative as the positron eventually localises away from the defect.

1.3.3.5 Conclusion and directions for future work

The main conclusion to be drawn here is that there is overwhelming evidence, from both PAS experiments and DFT simulations thereof, to suggest that in irradiated UO_2 the annihilation characteristics of electron-positron pairs constitute the signature of a neutral Schottky trio; with a small contribution of negative uranium vacancies and oxygen interstitials.

In nonstoichiometric UO_{2+x} however and so long as the ionic model reflects the behaviour of the material, the classical Schottky equilibrium would suggest that the abundance of neutral tri-vacancies is only temperature dependent (see section 1.3.2). On the other hand, the concentration of single uranium vacancies (which are likely charged depending on the position of the Fermi level), is expected to increase substantially at constant temperature and with increasing oxygen content (See section 1.3.2, or (Lidiard, 1966). The question therefore is whether or not it is possible to pick up from PAS characterisations the signature of thermodynamically induced uranium vacancy defects and how those compare to the signature of Schottky trios. Assuming such evidence is available, what can the contribution of oxygen interstitials to annihilation characteristics be? These questions we tackle in Chapter 3 and 4 of this thesis.

1.3.4 Uranium self-diffusion

The understanding of uranium self-diffusion is critical to improve our knowledge of fuel performance, in particular fuel creep. Creep is the time dependent plastic deformation resulting from the application of a constant stress on a sample over time. The following section provides a critical review of the literature related to uranium self-diffusion in UO_2 and UO_{2+x}, and its correlation to non-irradiated fuel creep. We start with expressing the expected theoretical correlations between strain rates and cation self-diffusion. Based on this we compare self-diffusion data obtained from low-stress creep and self-diffusion experiments thus demonstrating some of these correlations quantitatively. The data covers a wide range of deviation-from-stoichiometry.

1.3.4.1 Diffusion and creep

Many mechanisms have been proposed for high temperature thermal creep of non-irradiated uranium dioxide. The major creep mechanisms reported can be categorized as involving cation self-diffusion (diffusion controlled Nabarro-Herring and Coble creep), grain-boundary (GB) sliding and dislocation glide/climb also known as restoration creep.

Nabarro and Herring (Herring, 1950) proposed a vacancy-defect diffusion controlled deformation mechanism of poly-crystalline materials with different grain geometries. At high stress, but low enough so as not to activate the slip systems, the concentration of thermal vacancies is changed. Vacancies are assumed to be in equilibrium at free surfaces but there is a global chemical potential imbalance and a flow of vacancy from the surface in tension to the surface in compression occurs. The general expression of strain rate $\dot{\varepsilon}$ involving the volume diffusion of vacancies is:

$$\dot{\varepsilon}_{N-H} = \frac{A_{NH}\sigma D_U^V \Omega}{d^2 kT} \tag{1.12}$$

, where σ is the applied stress, D_{U_V} is the uranium volume self-diffusion coefficient, Ω is the atomic volume, d is the average grain size and A_{NH} is a dimensionless proportionality constant (~28), k is the g constant and T is the temperature (Mohamed and Soliman, 1982). The diffusion of vacancies at grain-boundaries may dominate creep in the case where the total area of interfaces is very large (e.g. samples with fine grains). On the basis of Nabarro-Herring's work, Coble extended the model accounting for this fact (Coble, 1963):

$$\dot{\varepsilon}_{Co} = A_{Co}\left(\frac{b}{d}\right)^3 \frac{D_U^{gb} b}{kT}\sigma \tag{1.13}$$

, where b is the Burgers vector. In this formula, the strain rate depends linearly on the experimental grain-boundary diffusion coefficients D_U^{gb} and applied stress. On the basis of diffusion-controlled creep models, Raj *et* Ashby (Raj and Ashby, 1971), followed by Ashby et Verrall (Ashby and Verrall, 1973) proposed a model for grain-boundary sliding with diffusion accommodation which also takes the interface reaction into account.

$$\dot{\varepsilon} = A_{RA}\frac{\Omega}{kTd^2}\left\{\sigma - \frac{0.72\Gamma}{d}\right\}D_{U_V}\left(1 + \frac{3.3\delta}{d}\frac{D_U^{gb}}{D_{U_V}}\right) \quad (1.14)$$

where, Γ represents the grain boundary free energy, and other symbols are the same as in equation 2.1 and 2.2.

At higher stresses, slip systems are activated. At those levels of stress, the strain rate is controlled by a restoration mechanism involving dislocation climb. As a result Weertman (Weertman, 1957, 1955) assumes that the rate- controlling process is vacancy diffusion and he derived the following strain rate expression:

$$\dot{\varepsilon} = A_W\frac{D_U^V}{b^{3.5}M^{0.5}}\left(\frac{\sigma}{\mu}\right)^{4.5}\frac{\mu b^3}{kT} \quad (1.15)$$

M represents the density of dislocation sources, independent of stress; b is the Burger vector, and μ is the shear modulus.

A distinct creep mechanism based on observations in pure Aluminium (Harper and Dorn, 1957; Yajima et al., 1966) (Harper-Dorn or H-D model) was also proposed for uranium dioxide. This deformation mechanism has characteristics that are similar to Nabarro-Herring creep in that it is proportional to the applied stress and lattice diffusion coefficient. However it differs from it in that it yields strain rates at low stresses that are several orders of magnitude greater than in the case of Nabarro-Herring creep. It is a process in which the dislocation density is independent of stress or grain size (Langdon and Yavari, 1982; Nabarro, 2002).

$$\dot{\varepsilon} = A_{HD}\left(\frac{D_U^V b}{kT}\right)\left(\frac{\sigma}{\mu}\right)^{1.0} \quad (1.16)$$

In uranium dioxide, oxygen diffusion coefficients are greater than uranium, so uranium self-diffusion is rate-limiting during creep-induced deformations at any grain size, stoichiometry or temperature (Philibert, 1991). The most abundant cation defects in stoichiometric and hyper-stoichiometric UO_2 are uranium vacancies (see section 1.3.2) so that in most cases, uranium vacancy movement is the rate controlling phenomenon.

1.3.4.2 The uranium self-diffusion coefficients in UO_2 and UO_{2+x} from diffusion and creep experiments

Stoichiometric UO_2

In polycrystalline uranium dioxide, diffusion of atoms is thought to occur at a much slower rate in the bulk than at interfaces such as grain-boundaries (Matzke, 1987). A number of studies have reported uranium diffusion coefficients in nominally stoichiometric UO_2 by different techniques at various temperatures. Figure 1.6 presents uranium diffusion coefficients obtained from diffusion experiments (Alcock et al., 1966; Auskern and Belle, 1961; Matzke, 1969; Nagels et al., 1966; Reimann and Lundy, 1969; Sabioni et al., 2000, 1998; Schmitz and Lindner, 1965; Yajima et al., 1966) and creep tests (Bohaboy et al., 1969; Burton and Reynolds, 1973a; Chung and Davies, 1979; IAEA, 1962; Knorr et al., 1989; Poteat and Yust, 1968; Wolfe and Kaufman, 1967) reported in the literature. The available data, although apparently abundant, appear to be extremely scattered. This is true for both volume or bulk diffusion (D_U^V) and grain boundary diffusion (D_U^{gb}) obtained from tracer diffusion experiments (black lines in Figure 1.6). The scatter may be due to a number of complex effects inherent to the systems that people have studied. One major source of scatter is no doubt related to an insufficient control of experimental conditions such as the equilibrium oxygen partial pressure and the concentration of aliovalent cation impurities inevitably present on the cation sub-lattices. Also, the short-circuit, grain-boundary diffusion mechanisms may be active in poly-crystalline UO_2 that are not necessarily taken into account in the interpretations. Matzke (Matzke, 1983) points out some complications due to surface effects, such as evaporation of the tracer, material redistribution as a result of annealing of surface polishing damage and interface diffusion.

Pink lines in Figure 1.6 report uranium self-diffusion coefficients derived from creep data and equations (1.12) and (1.13). The bulk and grain boundary diffusion coefficients derived from creep experiments are in general higher than those obtained from self-diffusion experiments (black lines). One explanation for this may lie in the fact that the models used do not correctly describe the deformation process (see reference (Wang and Nieh, 1996)). An in-depth comparison of results derived from different authors would require a detailed discussion of the mechanical models used in analysing the raw data and this goes beyond the scope of the thesis.

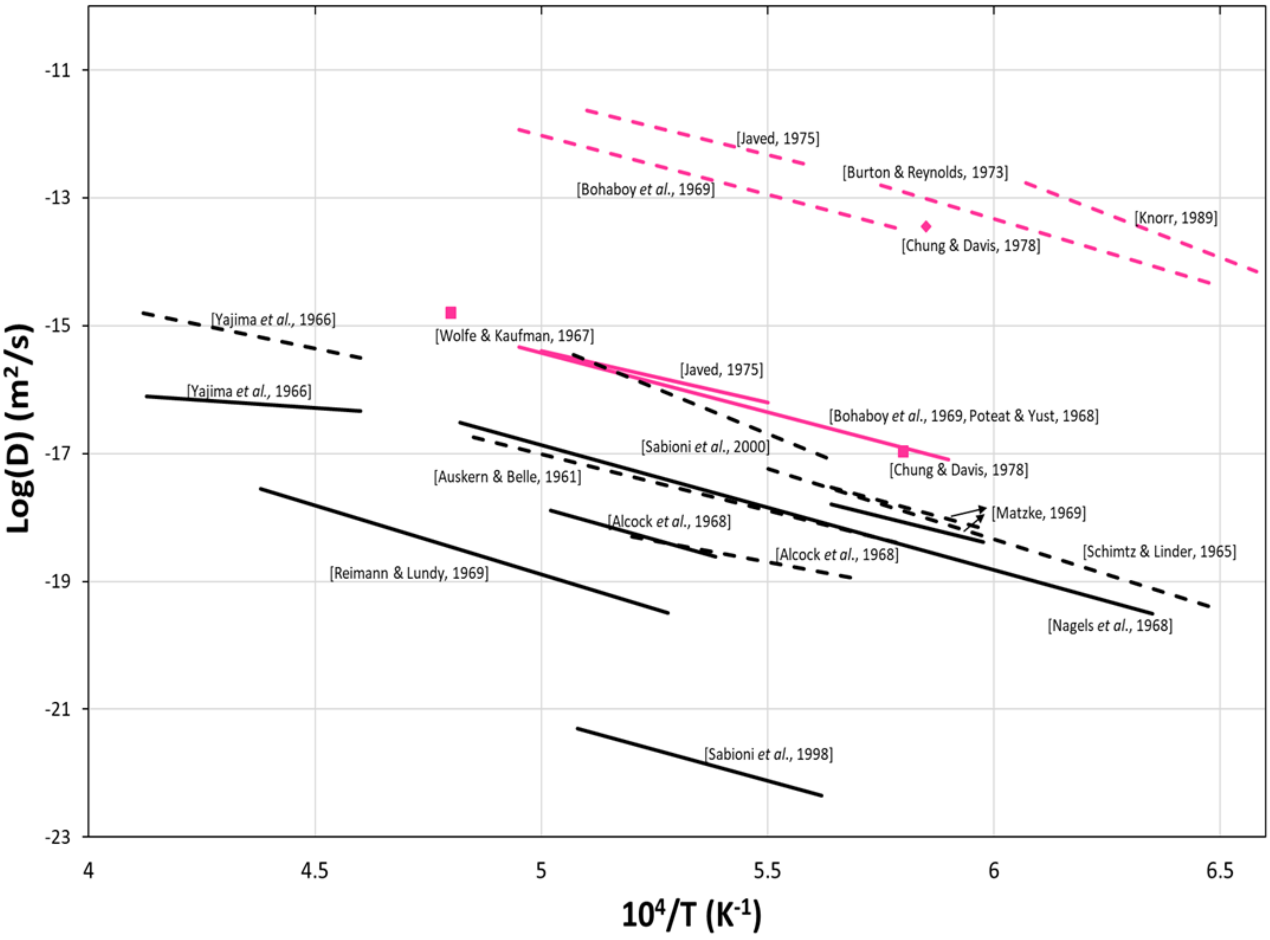

Figure 1.6: Uranium diffusion coefficient measured in nominally stoichiometric UO_2. Solid lines represent volume diffusion coefficients while dashed lines are grain-boundary diffusion coefficients. The lines in black are data from tracer diffusion experiments, and those in pink are data from creep tests applying Nabarro-Herring (solid) or Coble models (dash).

The activation energies for uranium volume diffusion in single crystalline UO_2 are reported by (Sabioni et al., 1998), (Matzke, 1969) and (Reimann and Lundy, 1969) to be 425 kJ/mol, 540 kJ/mol and 411 kJ/mol respectively. The activation energies derived from self-diffusion tests in poly-crystalline UO_2 extends over a larger range between 215 kJ/mol and 463 kJ/mol (Alcock et al., 1966; Auskern and Belle, 1961; Matzke, 1969; Schmitz and Lindner, 1965; Yajima et al., 1966) (except a value of 540 kJ/mol reported by (Matzke, 1983)). The reported values from low-stress creep tests for nominally stoichiometric UO_2 also vary substantially from 294 kJ/mol to 397 kJ/mol. The high value of 540 kJ/mol is consistent with activation energies derived from high-stress creep tests (552 kJ/mol in (Bohaboy et al., 1969), 523 kJ/mol in (Dherbey et al., 2002), 549 kJ/mol in (Salvo et al., 2015)). The generally lower activation energies reported in poly-crystalline UO_2 in comparison to single crystalline UO_2 could be due to short-circuit mechanisms involving grain boundary or surface (grain-boundary) modifications possibly caused by oxidation.

Hyper-stoichiometric UO_2

Few studies have reported uranium self-diffusion coefficients in hyper-stoichiometric UO_{2+x} at different deviations-from-stoichiometry. Figure 1.7 presents the evolution of D_U measured at 1500 ℃ as a function of deviation-from-stoichiometry in UO_{2+x}. The apparent uranium self-diffusion coefficients for poly-crystalline UO_{2+x} obtained by (Marin and Contamin, 1969) at 1500 ℃ appear to be somewhat lower than other reported values. The differences in values may be caused by a number of effects including poor control of experimental conditions. The quality of the specimens used are also sometimes in doubt as suggested by (Matzke, 1983) (*e.g.* the sample may have organic polishing residues at the surface which may release oxygen during high temperature annealing).

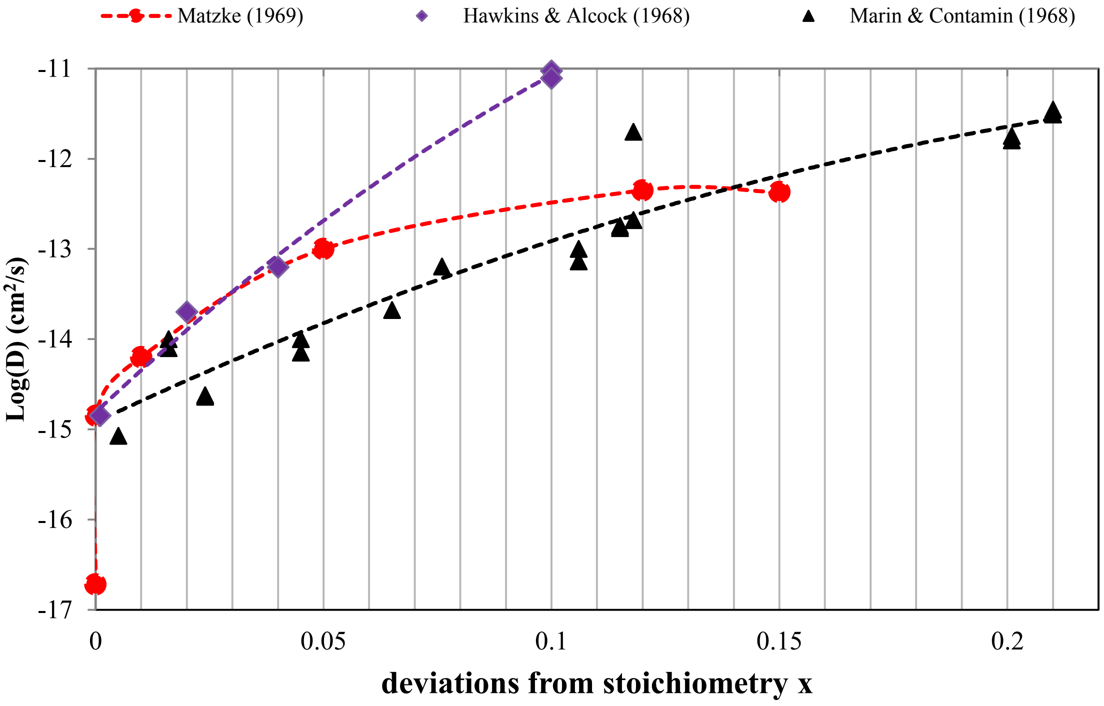

Figure 1.7: Uranium self-diffusion coefficients in UO_{2+x} measured at 1500 ℃ (Hawkins and Alcock, 1968; Marin and Contamin, 1969; Matzke, 1973).

Despite that, Matzke (Matzke, 1973) and Hawkins *et* Alcock (Hawkins and Alcock, 1968) obtained quite similar self-diffusion values in the low-deviation-from-stoichiometry region. Uranium volume and grain-boundary diffusivities derived from creep data for UO_{2+x} are, as for UO_2, significantly higher than values reported in self-diffusion experiments. In addition to the difficulty reported earlier related to the choice of a model to interpret the creep data, in this low stoichiometry region ($0<x<0.04$) which is of particular interest to us, we are faced with the additional difficulty that D_U increases significantly when the material picks up only small quantities of oxygen. We aim to examine the correlation between the apparent diffusion coefficients and stoichiometry in UO_{2+x}, particularly at low deviations-from-stoichiometry with an emphasis on control of thermodynamic conditions.

The activation energies in hyper-stoichiometric UO_{2+x} derived from self-diffusion studies show a scatter similar to that observed in stoichiometric material. For uranium volume diffusion, Hawkins *et* Alcock report values ranging from 335 to 435 kJ/mol for $0.01 \leq x \leq 0.15$, with an initial increase followed by a decrease with increasing oxygen content. Marin and Contamin as well as Matzke have reported values of 352 kJ/mol (for $0.03 \leq x \leq 0.27$) and 250kJ/mol (stoichiometry is not specified) respectively through tracer diffusion experiments in poly-crystalline UO_{2+x}. The most consistent reported activation energy values for UO_{2+x} self-diffusion concern the high deviation from stoichiometry (x>0.01). No reliable result has been obtained for near-stoichiometric UO_{2+x}. Several creep tests have reported the activation energies for UO_{2+x} single- and poly- crystals between 215 kJ/mol and 552 kJ/mol, with a tendency to decrease with increasing oxygen composition (Armstrong and Irvine, 1963; Bohaboy et al., 1969; Burton and Reynolds, 1973b; Scott et al., 1959; Seltzer et al., 1972). The values from creep tests are self-consistent but quite different from the diffusion tests results. Evidently, further work is required to clarify these ambiguities.

1.3.4.3 Tentative interpretation for the dependency of the uranium self-diffusion with non-stoichiometry

The correlation between uranium self-diffusion coefficient, uranium vacancy defect concentrations and oxygen partial pressure has not been reported in general. In Dorado et al.'s work uranium diffusion is described by combining a point defect model, energetics derived from first principles (formation and migration energies) and existing experimental data (Dorado et al., 2012). In tracer diffusion experiments, the oxygen partial pressure is usually neither measured nor controlled. Rather, the majority of diffusion experiments studied the dependence of uranium self-diffusivities directly upon non-stoichiometry x which itself is a property.

Lidiard et al. (Lidiard, 1966) pointed out a dependence upon x^2 of reported uranium self-diffusion coefficient which he interpreted using basic point-defect equilibria. This dependence was verified by Matzke (Matzke, 1969) experimentally. However, the dependence derived from the experiment measurements for x ranging between x=0.005 to 0.2 and for temperatures in the range 1573 – 1923 K showed certain deviations from the expected values. Matzke obtained a dependence of $x^{1.5}$ from diffusivities measured at 1773 K. Marin *et* Contamin extrapolated the uranium self-diffusion coefficients at 1773 K using $x^{1.9}$ (Marin et al., 1967) and x^2 (Marin and Contamin, 1969) dependencies. Hawkins et Alcock (Hawkins and Alcock, 1968) obtained a value of 2.67 ±0.2 for the exponent, but suggested a theoretical value of 2.5 assuming the U^{5+} ions are responsible for the diffusion via a vacancy mechanism. So at high deviations-from-stoichiometry, the exponents reported are all roughly around 2. At lower deviations from stoichiometry this is no longer the case (Knorr et al., 1989) possibly because low deviations-from-stoichiometry not as easy to measure accurately. In addition to this, if the gas composition is not controlled properly, the oxygen content of the material will change during the experiment.

In our study we intend to adopt a different experimental strategy and characterise the self-diffusion coefficient as a function of equilibrium thermodynamic conditions, *i.e.* oxygen partial pressure and temperature. The former quantity is by contrast to deviation-from-stoichiometry, a true intensive thermodynamic quantity, equivalent to temperature.

1.4 Conclusions

We have seen in this chapter that the U-O system is made complex by the variety of possible crystalline imperfections it can accommodate: electronic or point defects with different charge states, both on the anion and cation sublattices. The defect populations in UO_{2+x} have several general characteristics:

1- Electronic defects constitute the majority point defect population, and defect concentrations on the anion sublattice are greater than those on the cation sublattice. Their mobility follows the same decreasing order.
2- Increased deviation from stoichiometry produces a concomitant increase in oxygen interstitial and uranium vacancy concentrations.
3- Increasing deviation from stoichiometry moves the material away from a purely ionic behaviour. Anion defects tend to cluster in an effort to reduce the overall energy of the system.
4- Defects will tend to take on a neutral charge state with increasing deviation from stoichiometry for the same reason as above. Di-interstitial oxygen clusters are shown in certain conditions to have an apparent charge of -1 as opposed to -4 expected if ionic behaviour were relevant. Uranium vacancies have a -4 charge state for a stoichiometric composition but there is circumstantial evidence that they become neutral at higher deviations from stoichiometry.

These changes in defect populations induce changes in corresponding properties. Anion clustering can be correlated to a reduction in the chemical diffusion of oxygen with increasing deviation from stoichiometry. However there is a good deal of uncertainty about the detailed nature of the defect clusters involved. Neutron scattering is a powerful technique for studying such anion defects and this topic is further developed in Chapter 3 in which we describe a number of Pair Distribution Function analyses.

Because deviation from stoichiometry is also expected to induce an increase in the uranium vacancy concentration, it is accompanied by a corresponding increase in the uranium self-diffusion coefficient and other properties closely related to uranium vacancy defect behaviour (fission product diffusion, creep, etc.). Amongst the spectroscopic methods which can be envisaged for characterising uranium vacancies, PAS has proved a very promising. In Chapter 4 of this document we describe a set of PAS experiments carried out on several stoichiometric and non-stoichiometric samples in an attempt to determine: 1- whether thermodynamically induced uranium vacancy defects can be detected using this method and if so, 2- how their annihilation characteristics compare to those encountered in irradiated UO_2 studies. In Chapter 5, we attempt to develop an isotopic tracer method using SIMS for characterising uranium self-diffusion. This method is applied to single and polycrystalline samples. The aim here is to measure this property as a function of temperature and oxygen partial pressure in an effort to derive quantitative information about uranium vacancy defects and associated defect equilibria.

The main results that have surfaced in the course of this work are highlighted and summarised in Chapter 6 in which we also outline a number of areas in which experimental or theoretical progress could be made in relation to these topics.

Chapter 2 Materials and experimental techniques: principles and applications

2.1 Introduction

This chapter presents the materials and experimental techniques that have been used in the course of this work. Details regarding the manufacturing route for single-crystal, poly-crystalline and Chromium doped uranium dioxide samples are succinctly presented in section 2.2. Descriptions of the materials' resulting microstructures are also given.

Section 2.3 describes the various protocols relative to the bulk and surface preparation of samples which are specific to the different types of experiments carried out: neutron scattering, positron annihilation spectroscopy and self-diffusion. In particular, we provide details about the controlled oxidation of UO_{2+x} samples which was carried with a specifically designed device (Garcia, 2011) that can be used for *in situ* electrical conductivity measurements but also enables annealing and quenching of small sized specimens under controlled thermodynamic conditions. This and a second tungsten furnace were used for diffusion annealing samples.

Sections 2.4 and 2.5 present the main experimental techniques used for point-defect characterization. Section 2.4 focuses on the principles that underpin the neutron diffraction and the Pair Distribution Function (PDF) analyses which we have mainly used to characterize anion disorder in UO_{2+x}. Section 2.5 is devoted to positron annihilation spectroscopy (PAS) which we had originally thought of for characterizing uranium vacancy defects. The techniques we have used are Doppler broadening and lifetime spectroscopy experiments. In these sections, we present theoretical and experimental aspects along with data processing procedures.

In section 2.6, we present the experimental methods adopted for self-diffusion measurements. We describe how an enriched $^{235}UO_2$ layer is created at the depleted substrate surface. Details are given for ^{235}U depth profiling using Secondary Ions Mass Spectrometry (SIMS) following high temperature diffusion annealing.

2.2 Materials manufacturing conditions and resulting microstructure

In this study, we have investigated three different microstructures:

- Undoped single-crystal UO_2
- Undoped poly-crystalline UO_2
- Poly-crystalline UO_2 doped with Chromium

The first microstructure concerns materials which were obtained from cooling of molten uranium dioxide. Although we refer to these samples as being “single crystals”, the process actually produced high density materials with millimeter size grains as indicated in the SEM image in a back scattered electron (BSE) mode shown in Figure 2.1. The emerging planes at the surface of the sample have an orientation which is close to {110}. Note that all SEM images were acquired in the Uranium fuels laboratory (Laboratorie des Combustibles Uranium, LCU) at CEA Cadarache with an FEI Nova Nano 450 SEM operating under high vacuum. A high-voltage electron beam (10 kV) is used and images are taken either in secondary or backscattered electron mode (i.e. SE or BSE respectively).

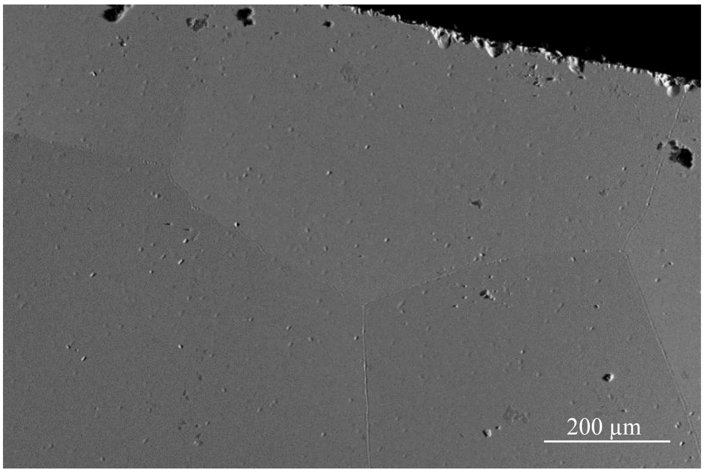

Figure 2.1: SEM image (BSE mode) of a ‘single-crystal’ sample.

The second microstructure is that of pellets which were prepared from pressing a dry route uranium oxide powder and sintering the green pellets at a temperature of 1700 ℃ for four hours under a flowing gas mixture of argon and 5% hydrogen. The sintered pellets had a final density of 10.76 g/cm^3 which corresponds to about 98.2% of the theoretical density. Their diameter was around 8.2 mm and the average grain size 12.7 ±6.4 µm. The SEM image in Figure 2.2.a is typical of these pellets’ microstructure. Some pellets used in the PDF work had a similar microstructure but were sintered to different specific geometries as indicated in Figure 2.2.b.

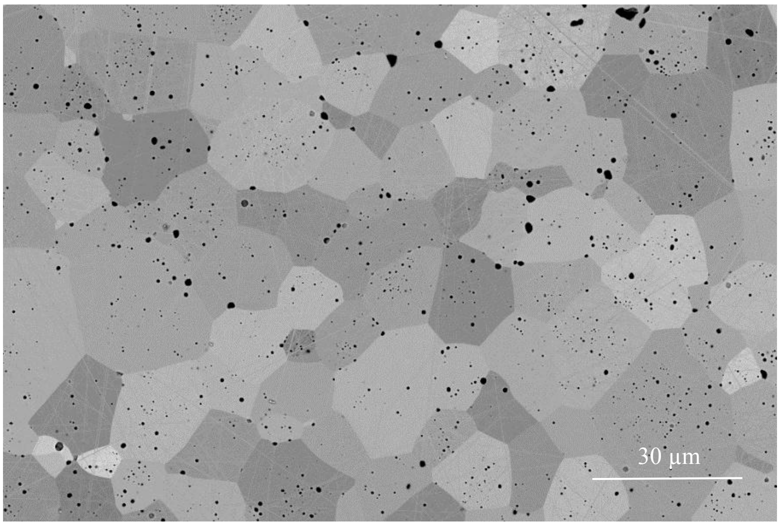

a) Poly-crystalline UO_2 grains;

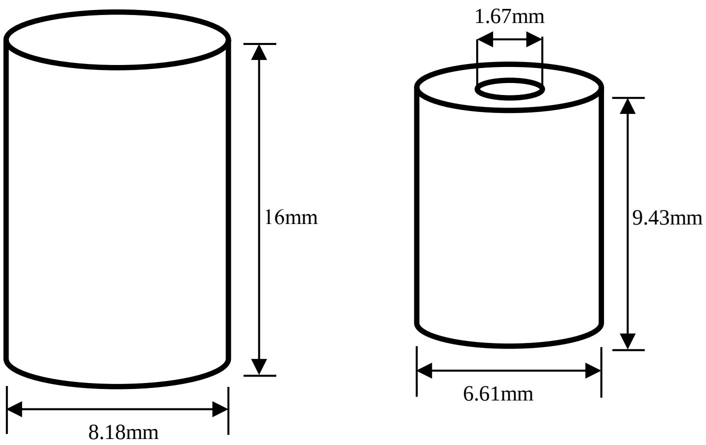

b) Different sintered pellet geometries;

Figure 2.2: a) SEM image (SE mode) of a poly-crystalline sample; b) Schematics of sintered UO_2 pellets: left: full pellets; right: annular pellets.

The third microstructure pertains to a poly-crystalline material containing chromium obtained from blending UO_2 and Cr_2O_3 powders (roughly 0.2 wt% of Cr_2O_3), subsequently pressed and sintered. This resulted in a near homogeneous chromium distribution. Green pellets were sintered at 1760 ℃ under an oxygen potential of -396 kJ/mol (humidified mixture of Ar with 5% H_2). Figure 2.3 shows a Cr-O stability diagram indicating the conditions in which sintering took place.

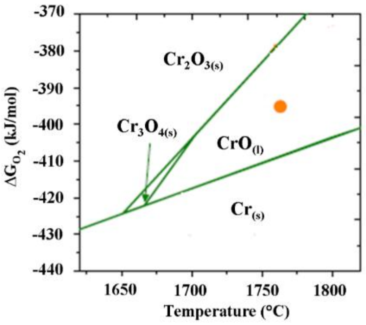

Figure 2.3: Cr-O stability diagram indicating appropriate sintering conditions (orange dot) for the Cr_2O_3-doped UO_2 fuel analysed in this work.

Figure 2.4.a is illustrative of the microstructure of the Chromia-doped fuel obtained from the above mentioned sintering conditions. A pellet cross-section was also analysed by EBSD (Electron Backscattering Diffraction) and showed that the grains were randomly oriented. The grain sizes derived from EBSD maps of the type shown in Figure 2.4.b are smaller at the pellet periphery (35.4 ±18.8 µm) than in the pellet centre (approximately 80 ± 40 µm). Figure 2.4.c shows that chromium rich precipitates appear to be located at the centre of large sized pores.

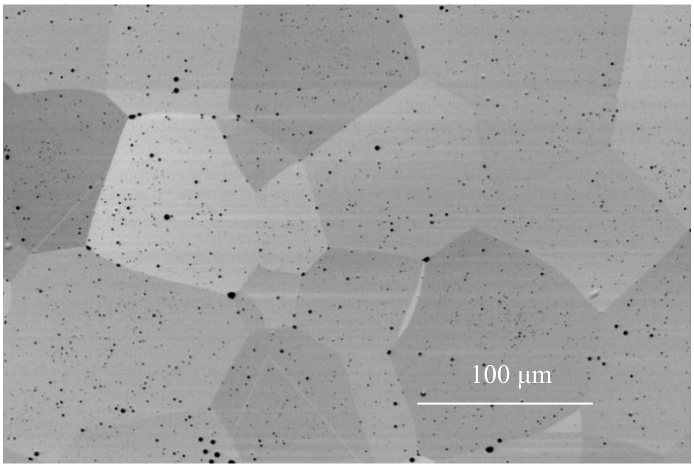

a) Chromium-doped UO_2 grains;

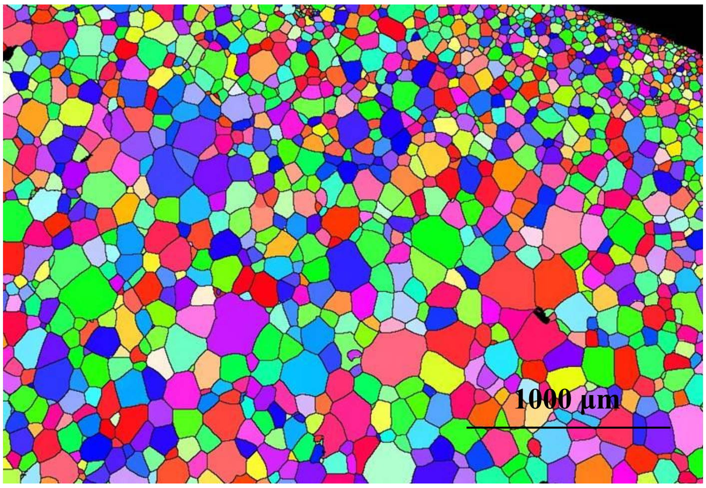

b) EBSD map of a Cr-doped UO_2 pellet cross-section. Colours correspond to different grain orientations.

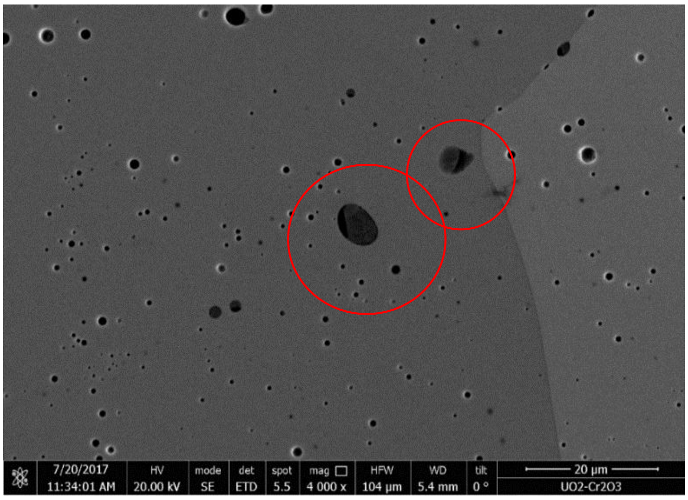

c) Chromium-rich precipitates

Figure 2.4: SEM images illustrative of Cr-doped UO_2 microstructure: a) Cr-doped UO_2 grains (SE mode); b) EBSD map of grains from the central and peripheral region of the pellet, c) Chromium-rich precipitates (SE mode); red circles indicate the locations of precipitates.

2.3 UO_{2+x} sample preparation and characterization

2.3.1 Cutting, polishing and pre-annealing

All samples were prepared for SEM or optical characterizations before being oxidised to the desired degree of non-stoichiometry. Full cylindrical pellets were cut into 1 mm-thick disks of the same radius using a diamond wire saw. Single crystals were cut in slabs. Annular pellets were untouched. All disks and single-crystal slabs were polished on one-side. Samples were first subjected to polishing with a diamond paste and subsequently with a colloidal silica suspension (20 nm particle size).

All samples, except the Cr-doped UO_2, were then annealed for 24 hours under the same conditions as for sintering, i.e. a mixture of Ar and 5% H_2 at 1700 °C. This step is designed to eliminate impurities and polishing residues but also to anneal out all traces of strain induced at the cutting and polishing stages of the process. However it must be noted that for smaller grained polycrystalline samples, this induces a substantial level of surface roughness as is illustrated in the chromatic confocal images shown in Figure 2.5. These images provide an altitude map of the sample surface (see section 2.6). Deep furrows have formed at the interface between two grains.

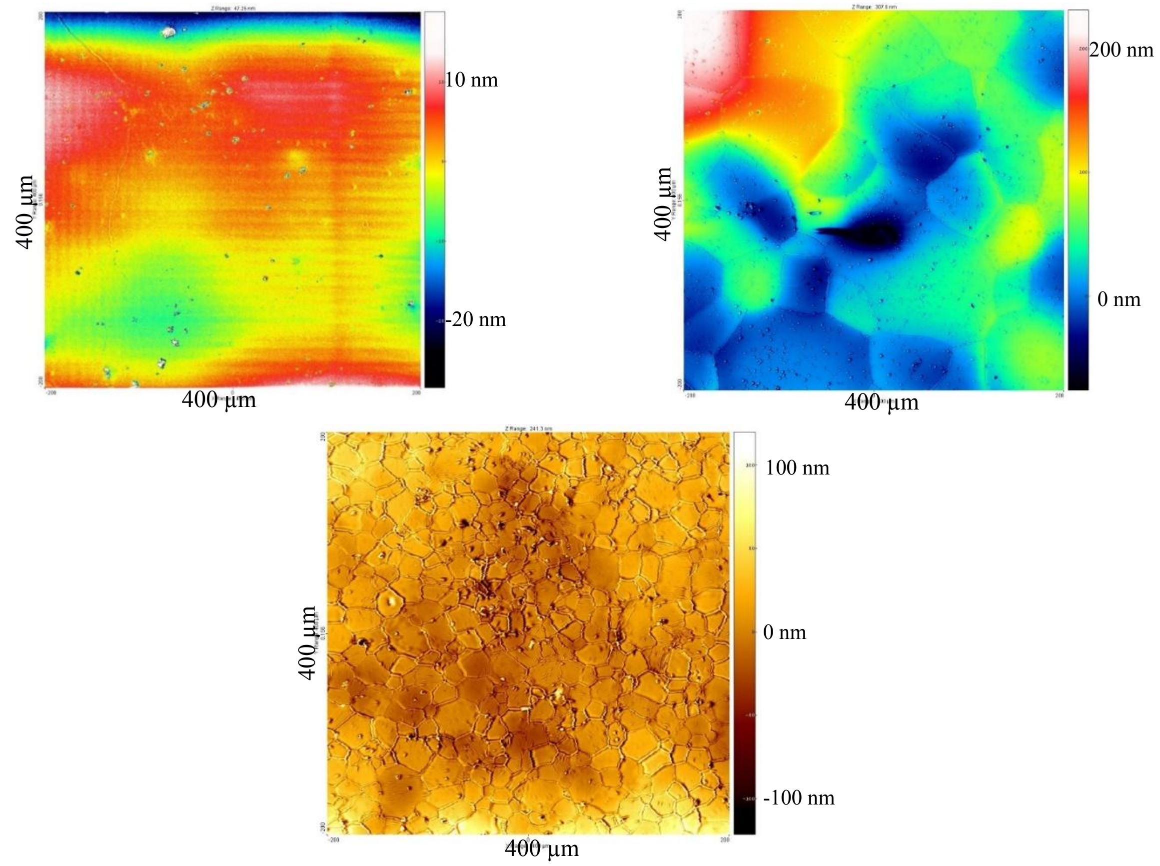

Figure 2.5: 400×400 µm^2 chromatic confocal microscope images of samples: top left – single-crystal UO_2 following annealing at 1700 °C; top right – Cr-doped UO_2 following the last polishing stage; bottom – poly-crystal UO_2 following annealing at 1700 °C.

2.3.2 Controlled oxidation experiments

2.3.2.1 Annealing setups

Following polishing and pre-annealing at 1700 ℃, stoichiometric UO_2 samples were subjected to a controlled oxidation. Two different furnaces were used for this: a small volume (roughly one litre) alumina furnace, equipped with a variety of other features, a schematic description of which is indicated in Figure 2.6 (Garcia, 2011); and a large volume (roughly forty litres) tungsten furnace. This latter equipment was exclusively used in the diffusion experiments to study temperatures in excess of 1400 ℃. But because the heating elements and thermal shielding are in tungsten, the oxygen partial pressures were limited to very low values. The temperature ramps never exceeded 20 ℃ per minute with either of the heating devices. The essential feature of both devices is that they are equipped, upstream and downstream, with systems that control and monitor the oxygen partial pressure that samples are annealed under. This is because for a given temperature, the thermodynamic conditions will determine the non-stoichiometry of the material hence point defect concentrations.

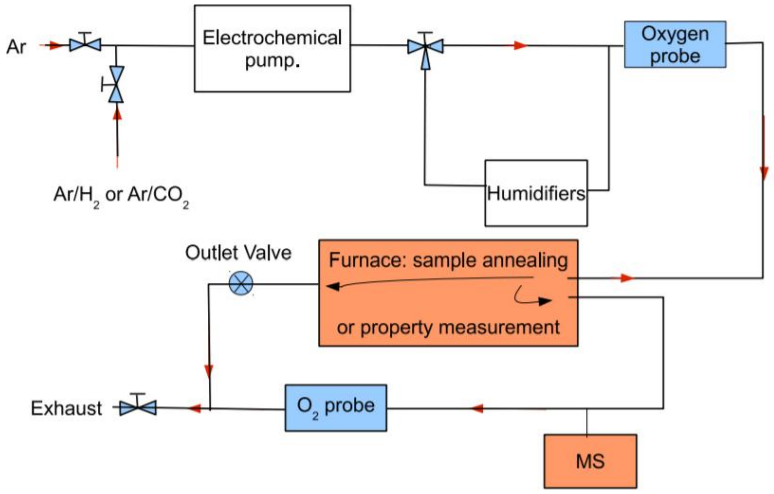

Figure 2.6: Schematic diagram of the alumina furnace.

The oxygen partial pressure was controlled by one of the following gas-phase reactions:

$$H_2(g) + \frac{1}{2}O_2(g) \leftrightarrow H_2O(g) \tag{2.1}$$

And

$$CO(g) + \frac{1}{2}O_2(g) \leftrightarrow CO_2(g) \tag{2.2}$$

Each is characterised by its equilibrium constant:

$$K_{H_2O} = \frac{p_{H_2O}}{p_{H_2} \times \sqrt{p_{O_2}}} \tag{2.3}$$

And

$$K_{H_2O} = \frac{p_{CO_2}}{p_{CO} \times \sqrt{p_{O_2}}} \tag{2.4}$$

where p_{H_2O}, p_{H_2}, p_{CO_2}, p_{CO} and p_{O_2} are the water vapour, hydrogen, carbon dioxide and carbon monoxide and oxygen partial pressures respectively.

The two essential features in Figure 2.6 are the solid electrolyte zirconia oxygen pump (Caneiro et al., 1981; Fouletier et al., 1975) and the oxygen probes. The latter are used to measure the oxygen partial pressures of the gas upstream and downstream from the sample. These sensors are made up of an yttria stabilised zirconia (YSZ) solid electrolyte maintained at 650 ℃ and platinum coated on either side (Fouletier et al., 1975). The gas on one side of the electrolyte constitutes one electrode, and a reference electrode made from an intimate mixture of palladium and palladium oxide constitutes the second electrode. Assuming the YSZ is a purely ionic conductor, Nernst law applies and the oxygen pressure of the gas phase may be derived from the potential drop measured between the two electrodes.

The electrochemical pump is a platinum coated YSZ tube maintained at 800 ℃. The polarisation of the pump induces a current through the thickness of the tube. Because conduction occurs as a result of the movement of oxygen ions, small quantities of molecular oxygen can be injected or extracted from the gas stream. When hydrogen is present and oxygen is injected for example, reaction (2.1) takes place to produce steam. and this induces an increase in the oxygen partial pressure (see equation (2.3). When carbon dioxide is originally present in the gas phase, oxygen is extracted from it which sets up equilibrium (2.2).

It is reasonable to assume that if oxygen partial pressures are identical upstream and downstream from the sample, then the gas phase in the system is **buffered** and the oxygen partial pressure the sample is effectively subjected to can be calculated by extrapolating the measured values at the temperature of the sample. For a given temperature and oxygen partial pressure, the non-stoichiometry of the material can be estimated for example from the NEA data base (OECD NEA/NSC, 2014) or Perron's correlations (Perron, 1968, see chapter 1 section 1.2.2.1) providing a sufficiently long period of time is left for the sample to equilibrate.

At the end of the annealing period, the samples, which are mounted on a mobile sample holder, are quenched by extracting the sample holder into the cold portion of the furnace. In this work, UO_{2+x} samples with deviations-from-stoichiometry ranging from 2.002 to 2.21 were prepared. Deviation from stoichiometry is estimated to within $\pm 2 \cdot 10^{-3}$. The choice of annealing times was based on estimates of the oxygen chemical diffusion coefficients $\widetilde{D}_O$ which can be found in (Ruello et al., 2004), to guarantee the oxygen distribution within the disks was homogeneous, or in other words, that the oxidation process was complete.

2.3.2.2 SEM characterization of UO_{2+x} materials

Several hyper-stoichiometric samples with various oxidation levels were characterized using scanning electron microscopy. Figure 2.7 shows the microstructures of UO_2, $UO_{2.007}$, $UO_{2.012}$, $UO_{2.04}$, $UO_{2.11}$, and $UO_{2.16}$ observed at room temperature. As Figure 2.7.a and Figure 2.7.b suggest, there is very little difference between the microstructures of UO_2 and $UO_{2.007}$ (the white dots in a grain may be due to polishing residues). With increasing oxidation, as can be seen in Figure 2.7.c), small light grey cross shaped structures were observed (circled in red) within the grains. These grey crosses are oriented in certain directions indicated by the arrow, and branches are at 90 degrees.

The area covered by the grey patterns within a grain grows as deviation-from-stoichiometry increases, and their shapes become irregular, but their edges are arranged parallel to the directions indicated by arrows in Figure 2.7.d) and f). Early work has reported the precipitation of U_4O_9 in UO_{2+x} (e.g. $UO_{2.08}$ and $UO_{2.11}$) leads to a *Widmanstätten needle structure* or the formation of platelets (Tuxworth and Evans, 1959) . Such patterns are parallel to the (111) planes of the parent UO_{2+x} phase (Ambler and Slattery, 1961). Past characterizations using transmission electron microscopy of oxidized spent fuel (Thomas et al., 1989) and fresh fuel (Leinders et al., 2016) has identified U_4O_9 within the grains and along the grain boundaries of uranium oxide. The grey area therefore should correspond to **ordered** U_4O_9 which exists in hyper-stoichiometric material at room temperature. The EBSD analyses do not reveal any misorientation within the grain.

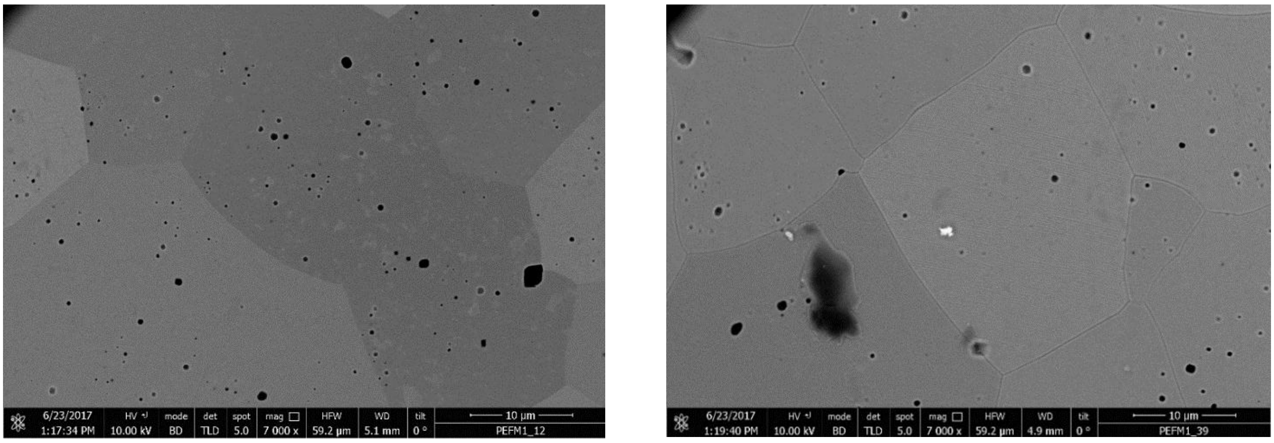

a) poly-crystal UO_2

b) poly-crystal $UO_{2.007}$

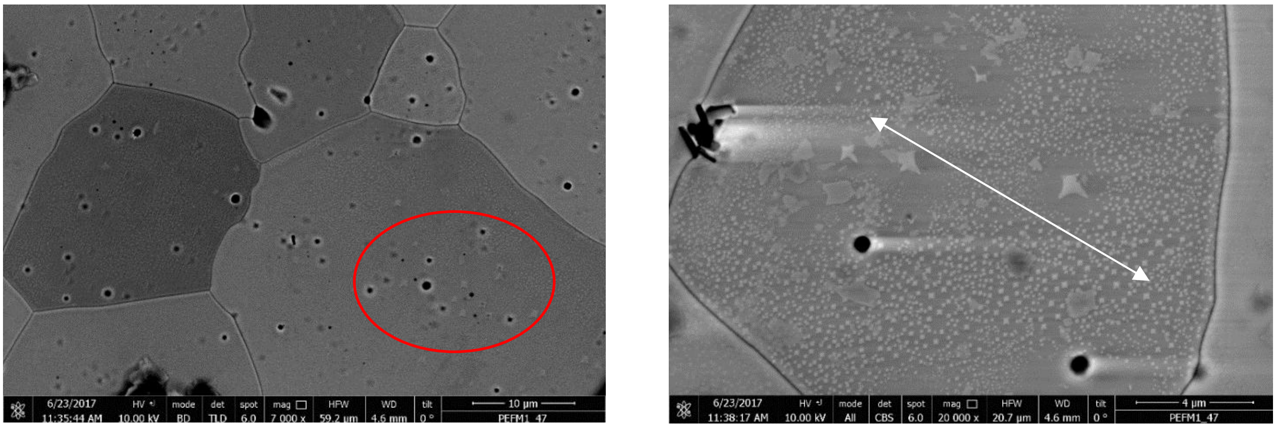

c) poly-crystal $UO_{2.012}$ -1

d) poly-crystal $UO_{2.012}$ -2

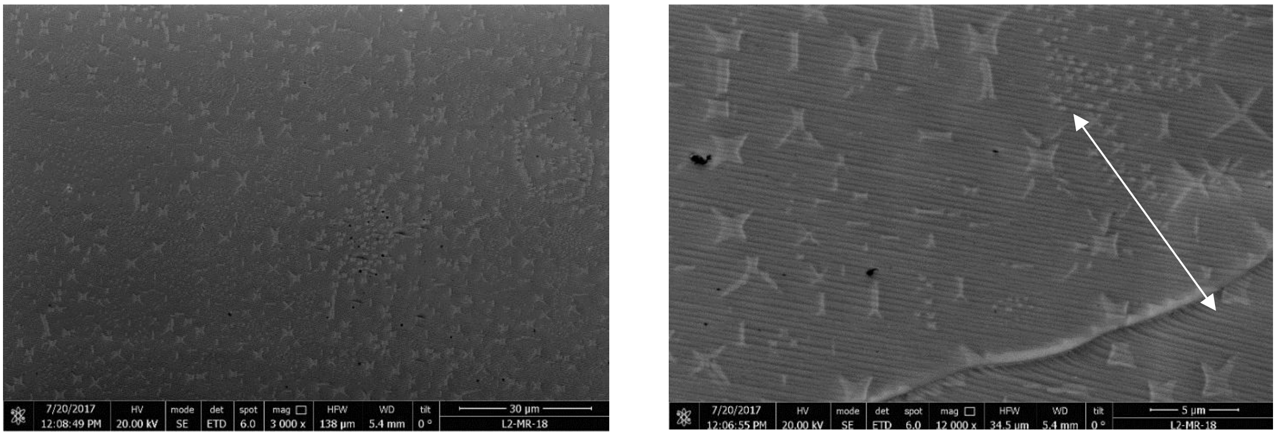

e) single-crystal $UO_{2.012}$ -1

f) single-crystal $UO_{2.012}$ -2

Figure 2.7: SEM images of surfaces corresponding to UO_{2+x} samples with low deviations-from-stoichiometry: a) and b) poly-crystal UO_2, $UO_{2.007}$ (in a BSE mode); c) and d) poly-crystalline $UO_{2.01}$ (BSE mode); and e) and f) single-crystal $UO_{2.012}$ (SE mode).

The regions within a grain that have a different electronic contrast (grey areas) grow with increasing levels of oxidation and their shapes appear to change to rectangular platelets such as reported in the past (Tuxworth and Evans, 1959) (see Figure 2.8). It may also be worth noting that fractional area of grey patterns is roughly identical in grains of identical samples as expected if they reflected homogenous oxidation.

He and Shoesmith carried out an SEM analysis of a $UO_{2.13}$ sample in which they claimed oxidation was inhomogeneous (He and Shoesmith, 2010). They interpreted the parallel ridges which can be seen particularly well in Figure 2.8.c as an indication of oxidation. We believe the features are simply caused by the high-temperature mechanical equilibration of the free surface. Because surface tension is a grain orientation dependent property, it is only natural that these ridges have different orientations in different grains.

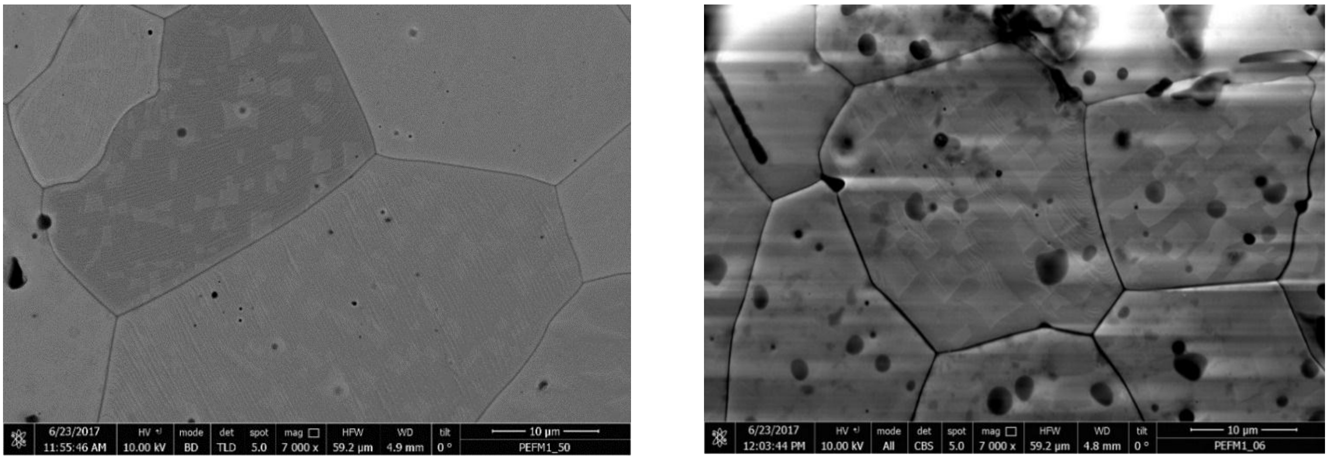

a) $UO_{2.042}$ b) $UO_{2.11}$

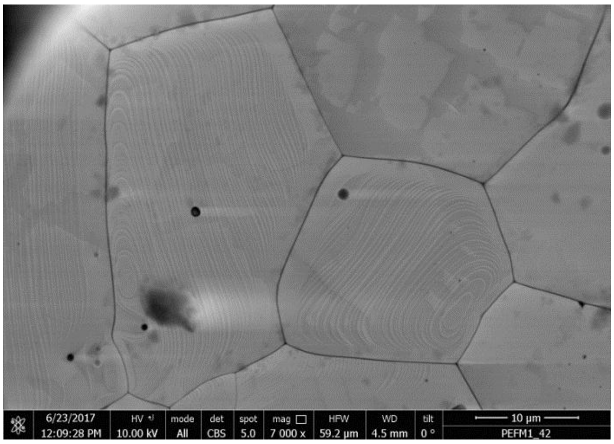

c) $UO_{2.16}$

Figure 2.8: SEM images in BSE mode of poly-crystalline UO_{2+x} samples surfaces with large deviations-from-stoichiometry: a) $UO_{2.042}$, b) $UO_{2.11}$ and c) $UO_{2.16}$.

2.3.3 Sample preparation for neutron scattering experiment

Two samples were equilibrated at 1370 ℃ but in gas mixtures containing different proportions of hydrogen and water vapour. The estimated deviations-from-stoichiometry corresponding to the annealing conditions for these two UO_{2+x} samples are 0.007 ± 0.002 and 0.158 ± 0.002. Annular pellets were used for the higher deviation from stoichiometry experiment. Oxidising conditions were maintained for eight hours for $UO_{2.007}$ and over twenty-four hours for $UO_{2.16}$.

2.3.4 Sample preparation for positron annihilation spectroscopy experiments

For this PAS study, samples were prepared in pairs in order to carry out lifetime spectroscopy measurements (see section 2.5.4). Six pairs of samples were equilibrated at 1350 ℃ using different gas mixtures. Two pairs of samples were annealed at 1280 ℃ and 900 ℃. This latter temperature was chosen so as to avoid the formation of thermally induced uranium vacancies (see chapter 1). Samples were annealed over different lengths of time based on the oxygen chemical diffusion coefficients which are known to be dependent upon the oxidation level. In addition, several stoichiometric UO_2 samples were prepared whose preparation differed substantially from the rest: 1. two disks were polished only and underwent no annealing; 2. two were polished and annealed at 1700 ℃; and 3. two were polished and annealed at 1400 ℃ in a mixture of Ar and 5% hydrogen. Table 2.1 provides the list of samples and preparation/annealing conditions we have studied.

Table 2.1: PAS sample preparation conditions.

#	T (℃)	pO_2 (atm) @650 ℃	Stoichiometry	Gas composition	Annealing time (hours)
1	1350	$8 \cdot 10^{-26}$	2.002	Ar + H_2 + H_2O	10
2		$2 \cdot 10^{-23}$	2.005		10
3		$1 \cdot 10^{-22}$	2.007		14
4	1280	$1 \cdot 10^{-19}$	2.03		24
5	1350	$5 \cdot 10^{-19}$	2.042		27
6		$1 \cdot 10^{-19}$	2.042	Ar + CO_2+CO	27
7		$2 \cdot 10^{-17}$	2.16		13
8	900	$3 \cdot 10^{-7}$	2.21	Ar	15
UO2_PFEM	1700 ℃ annealed + OPU polishing, no oxidation treatment				
UO2_GA16	1400 ℃ annealed + OPU polishing, no oxidation treatment				
REF_OPU	OPU polishing only; no oxidation treatment				

2.3.5 Sample preparation for uranium self-diffusion experiments

The uranium diffusion experiments are based on a solid-solid isotopic exchange phenomenon which occurs at the surface of the samples following the deposit of 97.7 ±0.1% ^{235}U enriched uranyl nitrate (Noyau, 2012; Philibert, 1991). In addition to the various steps described in section 2.3.1, four additional stages are added in order to prepare the samples for SIMS depth profiling (section 2.3.5):

1- Equilibration for an appropriate length of time (see section 2.3.2.1) in the conditions in which diffusion will be studied.
2- Deposit of several ^{235}U enriched uranyl nitrate drops which are left to dry.
3- Low temperature annealing under reducing conditions in order to transform the uranyl nitrate into oxide (Bourdineaud-Bordere, 1989; Kozlova et al., 2007).
4- Diffusion annealing so that isotopic exchange occurs in the bulk of the samples.

Table 2.2 shows the list of samples and annealing conditions studied in this work including those for steps 3 and 4. More samples were actually prepared but have not been examined, i.e. samples number are in red. For each type of sample, two identical disks were prepared. Samples were equilibrated under the desired oxygen partial pressure and temperature (stage 1). Once deposited with ^{235}U enriched uranyl nitrate, a light yellow UO_2 (NO_3) $6H_2O$ layer is formed after sufficient time is left for dehydration at room temperature (Kozlova et al., 2007) (stage 2).

Table 2.2: Sample preparation conditions for self-diffusion experiments.

Sample number	**Sample name**	**Stage 3: Low temperature annealing**			**Stage 4: Diffusion annealing**			**Estimated deviation-from-stoichiometry**
		T (℃)	**p_{O_2}(atm)**	**Time (hrs)**	**T (℃)**	**p_{O_2}(atm)**	**Time (hrs)**	
SC-1	L2_MR_23, 24	400	$1 \cdot 10^{-14}$	4	1350	$8.5 \cdot 10^{-12}$	18.5	2.004 ±10^{-4}
SC-2	L2_MR_19, 27	700	$9.4 \cdot 10^{-13}$	12	1500	$9.4 \cdot 10^{-13}$	24	2.001 ±10^{-4}
SC-3	L2_MR_28, 22		$5.0 \cdot 10^{-12}$			$5.0 \cdot 10^{-12}$		2.002 ±10^{-4}
SC-4	L2_MR_17, 14		$4.7 \cdot 10^{-11}$			$4.7 \cdot 10^{-11}$		2.004 ±10^{-4}
SC-5	L2_MR_21, 20		$4.7 \cdot 10^{-12}$		1600	$4.7 \cdot 10^{-12}$		2.001 ±10^{-4}
PC-1	PEFM_30, 29	400	$1 \cdot 10^{-14}$	4	1350	$8.5 \cdot 10^{-12}$	18.5	2.004 ±10^{-4}
PC-2	pc-du-4, 5	700	$9.4 \cdot 10^{-13}$	12	1500	$9.4 \cdot 10^{-13}$	24	2.001 ±10^{-4}
PC-3	pc-du-8, 7		$5.0 \cdot 10^{-12}$			$5.0 \cdot 10^{-12}$		2.002 ±10^{-4}
PC-4	pc-du-11,12		$4.7 \cdot 10^{-11}$			$4.7 \cdot 10^{-11}$		2.004 ±10^{-4}
PC-5	pc-du-16, 15		$4.7 \cdot 10^{-12}$		1600	$4.7 \cdot 10^{-12}$		2.001 ±10^{-4}
CrPC	J72, J73	700	$9.4 \cdot 10^{-13}$	12	1500	$9.4 \cdot 10^{-13}$	24	
CrPC-2	J65, J67		$5.0 \cdot 10^{-12}$			$5.0 \cdot 10^{-12}$		
CrPC-3	J68, J69		$4.7 \cdot 10^{-11}$			$4.7 \cdot 10^{-11}$		
CrPC-4	J79, J80		$4.7 \cdot 10^{-12}$		1600	$4.7 \cdot 10^{-12}$		
CrPC-5	J77, J78	400	$1 \cdot 10^{-14}$	4	1350	$8.5 \cdot 10^{-12}$	18.5	

Sample surfaces were analysed **qualitatively** by energy-dispersive X-ray spectroscopy (EDX) before further treatment to obtain information about elements such as U, O and N, nitrogen being a tracer of the presence of nitrate. The presence of nitrogen at the surface of all the samples is indeed confirmed by EDX analyses prior to heat treatment. The following figures concern SC-2, PC-2 and CrPC samples. The average relative mass of nitrogen was approximately 20% for Cr-doped UO_2, 10% for the single-crystal, and 17% for the poly-crystal, as compared to 5 % for the sample prior to deposit (Figure 2.9.a). Figure 2.9.b shows an example of EDX analysis of poly-crystalline UO_2 sample PC-2 following the deposit (stage 2), prior to the low temperature annealing (stage 3).

Samples are then annealed at low temperature in order to convert the dehydrated deposit into a ^{235}U-enriched oxide layer (Bourdineaud-Bordere, 1989) (stage 3). EDX analyses were carried out following stage 3 to confirm the levels of nitrogen had returned to the levels detected prior to the nitrate deposit.

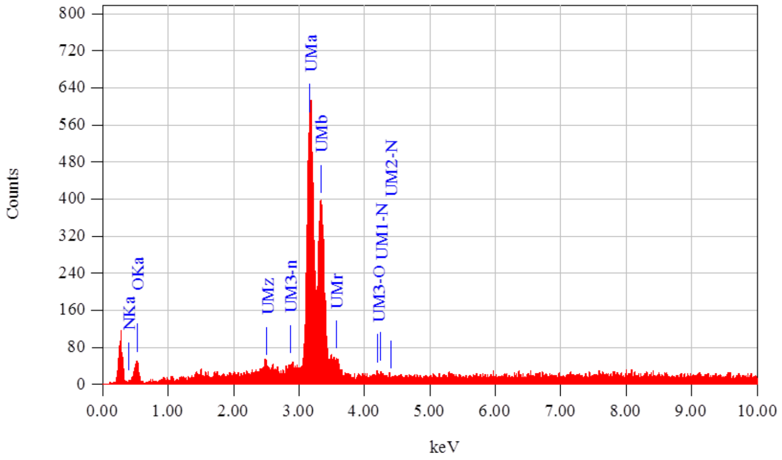

a) EDX analysis of an as-prepared poly-crystalline UO_2 sample prior to the nitrate deposit: the relative concentrations of three elements of interest are: N – 5 %; O – 16%; U – 79%.

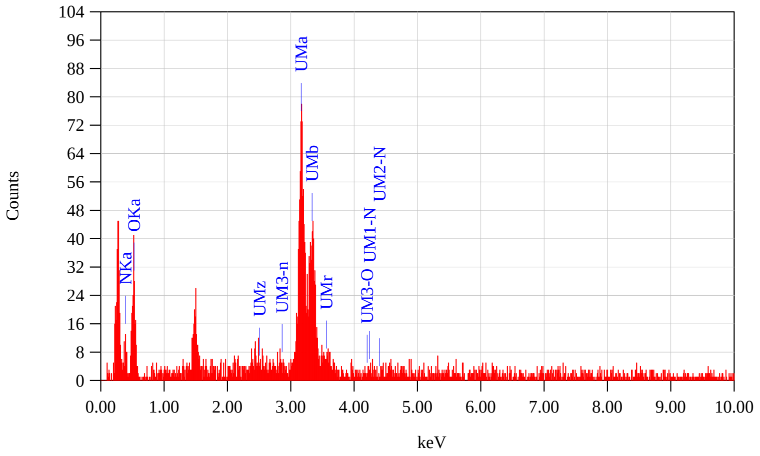

b) EDX analysis of a poly-crystalline UO_2 sample following the nitrate deposit to low-temperature annealing: the relative concentrations: N – 19%; O – 36%; U – 45%.

Figure 2.9: Elemental concentrations at the surface of a poly-crystalline sample a) before deposit and b) after deposit but prior to low-temperature annealing.

Following stage 3, diffusion annealing treatments were carried out. In the tubular alumina furnace, one poly-crystalline and one single-crystal sample were placed in the centre of the furnace. Because the volume of the furnace is small, the gas renewal rate (~5 mins) is high. The rest of samples prepared for diffusion experiments were annealed in a large tungsten furnace which has a slow gas renewal rate.

Surface roughness study

Due to differences in surface roughness prior to the nitrate deposit and sample shapes, the amount of deposit (*i.e.* the thickness of the deposited layer) and its homogeneity will vary between samples. In what follows, we provide an example of a particular experiment in order to illustrate the effects the above mentioned steps 2 and 3 have on the sample and in particular on the sample surface. This will be useful in order to understand some of the scatter subsequently observed in the ^{235}U depth profiles (chapter 5).

Figure 2.10, 2.11 and 2.12 are SEM images of the surface of three types of samples after deposition of ^{235}U enriched uranyl nitrate and dehydration. On the left hand side are the surface images before annealing at 700 ℃. On the right hand side are images of samples following annealing at 700 ℃. The $^{235}UO_2$ (NO$_3$) 6H$_2$O layer on the single-crystal is relatively flat and more homogeneous than on the undoped and Cr-doped poly crystalline UO$_2$ samples. The deposited layer has formed stripes. The grain size for Cr-doped UO$_2$ is very large and the nitrate appears to form parallel stripes as observed on the single crystal surface. The deposited layer on the undoped poly crystalline sample is more randomly distributed and forms uneven shapes.

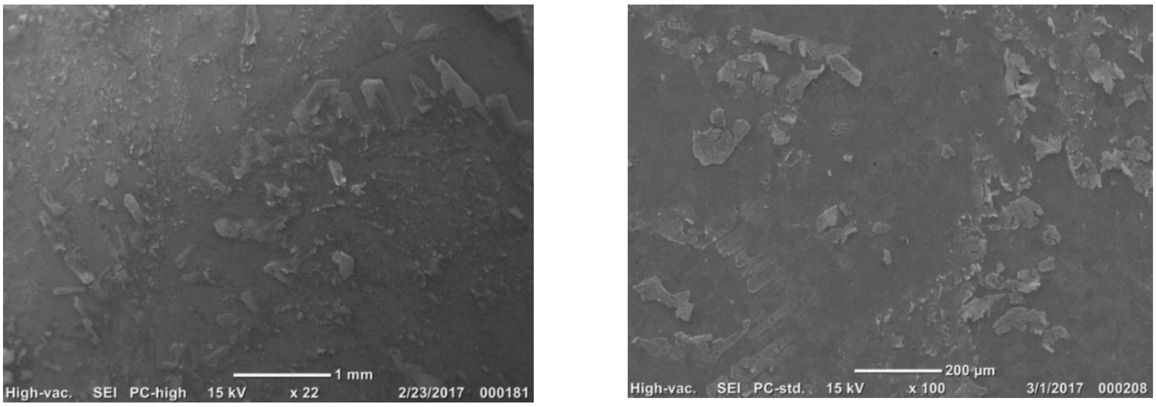

Figure 2.10: SEM images (SE mode) of the surface of a poly-crystalline sample with uranyl nitrate deposit, prior to annealing at 700 ℃ (left), and following annealing (right).

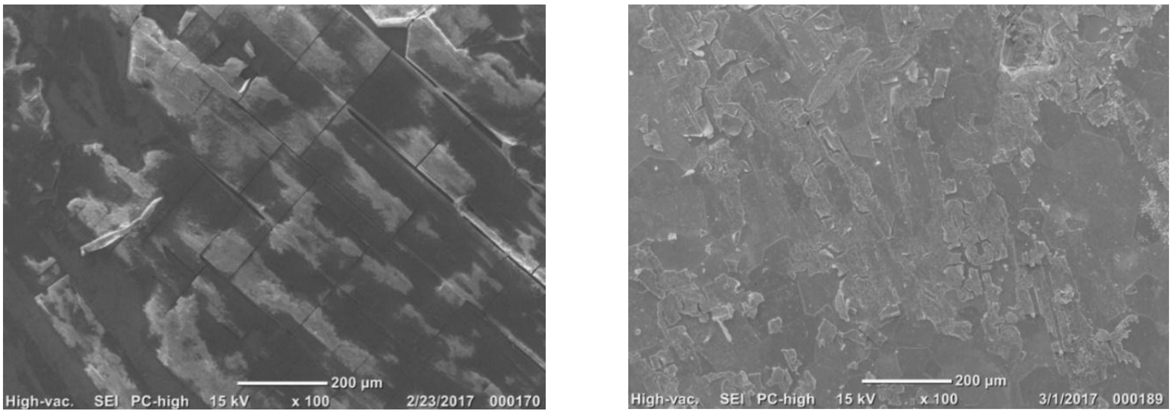

Figure 2.11: SEM images (SE mode) of the surface of a Cr-doped UO_2 with uranyl nitrate deposit, prior to annealing at 700 ℃ (left), and following annealing (right).

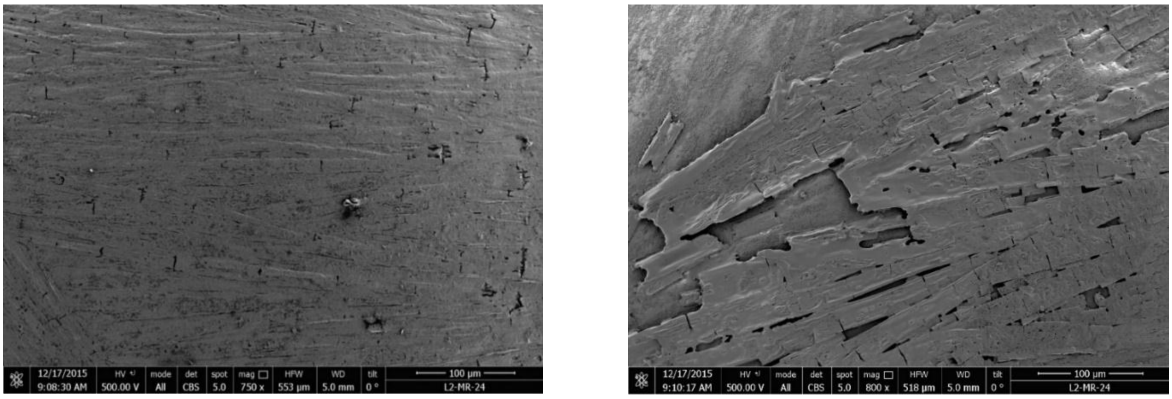

Figure 2.12: SEM images (BSE mode) of the surface of a single-crystal sample with uranyl nitrate deposit, prior to annealing at 700 ℃ (left), and following annealing (right).

A careful examination of pictures taken before and after annealing at 700 ℃ indicates that the intervals between the deposited layers become larger following the stage 3 heat treatment. Also the thickness of the deposited nitrate oxide layers observed is generally much higher at the periphery of the Cr-doped samples and single-crystal slabs as Figure 2.13 shows. We believe this effect is more significant in single-crystal samples because the original surface is extremely smooth.

Table 2.3: Roughness in *nm* averaged out over 400×400 μm^2 regions for each type of sample.

	Single-cryst. $^{235}UO_2$	**Poly-cryst. $^{235}UO_2$**	**Cr-doped $^{235}UO_2$**
Roughness prior to deposit	7 ±1	17 ±1	21 ±8
Roughness following deposit and low T annealing	47±15	344 ±206	163 ±28

The roughness of the samples is further examined by chromatic confocal microscopy following low temperature annealing but prior to diffusion annealing. The analysis is carried out over a surface area of 400×400 μm^2 using 0.4×0.5 μm^2 steps. Figure 2.14 shows colour coded altitude images obtained using chromatic confocal microscopy. The roughness of each sample is indicated in Table 2.3. These features appear to show a very uneven deposit at the surface of the samples which could make the data analysis following diffusion-annealing (Chapter 5) rather complex.

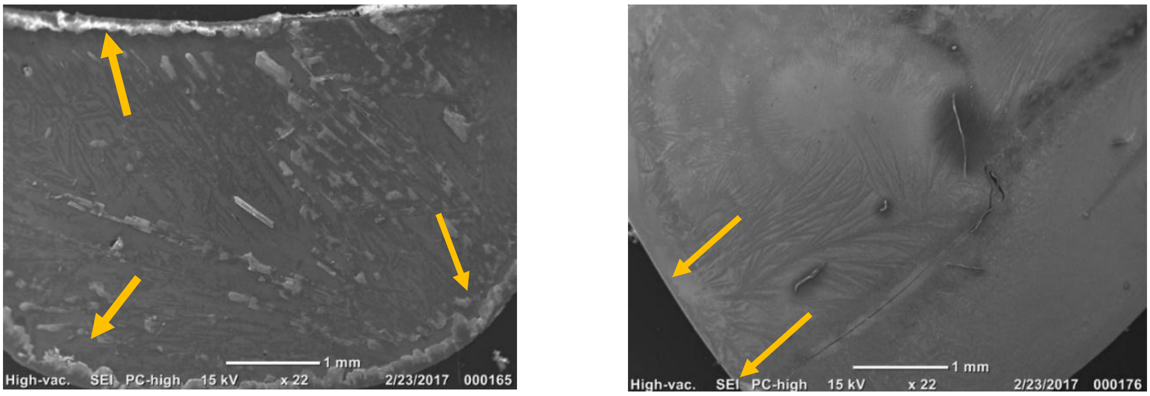

Figure 2.13: SEM images (SE mode) of the $^{235}UO_2(NO_3)\,6H_2O$ layer on the surfaces of Cr-doped UO_2 (left) and single-crystal UO_2 (right), prior to annealing at 700 ℃ for 6 hours. The arrows indicate the periphery regions with thicker nitrate oxide layers.

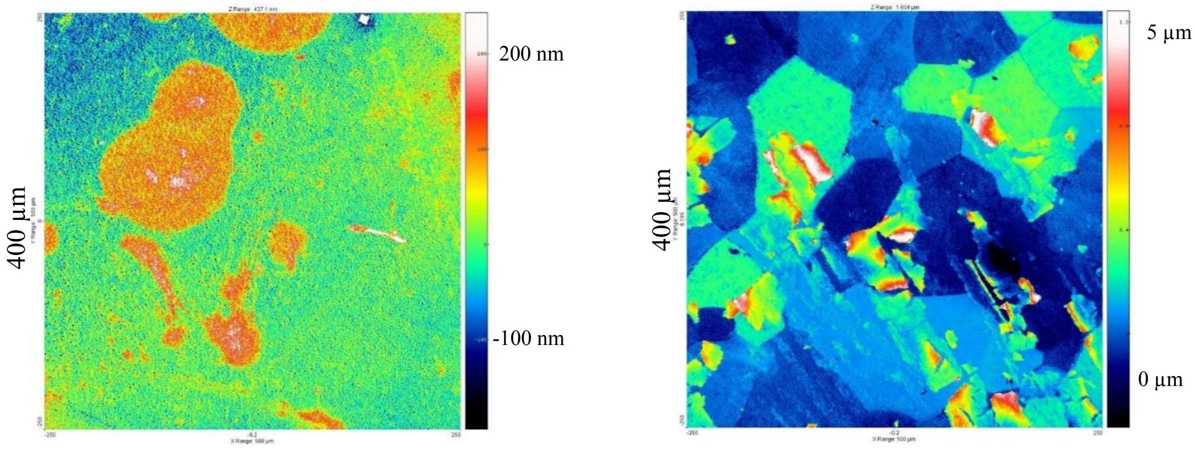

400 µm

400 µm

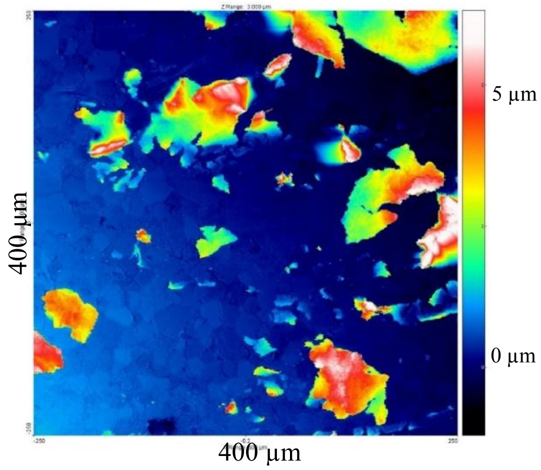

Figure 2.14: 400×400 µm^2 chromatic confocal microscope images of samples following deposit and low-temperature annealing: top left – single-crystal; top right – Cr-doped UO_2; bottom – poly-crystalline UO_2.

2.4 Oxygen defect characterization using neutron scattering and PDF analysis

2.4.1 The principles of neutron diffraction and structural analyses

2.4.1.1 Introduction

The aim of this section is to provide the reader with some theoretical background to the neutron scattering experiments we have carried out in this work. For structural and microstructural analyses, neutron diffraction has been preferred over X-ray diffraction because the scattering cross-sections of neutrons for O (σ=4.23 barns) is only about three times less than for U (σ=13.78 barns) (Sears, 1992). The larger penetration depth of neutrons also makes it a well-suited technique for the measurement of bulk properties. The following sections briefly introduce the theories behind the two neutron scattering techniques we have used, what information they provide and how the data are corrected and analysed. The point of using two different methods is that one (analysis of Bragg peaks) will provide structural (average) information, whereas the other (the pair distribution function analysis, PDF) will provide a local probe and is therefore better suited for describing disorder or defects as are expected in UO_{2+x}.

2.4.1.2 The total scattering structure function and Debye-Waller factor

When neutrons interact with the atoms of a sample, they scatter and the resulting scattering amplitude is given by the sum of all contributions. For a given wavelength, the specimen scattering amplitude for a diffraction measurement is expressed as (Egami and Billinge, 2012):

$$\Psi(\boldsymbol{Q}) = \frac{1}{\langle b \rangle} \sum_{v} b_v e^{i\boldsymbol{Q}\boldsymbol{R}_v} \tag{2.5}$$

where $\boldsymbol{Q} = \boldsymbol{k}_{incident} - \boldsymbol{k}_{scatter}$ is the diffraction vector or the momentum transfer, and $\boldsymbol{k} = \frac{2\pi}{\lambda}\boldsymbol{e}$ is the wave vector of the incident or the scattered beam in direction $\boldsymbol{e}$, $\boldsymbol{R}_v$ is the position of the v^{th} atom, b_v is the scattering length of the v^{th} atom and the sum extends over all atoms in the sample.

For elastic scattering, i.e. scattering that occurs with no change in energy of the incident particle, the incident and scattered beam wavelengths are the same, $|\boldsymbol{k}_{incident}| = |\boldsymbol{k}_{scatter}|$. So $|\boldsymbol{Q}|$ becomes:

$$|\boldsymbol{Q}| = 2k\, sin\theta = \frac{4\pi sin\theta}{\lambda} \tag{2.6}$$

, where 2θ is the angle between the two wave vectors and λ the incident neutron wavelength. In equation (2.5), $<b>$ represents a compositional average and $\Psi(\boldsymbol{Q})$ can be interpreted as the Fourier transform of the function $f(\boldsymbol{x}) = \sum_v b_v \delta(\boldsymbol{x} - \boldsymbol{R}_v)$, and contains all structural information. However, the scattered amplitude $\Psi(\boldsymbol{Q})$ cannot be measured directly. Only accessible to observations is the intensity of the diffracted beam, which is related to the square of norm of $\Psi(\boldsymbol{Q})$. The quantity that is measured (the intensity of diffracted beam) is proportional to $\Psi(\boldsymbol{Q})\Psi^*(\boldsymbol{Q})$ where the star sign designates the complex conjugate:

$$I(\boldsymbol{Q}) \propto \Psi(\boldsymbol{Q})\Psi^*(\boldsymbol{Q}) = \frac{1}{\langle b\rangle^2}\sum_{\nu}\sum_{\mu} b_\nu b_\mu^*\, e^{i\boldsymbol{Q}(\boldsymbol{R}_\nu-\boldsymbol{R}_\mu)} \tag{2.7}$$

$\boldsymbol{R_\nu}$ is the sum of three contributions:

$$\boldsymbol{R_\nu} = \boldsymbol{R_\nu^0} + \boldsymbol{u_\nu} + \boldsymbol{v_\nu} \tag{2.8}$$

- $\boldsymbol{R_\nu^0}$ the mean position of the atom in the sample.
- $\boldsymbol{u_\nu}$ which results from thermal motion with $\langle \boldsymbol{u_\nu}\rangle_{\boldsymbol{time}} = \boldsymbol{0}$.
- $\boldsymbol{v_\nu}$ which is a static displacement also due to temperature increases.

We can write equation (2.7) as:

$$\frac{1}{N}\Psi(\boldsymbol{Q})\Psi^*(\boldsymbol{Q}) = \frac{1}{N\langle b\rangle^2}\sum_{\nu}\sum_{\mu,\nu=\mu} b_\nu b_\mu^*\, e^{i\boldsymbol{Q}(\boldsymbol{R}_\nu-\boldsymbol{R}_\mu)} + \frac{1}{N\langle b\rangle^2}\sum_{\nu}\sum_{\mu,\nu\neq\mu} b_\nu b_\mu^*\, e^{i\boldsymbol{Q}(\boldsymbol{R}_\nu-\boldsymbol{R}_\mu)} \tag{2.9}$$

$$= 1 + \frac{1}{N\langle b\rangle^2}\sum_{\nu}\sum_{\mu,\nu\neq\mu} b_\nu b_\mu^*\, e^{i\boldsymbol{Q}(\boldsymbol{R}_\nu-\boldsymbol{R}_\mu)} \tag{2.10}$$

$\frac{1}{N}\Psi(\boldsymbol{Q})\Psi^*(\boldsymbol{Q})$ is denoted $S(\boldsymbol{Q})$ and is called the total scattering function because, as it will be shown hereafter it contains both information about the perfect average long range order and also information about deviation from this average, i.e. local disorder. Applying equation (2.8), equation (2.10) can be further expanded as:

$$S(\boldsymbol{Q}) = 1 + \frac{1}{N\langle b\rangle^2}\sum_{\nu}\sum_{\mu,\nu\neq\mu} b_\nu b_\mu^*\, e^{i\boldsymbol{Q}(\boldsymbol{R}_\nu^0-\boldsymbol{R}_\mu^0)} \,.\, e^{i\boldsymbol{Q}(\boldsymbol{u}_\nu-\boldsymbol{u}_\mu)} \,.\, e^{i\boldsymbol{Q}(\boldsymbol{v}_\nu-\boldsymbol{v}_\mu)} \tag{2.11}$$

Since the solid is in thermal equilibrium, several states contribute to the energy of the set of oscillators in the solid with a probability given by the Maxwell Boltzmann law. S(Q) is averaged over these states (Ashcroft and Mermin, 1976). The term $e^{i\boldsymbol{Q}(\boldsymbol{u}_\nu-\boldsymbol{u}_\mu)}$ therefore can be computed as averaged over these states.

According to (Mermin, 1966):

$$\langle e^{i\boldsymbol{Q}(\boldsymbol{u}_\nu-\boldsymbol{u}_\mu)}\rangle = e^{-\frac{1}{2}\langle(\boldsymbol{Q}\cdot\boldsymbol{u}_\nu)^2\rangle} \,.\, e^{-\frac{1}{2}\langle(\boldsymbol{Q}\cdot\boldsymbol{u}_\mu)^2\rangle} \,.\, e^{-\frac{1}{2}\langle(\boldsymbol{Q}\cdot\boldsymbol{u}_\nu)(\boldsymbol{Q}\cdot\boldsymbol{u}_\mu)\rangle} \tag{2.12}$$

$$= e^{-\boldsymbol{M}_\nu}e^{-\boldsymbol{M}_\mu} \tag{2.13}$$

, where $\boldsymbol{M_\nu}$ and $\boldsymbol{M_\mu}$ define the Debye-Waller attenuation with $\boldsymbol{M_\nu} = \frac{1}{2}\langle(\boldsymbol{Q}\cdot\boldsymbol{u_\nu})^2\rangle$.

The wavevector $\boldsymbol{Q}$ may be written as a linear combination of unit vectors of the reciprocal space $\boldsymbol{Q} = h\boldsymbol{a} + k\boldsymbol{b} + l\boldsymbol{c}$, then the Debye-Waller attenuation term in equation (2.13) is written as:

$$M_\nu = [hkl]\overline{\overline{B_\nu}}[hkl]$$

Where $\overline{\overline{B_\nu}}$ is symmetrical and contains 6 anisotropic Debye-Waller factors. Hence, the temperature factor for a crystal with harmonic interatomic forces is in a Gaussian form as:

$$T_\nu(Q) = exp[-(b_{11}^\nu h^2 + b_{22}^\nu k^2 + b_{33}^\nu l^2 + b_{12}^\nu hk + b_{23}^\nu kl + b_{13}^\nu hl)] \tag{2.14}$$

, where b_{ij}^ν presents the anisotropic temperature factor defining the size and orientation of the thermal vibration ellipsoid (Rouse et al., 1968). If occupied sites of atoms have cubic point symmetry, the ellipsoid degrades into a sphere and the anisotropic temperature factors can be replaced by a single isotropic term B_n:

$$T_n(Q) = \exp M_\nu = \exp(-\overline{\overline{B_\nu}}\sin^2\theta/\lambda^2) \tag{2.15}$$

And

$$\left|\overline{\overline{B_\nu}}\right| = \frac{8}{3}\pi^2\langle u_{\nu_{ij}}^2\rangle \tag{2.16}$$

which is also called as the Debye-Waller factor. The DW factor is highly dependent on the temperature T, whereas the general shape of the DW factor $B_\nu(T)$ is linear. In X-ray or neutron crystallographic refinements, the general anisotropic vibration parameters will be given by a $[u_{ij}]$ matrix often denoted as β:

$$\beta = \begin{pmatrix} \langle u_1^2\rangle & \langle u_1u_2\rangle & \langle u_1u_3\rangle \\ \langle u_2u_1\rangle & \langle u_2^2\rangle & \langle u_2u_3\rangle \\ \langle u_3u_1\rangle & \langle u_3u_2\rangle & \langle u_3^2\rangle \end{pmatrix} \tag{2.17}$$

In our subsequent diffraction analyses both $u_{ij}(T)$ and $\overline{\overline{B}}$ were fitted. $\overline{\overline{B}}$ accounts for the smearing function properties. As it will be reported in our results (Chapter 3) although thermal vibration could be thought to be non-isotropic with a $\bar{4}3m$ symmetry for the normal oxygen atoms for instance, no improvement in fits could be gained with a non-spherical smearing function.

We denote $b_\nu e^{-\boldsymbol{M_\nu}}$ as b'_ν, then equation (2.11) can be written as:

$$S(\boldsymbol{Q}) = 1 + \frac{1}{N\langle b\rangle^2}\sum_{\nu}\sum_{\mu,\nu\neq\mu} b'_\nu b_\mu^{*\prime}\, e^{i\boldsymbol{Q}(\boldsymbol{R}_\nu^0 - \boldsymbol{R}_\mu^0 + \boldsymbol{\nu}_\nu - \boldsymbol{\nu}_\mu)} \tag{2.18}$$

$$= 1 + \frac{1}{N\langle b\rangle^2}\sum_{v}\sum_{\mu,\nu\neq\mu} b'_\nu b^{*\prime}_\mu\, e^{i\boldsymbol{Q}(\boldsymbol{R}^0_\nu-\boldsymbol{R}^0_\mu)} + \frac{1}{N\langle b\rangle^2}\boldsymbol{Q}\sum_{v}\sum_{\mu,\nu\neq\mu} b'_\nu b^{*\prime}_\mu\, (\boldsymbol{v}_\nu-\boldsymbol{v}_\mu) e^{i\boldsymbol{Q}(\boldsymbol{R}^0_\nu-\boldsymbol{R}^0_\mu)} \tag{2.19}$$

If $\|\boldsymbol{v}\|$ is small enough to limit the Taylor expansion of the exponential to its first order, the contribution $\frac{1}{N\langle b\rangle^2}\sum_{v}\sum_{\mu,\nu\neq\mu} b'_\nu b^{*\prime}_\mu\, e^{i\boldsymbol{Q}(\boldsymbol{R}^0_\nu-\boldsymbol{R}^0_\mu)}$ is the *Laue* term which accounts for the diffraction of the perfect mean lattice, which is analysed by means of a Rietveld analysis (section 2.4.1.3). The latter contribution in equation (2.19) gives an insight in the local disorder in the lattice and can be analysed by a PDF analysis (section 2.4.1.4).

2.4.1.3 Laue intensity analysis using the Rietveld method

The point of the previous chapter was to introduce the total scattering structure function and the Debye-Waller factors. The former quantity is the basic experimental data and is used in this work either in the context of space and time averaged quantities (analysis of Bragg peaks) or more unusually, in the context of the analysis of local order (PDF analysis, see following section). Note that the analysis of Bragg peaks is carried out in the framework of powder diffraction because the grain size is of the order of 12 µm and we know that the manufacturing (pressing and sintering) process produces no texture. Bragg peak analysis is typically carried out using the Rietveld least squares method.

In addition to enabling the indexing of Bragg lines and determining the symmetry of the crystal, an atomistic model of the unit cell provides time and space averaged structural information such as the lattice parameter, the average positions of uranium and oxygen ions and the Debye Waller factors. For completeness, it is also worth mentioning, although this was not looked into in this work, that microstructural information such as the size of diffracting domains may also be derived from the analysis.

However, in this type of analysis, diffuse scattering which can appear between the Bragg peaks as a result of static or dynamic disorder is subtracted from the *S(Q)* as background and we illustrate here the nature of the information that is subsequently lost by looking at the effect of temperature. Thermal agitation, causes a reduction of Bragg peaks corresponding to a *Q* diffraction vector by a factor proportional to $e^{\left(-\frac{1}{2}\langle Q.u\rangle^2\right)}$ where u represents the amplitude of atomic vibrations (see Debye Waller factor from the previous section). This reduction in Bragg peak intensities is lost as thermal diffuse scattering at the base of Bragg peaks in conventional Rietveld analysis. The effect this has on UO_2 is illustrated in Figure 2.15 whence it can be seen that 1) the intensity loss as the temperature increases is more important at high Q values, as expected from the above relationship 2) the background level increases with increasing temperature.

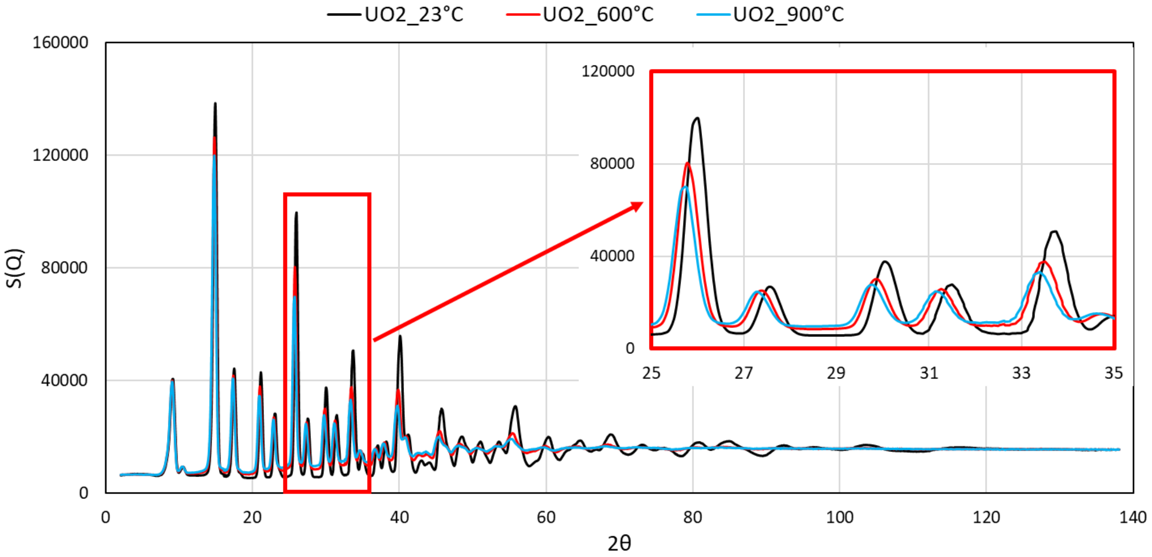

Figure 2.15: Structure function S(Q) of UO_2 measured at 23 ℃, 600 ℃ and 900 ℃.

To conclude, because the diffuse scattering observable between Bragg peaks is discarded in this type of analysis, the picture it provides is that of a space and time averaged structure. This contrasts with the PDF analysis presented in the next section.

2.4.1.4 The PDF analysis

Conventional methods of crystallographic structural analysis focus upon Bragg peaks which result from elastic scattering and contain information essentially relating to long-range order. Disordered, nano-structured, reduced-dimensional crystals or indeed defects in UO_{2+x} lack sufficient long-range order to produce sharp diffraction peaks. In this case, the information relating to disorder or defects is contained within the diffuse scattering intensities. Disorder generally induces a reduction in elastic (Bragg) scattering intensities and an increase of the intensities between peaks as seen in the preceding section. The Pair Distribution Function analysis makes use of this diffuse scattering.

The Fourier transform of diffraction data provides the pair-distribution function g(r) which defines the probability of finding two atoms separated by a distance r (Egami and Billinge, 2012; Fischer, 2013; Prince, 1981). The reduced pair distribution function G(r) can then be obtained as follows:

$$G(r) = 4\pi r \rho_0 (g(r) - 1) = \frac{2}{\pi} \int_0^\infty Q[S(Q) - 1] \sin(Qr)\, dQ \tag{2.20}$$

In which, ρ_0 is the atomic number density of the material, g(r) is the pair distribution function, and $\rho_0 g(r)$ represents the microscopic atomic pair density (Egami and Billinge, 2012). It is this reduced pair distribution function which we will analyse and model in the remainder of this work. There are several advantages to this. The main one is that G(r) is obtained directly from the experimental data as the Fourier transform of $S(\boldsymbol{Q})$ and so is most related to the experimental data. For example, the expression for G(r) given above (equation (2.20)) shows that as g(r) tends to 0 for small values of r (indeed if r is small enough, the probability of finding two atoms separated by a distance r tends to 0), the slope of G(r) should tend to $-4\pi\rho_0$. This means the slope of G(r) at $r \to 0$ can be checked against the atomic number density ρ_0.

A third related correlation function is worth mentioning. It is the radial distribution function (RDF) which is defined as follows:

$$R(r) = 4\pi r^2 \rho_0 g(r) \tag{2.21}$$

It is a useful function as $R(r)dr$ provides the number of atoms contained in an annulus of thickness dr at a distance r from another atom. In other words, when integrated between two distances, this function can provide coordination numbers. This function will be used in Chapter 3.

2.4.2 Diffraction setup and data reduction

The neutron diffraction experiments were carried out at the D4c diffractometer at ILL Grenoble as shown in Figure 2.16.a (Desgranges et al., 2014). Samples were sealed under vacuum in silica tubes, which were then mounted in the centre of a vanadium furnace. The maximum temperature the furnace is capable of reaching is 1000 ℃. The average height of the samples in the tubes is approximately equal to the diameter of the incident neutron beam which is roughly 26 mm. The goniometer surrounding the furnace can measure the diffraction pattern for 2θ values ranging between 1.5 °and 137 °with an angular resolution of 0.12 ° (Fischer et al., 2002). Two thermocouples are set up, one of which is under the metallic base of the sample holder and the other one in centre of the furnace above the samples as Figure 2.16.b illustrates. Temperature discrepancies between the measurements from the thermocouple and the central temperature imposed on the samples are considered when analysing the data.

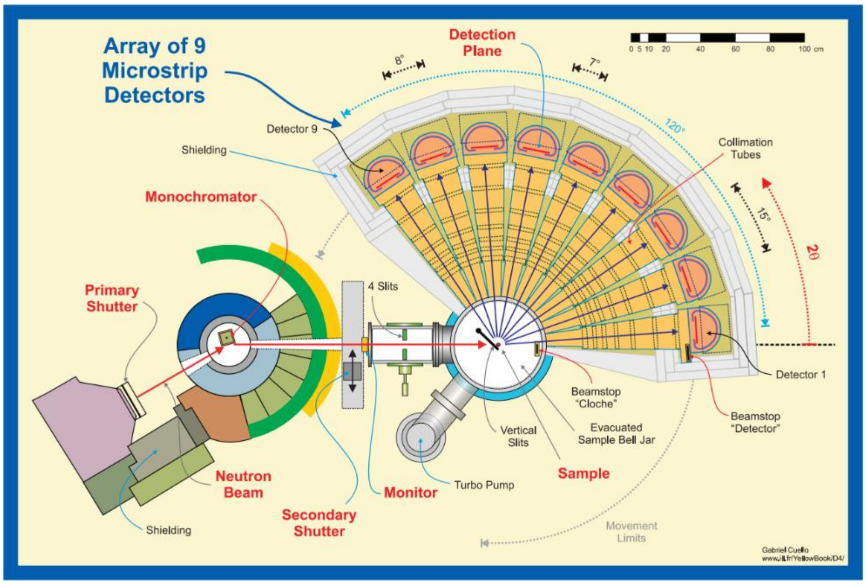

a) Schematic diagram of the D4c diffractometer with nine microstrip detectors and collimation tubes (Fischer et al., 2002)

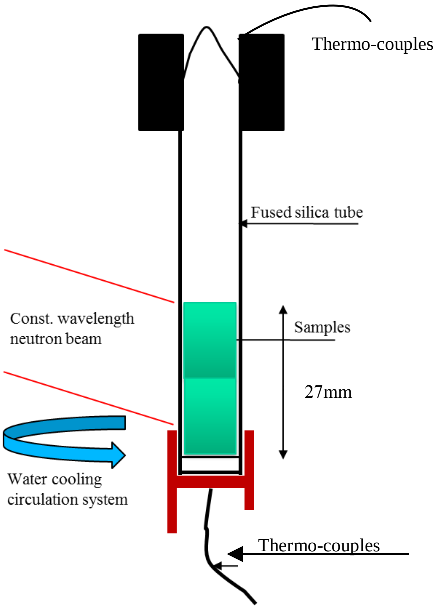

b) Schematic diagram illustrative of sample and container inside the furnace.

Figure 2.16: Schematics of D4c – beamline, furnace, detectors and samples.

When collecting data in such an experiment, one is essentially concerned with diffuse scattering from the sample. Diffuse scattering however is due to both the sample and its environment (i.e. vanadium furnace, silica container, etc.). It is therefore necessary to quantify the contribution of this environment. To this end, separate experiments were carried out at several temperatures between 20°C and 1000°C, involving the empty furnace and the furnace with an empty sample container. Diffraction data of UO_2

and UO_{2+x} samples measured subsequently were processed by subtracting the background relative to the environment. Additional corrections accounting for absorption, multiple scattering, and inelastic scattering effects (Placzek correction) were made to the diffraction patterns (Fischer, 2013). The inelastic correction to the differential scattering cross-section is necessary when the energy lost by the neutrons to phonons is no longer negligible against the incident energy E_0. The so-called static approximation is no-longer valid in this case. Following all data corrections, the reduced pair distribution function G(r) can be obtained by the inverse Fourier transform of the measured scattering intensity, *S(Q)* (with Q defined as $\mathrm{Q} = 4\pi\sin\theta/\lambda$, see equation (2.20).

A few comments are necessary here to provide an understanding of what is actually being measured in these experiments. The characteristic time for atomic motion is in the range from 10^{-13} to 10^{-12} s, which corresponds to energies of the order of several millielectronvolts, depending on the material and temperature of the experiment. The incident quantum energy $E_0 = \hbar\omega_0$ defines a characteristic time – the snapshot time $\tau_{snapshot} \sim \omega_0^{-1}\left(\frac{a}{\lambda_0}\right)$ – which corresponds to the time required for an incident quantum (X-ray or neutron) with a wavelength λ_0 to travel one interatomic distance a. For neutron diffraction, the snapshot time is in a range from 10^{-15} to 10^{-13} s (Fischer, 2016). Hence, the PDF intensity is an instantaneous snapshot of mobile atoms averaged over a large quantity of matter.

Note also that short wavelength (0.5 Å) incident neutrons not only assure a high Q_{max} ($=\frac{4\pi Sin(\theta)}{\lambda}$) and thus a good R-space resolution of about FWHM_r=0.16 Å ($\sim 2\pi/Q_{max}$), but their relatively high speed implies also a very short snapshot time for each neutron's diffraction event, in our case about 10^{-14} seconds. The PDF(r) therefore represents an ensemble average (across the sample's volume) of the local structure probed quasi-instantaneously by each diffracting neutron. The structural distance range probed by each neutron is given by the size of its coherence volume, which depends on the monochromaticity and collimation of the incident neutron beam, and which for our 0.5 Å wavelength neutrons is roughly spherical with a FWHM of about 60 Å. PDF analysis is therefore a local probe both in the spatial and in the temporal sense, whereas Rietveld analysis of the elastic intensity of Bragg peaks averages over both space and time.

2.4.3 Data refinement

The PDF data, G(r), were refined using the PDFGUI software (Farrow et al., 2016, 2007; Proffen and Billinge, 2003). The purpose of using this software is to determine the atomic arrangement in a model which best reproduces the experimental data. This is done through minimising the difference between the experimental G(r) and that calculated based on the structural model for the material. The structural model is defined by the space group of the crystalline material, *e.g.* $Fm\overline{3}m$ for UO_2, and the nature of atoms.

In this work, two strategies were used. In the first, the experimental PDF is compared to calculations from **the smallest possible cell**. As PDFGUI applies the symmetries of the space group, this corresponds to the fourfold cell for UO_2. This fourfold cell is repeated periodically in order to calculate the PDF to the required distance r_{max}. In order to focus on distances relevant to defect clusters and avoid the influence of information contained in the PDF relative to possible correlations between defect clusters, the maximum range for analysing the data was limited mainly to 6 Å but sometimes refinement was carried out over 12 Å. The distribution in atomic distances are accounted for by convoluting the resulting PDF with Gaussian functions that represent phenomena relating to the material or instrumentation. The second strategy involved calculating the PDF by modelling the sample in a large box, *i.e.* **supercell**, whose size is larger than the range of interest r_{max}. In this model, the atomic arrangements are explicitly described and structural models for the defects may be tested.

The parameters describing the structure are:

- L: the lattice parameter;
- The atom positions $(x, y, z) = \boldsymbol{R}_{\boldsymbol{\nu}}^{\boldsymbol{0}} + \boldsymbol{v}_{\boldsymbol{\nu}}$, corresponding chemical nature and site occupancy, which should lead to the appropriate stoichiometry;
- u_{ij} : the relative atomic thermal displacements between two atoms i or j, for both uranium and oxygen ($\boldsymbol{R}_j(t) - \boldsymbol{R}_i(t) = \boldsymbol{R}_{ij}^0 + \boldsymbol{u}_{ij}(t)$ at a given temperature);

In addition, a set of material and instrumental parameters are introduced:

- At long distances, the motion of two contributing atoms is uncorrelated. At small distances however, the motion of atoms can be strongly correlated leading to sharper peaks. This is taken into account in the modelling through two empirical parameters noted δ_1 and δ_2 (Farrow et al., 2016, 2007) for the low-temperature and high-temperature contributions respectively.
- Q_{broad}: the peak broadening factor due to increased noise at higher Q values;

Thus, the peak width which is correlated with the atomic thermal displacement parameter, is modulated as follows:

$$\sigma_{ij} = \sigma'_{ij}\sqrt{1 - \frac{\delta_1}{r_{ij}} - \frac{\delta_2}{r_{ij}^2} + Q_{broad}^2 r_{ij}^2} \tag{2.22}$$

Where σ'_{ij} is the G(r)'s peak width assuming no correlated movement between atoms i and j, ${\sigma'_{ij}}^2 = \langle \vec{u}_{ij}^2 \rangle$ and is computed from the anisotropic displacement parameters, r_{ij} is the distance between two atoms.

- Q_{damp}: the PDF Gaussian dampening envelope due to limited reciprocal space (Q) resolution which reflects the quality of collimation and instrument resolution. (Toby and Egami, 1992).;

The discrepancy between an experimental and modelled PDF between r_{min} and r_{max} is measured by the agreement factor A, which is defined as:

$$A^2 = \frac{\int_{r_{min}}^{r_{max}} \left[G_{exp}(r) - G_{mod}(r)\right]^2 dr}{\int_{r_{min}}^{r_{max}} dr} \tag{2.23}$$

The parameters listed above are refined by minimizing A. In this work, the quality of a PDF model is assessed by the goodness-of-fit (GOF), which is defined as $\frac{A^2}{A_{min}^2}$ where A_{min} relates to the minimum A value one can expect in view of the experimental uncertainty due to the statistical nature of neutron scattered intensity. It is obtained from error-propagation calculations of g(r) (Egami and Billinge, 2012; Mamontov and Egami, 2000). In addition, we have taken into account the loss of goodness of fit as the number of fitted parameters n_p increases with regard to the number of independent experimental points n_e by calculating the relative goodness-of-fit (RGOF) through the expression:

$$RGOF = A \times n_e^{\frac{1}{2}}/(n_e - n_p)^{\frac{1}{2}} \tag{2.24}$$

, where n_p is the number of refined parameters, mainly dependent upon the defect structure, and n_e is the total independent information or number of data points contained in the experimental PDF, which according to the Nyquist-Shannon sampling theorem (Farrow et al., 2011) is given by:

$$n_e = (r_{\max} - \mathrm{r}_{\min}) \cdot \mathrm{Q}_{\max}/\pi \tag{2.25}$$

For a refinement over a r range between 1 and 6 Å, n_e is 37. It is equal to 82 for a refinement up to 12 Å.

The Nyquist-Shannon sampling scheme is chosen here to minimize the statistical correlations between data points in the PDF and to avoid oversampling. In addition it guarantees a good estimate of uncertainties in the refinement parameters (Farrow et al., 2011) and provides a means of testing structural models with the assumption that there are no systematic errors.

2.5 Positron annihilation spectroscopy – vacancy defect study

2.5.1 Introduction

This section provides some background relating to the theory of positron annihilation in solids and how the method is implemented. It is not meant to constitute an exhaustive account of the theory or the technical aspects of the set up as detailed accounts of these can be found elsewhere (Barthe et al., 2003; Krause-Rehberg and Leipner, 1999b). In section 2.5.2, we provide an overview of the basic concepts used for describing the interaction between positrons and solids. Sections 2.5.3 and 2.5.4 are more specifically devoted to the two experimental implementations that we have used and are most frequently applied to the study of semiconductors, i.e. Doppler broadening spectroscopy (2.5.3) and positron lifetime spectroscopy (2.5.4). These techniques enable the determination of two following positron related characteristics: the momentum distribution of the annihilating electron-positron pairs and the positron lifetime distribution. In both these sections we describe the corresponding experimental setups and how the data treatment is carried out. In section 2.5.5, we describe a three-state positron trapping model (Krause-Rehberg and Leipner, 1999b), which we use in Chapter 4 to estimate defect concentrations in our material.

2.5.2 Positron behaviour in solids

2.5.2.1 Positron implantation and thermalisation

Positrons are emitted from a radioactive source (e.g. ^{22}Na, ^{64}Cu, ^{19}Ne, ^{58}Co, etc.) as a result of a β^+ decay process. The energy distribution of the positron is continuous and in this work positrons are emitted from a ^{22}Na source with a maximum energy of 540 keV (Barthe et al., 2003). When a high kinetic energy positron penetrates a solid, it loses its energy as a result of interactions through one of two mechanisms (Brandt and Arista, 1982). The most important one is due to ionisation and excitation of electrons in the medium, i.e. the electronic stopping power of the medium. The second, which occurs at lower energies is dominated by phonon processes. Thermalisation times (Dupasquier and Mills, 1997) at room temperature for both metals and semiconductors (1-3 ps), are considerably less than the lifetime measured for annihilation (~200 ps) as discussed later.

2.5.2.2 Positron diffusion

The thermalized positrons diffuse in the solid until they either annihilate or are trapped at different defect sites. D_+ is the positron diffusion coefficient determined according to the Nernst-Einstein relationship:

$$D^+ = \frac{\mu_+}{e} k_b T = \frac{k_b T}{m_+} \tau_{relax} \tag{2.26}$$

, where $k_B$is the Boltzmann constant, and e is electron charge, μ_+ is the mobility of positrons, m_+ the effective positron mass, τ_{relax} is known as the relaxation time for positron diffusion. This defines a positron mean-free path given by (Bergersen et al., 1974):

$$l_+ = \frac{3D_+}{\sqrt{\frac{3k_B T}{m_+}}} \tag{2.27}$$

The experimental value of D_+ at 300K for metals or semiconductors is of the order of 1 to 2 cm^2/s (Soininen et al., 1992) and the corresponding mean-free path has been estimated in metals at 5 to 10 nm (Barthe et al., 2003). The diffusion length, or rather the square root of the mean square displacement, in a defect free semiconductor can be estimated from the measured average lifetime and the positron diffusion coefficient. It is thought to be around 100 nm to 200 nm (Iwai et al., 2007; Paulin et al., 1974). So in metals, since the positron mean free paths is about one order of magnitude below the diffusion length, random walk theory may be readily applied. In uranium dioxide however, as will be seen later, the diffusion lengths obtained by analysing the Doppler broadening characteristics for stoichiometric UO_2 is around 9 to 11 nm (Barthe et al., 2007, 2004). This could possibly indicate a lower diffusion coefficient for positrons in UO_2 and cast doubt as to whether random walk theory may indeed be applied to describe effective positron diffusion.

2.5.2.3 Positron annihilation

The annihilation of the positron with an electron corresponds to the conversion of the electron-positron pair to a gamma electromagnetic radiation:

$$e^- + e^+ \rightarrow n\gamma \tag{2.28}$$

During this annihilation process, the energy, spin, charge and momentum of the system are conserved. The number of photons emitted in the process depends upon various parameters:

- The reaction cross section involving emission of a single γ ray is only at all substantial for positron energies above 1 MeV which is more than the maximum positron energy (540 keV) we are concerned with here (^{22}Na source).
- Because annihilation of an electron-positron pair involves energies (~511 keV) far in excess of that of the electron (~eV) or the thermalized positron (~1/10 eV), conservation of energy and momentum requires the production of at least two photons (n=2) emitted in opposite directions, if no other particle participates in the reaction.
- Annihilation with emission of an additional photon requires the reaction cross section to be multiplied by a factor of roughly 1/137 (Janot, 1976) which makes this event improbable.

To summarise, in solid condensed matter, the most common annihilation reactions involve the emission of two gamma photons.

We now consider this most-likely case. Because the kinetic energy of the electron and positron are negligible in comparison with the energy involved in the reaction, conservation of momentum and energy requires that photons be emitted in quasi-opposite directions (i.e. approximately at 180 °) and with an energy roughly determined by the mass-energy equivalence principle:

$$E = m_0 c^2 \tag{2.29}$$

, where c is the speed of light, and m_0 is the mass of an electron (or positron). However the annihilating electron-positron pair is not strictly at rest and energy and momentum conservation principles require: 1) that the photons be emitted in directions that are not strictly opposite but at 180 °- $\Delta\theta$ ($\Delta\theta$ small) and 2) their energy differs by an amount $2\Delta E$ (ΔE small). These energy and angular deviations ΔE and $\Delta\theta$ are obtained from writing the conservation of energy and momentum of the system:

$$\Delta E = \frac{cP_L}{2} \tag{2.30}$$

$$\Delta\theta = \frac{P_T}{m_0 c} \tag{2.31}$$

where P_L (resp. P_T) is the longitudinal (resp. transverse) component of the e^+/e^- pair momentum. We assume that the annihilating positron momentum is negligible in comparison to that of the annihilating electron which is reasonable since positrons are thermalized. Then, equation (2.30) shows that a measure of the energy broadening distribution (ΔE) of the photons, known as Doppler broadening spectroscopy, provides a measure of the distribution of the longitudinal component or one-dimensional momentum distribution $\rho(P_L)$ of annihilating e^+/e^- pairs. The measured photon energy distribution is centred on 511 keV. Similarly, the measure of the distribution of $\Delta\theta$ angles, equation (2.31), is a measurement of the distribution of the transverse components of annihilating electrons and is referred to as angular correlation of electron-positron annihilation radiation.

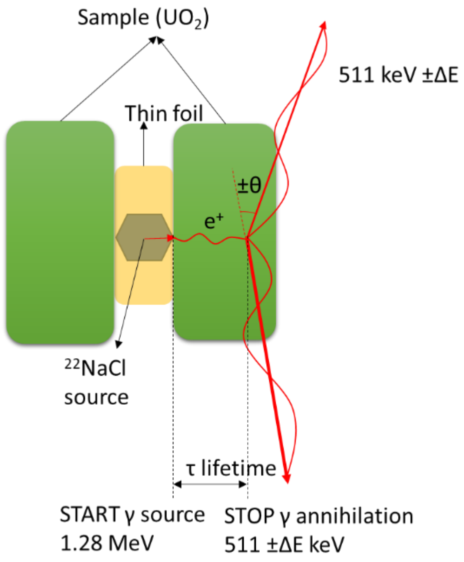

Figure 2.17: Three characteristic quantities relating to positron annihilation spectroscopy.

Figure 2.17 shows the three principle characteristics we are concerned with in PAS. In addition to Doppler broadening (ΔE) and angular correlation ($\Delta\theta$), positron lifetime τ provides much information about defects in the material. This quantity is defined as the time that elapses between the entry of the positron in the material and its annihilation. In this work, we have carried out positron lifetime and Doppler broadening spectroscopy only. The technical details relating to these are provided in sections 2.5.3 and 2.5.4.

Delocalised annihilation states

After implantation and thermalization, a positron may annihilate either from a delocalised state, i.e. in the lattice, or, if it is trapped in a defect induced potential well, from a localised state. We are concerned here with describing the delocalised states (or Bloch states). The positron wave function in a perfect crystal follows the periodicity of the crystal lattice. This can be understood as a consequence of the Coulomb potential which is such that positrons are repelled by the nuclei and attracted in the regions in between the nuclei. Annihilation in the lattice or in a delocalised state is associated with a characteristic lifetime (usually noted τ_L) and momentum distribution.

Localised annihilation states

Because the positron is positively charged, its potential energy decreases in regions which are void of nuclei such as vacancies, voids or regions around dislocations which are in tension (Trumpy, 1994). These sites are therefore traps for positrons. In ionic crystals, positrons may also be trapped at negatively charged ions in Rydberg states, which are relatively shallow traps (Krause-Rehberg and Leipner, 1999b).

In such sites, positrons explore the electronic density around them and the consequence of this is that annihilation characteristics are modified with respect to the perfect crystal. **This constitutes the basis for defect characterisation with PAS.** In semi-conductors, annihilation characteristics are modified differently depending upon whether one is dealing with vacancies or negative ions. When vacancies are present, the average positron lifetime will increase, depending of course on the nature of the vacancy (charge state and volume) and vacancy concentration. Because vacancies are regions of low core electron density, positrons trapped at such sites will more probably annihilate with low momentum electrons. This will translate in an increase (resp. decrease) in the fraction of positrons annihilating with low (resp. high) momentum electrons and the energy distribution of detected photons will narrow. The situation is different for negative ions for which the average lifetime and momentum distribution are expected to be comparable to those of the lattice. **The effect of oxygen interstitials in UO_2 is only known from a limited number of theoretical studies.**

2.5.3 Doppler broadening spectroscopy

2.5.3.1 Slow positron beam

Positrons used for Doppler broadening spectroscopy are emitted from a radioactive source ^{22}Na and have a maximum energy of 540 keV. To study defects at surfaces, in thin layers or at the interfaces, a low mono-energetic positron beam is used. With variable incident positron energies, one can probe the material at different depths. A slow-positron beam is available in CEMHTI, Orleans. Positrons are initially thermalized using a thin tungsten sheet as moderator as illustrated in Figure 2.18. The positrons that emerge at the surface of the tungsten moderator have a very narrow energy distribution and are accelerated electrostatically to energies ranging between 0 and 25 keV in a direction normal to the moderator.

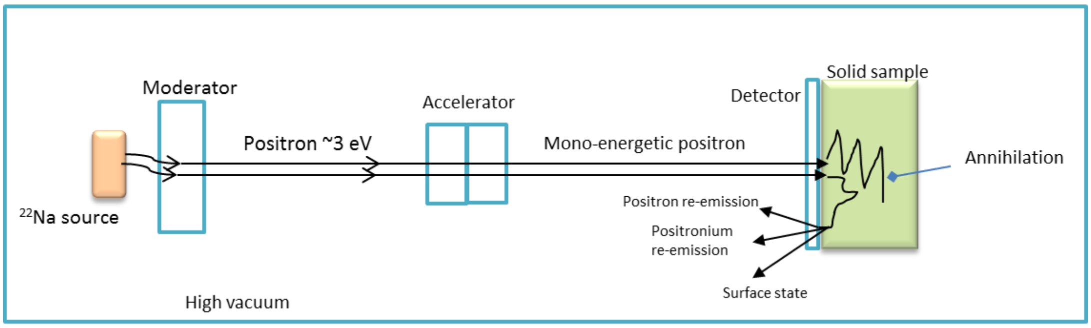

Figure 2.18: Schematic diagram illustrative of the slow-positron-beam Doppler broadening spectroscopy setup.

2.5.3.2 Positron implantation profiles

The implantation profile for mono-energetic positrons from a slow-positron beam is derived from a Gaussian distribution (Krause-Rehberg and Leipner, 1999a):

$$P(z) = -\frac{d}{dz}(\exp\left(-\left(\frac{z}{z_0}\right)^m\right) \tag{2.32}$$

and,

$$z_0 = \frac{z_m}{0.886}\ and\ z_m = \frac{A}{\rho}E^n \tag{2.33}$$

In which, z_m is the mean implantation depth (cm), E is the implantation energy (keV). A, m, n are constants specific to a given material and ρ is the material density (for our high density UO_2, ρ =10.76 g/cm^3). The implantation profile is essential to the analysis of Doppler broadening measurements, because it is related to the number of positrons annihilating in a layer of given thickness below the surface thus providing depth dependent microstructural information.

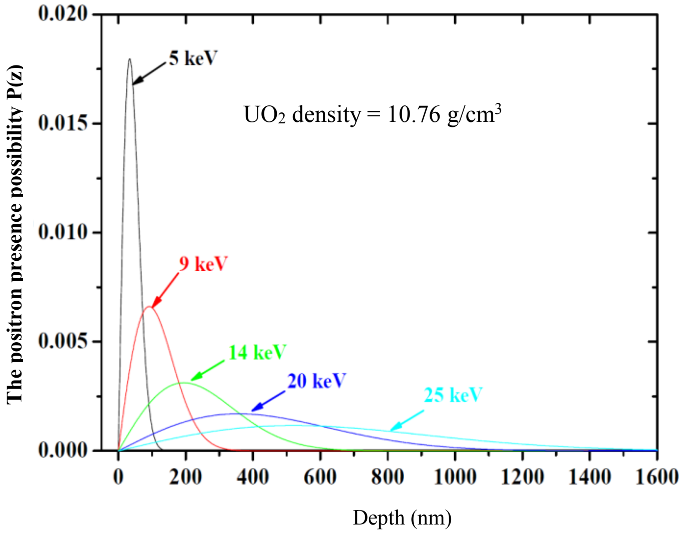

Figure 2.19: Implantation profiles of mono-kinetic slow positrons in UO_2.

In this work, we have applied values reported in previous studies (Soininen et al., 1992) in equation (2.32) and (2.33) ($A=2.95\cdot10^{-6}$ µg/cm^2, m=2, and n=1.7). Note that the average penetration depth of a 5 keV positron is less than 200 nm. A 25 keV positron probes a maximum depth of *circa.* 1.3 µm. In the former case, as illustrated in Figure 2.19, the depth resolution is rather high, whereas for the higher energy positrons resolution is poor as a result of broad positron distribution. The depth probed by 25 keV positrons remains less than that for other materials such as Si and GaN (~6 µm).

2.5.3.3 Doppler broadening spectrometer

The spectrometer essentially comprises a high purity germanium detector which operates at liquid nitrogen temperature to limit thermally induced noise. It is a high resolution, high efficiency detector polarised at 3 kV (Barthe et al., 2003). The high resolution is required as Doppler spectra are usually quite narrow. An electronic chain comprising an amplifier, an anti- pile-up system (for high counting rates) and a multichannel analyser enables photons to be counted in the appropriate energy class.

In addition, we performed *in situ* temperature-dependent Doppler broadening spectroscopy on one sample in this work. The sample was placed on a copper sample holder which can be heated up to 550 °C. The multi-temperature characterization enables us to investigate the evolution of defects as a function of temperature.

2.5.3.4 Data treatment

Figure 2.20 shows a Doppler broadening spectrum (acquired with a beam energy of 0.5 keV) of a polished UO_2 stoichiometric sample further pre-annealed at 1700 °C. Apart from the maximum at 511 keV, the other outstanding feature of this distribution lies in the background noise at lower energy levels. This noise is due to Compton scattering of photons produced by the 511 keV annihilation line. As the scattered photons necessarily have a lower energy than that of photons before scattering occurs, the noise level is greater to the right of the 511 keV annihilation line than to the left. Once the data is collected, the background noise has to be subtracted so that further analyses can go ahead:

$$BG(E) = A + (B - A)\frac{F(E)}{F_{total}} \tag{2.34}$$

BG(E) represents the background noise at an energy level E, and A and B are the average noise on the right (E_R >523 keV) and left sides (E_L <504 keV) of a peak. F(E) represents the area of the spectrum between energies E and E_R, while F_{total} is the total area below the curve. The noise is measured to the left of the spectrum below $E_L \approx$ 504 keV and to the right above 523 keV (Barthe et al., 2003).

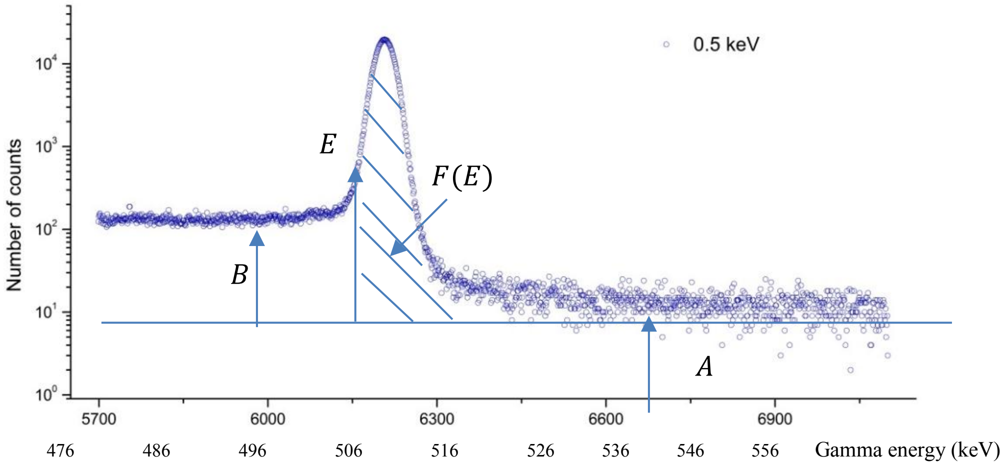

Figure 2.20: Doppler broadening spectrum for stoichiometric UO_2 at positron energy of 0.5 keV.

Figure 2.21 shows the Doppler broadening spectrum corrected for background noise. The surface in green below the spectrum indicated as S in this figure represents the fraction of annihilating e+/e- pairs of low momentum. This quantity (S) is defined as the ratio of the counts in the central region of the annihilation line to the total number of counts. W (surface in pink) represents the fraction of positrons annihilating with high momentum electrons obtained from integrating in the wings of the distribution. It is defined as the ratio between the number of counts of the corresponding region in Figure 2.20 to the total number of counts. S and W are defined so as to represent the fraction of positrons annihilating with valence and core electrons respectively. The window for S is chosen so as to retain the statistical benefits of collecting a large number of counts: typically S≈0.5. While the window chosen for W must be far enough from the centre of the annihilation line to guarantee a minimal contribution of valence or free electrons (Tuomisto and Makkonen, 2013). An additional criterion for selecting the windows can be to try to maximize the changes in S or W between two samples. One can be guided in doing so by theoretical momentum ratio curves. The momentum windows commonly used for analysing the spectra of UO_2 are (-2.80, 2.80) $\cdot 10^{-3}$ m_0c for S, and (-26.35, -10.61) / (10.61, 26.35) $\cdot 10^{-3}$ m_0c for W.

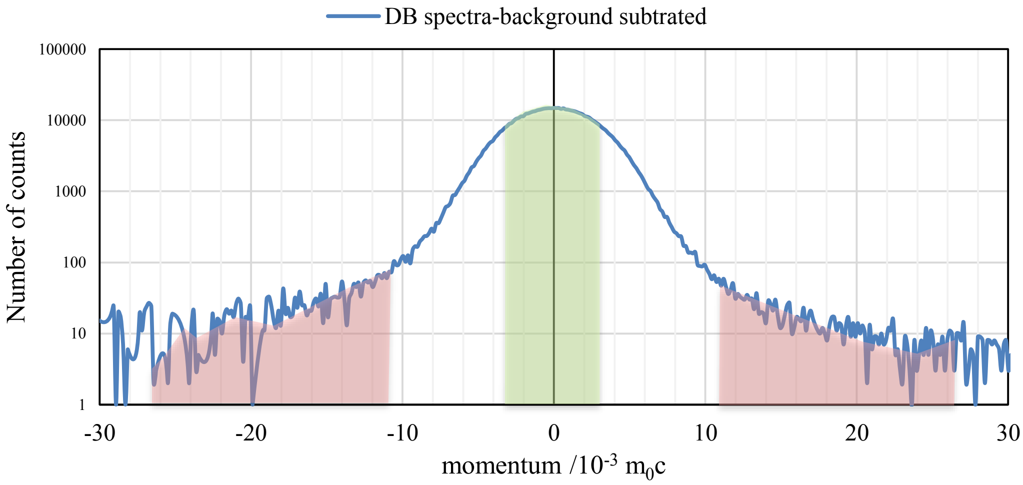

Figure 2.21: Doppler broadening spectrum measured for polished and pre-annealed UO_2 corrected for background noise.

S and W for a defect-free lattice are noted S_L and W_L. As has been highlighted previously (section 2.5.2.3), when defects are present in crystalline solids, the annihilation states can change. However, one must note that the absolute values of S and W have no straightforward absolute significance as they are dependent upon experimental features of the setup such as the detector resolution, the amplifier gain, etc. Therefore, in general, one carries out comparative analyses and the S and W parameters are normalised to the corresponding values of a reference sample in which it is assumed there are no defects. **The fact that (W, S) data points for different samples line up, is often taken as evidence that the defect being probed is the same but present in the samples at different concentrations.**

2.5.4 Positron lifetime spectroscopy

The positron lifetime is the time that elapses between the moment a positron enters the solid and the moment at which it annihilates. Measuring it requires two signals be detected corresponding to the creation of the positron and its annihilation. The former comes in the form of a 1.28 MeV gamma particle which is quasi-simultaneous to the ^{22}Na β^+ disintegration. The latter corresponds to the detection of one of the two 511 keV gamma particles produced when the positron annihilates.

2.5.4.1 Fast positron source

The positron source is prepared by depositing a sodium chloride solution, enriched in ^{22}Na on a fine metal sheet (in our case a 5 µm Al foil). The solution is left to dry and the source is then placed between two identical samples (same material and geometry), so that all the positrons emitted from the source annihilate in the material. As the emitted positrons penetrate the sample, they rapidly lose their energy by interacting with electrons. Because positrons are emitted from the source with a broad range of energies, the stopping profile is not that provided by equation (2.32). Rather, it is given by:

$$P(z) = \exp(-\alpha z) \tag{2.35}$$

, where z is the implantation depth, and α is the attenuation coefficient in the material. α is proportional to the material density and the inverse of maximum kinetic energy E_{max} of positrons (which is about 540 keV for a ^{22}Na source) (Paulin et al., 1974):

$$\alpha = 16 * \frac{\rho}{E_{max}^{1.4}(MeV)} \tag{2.36}$$

The implantation profile for fully dense UO_2 indicates that the maximum positron penetration depth is about 130 μm which is usually much less than the sample thickness (roughly 1 mm in this work). Therefore virtually all positrons created are implanted in the samples and furthermore they are probing bulk material properties.

An important point that should be made here, because of its practical and theoretical implications, is that **at any given time, there is at most only a single positron in the sample most of the time.** The reason for this may be understood from the fact that the typical activity of a source is in the region of $7 \cdot 10^5$ Bq so that on average, one positron is emitted by the source every 1 to 2 μs. This value is about four orders of magnitudes above the average lifetime in our material. The practical implications of this will be alluded to in the next section and the consequences vis-à-vis the data analysis in section 2.5.5.

2.5.4.2 Lifetime spectrometer

The lifetime spectrometer is used to measure the time that separates the detection of the 1.28 MeV gamma particle marking the birth of a positron and that of the 511 keV particle marking its annihilation. This measurement is carried out by two coupled detection lines each comprising a scintillator and photomultiplier, each of which is optimised to detect one or the other gamma particle. Figure 2.22 shows the two photomultipliers and the sample-source-sample system sandwiched in between (Barthe et al., 2003).

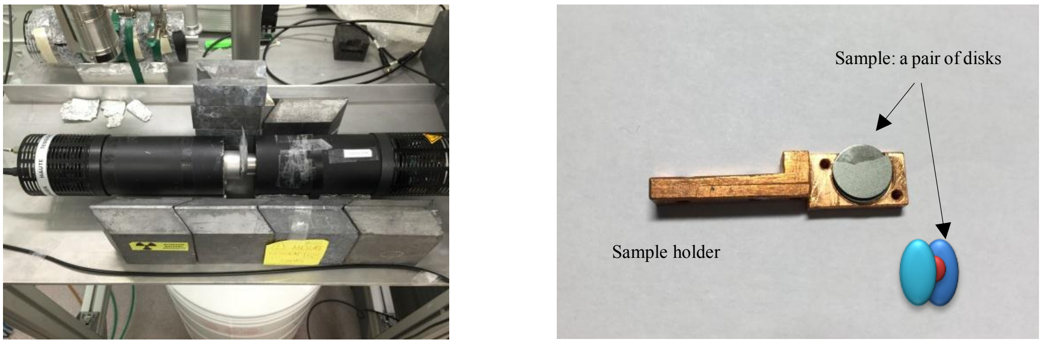

a) The two detection lines

b) The sandwich setup

Figure 2.22: Positron lifetime experiment.

The signals collected by two detectors are analysed with analog nuclear instrumentation electronics (Tuomisto and Makkonen, 2013) which include:

1- Two constant fraction discriminators (one for each line). Their function is to enable the selection of photons of appropriate energy and determine accurately the time at which they are detected.
2- A time to amplitude converter which collects in coincidence the signals from the two lines of the 1.28 MeV and 511 keV photons. It further generates a signal with an amplitude that is proportional to the time separating the two events.
3- A multichannel analyser (MCA). The information it receives from the time to amplitude converter is used to count the number of events corresponding to a given lifetime in the appropriate channel.

The end result is a histogram of annihilation events as a function of the time difference between the birth and annihilation of the positron. A key feature of positron lifetime spectroscopy is that it should enable the separation of different lifetime components so the spectrometer resolution is essential. There are many parameters that affect the resolution function of the spectrometer but ultimately, it is measured using a ^{60}Co source. The resolution of the spectrometer at CEMHTI is in the region of 230 ps.

2.5.4.3 Lifetime spectrum analysis

As mentioned in a preceding section there is seldom more than one positron at a time in a sample. This is not quite true to the extent that corrections must sometimes be made for false coincidences that can occur in high activity sources (Tuomisto and Makkonen, 2013). Notwithstanding this, lifetime spectra analyses are based upon the ergodic principle so that the time average of single sequential events (for a sufficiently large number of events) can replace a fictitious ensemble average. What we are concerned with here is how to correlate experimental lifetime spectra to meaningful physical quantities.

There are basically three types of corrections required before the actual lifetime characteristics of the sample may be determined. The first is known as the source correction. This correction is tricky and covers a number of different phenomena. It stems from the fact that a fraction of positrons annihilate in the source rather than in the sample either because they are emitted from the source with a low energy or because they have back-scattered off the sample (Barthe et al., 2003). Due account of this has been taken from characterising the source along with reference samples which only show a single lifetime component. In this work three components were identified as being due to the source and characterised at 230 ps, 450 ps and 1500 ps. The corresponding intensities were estimated at 37 %, 3.9 % and 0.4 % respectively. The source (NaCl) and the surface effects produce the latter two lifetime components: 230 ps and 450 ps. The 1500 ps component is related to positronium formation at the sample surface.

The second correction is due to background noise which must be subtracted. The third correction accounts for the resolution function of the lifetime spectrometer as characterised using a ^{60}Co source. *In fine*, the measured positron lifetime spectrum N can be written as the following convolution between the annihilation probability density p(t) and the spectrometer resolution function R (Tuomisto and Makkonen, 2013):

$$N(t) = \int_{-\infty}^{\infty} R(s) \cdot p(t-s)\, ds \tag{2.37}$$

, where R is the resolution function of the spectrometer and p(t) is the positron probability density at time t. $p(t)$ is related to the number $dn(t)$ of positron annihilations between t and t+dt in the following way:

$$dn(t) = -n_0 \cdot \mathrm{p}(t)\, dt \tag{2.38}$$

, where n_0 is the total number of positrons (or annihilation counts). Now for a material containing an indefinite number of annihilation states, it can be shown using trapping models, that the probability density p(t) may be written as:

$$p(t) = \sum_i \frac{I_i}{\tau_i} \exp\left(-\frac{t}{\tau_i^*}\right) \tag{2.39}$$

, where τ_i is a characteristic lifetime component in the i^th^ state and I_i is the lifetime component intensity. Note that τ_i cannot be interpreted as simply as the average lifetime in state i. Indeed, the simplest of models, covering for instance positron annihilation of a monoatomic metal whose sole defects are vacancies, describes annihilations as occurring either in the lattice or in deep trap states. If κ_V is the positron trapping rate at vacancy defects, $1/\tau_L$ and $1/\tau_V$ the annihilation probabilities in the lattice (bulk) and in vacancies, then (Krause-Rehberg and Leipner, 1999b):

$$\frac{1}{\tau_1} = \kappa_V + \frac{1}{\tau_L} \tag{2.40}$$

$$\frac{1}{\tau_2} = \frac{1}{\tau_V} \tag{2.41}$$

Figure 2.23 shows two typical lifetime spectra collected by the lifetime spectrometer which contains roughly 10^5 annihilation events. The solid line represents the lifetime spectrum of polished and pre-annealed UO_2, which has only one lifetime component of approximately 170 ps. The dashed line represents the lifetime spectrum of $UO_{2.042}$ oxidized at high temperature (1350 ℃). It has a second long lifetime component at 316 ps, which will be further discussed in the following sections.

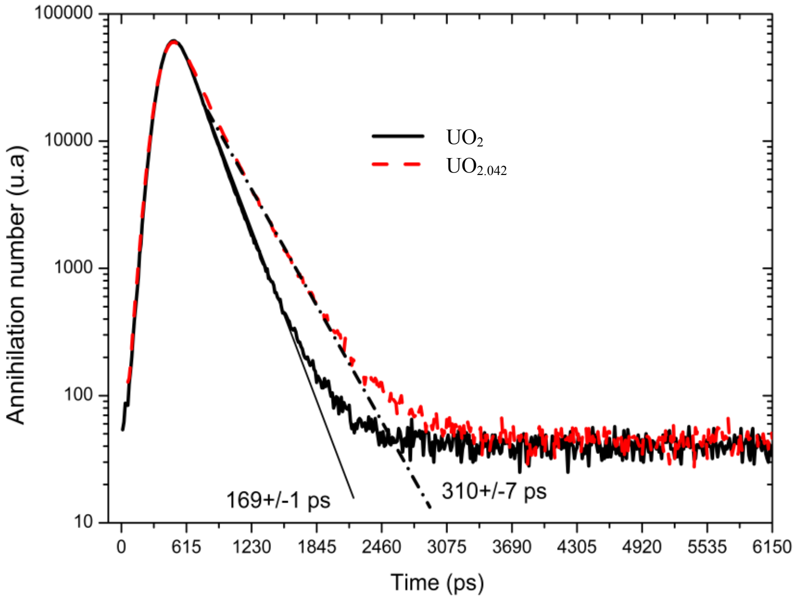

Figure 2.23: Two raw positron lifetime spectra measured in UO_2 and $UO_{2.04}$ at room temperature (300 K).

To determine positron lifetime components and intensities corresponding to different annihilation states, the Posfit (Kirkegaard and Eldrup, 1972) program is used. Before the data analysis is carried out, the background noise is subtracted. Posfit assumes a Gaussian resolution function.

In practice, it is difficult to resolve lifetime components that differ by less than a factor of 1.3-1.5 which implies three components at the most may be resolved in a spectrum. A suitable determination of the lifetime components is obtained for a spectrum composed of at least $6 \cdot 10^5$ counts.

2.5.5 Three-state positron trapping model

The ergodic assumption enables the positron probability density to be described through a time and space dependent Fokker-Planck type equation (Tuomisto and Makkonen, 2013) associated with appropriate boundary and initial conditions; the latter being the fast positron implantation profile (section 2.5.4.1). However, in the case of near-homogeneous materials as is expected of oxidised samples, the space dependency vanishes and the Fokker-Plank type diffusion equation reduces to a set of coupled, first order, ordinary differential equations describing the rate of change of the number of positrons in the various traps the model assumes.

We have seen in previous sections that it is usually not possible to accurately determine more than three components in a lifetime spectrum, so one may well wonder what the point is of analysing the data with a model that describes annihilation from three localised trap-states and one delocalised state. There are mainly two motivations behind this. The first is that key to determining defect concentrations, is the fact that the trapping rate for any defect is the product of the defect concentration with the trapping coefficient. Trapping coefficients, or the probability that a given defect will trap a positron, can be determined theoretically for a given type of defect from the application of Fermi's Golden Rule (Puska and Nieminen, 1994). Trapping rates on the other hand, as will be formulated explicitly in the following, can possibly be determined experimentally from the knowledge of annihilation fractions at various traps. These latter quantities are obtained indifferently from lifetime or Doppler broadening spectroscopy so that the trapping model appears as a means of ascertaining the consistency between both spectroscopic techniques and possibly even with theoretical approaches as they are made available.

In our material, and under the oxidation conditions the various samples we have studied have been subjected to, one can assume that three trap sites must be considered: the neutral, uranium vacancy containing defect (V_0), the negatively charged uranium vacancy containing defect (V_-) and negatively charged ions (ST) assumed to constitute shallow traps and essentially comprising oxygen interstitials or clusters thereof (see Figure 2.24). The corresponding differential equations describing the rate of change in the number of positrons in each of the four different states may be written as (Krause-Rehberg and Leipner, 1999b):

$$\frac{dn_L}{dt} = -\left(\lambda_L + \kappa_{V_0} + \kappa_{V_-^*} + \kappa_{ST}\right) \cdot n_L + \delta_{ST} n_{ST} \tag{2.42}$$

$$\frac{dn_{V_0}}{dt} = \kappa_{V_0} n_L - \lambda_{V_0} n_{V_0} \tag{2.43}$$

$$\frac{dn_{V_-}}{dt} = \kappa_{V_-^*} n_L - \lambda_{V_-} n_{V_-} \tag{2.44}$$

$$\frac{dn_{ST}}{dt} = \kappa_{ST} n_L - (\lambda_{ST} + \delta_{ST}) n_{ST} \tag{2.45}$$

ST stands for shallow traps and L stands for the lattice. δ_D and κ_D are the detrapping and trapping rates in a given defect D. Subscript V_0 represents the neutral vacancy, and V_- the negative vacancies, from which detrapping may occur from an associated Rydberg state at high enough temperature. $\kappa_{V_-^*}$ represents the trapping rate that has taken into account the case of positrons which originally trap in other states (i.e. the Rydberg states) transit to the negatively charged vacancy. The detrapping rates δ_{ST} for the shallow traps (Manninen and Nieminen, 1981) are:

$$\delta_{ST} = \frac{\kappa_{ST}}{\rho_{ST}} \left(\frac{m * k_B T}{2\pi\hbar^2}\right)^{\frac{3}{2}} \exp\left(-\frac{E_{ST}}{k_B T}\right) \tag{2.46}$$

, where κ_{ST} is the positron trapping rate in shallow traps, ρ_{ST} is the shallow traps density, and E_{ST} is the binding energy of positrons to the shallow traps.

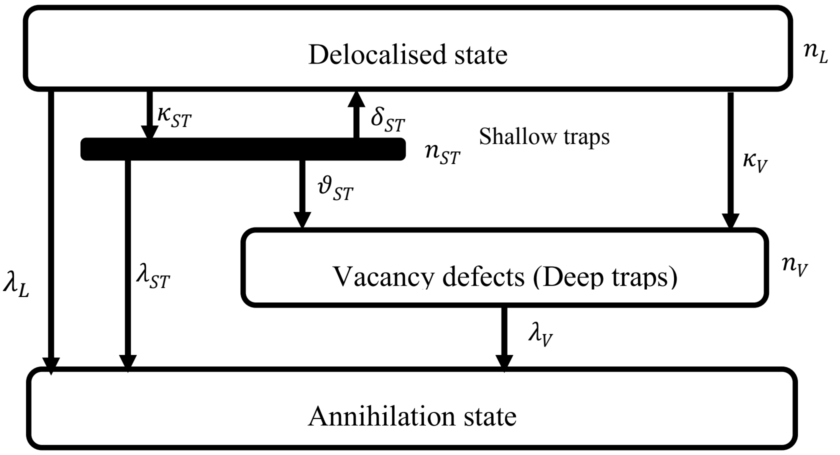

Figure 2.24: Positron trapping in various states (Krause-Rehberg and Leipner, 1999b).

Solving the equations (2.42)-(2.45) yields the total number of positrons at time t is:

$$n(t) = n_L(t) + n_{V_0}(t) + n_{V_-}(t) + n_{ST}(t) = \sum_i I_i \exp(-\lambda_i t)\,, i = 4 \tag{2.47}$$

If λ_1 to λ_4 represent the annihilation probabilities in a given state and τ_1 to τ_4 are the corresponding lifetime components, then they may be expressed as:

$$\tau_1 = \frac{2}{\Lambda+\Xi},\ \tau_2 = \frac{2}{\Lambda-\Xi},\ \tau_3 = \frac{1}{\lambda_{V_0}},\text{ and } \tau_4 = \frac{1}{\lambda_{V_-}} \tag{2.48}$$

τ_1 and τ_2 correspond to the positron lifetimes of the lattice and shallow traps, which normally correspond to the short lifetime component. The latter two provide the long lifetime components corresponding to the vacancy defects. The intensities I_1 to I_4 are given by:

$$I_1 = 1 - (I_2 + I_3 + I_4) \tag{2.49}$$

$$I_2 = \frac{\delta_{ST} + \lambda_{ST} - \frac{1}{2}(\Lambda - \Xi)}{\Xi} \times \left[1 + \frac{\kappa_{ST}}{\delta_{ST} + \lambda_{ST} - \frac{1}{2}(\Lambda - \Xi)} + \frac{\kappa_{V_0}}{\lambda_{V_0} - \frac{1}{2}(\Lambda - \Xi)} + \frac{\kappa_{V_-^*}}{\lambda_{V_-} - \frac{1}{2}(\Lambda - \Xi)}\right] \tag{2.50}$$

$$I_3 = \frac{\kappa_{V_0}(\delta_{ST} + \lambda_{ST} - \lambda_{V_0})}{[\lambda_{V_0} - \frac{1}{2}(\Lambda + \Xi)][\lambda_{V_0} - \frac{1}{2}(\Lambda - \Xi)]} \tag{2.51}$$

$$I_4 = \frac{\kappa_{V_-^*}(\delta_{ST} + \lambda_{ST} - \lambda_{V_-})}{[\lambda_{V_-} - \frac{1}{2}(\Lambda + \Xi)][\lambda_{V_-} - \frac{1}{2}(\Lambda - \Xi)]} \tag{2.52}$$

In equations (2.49) to (2.52), Λ and Ξ are given by:

$$\Lambda = \lambda_{\mathrm{L}} + \kappa_{ST} + \kappa_{V_0} + \kappa_{V_-^*} + \delta_{ST} + \lambda_{ST} \tag{2.53}$$

$$\Xi = \sqrt{\left(\lambda_{\mathrm{L}} + \kappa_{ST} + \kappa_{V_0} + \kappa_{V_-^*} - \delta_{ST} - \lambda_{ST}\right)^2 + 4\delta_{ST}\kappa_{ST}} \tag{2.54}$$

In real lifetime spectra it is not possible to distinguish the four components because the lifetimes τ_1 (lattice) and τ_2 (shallow traps) are very close, and those of both vacancy defects τ_3 (V_0) and τ_4 (V_-) are also similar. It follows that only two lifetime components are distinguished and they are:

$$\mathrm{I}_{2\mathrm{exp}} = \frac{(\tau_{avg} - \tau_{1exp})}{(\tau_{1exp} - \tau_{2exp})} \cdot 100 \tag{2.55}$$

$$\tau_{1exp} = [(I_1 \times \tau_1) + (I_2 \times \tau_2)] \cdot 10^{12}/(I_1 + I_2) \tag{2.56}$$

$$\tau_{2exp} = [(I_3 \times \tau_3) + (I_4 \times \tau_4)] \cdot 10^{12}/(I_3 + I_4) \tag{2.57}$$

The trapping rate κ_D of a particular type of defect is the product of the trapping coefficient $\mu_D$and defect concentration c_D:

$$\kappa_D = \mu_D \cdot c_D/N \tag{2.58}$$

, in which N is atomic density of the material. Temperature dependencies for positron trapping coefficients of vacancies of variable charge have been reported (Puska et al., 1990; Puska and Nieminen, 1994). Makinen et al. proposed a more general $T^{-\frac{1}{2}}$ dependence after analysing the positron lifetime spectra obtained from proton-irradiated Si, electron-irradiated Si, and *p*-doped Si, from 15 K to 150 K (Makinen et al., 1992). Therefore, for negatively charged defects (either uranium vacancies or oxygen ions), the trapping coefficient at a given temperature T is:

$$\kappa_{D_-} = \frac{\mu_0 \cdot c_{D_-}}{N}\sqrt{\frac{T_0}{T}} \tag{2.59}$$

, where μ_0 is the trapping coefficient at T_0 = 20 K. The trapping coefficient for a negatively charged vacancy defect $\kappa_{V_-^*}$ is slightly different. Although the thermal detrapping of positrons from vacancies is negligible due to the high binding energy, we have also included the Rydberg state for them which takes into account the long-range Coulomb potential. So the effective trapping rate at negative vacancies is written as:

$$\kappa_{V_-^*} = \kappa_{V_-} + \frac{\mu_{Ryd} c_{V_-}}{N} \cdot \sqrt{\frac{T}{T_0}} \cdot \frac{\vartheta_{Ryd}}{\vartheta_{Ryd} + \delta_{Ryd}} \tag{2.60}$$

, in which μ_{Ryd} is the trapping coefficient for the corresponding Rydberg state, ϑ_{Ryd} is the transition rate from the Rydberg states to lower-energy states associated with vacancies, and δ_{Ryd} is the detrapping coefficient from the Rydberg state corresponding to the negatively charged vacancy defect:

$$\delta_{Ryd} = \frac{\kappa_{Ryd}}{c_{V_-}} \left(\frac{m * k_B T}{2\pi\hbar^2}\right)^{\frac{3}{2}} \exp(-\frac{E_{Ryd}}{k_B T}) \tag{2.61}$$

$$\text{And } \kappa_{Ryd} = \frac{\mu_{0,Ryd} \cdot c_{V_-}}{N} \sqrt{\frac{T_0}{T}} \tag{2.62}$$

Note that the average lifetime for the three-state trapping model, which is expected to reproduce to the experimental lifetime, can be expressed as:

$$\tau_{avg} = \int_0^\infty t\left(-\frac{dn(t)}{dt}\right) dt = f_L \tau_L + f_{ST} \tau_{ST} + f_{V_0} \tau_{V_0} + f_{V_-} \tau_{V_-} \tag{2.63}$$

, where f represents the annihilation fraction in each state. It is also essential to note that the S and W characteristics from Doppler broadening spectroscopy can be expressed similarly as:

$$S = f_L S_L + f_{ST} S_{ST} + f_{V_0} S_{V_0} + f_{V_-} S_{V_-} \tag{2.64}$$

S_L (resp. W_L) represents the characteristics of the lattice, and the other three parameters S_D (resp. W_D) correspond to the saturation trapping in these three defects with respective annihilation fractions f_D: shallow traps (ST), neutral vacancy (V_0) and negatively charged vacancy (V_-). This could potentially enable us to combine Doppler broadening results and lifetime measurements as the annihilation fractions determined from the lifetime analysis can be used to interpret the Doppler broadening data.

2.6 Isotopic depth profiling using SIMS

2.6.1 Introduction

As mentioned in section 2.3.5, with regard to self-diffusion studies, following a sequence of treatments, samples are annealed at high temperature which induces a solid state isotopic exchange between the ^{235}U isotopes of the enriched surface oxide layer and the ^{238}U of the depleted substrate. The idea is then to derive physical quantities such as tracer diffusion coefficients from the resulting ^{235}U concentration profile and this is done using secondary ions mass spectroscopy (SIMS). SIMS provides in general relative isotopic concentrations which require some forms of normalisation to an ionic species characteristic of the matrix (Aucouturier et al., 1989). However, even if this normalisation is carried out, the derived isotopic concentrations are usually only relative. There is one exception to this which is when one is characterising an isotope of an element that constitutes the matrix, which is precisely the case at hand. So we can consider here that if the ^{235}U and ^{238}U signals are acquired simultaneously and that to a good approximation they are the only isotopes the samples contain, we can derive absolute ^{235}U concentrations.

Another isotope (^{238}U) of the same chemical element is thus used as an internal standard for normalising the signal relative to ^{235}U. Complications associated with differences in sputtering and ionisation yields between the matrix and the "impurity" species are therefore completely avoided (Garcia et al., 2010). Figure 2.25 provides a block diagram describing a SIMS analysis.

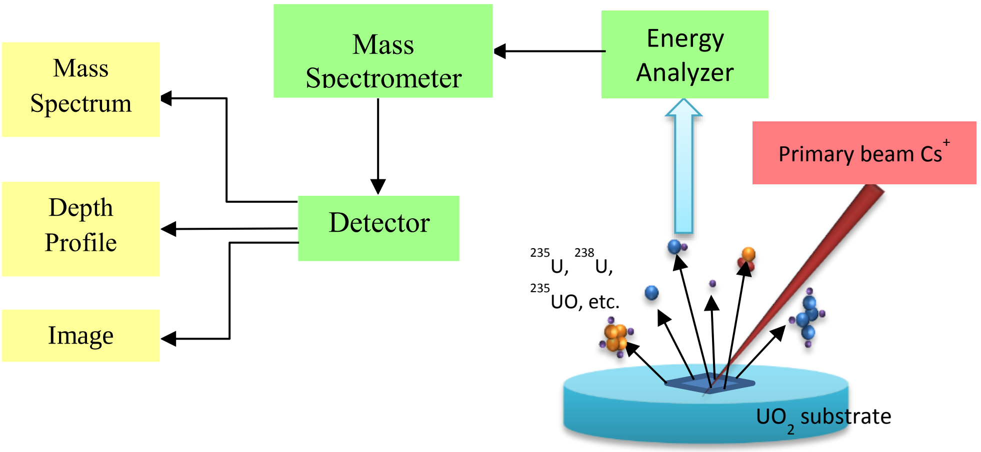

Figure 2.25: Block diagram of a SIMS operation on a UO_2 sample.

2.6.2 Analysis conditions

The ^{235}U concentration profiles were characterized using a shielded Cameca IMS 6f Secondary Ion Mass Spectrometer (SIMS) at CEA Cadarache. A 10 kV Cs$^+$ source and primary beam current of roughly 10 nA was used. The beam was rastered across the sample surface over an area of 150 µm by 150 µm. The differences in the primary beam current between the beginning and the end of the analysis were very small (less than 0.5 nA) and we checked that the total number of uranium counts was constant during the analysis (further justifying the hypothesis that ^{235}U and ^{238}U were by far the most abundant uranium isotopes present). The constant primary beam current is a guarantee of a quasi-constant sputtering rate. The measurements were performed with a negative (-5 kV) extraction field. Secondary ions $^{235}U^{16}O_2^-$ and $^{238}U^{16}O_2^-$ were collected in a region located in the centre of the crater roughly 30 µm in diameter in order to avoid crater edge effects (Magee et al., 1982).

These conditions were optimized and validated by studying two homogeneous samples, one of which was a depleted polycrystalline sample studied in this work (^{235}U enrichment c.a. 0.3%) and the other enriched at concentrations of approximately 4%. The concentration C of the ^{235}U tracer isotope can be determined by calculating the ratio of ion counts N at each analysis time:

$$C(^{235}U) = \frac{N(^{235}UO_2)}{N(^{235}UO_2) + N(^{238}UO_2)} \tag{2.65}$$

Results obtained on one of our reference samples are given in Figure 2.26. The average concentration and its associated standard deviation obtained from repeating the measurement a number of times was 4.3% ± 0.1%. We have then calculated the statistical error for each data point in Figure 2.26 assuming ^{235}U and ^{238}U counts are random variables which follow a normal distribution. This statistical error is estimated 0.1 % also and demonstrates that the error associated with concentration determinations is due to statistical fluctuations only.

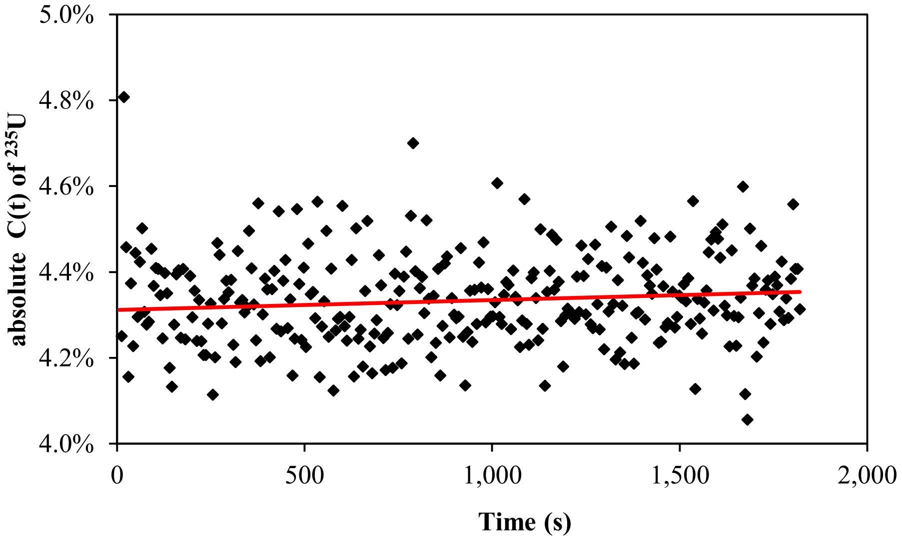

Figure 2.26: Concentration of ^{235}U in a reference enriched poly-crystalline UO_2 sample.

The SIMS setting (primary beam and secondary ion collection) for the remaining analyses were left unchanged. Data were collected as a function of the sputtering time $c(t)$. The next stage is to convert sputtering time dependent concentration profiles $c(t)$ into depth profiles by determining the rate at which the material is sputtered during the analysis.

2.6.3 Sputtering rate determination and depth profiling

Sputtering rates are estimated by dividing the crater depth by the total analysis time. Depths were characterised using a chromatic confocal microscopy technique developed by STIL SA (SPIP, 2011). The method relies on the chromatic aberrations of an optical system. A white light beam illuminates a point at the surface of the sample. This point constitutes a focal point for a single wavelength only because of optical aberrations. The wavelength is determined with the use of a light spectrometer and is directly related to the elevation of the point at the surface, i.e. the wavelength will be different for different illuminated points at different axial depths. Figure 2.27 shows the schematics of the system. The light beam approximately 3 µm in diameter is rastered over the region of interest (generally 500 µm by 500 µm) in 0.5 µm steps in both X and Y directions. The depth resolution has been estimated at roughly ±15 nm.

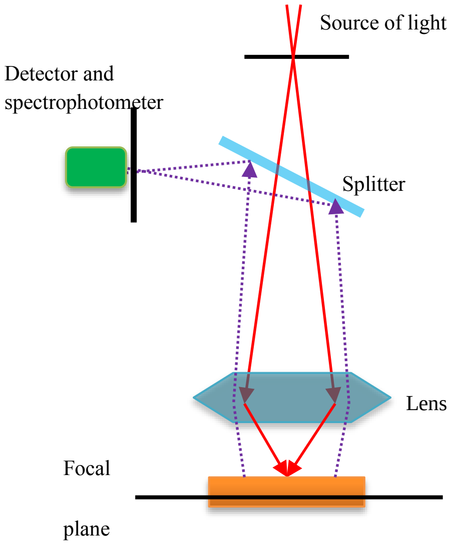

Figure 2.27: Schematic diagram of a chromatic confocal microscope.

Samples were then observed under the chromatic confocal microscope (see for example Figure 2.28) which provides a topological map of the crater and surrounding area. Because the secondary ions originate from a small area (roughly 30 µm across) at the centre of the crater, the depth data were collected from a slightly larger zone. Crater depths were measured, so one may convert the SIMS concentration profile (a function of sputtering time) to a depth profile (a function of crater depth). In Chapter 5, we describe the method used to determine the depth profile resolution, which eventually enables us to ascertain the error associated with the various physical quantities associated with a given experiment.

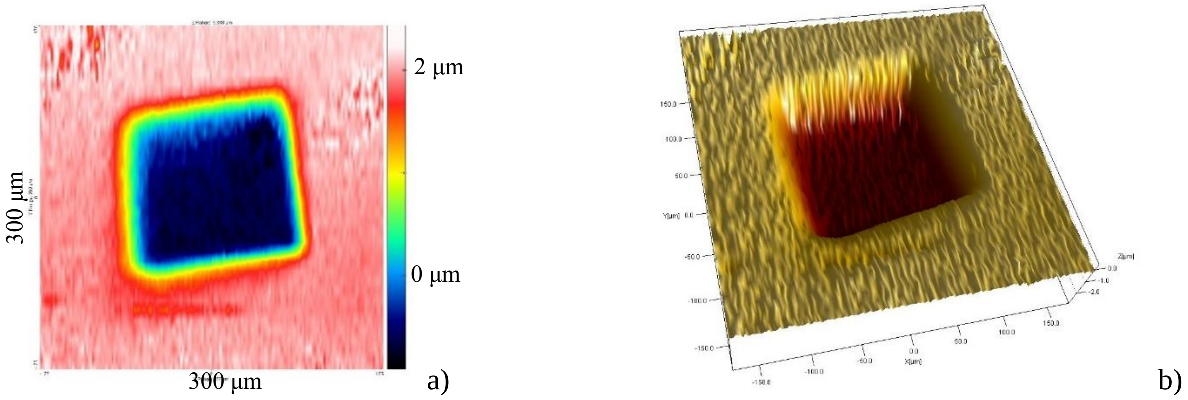

Figure 2.28: a) Colour coded image of one crater, b) 3-D illustrative of this crater on a single-crystal sample

2.7 Conclusions

This chapter provides a backdrop to the rest of the work carried out in this study. In particular, we describe:

1- The materials we have studied and their microstructure
2- The methods used for controlled oxidation experiments
3- The protocol adopted for depositing an enriched ^{235}U oxide layer for the self-diffusion experiments.

We are confident that the deviations-from-stoichiometry of the samples are relatively well estimated due to thermodynamic conditions being well controlled.

The main experimental techniques used in this thesis in terms of theory and applications are also described including 1- neutron diffraction for the study of structural disorder in UO_{2+x} and oxygen defects in particular (Chapter 3); 2- positron annihilation spectroscopy both in the Doppler broadening and lifetime spectroscopy configurations, the former being well suited to the characterisation of uranium vacancy defects (Chapter 4); and 3- secondary ions mass spectrometry which is essential to the tracer diffusion coefficient measurements (Chapter 5).

Chapter 3 Characteristics of oxygen defects in UO_{2+x} using neutron scattering and the PDF analysis

3.1 Introduction

The basic engineering properties of uranium oxide are essential to understand and predict the behaviour of fuels at all stages of the nuclear fuel cycle (fuel fabrication, in-reactor operation, reprocessing and storage). During oxidation experiments, extra mobile oxygen atoms are absorbed from the gas phase and incorporated into the UO_2 fluorite structure at interstitial sites (Willis, 1963a). $UO_{2\pm x}$ solid solution exists over a broad range of oxygen concentrations. As the amount of excess oxygen increases, oxygen ions have been reported to form clusters such as the so-called Willis di-interstitial (Willis, 1978). Enhanced understanding of these point defects can help to understand and ultimately to model thermodynamic or ionic transport properties. This knowledge may then be used to further understand more complex properties such as the high temperature deformation of the material (Dieckmann, 1984; Kofstad, 1995; Philibert, 1991). In this work, we focus on the single phase hyper-stoichiometric UO_{2+x} appearing at higher temperatures because of its practical significance with respect to technological applications.

X-ray diffraction (XRD) has been used to characterise the structure of the material and has been extensively applied to identify higher oxide phases. However XRD is essentially sensitive to heavy atoms (uranium) containing a high number of electrons and cannot provide structural information relative to the anion sub-lattice or only indirectly. Neutron diffraction techniques on the other hand have been successfully applied to probe both the anion and cation sub-lattices since scattering cross-sections of neutrons for O and U atoms have similar orders of magnitude (scattering cross-section for ^{16}O oxygen atom is 4.23 barns while that for ^{238}U uranium is 13.78 barns (Sears, 1992)).

The method we used for characterizing defects in this study is the Pair Distribution Function analysis (Egami and Billinge, 2012) which provides information about the local environment around uranium or oxygen ions. The Fourier transform of diffraction data provides the pair-distribution function g(r) which defines the probability of finding an atom at a distance r from another atom (Egami and Billinge, 2012).

Conventional methods of crystallographic structural analysis focus upon Bragg peaks which result from elastic scattering and contain information essentially relating to long-range order. Disordered, nano-structured or reduced-dimensional crystals often lack sufficient long-range order to produce those sharp diffraction peaks. In this case, the information relating to disorder or defects is contained within the diffuse scattering intensities which induce a reduction in elastic (Bragg) scattering intensities and an increase of the intensities between peaks. These diffuse intensities are usually subtracted away as ‘Background’ in a conventional Rietveld analysis. The PDF method however can pick them up after a Fourier transform, which makes it a possibly useful tool for studying point defects in crystalline materials (Egami and Billinge, 2012; Fischer, 2013).

To analyse the local environment of atoms in uranium dioxide, a high real-space resolution Δr is required. This can be obtained by collecting the data in reciprocal-space over a large Q range, i.e. high Q_{max}, since $\Delta r = 2\pi/Q_{max}$. The large Q ($=4\pi\sin\theta/\lambda$) range is achieved by gathering data at high diffraction angles and using a small neutron wavelength as is available on the D4c Diffractometer at Institut Laue Langevin in Grenoble. The PDF method has been extensively used for characterisation of liquids or other amorphous materials, as well as for some alloys and metals, but it has rarely been applied to uranium oxides. In the study of oxidation mechanisms from U_4O_9 to U_3O_8, Desgranges *et al.* (Desgranges et al., 2011) applied this method as a complement to the conventional Rietveld method to derive information relating to anion disorder.

This chapter is organized as follows: We report and interpret experiments involving PDF analyses of three polycrystalline UO_{2+x} samples with three different oxygen concentrations. Diffraction experiment results as a function of temperature are presented in section 3.2 for the three oxygen contents studied (2, 2.007, 2.16). The consistency between the Rietveld and the PDF methods is checked by analysing the UO_2 data in section 3.3. In addition, the local distortions on oxygen sites at high temperature are introduced. Then in section 3.4 we set up both fourfold cell and supercell models to reproduce the experimental PDF data using the PDFGui package (Farrow et al., 2007). Several types of oxygen defects are studied in an attempt to highlight which of these reproduce the experimental data most adequately. In section 3.5 we conclude our data interpretation in light of our understanding of how defects are expected to change as deviation-from-stoichiometry increases.

3.2 Reciprocal and real space scattering results

3.2.1 Phase transition temperature and material composition

One UO_2 and two UO_{2+x} (x~0.007 and x~0.16) samples were characterized by neutron diffraction. The diffraction spectra for the sample, empty container and furnace were collected and constitute the raw data. After instrument background subtraction and inelasticity corrections, data were used to generate the pair distribution functions G(r) in order to examine possible local disorder induced by excess oxygen.

We first examined the variations in Bragg-peak intensities of the diffraction patterns of our samples at various temperatures for a given composition. Figure 3.1 shows where the samples are located in relation to the binary U-O phase diagram. The O/U ratios estimated from the annealing conditions (pO_2 and T) are between 2.006 and 2.02 for the first sample, and between 2.14 and 2.16 for the second.

Figure 3.2.a and b show the diffraction patterns for $UO_{2.007}$ and $UO_{2.16}$ at various temperatures. The features observed in low-temperature diffraction patterns in the insets of both figures at 2θ values between 11.5 ° and 14 ° correspond to the Bragg peaks at Q ~2.74 $Å^{-1}$ of reported U_4O_9 diffraction data (Desgranges et al., 2011; Willis, 1978). It can be regarded as evidence of the presence of U_4O_9 in UO_{2+x} below the transition temperature. These features disappear at 300 ℃ for the low stoichiometry sample and at 700 ℃ for the high stoichiometry sample. Therefore, the non-stoichiometry determined from the phase transition temperature confirms our original estimate.

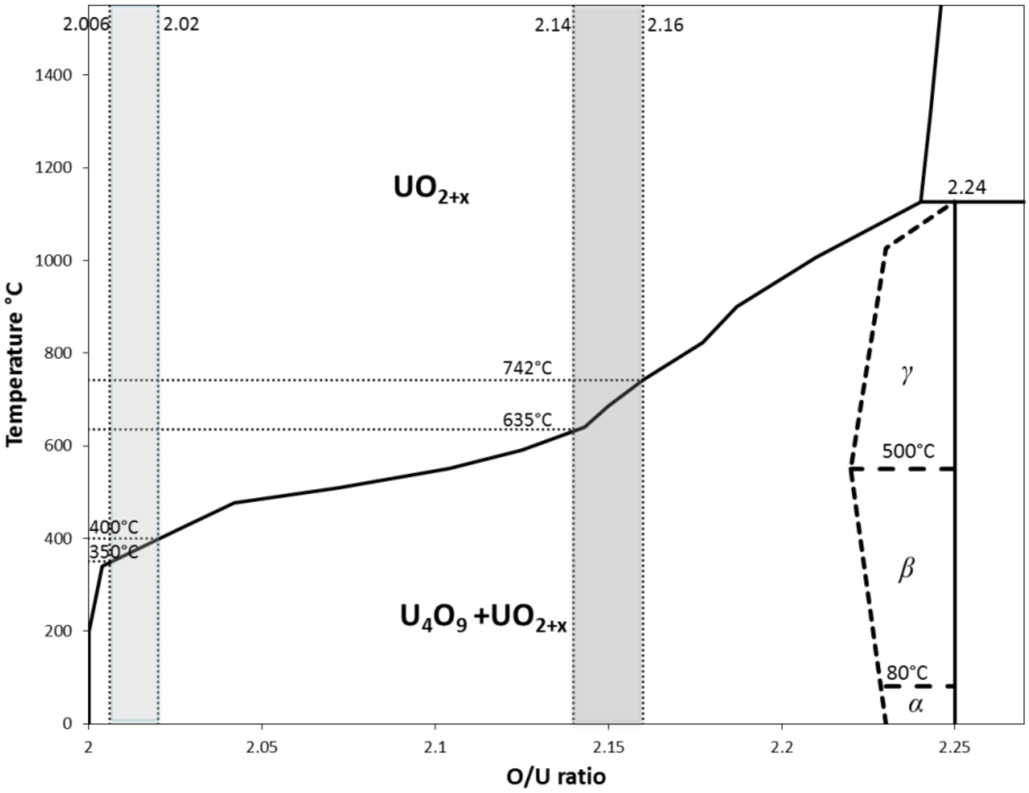

Figure 3.1: Stoichiometry of the two UO_{2+x} samples examined; two grey regions are relevant to the $UO_{2.007}$ and $UO_{2.16}$ sample respectively. The solid line delineates the phase transition temperature reported by Higgs's (Higgs et al., 2007) and Lewis's *et al.*(Lewis et al., 2004) critical analyses; the transition temperatures were taken from White and Nelson's work (White and Nelson, 2013).

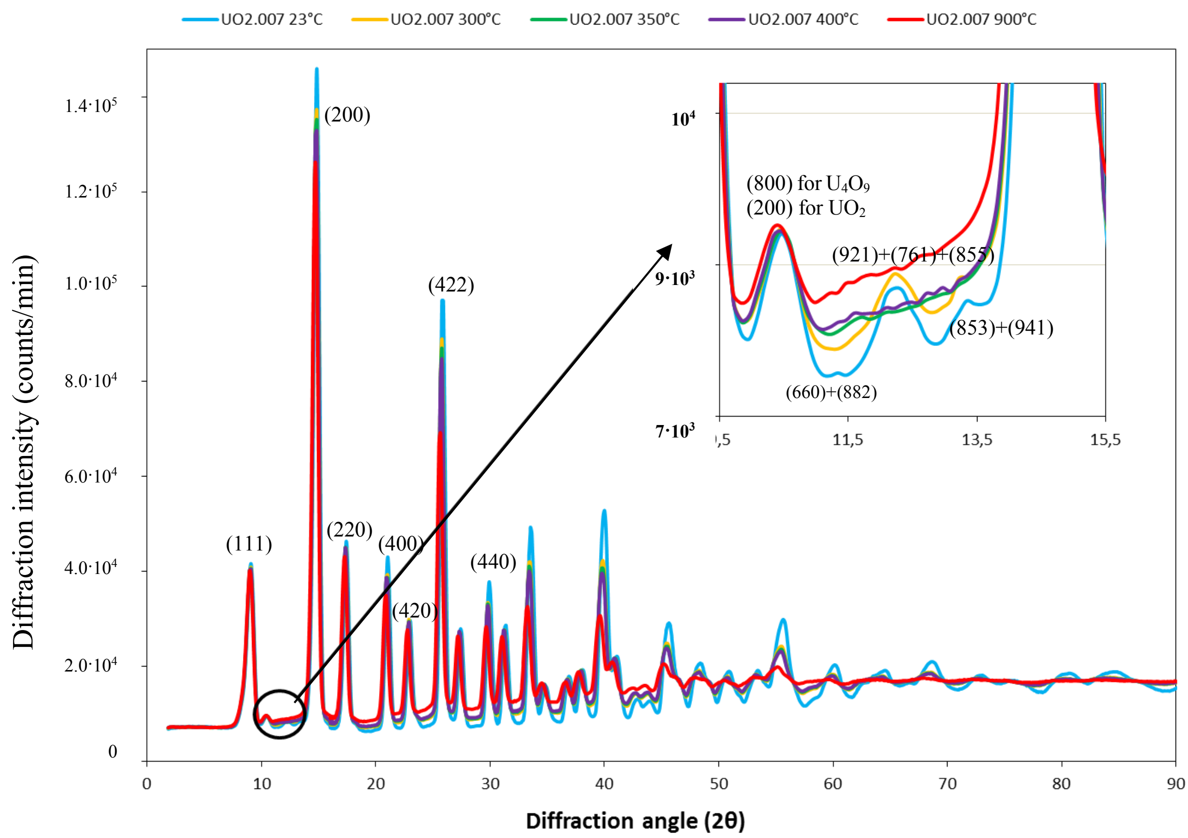

a) Powder diffraction spectra of $UO_{2.007}$ obtained at 23 ℃, 300 ℃, 350 ℃, 400 ℃, and 900 ℃; the inset shows the diffractogram at 2θ between 9.5° and 15.5°.

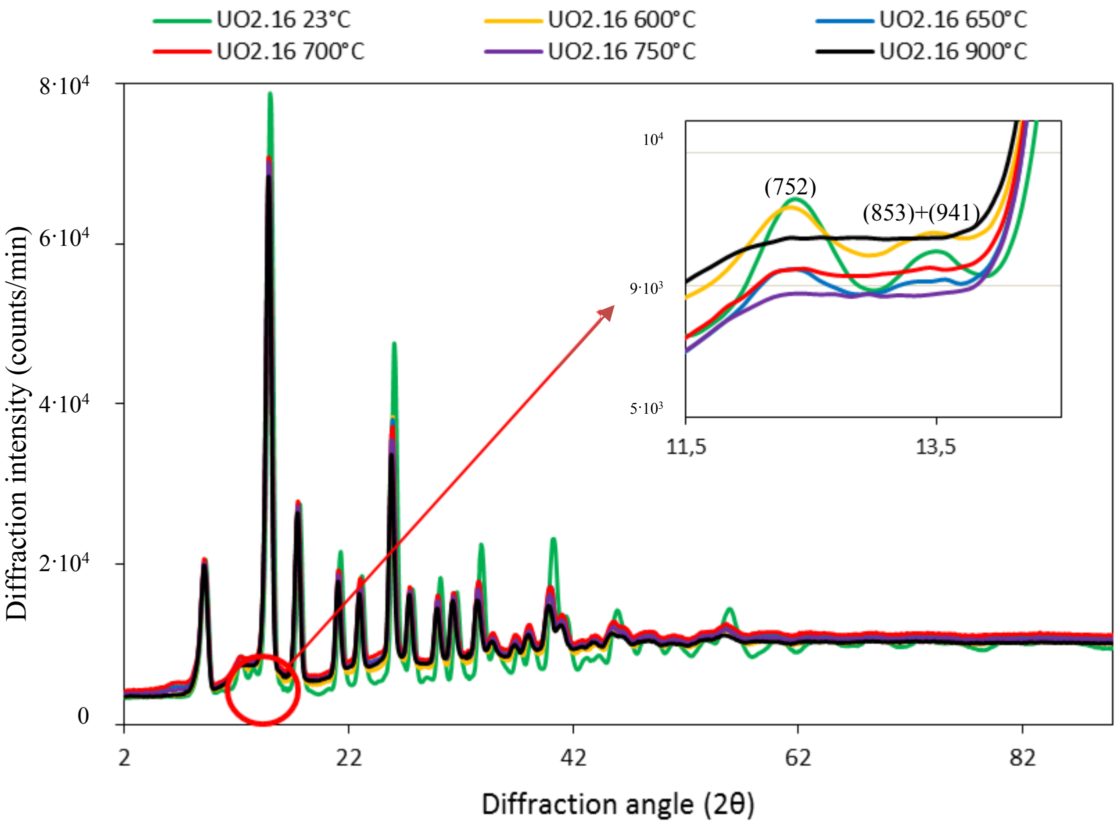

b) Diffraction spectra of $UO_{2.16}$ obtained at 23 °C, 600 °C, 650 °C, 700 °C, 750 °C, and 900 °C; the inset shows the diffractogram between 11.5 ° and 14 °.

Figure 3.2: Bragg intensities of $UO_{2.007}$ and $UO_{2.16}$ obtained by neutron diffraction.

3.2.2 Effect of temperature on diffraction patterns

Figure 3.2 also shows that the Bragg-peak intensities reduce as the temperature increases. This is because the time-averaged distribution of atoms broadens as a result of the increasing amplitude of atomic vibrations (Fischer, 2016). The lost integrated intensity is transferred to the thermal diffuse scattering spread at the base of the Bragg peaks (Fischer, 2013). The peak positions naturally shift to lower diffraction angles θ due to the thermal expansion of the lattice.

In addition to analyses of diffraction data in reciprocal space, we examined the pair-distribution-function data (PDF) obtained from the Fourier transform of *S(Q)*. Figure 3.3 presents an example of the PDF data for $UO_{2.16}$ at four temperatures over a range of interatomic distances between 0 and 12 Å. The expression for G(r) given in section 2.4.1.4 shows that as g(r) tends to 0 for small values of r, the slope of G(r) should tend to $-4\pi\rho_0$. As it is seen from Figure 3.3, the slope of the solid line indeed corresponds to a density of 0.078 atoms/Å^3, which is an indication that the PDF were accurately determined. At low values of R, below the shortest U-O distance, a small asymmetric peak appears that the R-space manifestation of the Q space magnetic form factor of uranium (Frandsen et al., 2014; Frandsen and Billinge, 2015).

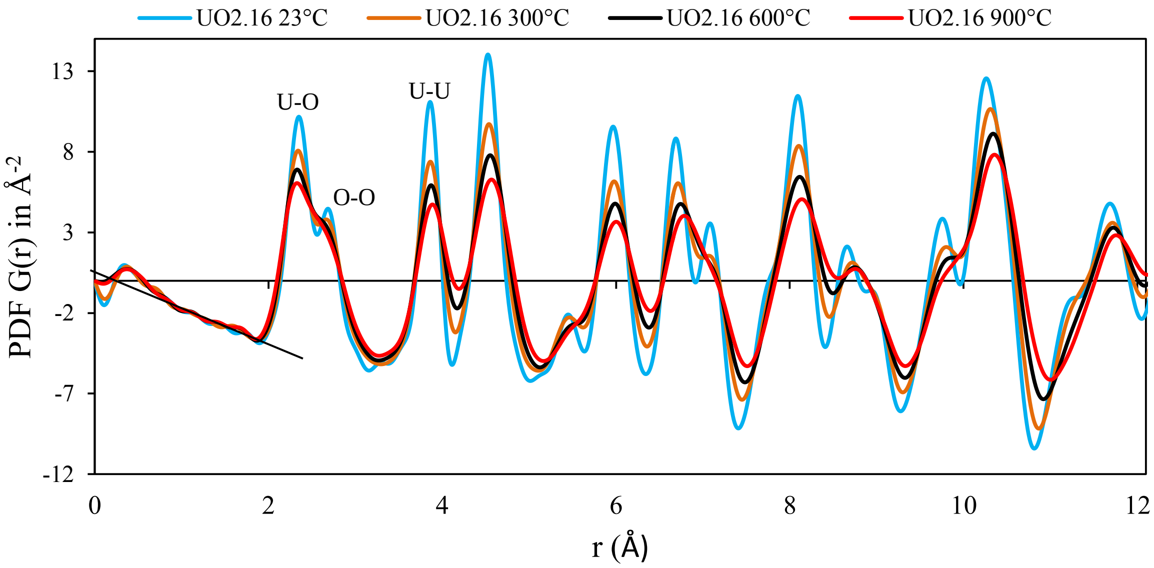

Figure 3.3: PDF data of $UO_{2.16}$ obtained at 23 ℃, 300 ℃, 600 ℃, 900 ℃ up to 12Å.

As the temperature rises, peaks appear to broaden and their amplitude to decrease. **Except for the first and shortest U-O and O-O bonds**, all bond-lengths increase. Skinner *et al.* (Skinner et al., 2014) first reported decreasing U-O bond lengths with increasing temperatures for X-ray PDF experiments. Thus we retrieved the values of the shortest U-O and U-U bonds of UO_2 at various temperatures from the radial distribution function (RDF) data (see Chapter 2, section 2.4.1.4). The U-O bond lengths derived from our RDF data (below 800K) follow the same trend as Skinner's at low temperature. The discrepancy at high temperature between our data and that of Skinners will be discussed in section 3.3.1. The increase with temperature of U-O bond lengths derived from our PDF data cannot be observed from the conventional analyses of Bragg peaks.

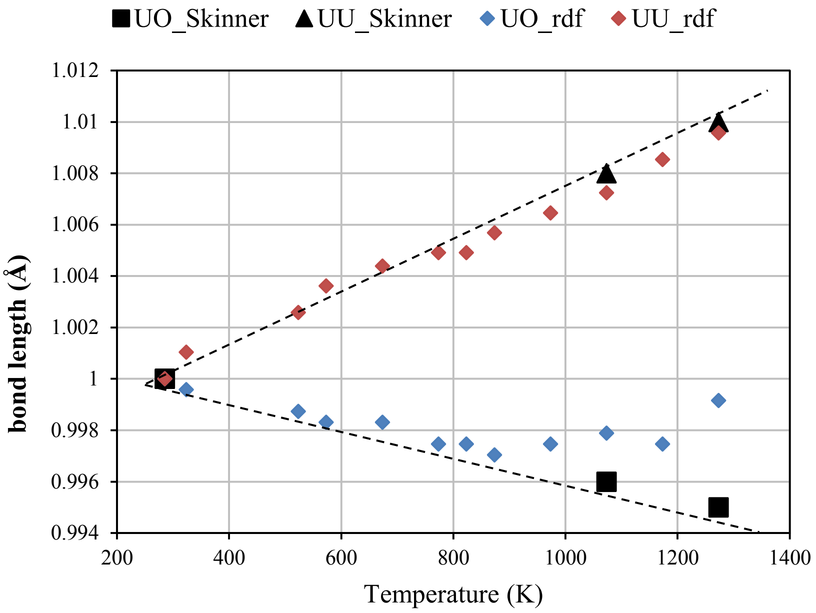

Figure 3.4: Nearest U-O (in blue) and U-U (in red) neighbours determined for UO_2 from the RDF data in comparison to Skinner et al. work (in black) (Skinner et al., 2014).

3.2.3 Effect of oxidation level on powder diffraction patterns and PDFs

The diffraction patterns of three samples are compared at different temperatures in Figure 3.5. The Bragg peaks shift to higher diffraction angles as the material oxidises which shows the expected contraction of the lattice parameter. **This is consistent with the fact that the oxidation state of uranium ions, which determines the structural properties of the material, increases, leading to increased atomic densities**. The Bragg peak intensities turn out to be a decreasing function of oxidation level. This is a sign of increasing disorder.

The evolution of PDFs with oxidation levels at different temperatures is shown in Figure 3.6. At a given temperature, the peak amplitude decreases as more oxygen ions are absorbed in the fluorite structure. All peak positions, hence the atomic bond-lengths, shift to the left as the O/U ratio increases, indicating that the unit-cell volume reduces as the oxygen content increases.

At a given temperature, the width of each peak increases as deviation-from-stoichiometry increases from 2 to 2.16 to the extent that two adjacent low amplitude peaks tend to overlap to form a shoulder. This is an indication of increasing static and dynamic disorder in the original fluorite structure.

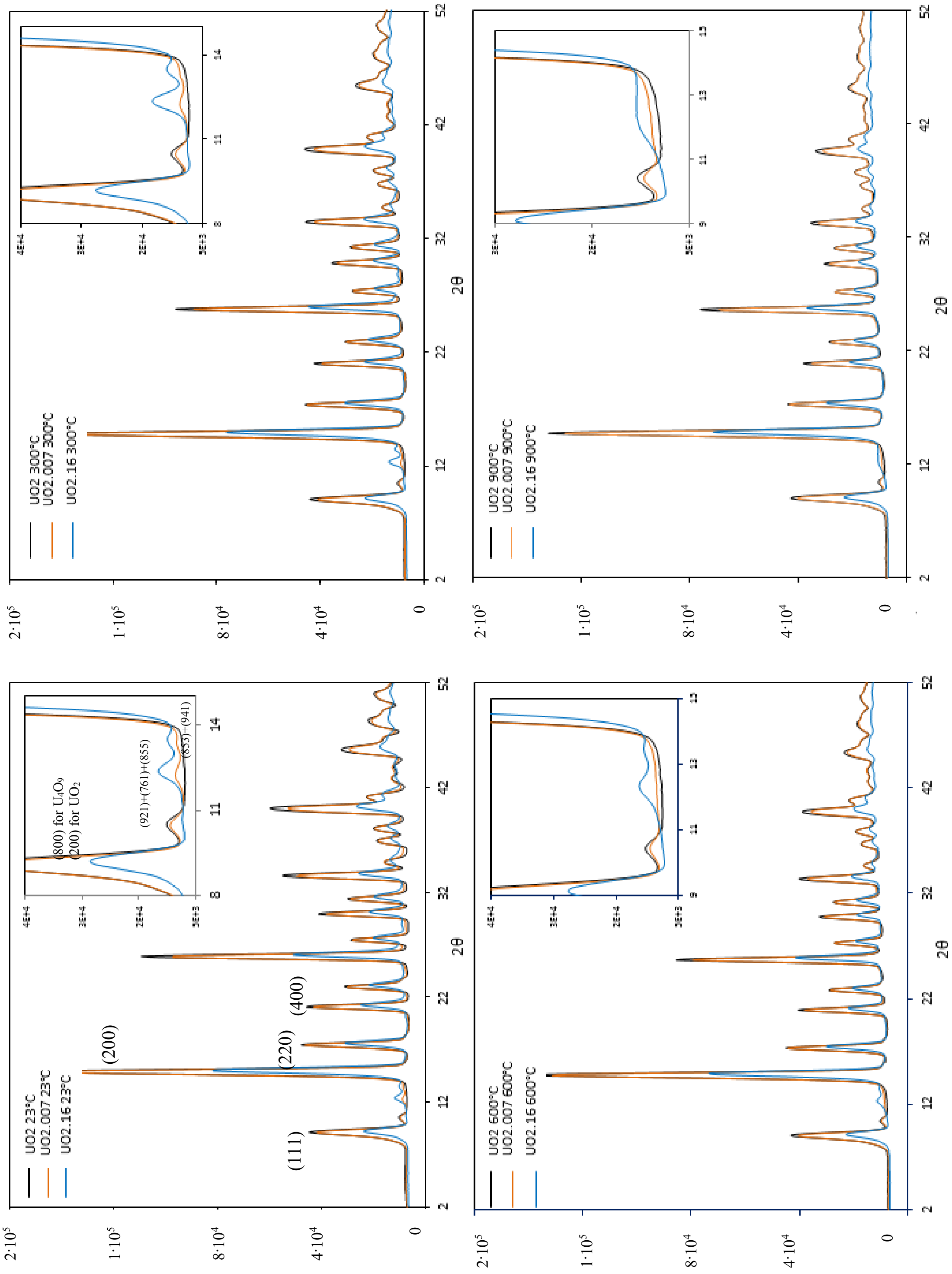

Figure 3.5: Comparison of powder diffraction patterns for UO_2, $UO_{2.007}$ and $UO_{2.16}$ at temperatures of 23 ℃, 300 ℃, 600 ℃ and 900 ℃; the insets weak reflections related to the present of U_4O_9 in UO_{2+x} below the phase-transition temperature. The (hkl) planes are the same as in Figure 3.2.a.

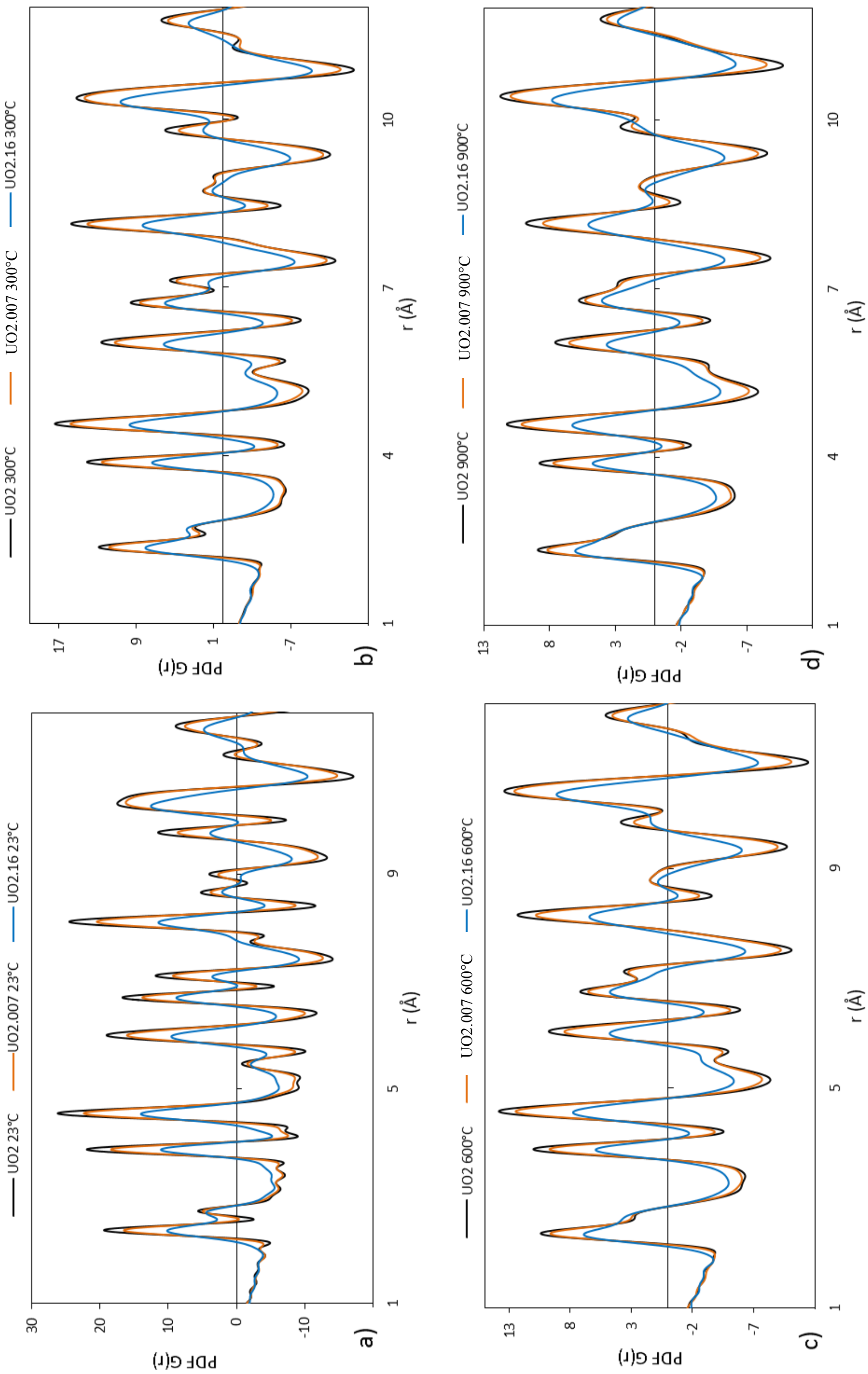
a)
UO2 23°C
UO2.007 23°C
UO2.16 23°C
PDF G(r)
30
20
10
0
-10
1
5
9
r (Å)
b)
UO2 300°C
UO2.007 300°C
UO2.16 300°C
PDF G(r)
17
9
1
-7
1
4
7
10
r (Å)
c)
UO2 600°C
UO2.007 600°C
UO2.16 600°C
PDF G(r)
13
8
3
-2
-7
1
5
9
r (Å)
d)
UO2 900°C
UO2.007 900°C
UO2.16 900°C
PDF G(r)
13
8
3
-2
-7
1
4
7
10
r (Å)

Figure 3.6: PDFs of UO_2, $UO_{2.007}$ and $UO_{2.16}$ at 23 ℃, 300 ℃, 600 ℃ and 900 ℃ up to 12Å.

The following summary may be obtained from neutron diffraction and PDF data:

- In the analyses of Bragg peaks at different temperatures, the phase transition temperatures – from bi-phasic (U_4O_9 + UO_{2+x}) to single-phase (UO_{2+x}) – can be estimated and confirms the expected compositions of the materials (*i.e.* 2.007 and 2.16). This gives credit to the sample preparation conditions.
- The change of Bragg peaks upon temperature for a given composition is consistent with the expected thermal expansion. However, the change with temperature of the shortest U-O and O-O bond-lengths derived from the PDF data contradicts to the expected trend predicted by a hard sphere model which assumes a fourfold-cell fluorite structure. This will be clarified in the following sections.
- The decrease in Bragg peak intensities induced by the increasing oxygen content indicates the disorder in the structure, which is correlated to the presence of oxygen defects in the material, is increasing. In the next section the defect structure will be quantified through modelling.

3.3 Local disorder in the fluorite structure characterised by neutron diffraction

3.3.1 Rietveld and PDF analyses of UO_2

Before studying the hyper-stoichiometric material, we first looked at the diffraction S(2θ) and PDF G(r) data for stoichiometric UO_2. The PDF data is fitted using the smallest fourfold model (or the average cell, U_4O_8) with a $Fm\bar{3}m$ symmetry (see Table 3.1). The experimentally determined accessible limit for Q_{max} is 23.5 Å. Parameters for peak shape corrections (see Chapter 2 section 2.4.3), Q_{damp}, and Q_{broad} in this work for UO_2 analysis are 0.055, and 0.04 respectively determined from the fitting of a Nickel sample test.

Table 3.1: Positions of uranium and oxygen in an average-cell model belonging to the $Fm\bar{3}m$ symmetry

	U	U	U	U
(x,y,z)	(0, 0, 0)	(0, ½, ½)	(½,½, 0)	(½, 0, ½)
	O	O	O	O
(x,y,z)	$\left(\frac{1}{4},\frac{1}{4},\frac{1}{4}\right)$	$\left(\frac{1}{4},\frac{3}{4},\frac{1}{4}\right)$	$\left(\frac{3}{4},\frac{3}{4},\frac{1}{4}\right)$	$\left(\frac{3}{4},\frac{1}{4},\frac{1}{4}\right)$
	O	O	O	O
(x,y,z)	$\left(\frac{1}{4},\frac{3}{4},\frac{3}{4}\right)$	$\left(\frac{3}{4},\frac{1}{4},\frac{3}{4}\right)$	$\left(\frac{1}{4},\frac{1}{4},\frac{3}{4}\right)$	$\left(\frac{3}{4},\frac{3}{4},\frac{3}{4}\right)$

As Figure 3.7 illustrates, both the PDF data and the Bragg peaks are refined. The lattice parameters for UO_2 at various temperatures ($0 \leq T \leq 1273K$) obtained by the Rietveld and PDF analyses are shown in Figure 3.8 with Ruello *et al.* high-resolution X-ray diffraction study (Ruello et al., 2005).

Several comments can be made. Firstly, on the whole, the lattice parameters obtained are consistent with the data from the literature. The uncertainty associated with the obtained cell parameter is estimated to be ±0.001 Å. Secondly, data were obtained upon both heating and cooling. Apart from the two data points at 623 K and 673 K, the lattice parameter values are identical suggesting there is no change in the microstructure of the sample as a result of annealing. Note that, the temperature quoted in Figure 3.8.a is the average value provided by two thermocouples placed above and below the samples as shown in Figure 2.16.a. It is possible that the actual temperature of the sample may differ by about 50 K.

The thermal expansion coefficients (TEC) are also calculated and shown in Figure 3.8.b. The results agree with Martin's recommendations drawn from many different UO_2 studies (Martin, 1988). The errors made in estimating the TEC are indicated by Martin's upper and lower bound recommendations. The blue points shown in the graph indicate that our results are consistent with a 50 K underestimation of the actinide sample temperature.

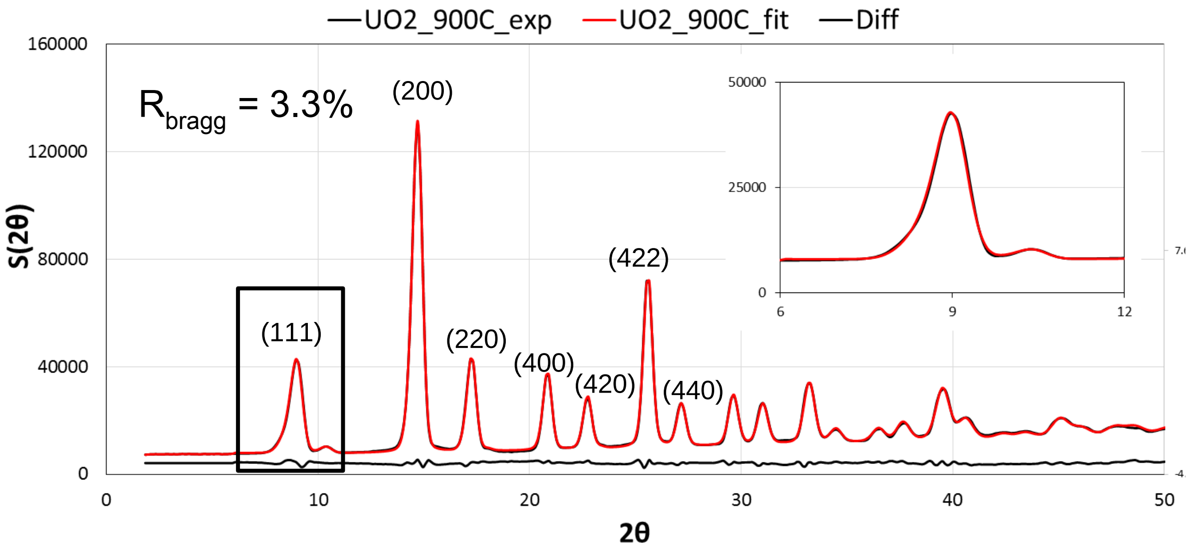

a) Experimental (blue) and modelled (red) $S(2\theta)$ of UO_2 at 900 ℃. Model calculations are obtained from a Rietveld refinement; the line at the bottom is the difference between the two patterns; the inset is an illustrative of how the (111) peak is refined.

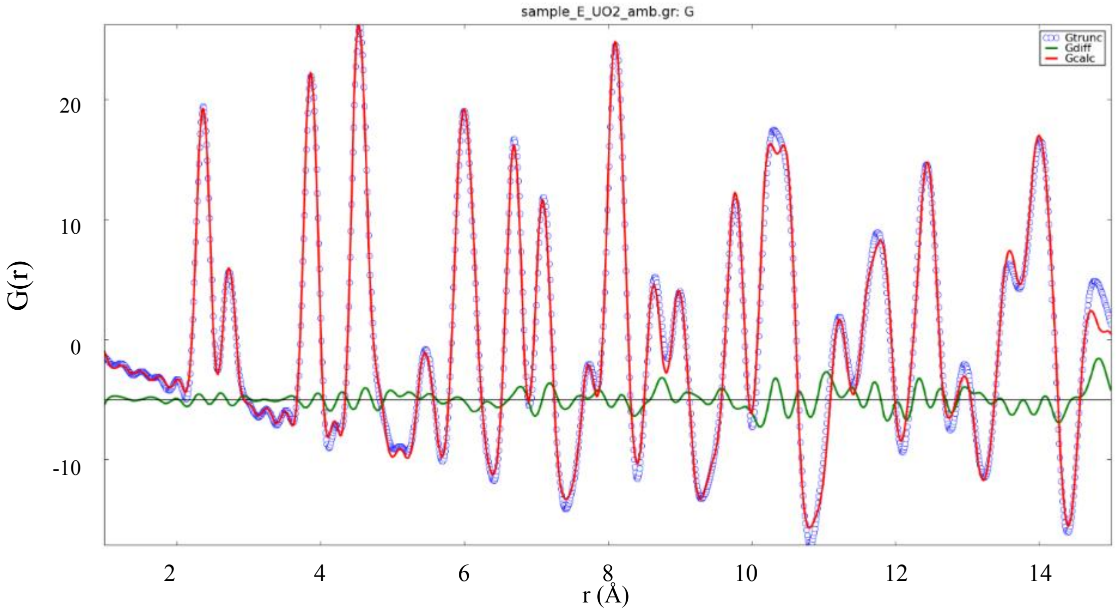

b -1 PDF G(r) at room temperature

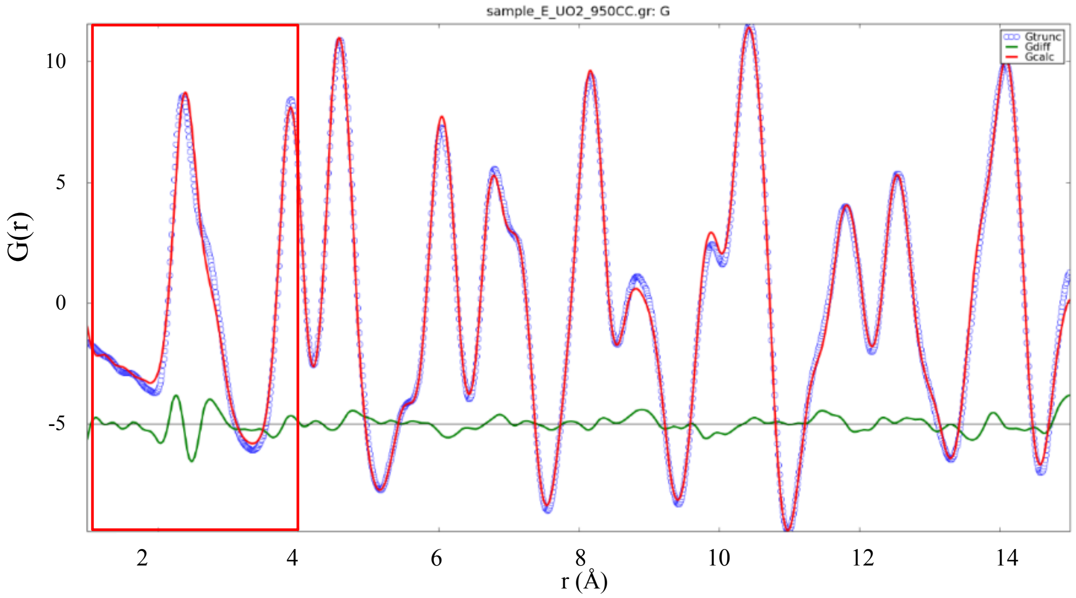

b-2 G(r) at 950 ℃

b) Experimental (in blue) and calculated (in red) G(r) of UO_2 at 23 ℃ (above) and at 950 ℃ (below) by PDF modelling; the green line is the linear difference between the two functions.

Figure 3.7: Refined *S(2θ)* and G(r) by Rietveld and PDF models.

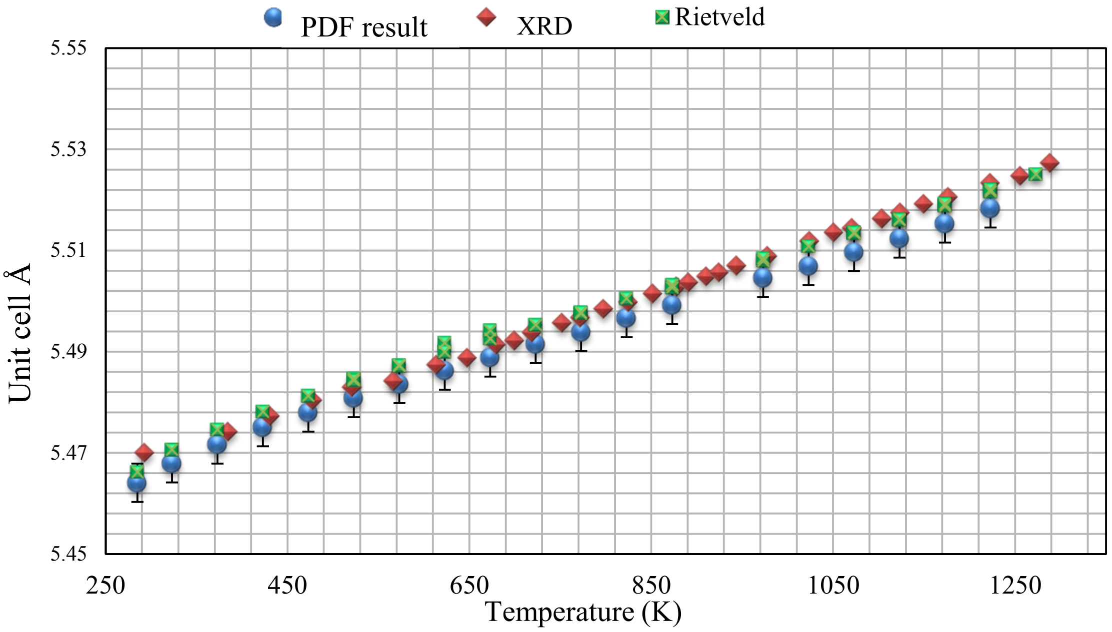

a) Lattice parameter as a function of temperature determined by PDF and Rietveld modelling in comparison to XRD results taken from (Ruello, 2001).

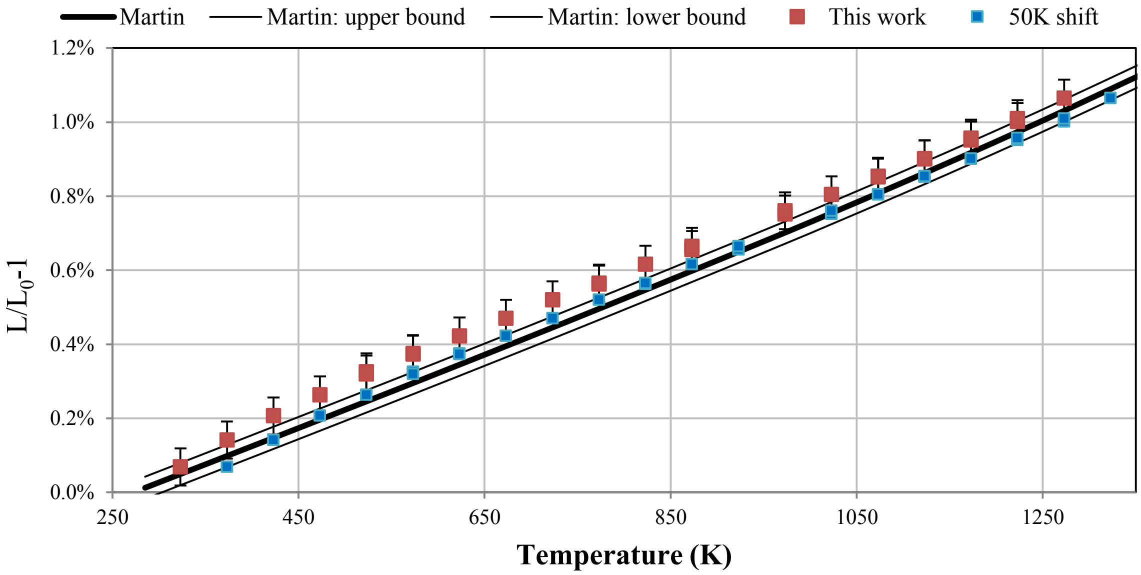

b) Thermal expansion coefficients of UO_2 calculated from structure parameters obtained from the PDF (red squares) analyses between 20 ℃ and 1000 ℃, data corresponding to a 50 K-temperature shift (blue squares) and comparison to Martin's recommendations (in black lines).

Figure 3.8: Lattice parameters and thermal expansion coefficients determined from refinement of PDF and diffraction data in comparison to the literature.

In general, the consistency in between the PDF and Rietveld results confirms the quality of the data collection and pre-treatments (i.e. background subtraction and inelastic corrections). More importantly, both analyses suggested that the spacially averaged structure refined for UO_2 is $Fm\bar{3}m$.

3.3.2 Oxygen anharmonic behaviour and the local disorder in the fluorite structure

As highlighted in Figure 3.7.b, the first U-O and O-O peaks cannot be correctly reproduced by the model assuming a defect-free fluorite structure. The temperature factors (Debye-Waller factors) for uranium and oxygen atoms have been calculated (see Chapter 2 section 2.4.1.2) and are reported in Figure 3.9. To calculate the Debye-Waller factors for oxygen ions, it is necessary to take into consideration the anharmonic behaviour of oxygen ions at high temperature (Rouse et al., 1968).

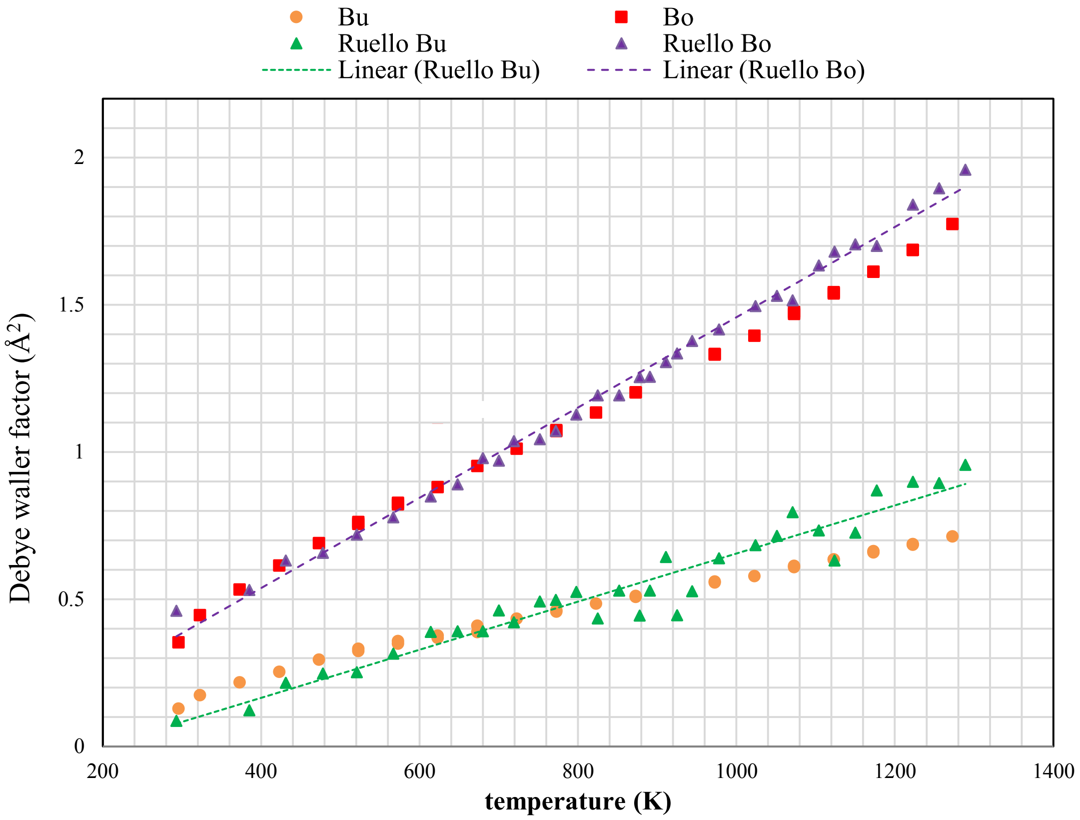

Figure 3.9: Debye Waller factors for uranium (orange circles) and oxygen (red squares) based on S(Q) data analysis in comparison to previous neutron diffraction results (Ruello et al., 2005).

Willis (Willis, 1963b, 1963a) was the first to recognise the necessity to take into account anharmonicity at high temperature, or equivalently allow oxygen ions to relax in <111> directions, to simulate Bragg peak intensities satisfactorily. Others followed his work (Hutchings, 1987; Rouse et al., 1968; Ruello et al., 2005) also reported distortions corresponding to oxygen ions being displaced from the $(\frac{1}{4},\frac{1}{4},\frac{1}{4})$ to the $(\frac{1}{4}+\delta,\frac{1}{4}+\delta,\frac{1}{4}+\delta)$ coordinate position, thus moving away from the normal fluorite sites to the nearest empty octahedral sites.

This type of distortion may be related to the symmetry of the $Pa\bar{3}$ space group. The $Pa\bar{3}$ space group is a sub-space group of the $Fm\bar{3}m$ space group, in which some symmetries belonging to $Fm\bar{3}m$ are lost (Desgranges et al., 2017). Other metal dioxides (SnO_2, GeO_2, and SiO_2) are also reported to adopt $Pa\bar{3}$ and $Fm\bar{3}m$ crystalline structures depending on the pressure (Gracia et al., 2007).

In our PDF analyses, to account for the high-temperature anharmonicity of oxygen, we enabled each oxygen ions in a U_4O_8 fourfold-cell to move along the <111> direction by using the point operators of $Pa\bar{3}$ space group. The symmetry operations relative to the D3d point group where applied to one of the oxygen atoms, the coordinates of which are $(\frac{1}{4}+\delta,\frac{1}{4}+\delta,\frac{1}{4}+\delta)$. This provides a set of new coordinates for oxygen ions which are a function of displacement δ and are given in Table 3.2. All uranium ions remain in their original position. Since the oxygen position is a special position and the displacement vectors (δ, δ, δ) belongs to a special direction (one of the $\bar{3}$ axes), applying the 24 relevant symmetries leads to only 8 different positions. It can be noticed that the sum of all eight displacement vectors over oxygen atoms in such a cell is zero thus maintaining an $Fm\bar{3}m$ average symmetry.

The high-temperature PDF data was modelled with this new fourfold-cell model. All modelling parameters remained unchanged compared with the PDF analyses of stoichiometric UO_2. As Figure 3.10 illustrates, the PDF data in the range of 1 Å to 3.5 Å (*i.e.* the peaks related to the first U-O and O-O bonds) are far better reproduced when applying the distortion. The refined displacement factor δ is 0.0142 ±0.0002 for a refinement up to 12 Å. This latter is very close to that suggested by Willis (*i.e.* 0.016 ±0.001) (Willis, 1963a) from neutron diffraction data.

Table 3.2: Atomic position of oxygen ions with/without anharmonic displacement δ.

O in Fm$\bar{3}$m	$\left(\frac{1}{4},\frac{1}{4},\frac{1}{4}\right)$	$\left(\frac{1}{4},\frac{3}{4},\frac{1}{4}\right)$	$\left(\frac{3}{4},\frac{3}{4},\frac{1}{4}\right)$	$\left(\frac{3}{4},\frac{1}{4},\frac{1}{4}\right)$
Position with δ	$\left(\frac{1}{4}+\delta,\frac{1}{4}+\delta,\frac{1}{4}+\delta\right)$	$\left(\frac{1}{4}-\delta,\frac{3}{4}+\delta,\frac{1}{4}+\delta\right)$	$\left(\frac{3}{4}-\delta,\frac{3}{4}+\delta,\frac{1}{4}-\delta\right)$	$\left(\frac{3}{4}+\delta,\frac{1}{4}+\delta,\frac{1}{4}-\delta\right)$
Displacement direction	+++	-++	-+-	++-

O in Fm$\bar{3}$m	$\left(\frac{1}{4},\frac{3}{4},\frac{3}{4}\right)$	$\left(\frac{3}{4},\frac{1}{4},\frac{3}{4}\right)$	$\left(\frac{1}{4},\frac{1}{4},\frac{3}{4}\right)$	$\left(\frac{3}{4},\frac{3}{4},\frac{3}{4}\right)$
Position with δ	$\left(\frac{1}{4}-\delta,\frac{3}{4}-\delta,\frac{3}{4}+\delta\right)$	$\left(\frac{3}{4}+\delta,\frac{1}{4}-\delta,\frac{3}{4}-\delta\right)$	$\left(\frac{1}{4}+\delta,\frac{1}{4}-\delta,\frac{3}{4}+\delta\right)$	$\left(\frac{1}{4}-\delta,\frac{1}{4}-\delta,\frac{1}{4}-\delta\right)$
Displacement direction	--+	+--	+-+	---

Figure 3.10 shows the comparison between our experimental data and the fourfold cell model refined up to 12 Å (but only plot up to 8 Å). The displaced oxygen positions account for the local disorder induced by oxygen anharmonic motion at high-temperature. Such kind of disorder can be captured by the neutron diffraction with a high real-space resolution at a time scale in a range from 10^{-15} to 10^{-13} s, and be revealed by the PDF analyses. The displacement of oxygen ions that occurs in UO_2 is expected to exist in the hyper-stoichiometric material too, but the extent of the distortion may change with the deviation-from-stoichiometry.

To simulate disorder such as the presence of oxygen interstitials (clusters) in UO_{2+x}, it is necessary to expand the model to a supercell. Therefore, the coordinates given in Table 3.2 for one oxygen cube are expanded by applying the 24 symmetry operators of the $Pa\bar{3}$ space group. Multiple-scale supercell models were built for UO_2 with distorted sites. In the supercell refinements, the value of δ shown in Table 3.3, is a decreasing function of the supercell size (it tends to zero in long-range order), and the refinement agreement factor is the same as for the $Fm\bar{3}m$ structure. **This indicates that the average structure of UO_2 still belongs to the $Fm\bar{3}m$ space group.**

For UO_2, the refinement is highly reliable for short-range order assuming $Pa\bar{3}$ symmetry, and is defective for longer range order, which is consistent with the average structure determined by Rietveld analyses. In the following sections, the PDF data of UO_{2+x} is modelled either over a range of 6 Å or 12 Å in an attempt to investigate the atomic arrangements of defects.

In conclusion, we have seen in the section that the distortion inferred from diffraction studies by Willis can be demonstrated directly from the experimental data using the PDF method.

Table 3.3: The displacement δ of ordinary lattice oxygen ions refined in supercell models.

cell size	1*1*1	1*1*1	1*1*1	1*1*1	2*2*2	2*2*2	2*2*2	2*2*2	3*3*3	3*3*3	3*3*3	3*3*3	4*4*4	4*4*4	4*4*4	4*4*4
	u4o8	u4o8	u4o8	u4o8	u32o64	u32o64	u32o64	u32o64	u108o216	u108o216	u108o216	u108o216	u256o518	u256o518	u256o518	u256o518
symmetry	Fm-3m	Pa-3	Fm-3m	Pa-3	Fm-3m	Pa-3	Fm-3m	Pa-3	Fm-3m	Pa-3	Fm-3m	Pa-3	Fm-3m	Pa-3	Fm-3m	Pa-3
refinement range	12	12	6	6	12	12	6	6	12	12	6	6	12	12	6	6
n_e	82	82	37	37	82	82	37	37	82	82	37	37	82	82	37	37
A (Rwp, GOF)	7.1%	6.6%	6.7%	4.4%	7.1%	8.1%	6.7%	6.80%	7.07%	7.27%	6.72%	6.82%	7.09%	7.09%	6.79%	6.80%
n_p	8	9	8	9	8	9	8	9	8	9	8	9	8	9	8	9
RGOF	7.4%	7.0%	7.6%	5.0%	7.4%	8.6%	7.6%	7.82%	7.44%	7.71%	7.59%	7.84%	7.46%	7.51%	7.67%	7.82%
δ	0	0.0124	0	0.0162	0	0.0014	0	0.0000	0	0.0007	0	0.0003	0	0.0003	0	0.0003

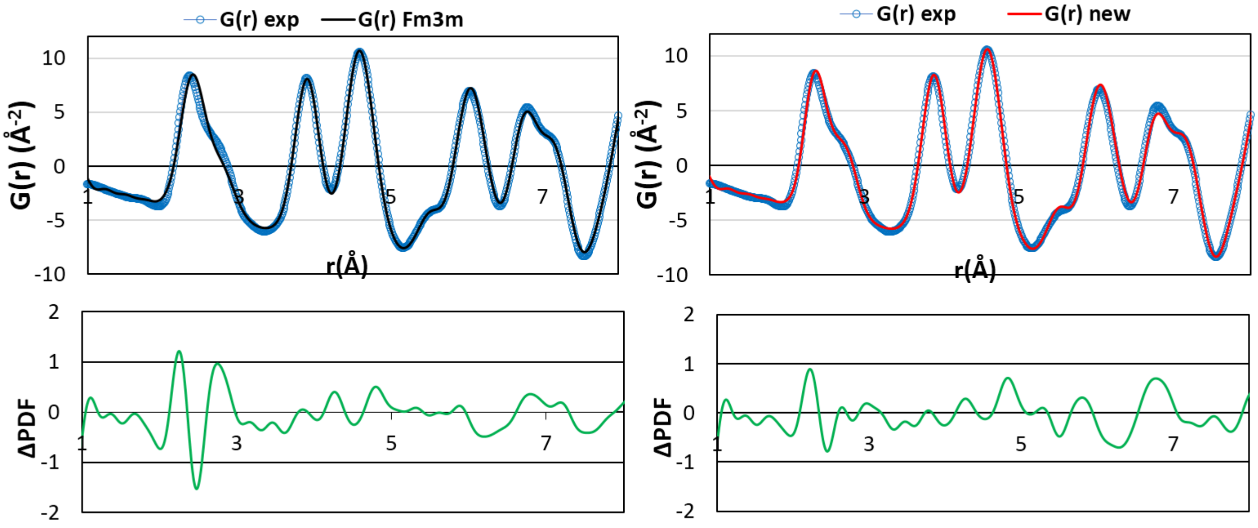

Figure 3.10: Experimental PDF (blue circles) of UO_2 at 900 ℃ refined assuming a $Fm\bar{3}m$ structure (black line) and oxygen anharmonic behaviour (red line) up to 8 Å; the difference between experimental data and refined results is illustrated in green.

3.4 PDF modelling of UO_{2+x}

3.4.1 Introduction

In hyper-stoichiometric material, non-stoichiometry is accommodated essentially by the anion sublattice so that disorder is due to the presence of oxygen interstitial defects. Disorder is manifest in the diffuse intensity. As mentioned previously, analysing the PDF data is a way of extracting the information relative to oxygen defects. PDF in relation to UO_{2+x} has not been characterized to our knowledge.

A general theoretical framework is not available for treating the PDF data relative to a bi-phasic material. In addition to this, our main interest lies in the nature of oxygen defects in the single-phase region which has the most technological significance. Hence we focus in this part, on the high temperature range (900 ℃).

This section is organised in three parts. In section 3.4.2, we look at the fourfold-cell modelling, which provides information as to the types of interstitials (e.g. direction of displacements) and clusters thereof we are dealing with, and their average compositions. In section 3.4.3 we build on this to derive a defect model using a supercell that helps us determine the local environment of defects.

3.4.2 The average cell modelling

3.4.2.1 Low deviation-from-stoichiometry material ($UO_{2.007}$)

Table 3.4 describes the hypotheses relative to model 1 and corresponding refinement results. The model defined in section 3.3.1 (Figure 3.7.b) will now be referred to as Model 1. Uranium ions form the face-centred cubic sub-lattice (fcc) while oxygen ions occupy the tetrahedral sites. Uranium and lattice oxygen ions are allowed to vibrate isotropically in model 1. The positions of two interstitial oxygen ions, characterised by parameters v and w, are refined as are the occupation numbers for lattice oxygen, O' and O'' ions. The occupation number for uranium ions is fixed at 1 in line with previous such models for hyper-stoichiometric UO_2. The refinement is restrained in order to ensure the overall composition is close to the stoichiometry expected in term of the sample preparation conditions. Parameters alluded to in Chapter 2 section 2.4.3 which describe PDF peak broadening are also refined. The number of parameters refined in a model are given in the corresponding column of Table 3.4.

Whereas in model 1, oxygen atoms vibrate isotropically, oxygen ions in model 2 given in Table 3.4 are allowed to move slightly along the <111> directions. The displacement of the lattice oxygen ions from their original sites are refined. Therefore, the total number of the refined parameters n_p increases by 1 in this case. Both models are refined up to 6 Å which corresponds to a total "information content" n_e of 37.

Table 3.4: Structures and refinement results of $UO_{2.007}$ at 900 ℃ using two fourfold-cell models. The coordinate of the uranium atom is fixed at (0,0,0), and the corresponding site occupancy is 1. In Model 2, the displacement δ along <111> directions for lattice oxygen ions is considered. The refined

displacements of either lattice oxygen or interstitial ions are in fractional coordinates of the lattice parameter. RGOF, the Relative Goodness-of-Fit for each model is also provided.

$UO_{2.007}$	**Model 1**			**Model 2**		
***L* (Å)**	5.510 ±0.002			5.525 ±0.002		
	Coordinates	Site occupancy	displacement	Coordinate	Site occupancy	displacement
O_L	$(\frac{1}{4},\frac{1}{4},\frac{1}{4})$	1.84 ±0.002	-	$(\frac{1}{4}+\delta,\frac{1}{4}+\delta,\frac{1}{4}+\delta)$	1.84 ±0.002	0.02 ±0.03
O'<110>	$(\frac{1}{2}+v,\ \frac{1}{2}+v,\frac{1}{2})$	0.0737 ±0.003	0.10 ±0.01	$(\frac{1}{2}+v,\ \frac{1}{2}+v,\frac{1}{2})$	0.0888 ±0.0025	0.13 ±0.02
O''<111>	$(\frac{1}{2}+w,\frac{1}{2}+w,\frac{1}{2}+w)$	0.0938 ±0.003	0.21 ±0.01	$(\frac{1}{2}+w,\frac{1}{2}+w,\frac{1}{2}+w)$	0.0787 ±0.0025	0.15 ±0.01
A	0.0734			0.0435		
n_p	7			8		
N_GOF	0.82			0.49		

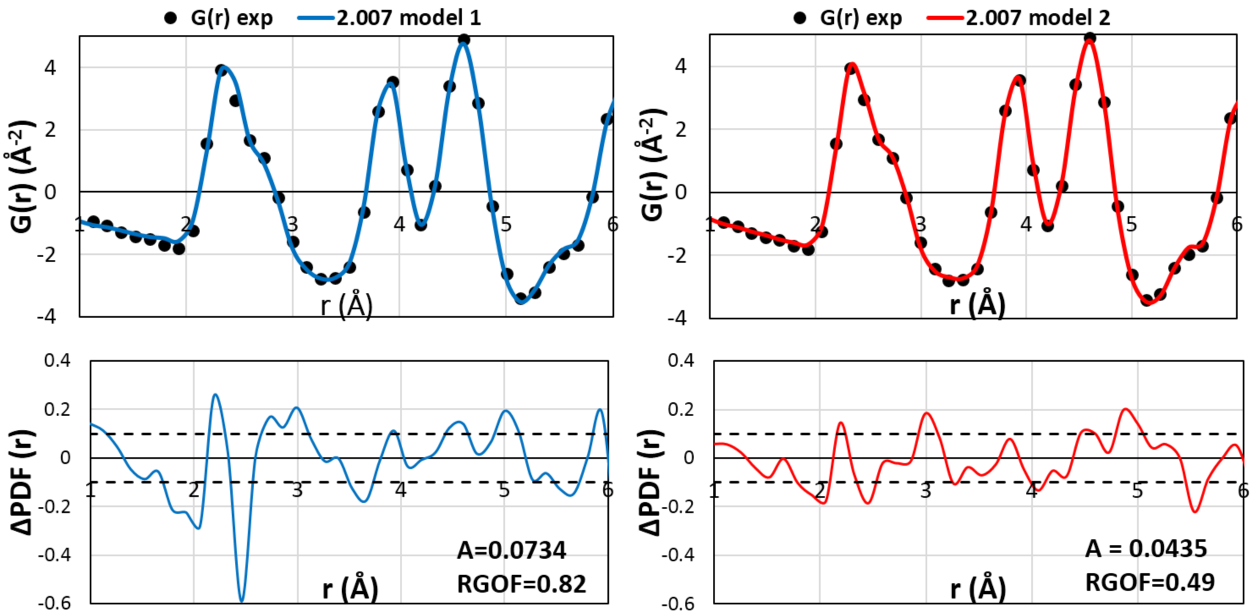

Figure 3.11: PDF data for $UO_{2.007}$ (black circles) up to 6 Å at 900 ℃ and fourfold-cell model results refined using PDFgui. On the left: Model 1; on the right: Model 2; The black dashed lines indicate the experimental uncertainties.

The refined PDFs and differences between the experimental data and models are presented in Figure 3.11. When lattice oxygen ions are allowed to move along <111> directions, there is substantial improvement in the relative goodness-of-fit. The differences between model and experiment, in particular in the first peak and adjacent shoulder and the second peak, which correspond to the shortest U-O, O-O and U-U bonds respectively, are significantly reduced in Model 2. The fundamental reason for the improved quality obtained with Model 2 is that it takes into account the distortion on the oxygen sub-lattice, which has been recognised since the early 1960s (Willis, 1978, 1963a), as a device to capture the anharmonic component of the Debye-Waller factor (Hutchings, 1987). As seen in Figure 3.11 the difference plots ΔPDF, i.e. the difference between experimental and modelled PDFs, show high frequency (short wavelength) oscillations that are presumably due to termination errors (Mamontov and Egami, 2000). These errors are characterized by a wavelength of $7.8/Q_{max} \sim 0.33$ Å (Warren, 1969), for a Q_{max} 23.5 $Å^{-1}$ as used in this work.

We have further studied two additional models on the basis of Model 2, in which oxygen interstitials could move from the unoccupied octahedral sites either along <110> or <111> directions only. Both models yielded marginally higher RGOFs (both 0.55) than Model 2, which indicates both two types of interstitial could indeed coexist. In addition, Table 3.4 shows that the oxygen vacancy concentration, derived from the lattice oxygen occupation numbers, is equivalent neither to the O’ or O’’ occupation numbers as would be expected in the case of a 2:2:2 cluster. It is difficult therefore to draw a clear-cut conclusion as to whether one or two types of interstitials are present or whether excess oxygen ions cluster in this low deviation-from-stoichiometry material.

3.4.2.2 High deviation-from-stoichiometry material ($UO_{2.16}$)

Using Model 1 and 2 described above, we have carried out an analysis of the data for the higher deviation-from-stoichiometry material. Figure 3.12 shows the experimental PDF and the model results. Again the best results are obtained when due account is taken of the anharmonic motion of the tetrahedrally coordinated lattice oxygen ions and they are free to move along the <111> direction, away from their nearest neighbours and towards the empty octahedral sites of the fluorite structure. In particular, the shortest U-O and O-O distances are better described with Model 2.

The displacements of O’ ions in Table 3.5 refined for both models are determined with very high standard deviations. Despite that, if one considers Model 1, the ratio between O’ and O” ions estimated from this PDF analysis is about 0.5, which is expected in the case where cuboctahedra are the predominant defect species. The average occupancy ratio between O’ and O’’ from Model 2 is 0.76. This value is between 0.5, expected in the case where cuboctahedra are the predominant defect species, and 1 expected if Willis clusters prevail.

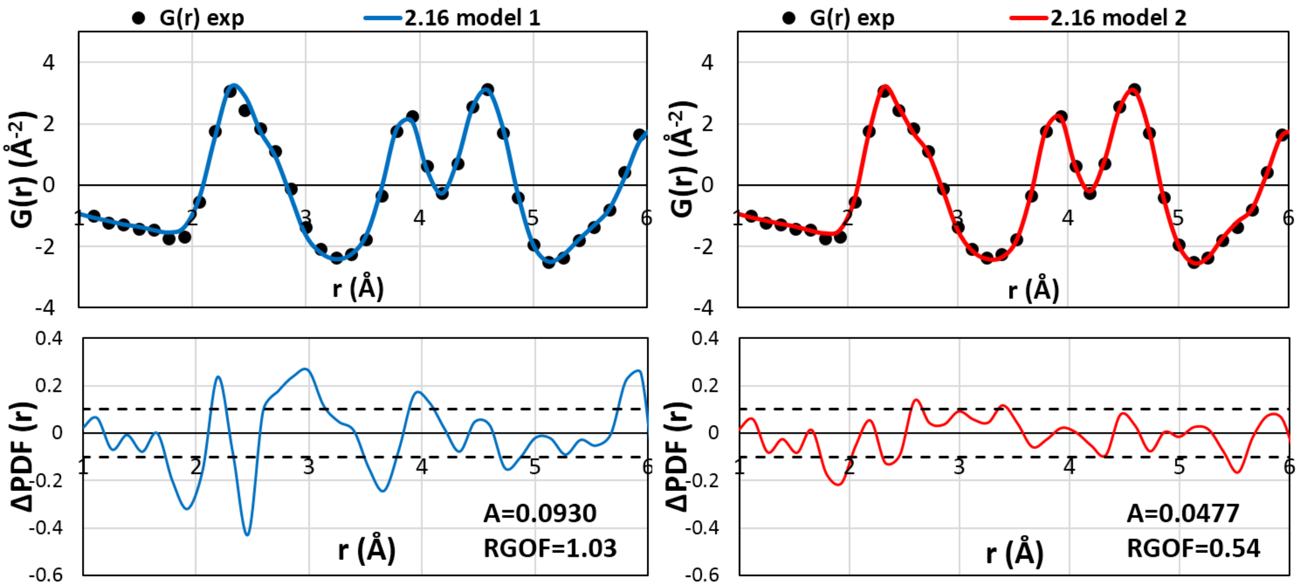

Figure 3.12: PDF data for $UO_{2.16}$ (black open circles) up to 6 Å at 900 ℃ and fourfold-cell model results refined using the PDFgui. On the left: Model 1; on the right: Model 2; The black dashed lines indicate the experimental uncertainties.

Table 3.5: Structures and refinement results of $UO_{2.16}$ at 900 ℃ using two fourfold-cell models. The space-group is $Fm\bar{3}m$. The coordinate of the uranium atom is fixed at (0,0,0), and the corresponding occupancy is 1. In Model 2, the thermal displacement δ along <111> directions for lattice oxygen ions are considered. The refined displacements of either lattice oxygen or interstitial ions are in fractional coordinates. The relative Goodness-of-Fit for each model RGOF is also provided.

$UO_{2.007}$	**Model 1**			**Model 2**		
***L* (Å)**	5.492 ±0.003			5.507 ±0.003		
	Coordinates	Site occupancy	Refined displacement	Coordinate	Site occupancy	Refined displacement
O_L	$(\frac{1}{4},\frac{1}{4},\frac{1}{4})$	1.88 ±0.002	-	$(\frac{1}{4}+\delta,\frac{1}{4}+\delta,\frac{1}{4}+\delta)$	1.90 ±0.002	0.021 ±0.001
O’<110>	$(\frac{1}{2}+v,\ \frac{1}{2}+v,\frac{1}{2})$	0.093 ±0.003	0.04 ±0.02	$(\frac{1}{2}+v,\ \frac{1}{2}+v,\frac{1}{2})$	0.113 ±0.003	0.02 ±0.02
O’’<111>	$(\frac{1}{2}+w,\frac{1}{2}+w,\frac{1}{2}+w)$	0.187 ±0.003	0.20 ±0.01	$(\frac{1}{2}+w,\frac{1}{2}+w,\frac{1}{2}+w)$	0.148 ±0.003	0.18 ±0.01
A	0.0930			0.0477		
n_p	7			8		
R_GOF	1.03			0.54		

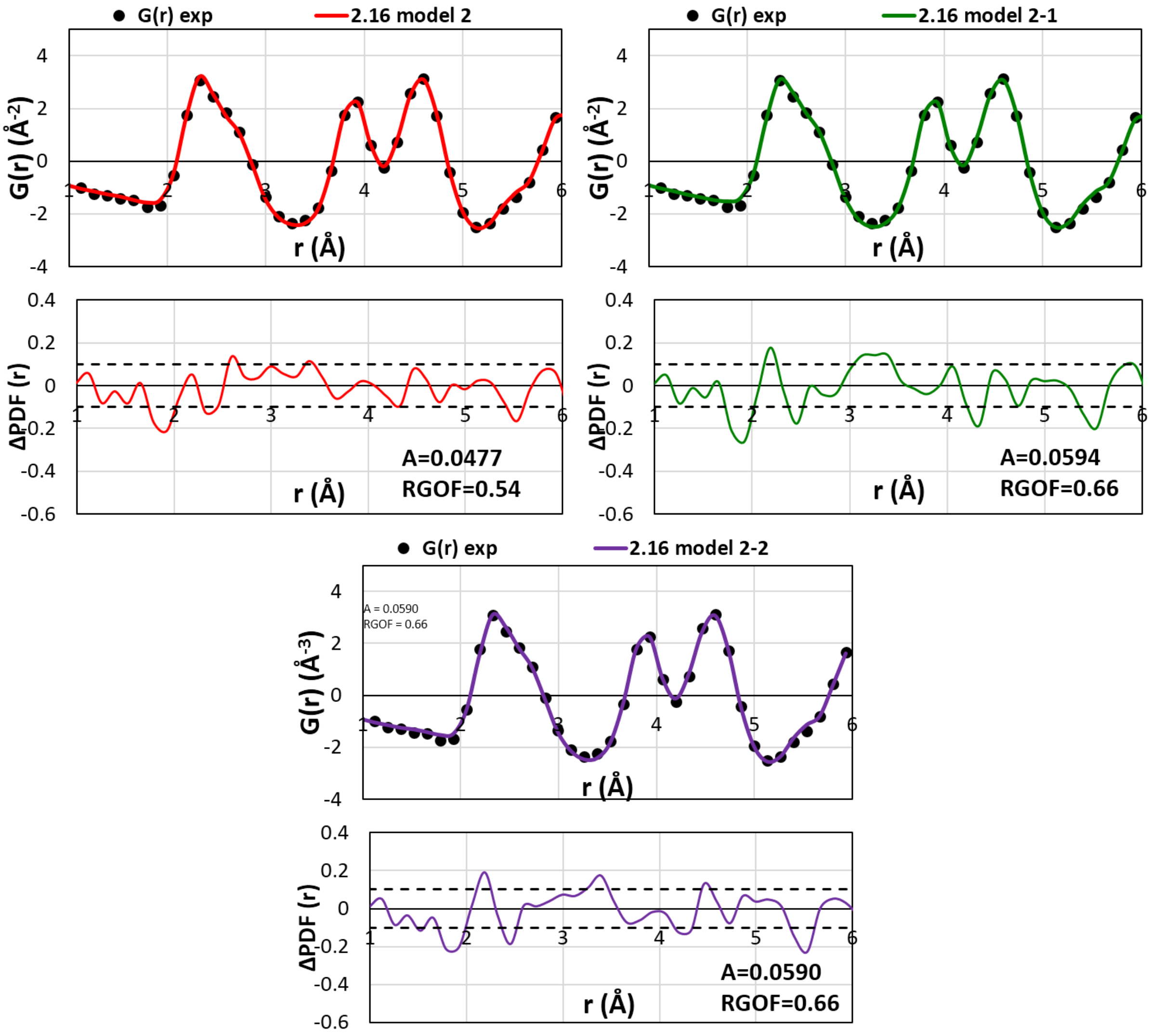

Figure 3.13: PDF data of $UO_{2.16}$ (black full circles) up to 6 Å at 900 ℃ and fourfold-cell model results refined using PDFgui. Model 2 in purple takes into account the distortions of oxygen sublattice along <111> directions. Model 2-1 and Model 2-2 assume only O’ or only O’’ type of interstitial in the material. The black dashed lines indicate the experimental uncertainty.

As for the low deviation from stoichiometry material, we have refined models assuming only one type of oxygen interstitial is present (either O’ or O’’) as illustrated in Figure 3.13. The results also suggest that the structural model containing two types of oxygen ions best represents the experimental data.

In the higher deviation from stoichiometry material, it appears that oxygen ions probably form clusters but the occupation numbers do not allow for any definite choice to be made between different defect models. The structure of clusters is more difficult to conclude in the case of the low deviation from stoichiometry material since assuming the presence of two types of interstitial ions only provides a marginal improvement of the model quality. In the following section, we refine supercell models involving different defect structures, in an attempt to shed light upon the nature of the most probable defect structure.

To summarize, the PDF fourfold-cell refinements suggest the deviations-from-stoichiometry for two UO_{2+x} samples are close to 0.007 and 0.16. In both materials, uranium atoms remain at the original fluorite positions. In $UO_{2.007}$, oxygen interstitial ions tend to move along <110> directions away from the octahedral sites. In $UO_{2.16}$, the types of oxygen interstitials and compositions are consistent with previous neutron diffraction results relative to $UO_{2.13}$ as studied by Willis. However, the fourfold cell model provides only a limited picture of atomic arrangements.

3.4.3 The supercell modelling

3.4.3.1 Low deviation-from-stoichiometry ($UO_{2.007}$)

We expanded the fourfold cell to a 4×4×4 ($U_{256}O_{512}$) supercell in an effort to describe the low deviation from stoichiometry material. Addition of two oxygen ions to this supercell increases stoichiometry of the system to 2.0078, which is close to the O/U ratio of our sample. Because deviation-from-stoichiometry is small, efforts were mainly devoted to modelling the isolated interstitial and the expected di-interstitial defects, *i.e.* the Willis 2:2:2 cluster and Andersson’s split di-interstitial. The lattice oxygen ions in the supercell model are also allowed to move along <111> directions.

To model the isolated interstitial, two non-adjacent octahedral sites are chosen and filled with two oxygen ions. For di-interstitials, excess oxygen ions are placed at two adjacent unoccupied octahedral sites, and we allow them to move along either <110> (for the 2:2:2 cluster) or <111> (for the split di-interstitial) directions. As expected, this movement is accompanied by a displacement of the corresponding nearest lattice oxygen ions away from its normal site along the <111> directions.

From Figure 3.14, it appears that all three models provide very similar PDFs. Neither of the models provides an entirely satisfactory description of the first two peaks corresponding to the U-O and O-O bonds. Information about the defects are provided in the Table 3.6. The oxygen lattice distortion is the same for all three models (0.015 in fractional coordinates). The displacements of oxygen interstitial ions from the octahedral sites are slightly larger for di-interstitial clusters than for the isolated interstitial. The displacements of lattice oxygen ions involved in the clusters are estimated with a poor level of accuracy, particularly for the split di-interstitial model. More importantly maybe, Figure 3.14 shows that the differences between model and experiment are virtually identical for all three models suggesting that the system is too dilute with regard to the sensitivity of the method for a conclusion to be drawn.

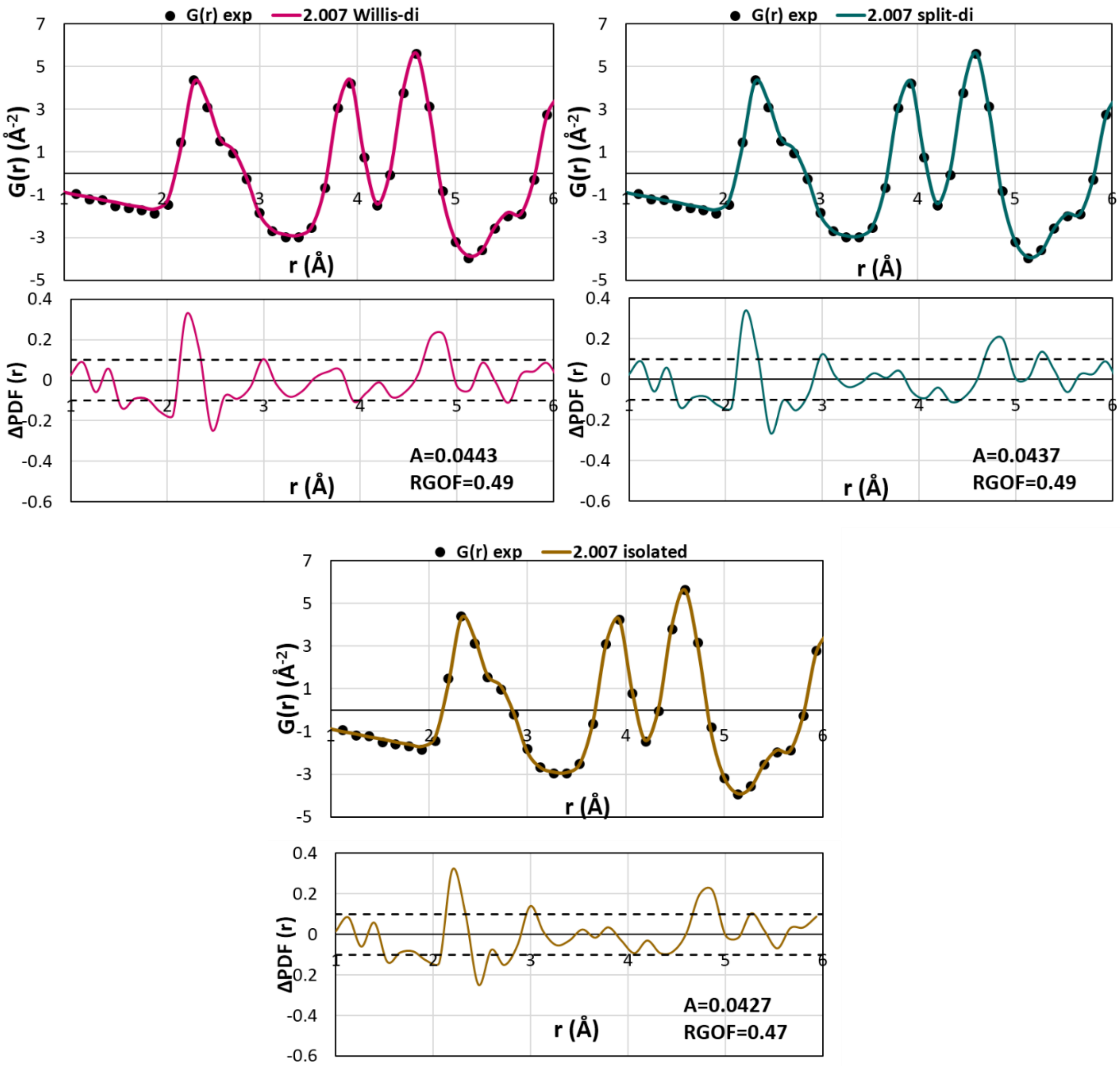

Figure 3.14: PDF data for $UO_{2.007}$ (black circles) up to 6 Å at 900 ℃ and model results refined using PDFgui with a 4×4×4 supercell. From left to right: the PDF model assuming Willis 2:2:2 cluster (in pink), a split di-interstitial (in green) and two isolated interstitial ions (in yellow). The black dashed lines indicate the experimental uncertainty.

Table 3.6: Refinement results of $UO_{2.007}$ using a 4×4×4 supercell. The displacements of either lattice oxygen or interstitial ions are in fractional coordinates.

$UO_{2.007}$	**Willis 2:2:2 cluster**	**Split di-interstitial**	**Isolated Oi**
Lattice para. ***L*** (Å)	5.519 ±0.002	5.518 ±0.002	5.518 ±0.002
displacement for interstitial ions (O’ or O’’)	0.21 ±0.12	0.28 ±0.12	0.15 ±0.08

displacement for lattice oxygen O''<111>	0.10 ±0.08	0.12 ±0.18	-
$\boldsymbol{A}$	0.0443	0.0437	0.0427
$\boldsymbol{n_p}$	7	7	6
RGOF	0.49	0.49	0.47

3.4.3.2 High deviations-from-stoichiometry ($UO_{2.16}$)

Because so widely reported as the basic defect in α-, β-, and γ-U_4O_9, it is reasonable to try to ascertain the presence of cuboctahedron clusters in the high deviation from stoichiometry material (Bevan et al., 1986; Cooper and Willis, 2004; Desgranges et al., 2016, 2011). The phase transition from the bi-phasic to the single-phase region would in this case simply occur through the disordering of such clusters. (Andersson et al., 2012) have suggested that these clusters may transform into more stable split quad interstitials so that these latter defects could also be relevant. Split-di interstitials and Willis type clusters have been reported from theoretical and experimental considerations (Andersson et al., 2009; Willis, 1978). These four types of defects have therefore been studied in a 2×2×2 supercell model $U_{32}O_{64}$, the stoichiometry of which (2.156) is close to our experimental value (2.158).

The first model contains two Willis 2:2:2 clusters and one isolated interstitial. There are many ways of choosing two adjacent empty octahedral sites in which to place a Willis type cluster in this 2x2x2 supercell. We have checked that the choice of these unoccupied sites does not modify the PDF modelling results in any appreciable way. Two such configurations are illustrated in Figure 3.15. In the second model, four interstitial ions form a split quad interstitial (Figure 3.16.a). In the third model, we have considered two split di-interstitials placed randomly (Figure 3.16.b). In the models above, the fifth oxygen ion is assumed isolated. The last model is a centre-occupied cuboctahedron cluster a schematic description of which is provided in Figure 3.17.a). It is made up of four oxygen interstitials (purple spheres) displaced away from their octahedral site along the <110> directions towards the centre of the defect structure which is occupied by an interstitial ion free to move along the <111> direction (orange spheres). The eight lattice oxygen ions associated with this cluster (red spheres) are displaced as illustrated in Figure 3.17.b). All models consider the distortion induced by movement of lattice oxygen ions.

(2La)

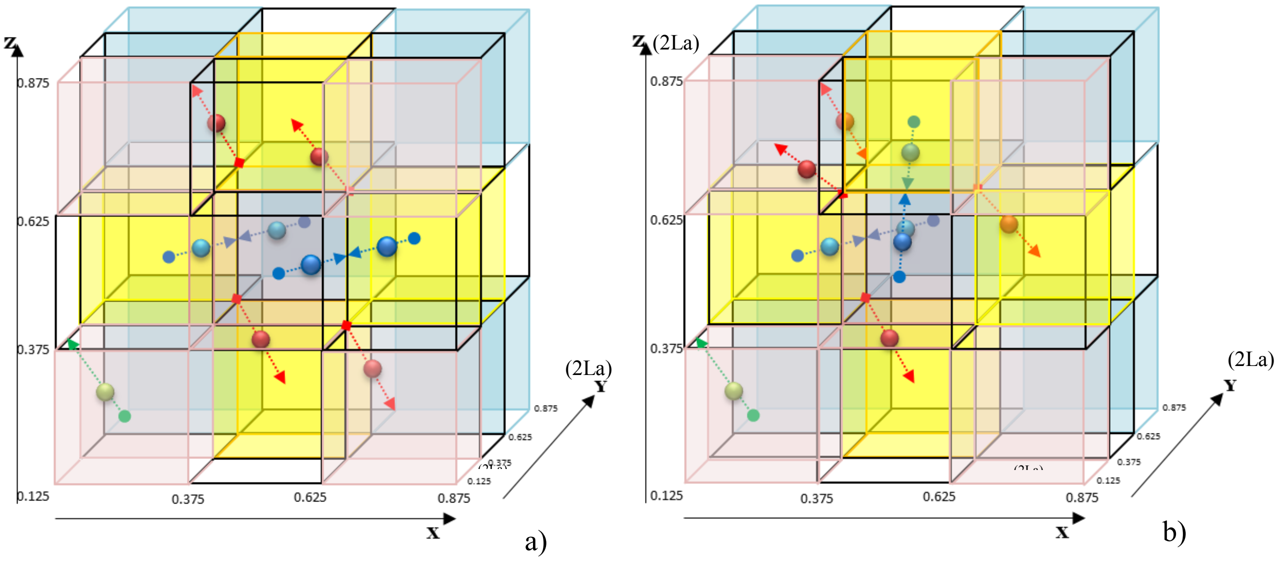

Figure 3.15: Two Wills di-interstitial clusters and one isolated interstitial; Only the oxygen sub-lattice is represented here, and cells with empty octahedral sites are coloured (in pink, yellow and blue); Red spheres are the displaced lattice oxygen ions, blue and green spheres are oxygen interstitial ions moving along <110> and <111> directions; a) Two Willis di-interstitials in parallel; b) The second Willis di-interstitial is rotated from its original position in a). The scale for coordinates is a fraction of twice the lattice parameter (2La).

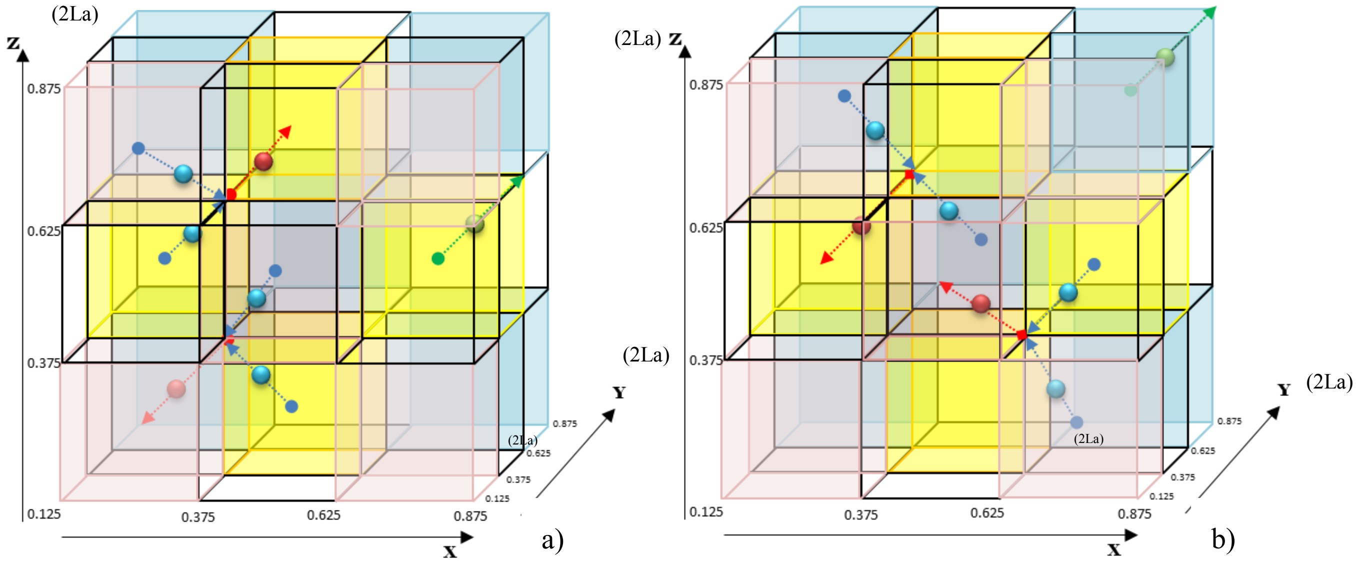

Figure 3.16: The configurations of two split di-interstitials and a single interstitial: a) Two split di-interstitials which constitute the split quad-interstitial; b) Two randomly distributed split di-interstitial. Other notations are the same as in Figure 3.15.

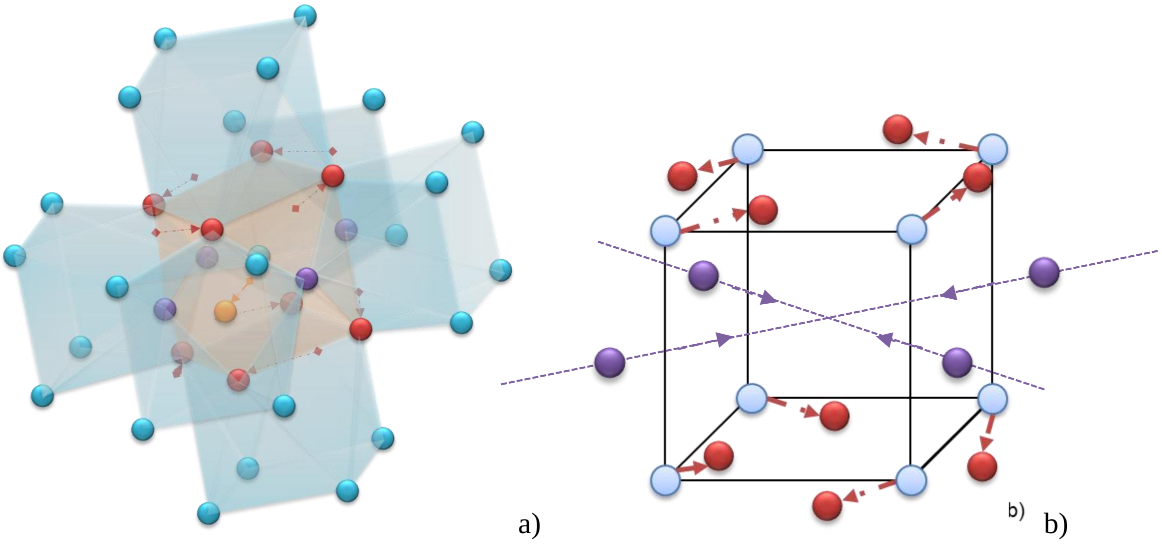

Figure 3.17: a) Oxygen cuboctahedron cluster: blue spheres – normal lattice oxygen ions; red spheres – the lattice oxygen ions displaced from their original position along the directions indicated by the red arrows; purple spheres – the interstitial oxygen ions moving along <110> directions from the central octahedral site (orange cube); orange sphere: an interstitial oxygen ion displaced from the centre of the defect along a <111> direction. b) The displacement of lattice oxygen ions of the cuboctahedron cluster in a).

The experimental PDF data is refined up to 6 Å with the four models described above. The refinement results plotted in Figure 3.18 appear to be satisfactory with respect to experimental uncertainties. The RGOF of the fourth model, although close to the one built upon the 2:2:2 clusters, is the lowest of all defect clusters.

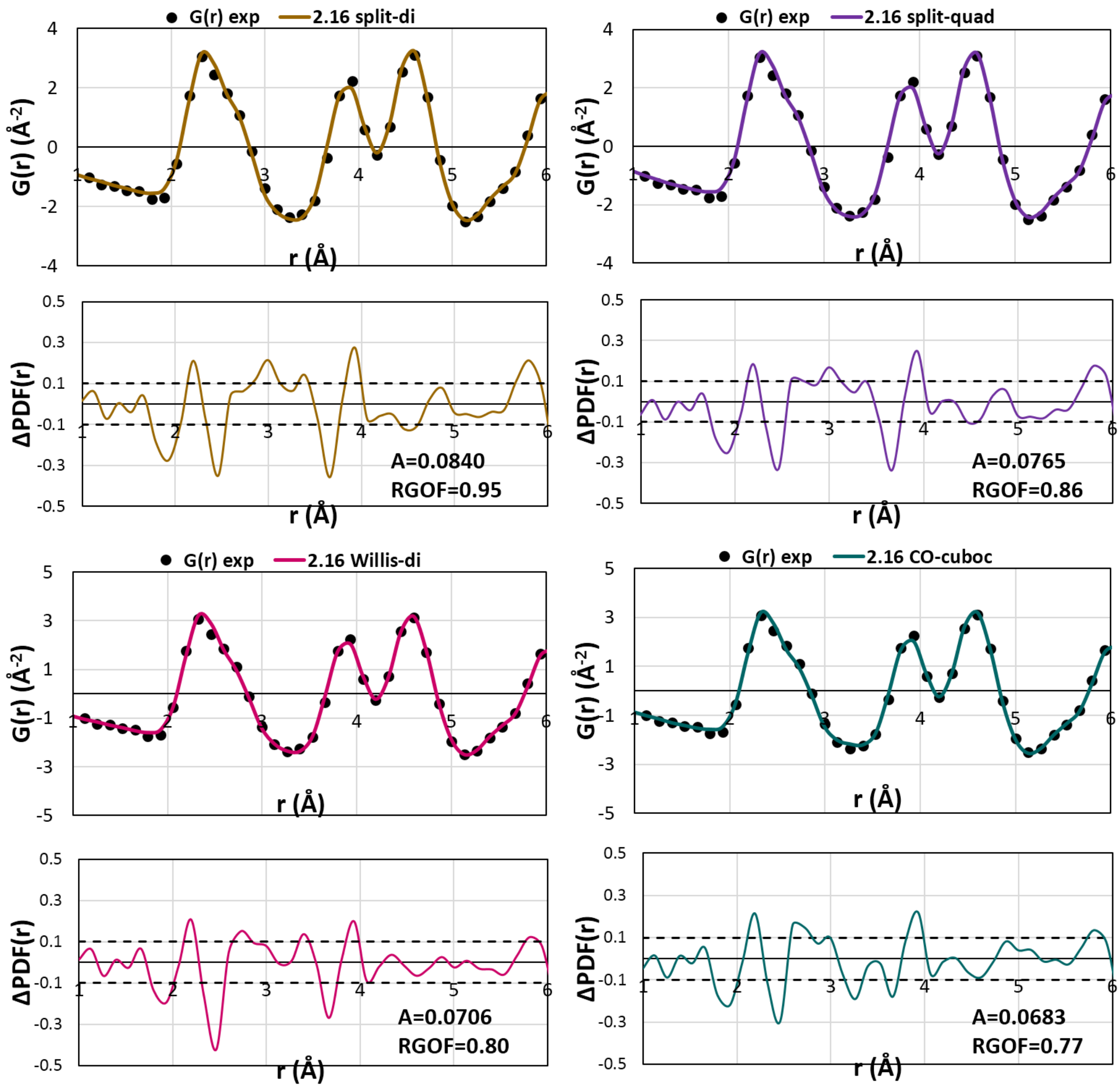

Figure 3.18: PDF data for $UO_{2.16}$ (black circles) up to 6 Å at 900 ℃ and model results refined using the PDFgui with a 2x2x2 supercell. From left to right and top to bottom: the PDF models containing the split di-interstitial cluster (in yellow), the split quad-interstitial clusters (in purple), the Willis 2:2:2 clusters (in pink), the centre-occupied cuboctahedron cluster (in green). The black dashed lines indicate the experimental uncertainty.

The supercell representation was then further expanded to a 3×3×3 $U_{108}O_{216}$ model containing three centre-occupied cuboctahedron clusters. Figure 3.19 shows a schematic diagram of the oxygen sub-lattice only. In this figure we have symbolised the cuboctahedron clusters as orange cubes. Each orange cube is surrounded by 6 coloured cubes (purple, pink or green) affected by the cuboctahedra. In this 3×3×3 supercell, the positions of cuboctahedron clusters as well as the surrounding distorted oxygen cubes are unique. Two extra interstitial ions were modelled either as a di-interstitial cluster or as isolated ions. The three cuboctahedron clusters are stable, the remaining interstitials tend to remain isolated. The structural information relative to the centre-occupied cuboctahedron clusters refined in 2×2×2 and 3×3×3 supercells is presented in Table 3.7.

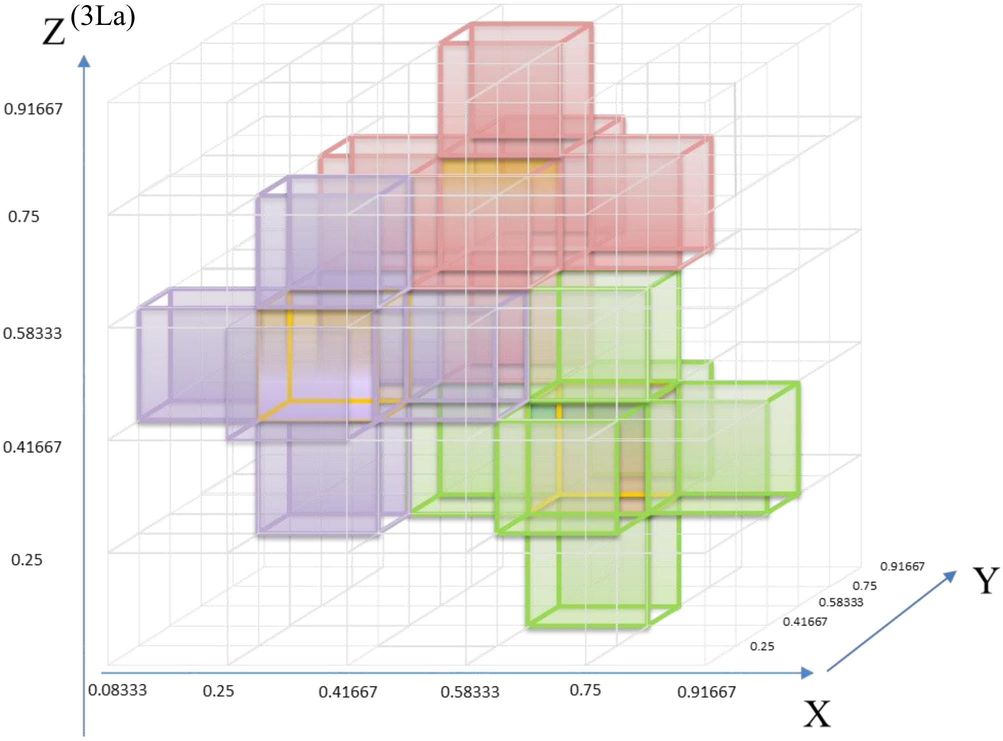

Figure 3.19: Three cuboctahedron clusters and surrounding distorted oxygen sub-lattice in a 3×3×3 supercell. The coordinates are given as a fraction of triple the lattice parameters 3La.

The lattice parameters for $UO_{2.16}$ at 900 ℃ obtained by two supercell models are roughly the same as for the Model 2 (average-cell) analysis. The displacements calculated from either of the supercell models are similar. In next section, we shall compare the structural information of our refined defect to the literature, and discuss the possible clustering process of oxygen interstitial ions on the basis of these refined defects.

Table 3.7: Details of cuboctahedron cluster modelled in 2×2×2 and 3×3×3 supercell models

900 ℃ PDF 6Å	**2×2×2**	**3×3×3**
Lattice parameter ***L*** **(Å)**	5.501 ±0.003	5.500 ±0.003
Displacement of interstitial ions O’ from the octahedral sites along <110>	0.11 ±0.07	0.14 ±0.01
Displacement of the interstitial ion O_C in the centre of cuboctahedron along <111>	0.01 ±0.01	0.04 ±0.04
Displacement of lattice oxygen ions involved in the cuboctahedron cluster O_L’’	0.17 ±0.01	0.17 ±0.01

Displacement of isolated interstitial along <111>	-	0.05 ±0.05
$\boldsymbol{A}$	0.0683	0.0692
$\boldsymbol{n_p}$	8	9
RGOF	0.77	0.80

3.5 Discussion

Although the focus of this work is to study short range defect arrangements, it remains interesting to look at the structural information obtained from the PDF analysis, such as the lattice parameter, and check to what extent it is consistent with reported structural analyses. The values obtained in the 20 ℃ to 900 ℃ temperature range for UO_2 compare favourably to values obtained from high resolution diffraction data (Ruello, 2001). The lattice parameter for the hyper-stoichiometric materials we have studied may be compared to values derived from Martin's recommendation for UO_{2+x} (Martin, 1988), and Grønvold's X-ray diffraction results (Grønvold, 1955). At 900 ℃ the lattice parameters derived from the PDF analyses are 5.519 ±0.002Å and 5.500 ±0.003Å, assuming a distortion of the oxygen sublattice. These values compare favourably to values derived from the literature, which are 5.525 ±0.005 Å, and 5.505 ±0.005 Å for $UO_{2.007}$ and $UO_{2.16}$ respectively.

It is a general rule that all our PDF analyses indicate that at 900 ℃ and at all oxygen concentrations studied, it is necessary to account for the anharmonic behaviour of oxygen ions to reproduce the first few U-O and O-O distances satisfactorily. This is manifested as a displacement of lattice oxygen ions away from their Wyckoff positions in the $Fm\bar{3}m$ space group along the <111> directions. The displacements of lattice oxygen determined based on the PDF analyses of stoichiometric UO_2 either in the average-cell or supercell models is 0.0165 ±0.0005 in fractional coordinates. This value is identical to that provided in the average-cell analysis of UO_2, 0.017±0.001, by Willis (Willis, 1978). Further, the refined displacement in the current average-cell analysis of UO_{2+x} (irrespective of x) is 0.020 ±0.002, so still very close to the value derived for UO_2. Thus this result does not seem to be affected by the amount of excess oxygen present. Another common feature to all our analyses, again irrespective of the deviation-from-stoichiometry, is that both types of interstitial ions are required to reproduce the experimental data. However, the occupancy ratio between O' and O'' determined for different samples are different, and the distances by which they are displaced from the octahedral sites vary depending upon the type of defect assumed and material composition.

There is unfortunately no published result we can compare our $UO_{2.007}$ data to. The refined occupancy numbers for O'<110> and O''<111> ions using the average-cell Model 2 in this work are similar (0.089 and 0.079 for O' and O'' ions respectively). However, these values are at odds with those derived for the corresponding values for anion vacancies which is estimated at 0.16. These values are not consistent with a typical 2:2:2 cluster. The refined displacements for interstitial ions is estimated at 0.11 for O' and 0.13 for O'' in fractional coordinates, which is close to the values reported for $UO_{2.06}$ at 927°C by first-principles, molecular dynamics simulations (0.091 ±0.02) (Wang et al., 2014). In the 4x4x4 supercell analysis, we have modelled three types of defects. However, Figure 3.4 shows virtually identical agreement between all three models. There may be two possible reasons for this. The first could be that this level of non-stoichiometry is close to what is expected to be the transition deviation-from-stoichiometry between a region where isolated defects predominate over anion di-interstitials (estimated at 5 10-3 between 973 and 1673 K according to Garcia's work (Garcia et al., 2017)). The second may be understood from the rather high vacancy concentrations derived from the average-cell model. This could be an indication that there is a substantial degree of Frenkel disorder at 900°C, which is not explicitly concerned in the supercell approach. At this degree of non-stoichiometry, the system is so dilute that the addition of two additional interstitial ions does not modify the PDF to any great extent. Taking Frenkel disorder into account could be a means of improving the modelling but is left for a future date.

For $UO_{2.16}$, the average occupancy of O' and O'' given in the average-cell Model 2 (0.11 and 0.15) compares favourably to the reported value for $UO_{2.12}$ at 500 ℃ by neutron diffraction experiments (0.08 and 0.16) (Willis, 1978) but the lattice oxygen occupancies do not clearly point to a 2:2:2 cluster. The occupancy ratio (O'/O'') however is much smaller than the ratios obtained by diffraction experiment of U_4O_{9-y} by (Bevan et al., 1986) at 500 ℃ (10), and computation of $UO_{2.13}$ (Wang et al., 2014) at 1727 ℃ (0.15/0.09). The defect proposed by the latter two studies were the cuboctahedron cluster and the split di-interstitial respectively. Also, our estimate of the O' displacement is small in comparison to other similar studies.

The results of the 2x2x2 supercell models are somewhat clearer. The fact that the second most suitable model involves 2:2:2 clusters in parallel is consistent with the average-cell analysis that both types of interstitials are present in the material. The refinement quality however is marginally improved when one assumes the presence of a centre-occupied cuboctahedron cluster. In our refinement process, we restrained lattice oxygen ions involved in the cuboctahedron cluster to move along <111> directions. The displacement of O' ions defines the lateral extent of the cuboctahedron cluster. The displacement of O'' ion defines both the longitudinal size, as well as the extent of skew. The excess O' ions are displaced from the octahedral sites along <110> direction by 0.11 in a 2x2x2 supercell model and 0.14 in a 3x3x3 supercell. These are in a good agreement with the refined values for $UO_{2.12}$ given by Willis (0.11 ±0.01 (Willis, 1978)). The eight lattice oxygen ions in the refined cuboctahedron are displaced along <111> directions by 0.17 in this work, which is higher than Willis's reported value (0.11 ±0.01). Two possible reasons may explain the discrepancy: first, our sample is more oxidized than $UO_{2.12}$ and could lead to oxygen ions to clusters being distorted to a greater degree. Secondly the refined displacement related to O'' in the average-cell analysis by Willis should be an average of all types of interstitials ions moving along <111> directions. This is not equivalent to our analysis as the value we report concerns the lattice oxygen ions involved in the cuboctahedron only. The cuboctahedron cluster refined for $UO_{2.16}$ may also be compared to the same cluster reported for β- and γ-U_4O_9. Cooper refined a model of the cuboctahedron based upon an analysis of a β-U_4O_9 single crystal diffraction data at 450 ℃ (Cooper and Willis, 2004). Although, his definition of the cuboctahedron cluster is different from ours in the sense that his defect is consistent with the β-U_4O_9 crystal symmetry, it is possible to compare the displacement of interstitial ions that make up the cluster. The displacement of O' in our work is close to the parameter he defined in relation to the size of the cuboctahedron cluster in β-U_4O_9 at 723 K

(0.094) (Cooper and Willis, 2004). Also, the displacement of the interstitial ion at the centre of the cuboctahedron (0.02) is very close to our cuboctahedron cluster (0.04). Similar to Cooper's result, the refined cuboctahedron cluster is not perfectly symmetric as the four triangular faces that are normal to the [±1,±1,1] tetrahedral directions are smaller than those normal to [±1,±1,-1].

Bevan pointed out that many fluorite-related anion excess structures adopt the defect involving a cuboctahedron of anions (Bevan et al., 1986). In the structure he resolved for β-U_4O_9, 13 anion clusters are centred on the 12-fold positions of the $I\bar{4}3d$ space group. One of the probable reasons why this type of defect is favoured lies in its capacity to accommodate a large number of excess ions (5) in a relative small volume. Now within a cluster, charge compensation occurs to allow for the presence of excess O^{2-} ions through oxidation of U ions into a 5+ state so long as the oxygen-excess crystal retains its cubic symmetry (Andersson et al., 2012; Crocombette et al., 2011; Dorado et al., 2010). Charge compensation may not be such that the charge of the defect is zero but it is necessarily less than would be expected from a purely ionic behaviour. So that the fundamental reason why oxygen clusters are favoured over isolated defects appears to lie in the localisation of charges of opposite sign in a stable cluster and the substantial energy reduction it brings about for the material. This is reflected in the binding energy of di-interstitials formed from two single interstitials in hyper-stoichiometric UO_2 (estimated at 0.7 eV (Garcia et al., 2017)). If lower charged defect clusters are generally 'more stable' than their isolated counterparts, it is interesting to reflect over what is expected to happen in an increasingly oxidized sample.

An analysis of deviation-from-stoichiometry and electrical conductivity data concludes that in the temperature range we are concerned with here, doubly-charged isolated oxygen interstitials give way to singly-charged di-interstitial clusters as deviation-from-stoichiometry rises. It has also been concluded from the formation energy calculations of charged defect clusters that increasing non-stoichiometry favours both anion clustering and a decrease in the charge state of the most stable cluster (Crocombette et al., 2011). The reason has to be found in the effect of entropy. In general, having single-type defects is favourable from the point of view of entropy, but unfavourable from the stand point of energy. However, as charged defect concentrations rise, the high entropy gain of having isolated defects is lost over the energy gain that is incurred from having them in a compact clustered form with a lower overall charge. One would expect therefore to see a gradual change in the majority anion defect population as deviation-from-stoichiometry increases from a mono-interstitial to a di-interstitial to possibly an even more compact structure such as a cuboctahedron.

3.6 Conclusion and prospects

Three types of UO_{2+x} samples were manufactured with stoichiometries close to 2, 2.007 and 2.16. We carried out *in situ* neutron scattering experiments on the D4c diffractometer at ILL with a small neutron wavelength which provides a high real-space resolution. Stoichiometric UO_2 was used as a model material to confirm the quality of the data acquisition and processing. Thermal expansion of the lattice was characterized from a Rietveld analysis and compared favourably to the literature. The pair distribution function (PDF) of the samples was then determined. Measurements are reported at 900 ℃. Comparison of the PDFs indicates an increasing level of disorder as the oxygen content of the samples rises. The changes in the Q-space spectra as stoichiometry increases can be seen essentially in a decrease in peak heights and an increase in the signal between the peaks indicating increased disorder.

Regarding the PDF of UO_2, it is interesting to note that the data gathered constitute physical results in their own right. We have seen that the shortest bond length is a decreasing function of temperature. No model is needed to come to this conclusion as it is derived directly from the PDF (RDF). This observation is related to the oxygen distortion derived inferred by Willis from a model interpretation of neutron diffraction experiments on single-crystal UO_2.

PDF data were interpreted assuming different types of clusters which have been reported either from experimental or first-principles studies. The average-cell (fourfold-cell) model indicates that experimental data between 1 and 6 Å are best reproduced when lattice oxygen atoms are allowed to move along <111> directions at high temperature reflecting the anharmonic thermal behaviour of oxygen ions. The study of $UO_{2.007}$ and $UO_{2.16}$ also suggests that both types of interstitial oxygen ions should be considered: O’ and O’’ ions which are displaced from the octahedral sites along <110> and <111> directions respectively. The experimental data are actually well described using this approach but an average cell approach provides only limited insight into the actual atomic scale arrangement. Data were also interpreted using a supercell approach. We expanded the cubic fluorite fourfold-cell to 96-atom (2x2x2, $U_{32}O_{64}$), 324-atom (3x3x3, $U_{108}O_{216}$) and 768-atom (4x4x4, $U_{256}O_{512}$) models. Results at low deviation-from-stoichiometry (x=0.007) suggest that the system is too dilute for a choice to be made between isolated or di-interstitial clusters. At high deviation-from-stoichiometry (x=0.16) several structural models were tested. The centre occupied cuboctahedron cluster provides the best refinement quality although differences with 2:2:2 clusters are small. The cuboctahedron characteristics derived from the analysis are quite similar to Cooper and Willis’s. The picture that emerges therefore could be that as the temperature increases, the arrangement of cuboctahedra that form the U_4O_9 phase in the bi-phasic material is lost but the cuboctahedra remain as the basic defect population.

There is room here for investigating other aspects to this work, notably the effect of temperature. Improvements to modelling the data could also be made. In particular, it transpires from the average cell model that the material may contain a significant amount of Frenkel disorder. This Frenkel disorder could be further investigated within the framework of a supercell model. Finally, correlating these results to *ab initio* molecular dynamics would no doubt provide some essential insight into anion cluster behaviour and should constitute the object of further investigations.

Chapter 4 A study of point defects in UO_{2+x} by positron annihilation spectroscopy

4.1 Introduction

During the oxidation process, lattice oxygen atoms are displaced from their ideal positions. In addition to different types of oxygen interstitials, uranium vacancies are liable to appear with increasing deviation from stoichiometry. Even at exact stoichiometry, uranium vacancies are expected to be more abundant than uranium interstitials since their formation energy is systematically reported to be much lower (Chapter 1). It is also reported that the oxygen-assisted uranium vacancy mechanism is the most likely mechanism for uranium diffusion in UO_{2+x} at relatively small deviations from stoichiometry (Dorado, et al., 2012) at least. In chapter 3 we used a neutron scattering technique to investigate oxygen defects induced by clusters of oxygen interstitials. One of the non-destructive methods that can be used to characterize vacancy defects in UO_{2+x} is positron annihilation spectroscopy.

Positron annihilation spectroscopy (PAS) has been widely applied to study material imperfections on an atomic scale. Being the electron anti-particles, positrons annihilate with a greater probability in regions of the material where the electron density is high and this provides for instance information about the chemical environment of atoms. Vacancy-type defects constitute regions in a material in which the electron density is low and the local potential well can be deep enough for them to constitute favourable sites for trapping positrons. Positrons can therefore be used to study vacancy-type defects based on their annihilation characteristics. Here, we focus upon two implementations of the technique which are a measure of the annihilating electron-positron pair momentum distribution and positron lifetime. The former characteristic is derived from the energy distribution of annihilation products and is known as Doppler broadening. The latter is a measure of the probability of finding a positron of a given lifetime.

The work described in this chapter was designed primarily to characterise vacancy-type defects (in particular uranium vacancies) in hyper-stoichiometric uranium oxide, the ultimate aim being to estimate their charge, size and concentration change with temperature and oxygen content. One should note however that PAS does not provide a direct determination of the nature and concentration of defects a material contains. Rather, the interpretation of results requires analyses with complex trapping models or comparisons to be made with other experimental techniques. Very often, first-principles electronic structure calculations are shown to be extremely useful as a guide for interpreting results.

In this work, we have carried out both Doppler broadening spectroscopy and positron lifetime measurements on non-stoichiometric UO_{2+x} samples in collaboration with the CNRS-CEMHTI laboratory, in Orleans, France. We report the main results in section 4.2. Additional minor results will be presented in the discussion (section 4.3). In section 4.3 we discuss these results in the light of previously published experimental data, electronic structure calculations and the positron trapping model described in Chapter 2 section 2.5.5.

4.2 Main Doppler broadening spectroscopy and positron lifetime results for UO_{2+x}

4.2.1 Doppler broadening characteristics of hyper-stoichiometric UO_2

All samples described in the previous section were characterized by Doppler broadening spectrometry at 300 K. The low and high momentum fractions (S and W) for all UO_{2+x} samples are plotted in Figure 4.1 as a function of positron energy. As can be seen from Figure 4.1, for all samples studied, *S* decreases and *W* increases rapidly as a function of the positron energy from 0.5 to 2.0 keV, and then more slowly up to 5.0 keV. S and W reach a plateau between 5 keV and 25 keV. The constant values of *S* and *W* beyond 5 keV, which correspond to the lattice and defect annihilation characteristics in the bulk, suggest that **the defects induced by the oxidation process are homogenously distributed. This confirms that the samples have been adequately prepared, and sufficient time has been left for them to equilibrate.**

Furthermore Figure 4.2 shows the low momentum fraction (S) as a function of the high momentum fraction (W) for all positron energies and for $UO_{2.002}$ and $UO_{2.042}$ samples. This illustrates the fact that the (W,S) data points line up on a straight line and indicates that the data may be described using only two annihilation states, (W_{surf}, S_{surf}) and (W_{bulk}, S_{bulk}) corresponding to the surface and bulk annihilation states (Barthe et al. 2003).

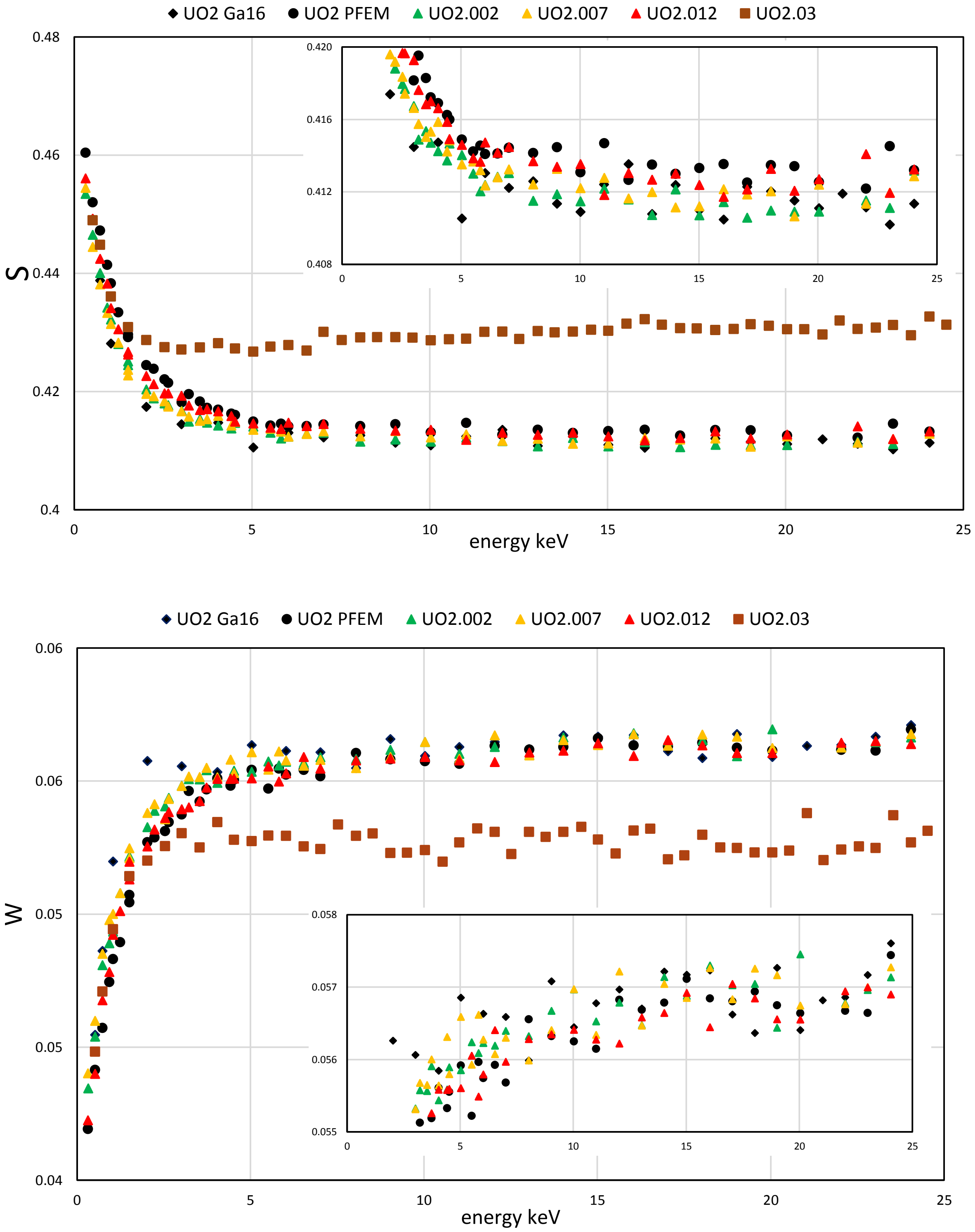

a) UO_{2+x} samples with low deviations-from-stoichiometry

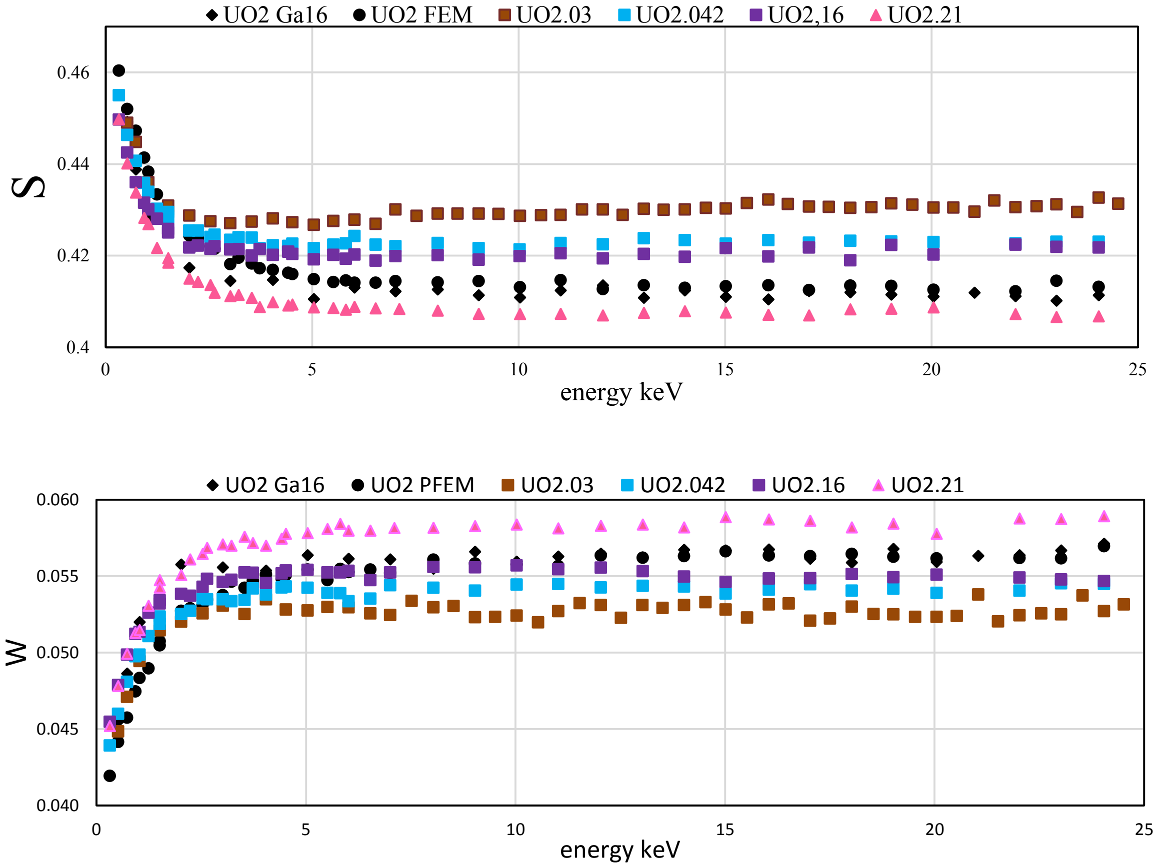

b) UO_{2+x} samples with high deviations-from-stoichiometry

Figure 4.1: Low (S) and high (W) momentum distribution fractions as a function of positron beam energy between 0.5 keV and 25 keV; a) UO_{2+x} samples with low deviations-from-stoichiometry and b) UO_{2+x} samples with high deviation-from-stoichiometry.

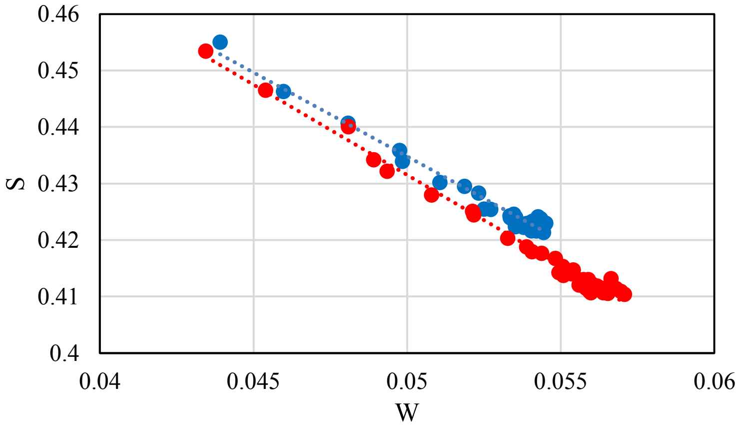

Figure 4.2: S of W for $UO_{2.002}$ and $UO_{2.042}$ at all positron energies.

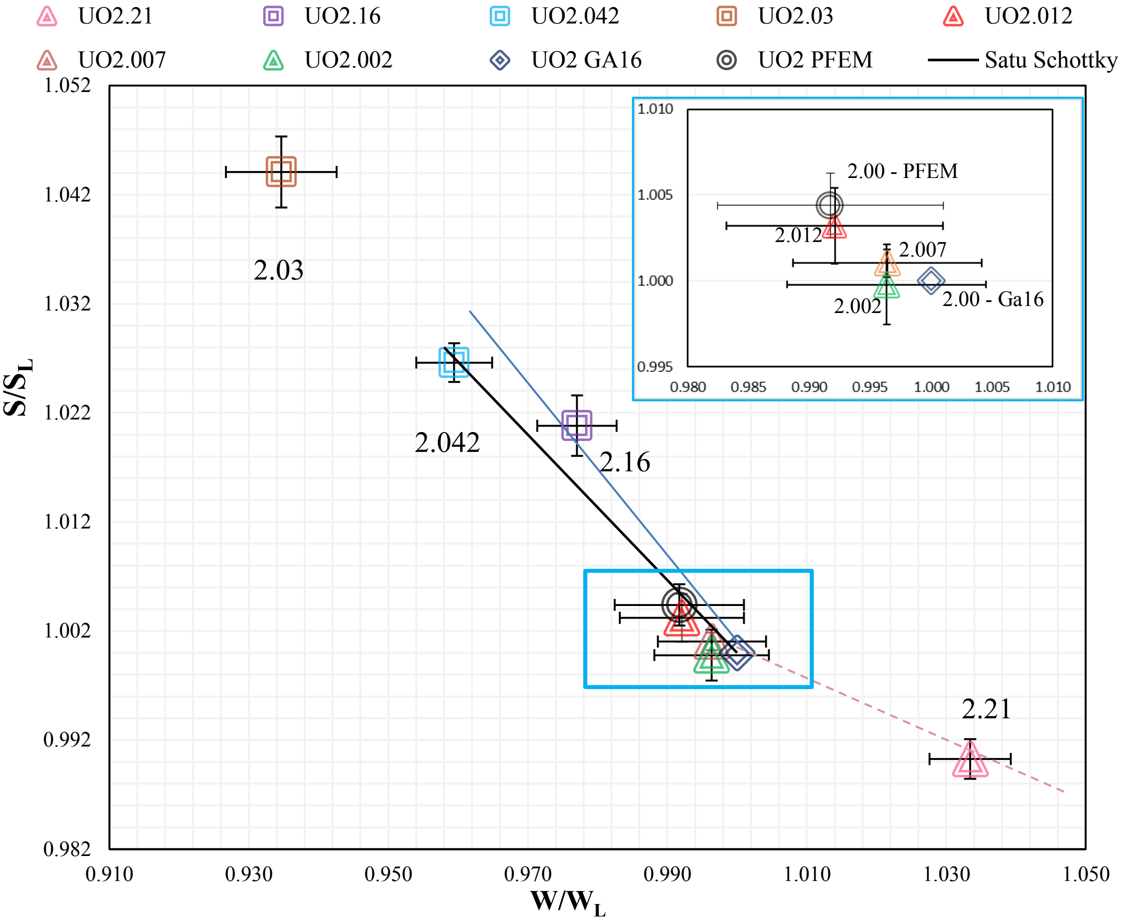

Figure 4.3: Low momentum fraction S as a function of high momentum fraction W for all UO_{2+x} and UO_2 samples. The dashed, solid and dotted lines illustrate three slopes.

The inset in Figure 4.3 shows that for the low deviations-from-stoichiometry samples, i.e. $UO_{2.0}$ to $UO_{2.012}$, the Doppler broadening characteristics are very close. It also reveals that the reference sample used in previous studies (UO_2_GA16) has very similar characteristics to the $UO_{2.002}$ sample. The reference UO_2 sample (UO_2_PEFM) we have purposely prepared for this study has the highest S and smallest W of all the low-deviation-from-stoichiometry samples.

As the stoichiometry increases from 2.002 to 2.03, the plateau values of S (resp. W) increase (resp. decrease). However, when the deviation-from-stoichiometry exceeds 0.03, i.e. for $UO_{2.03}$, $UO_{2.042}$, $UO_{2.16}$, and $UO_{2.21}$, S (resp. W) decreases (resp. increase) as illustrated in Figure 4.1.b and 4.3. The plateau low momentum fraction S (resp. W) for $UO_{2.03}$, $UO_{2.042}$, and $UO_{2.16}$ are still higher (resp. lower) than that of the UO_2 reference (both UO_2_GA16 and UO_2_PFEM). But the $UO_{2.21}$ sample has the lowest (resp. highest) S (resp. W). The lines drawn in the Figure 4.3 are only at this stage a guide for the eye. However their slopes can be regarded as characteristic of a particular type of defect (see section 3). This will be thoroughly discussed in section 4.3 in relation to previous studies.

One may note that the results relating to Doppler broadening spectroscopy were obtained by applying the following momentum windows: (-2.8, 2.8) $\cdot 10^{-3}$ m_0c for the low momentum fraction *S*, and (-26.35, -10.61), (10.61, 26.35) $\cdot 10^{-3}$ m_0c for the high momentum fraction *W*, which are the windows generally used for UO_2 studies (Barthe et al., 2004). We have also checked the effect of modifying the windows has on the results. In particular, we have used the windows ((-2.49, 2.49) $\cdot 10^{-3}$ m_0c for S and (-24.88, -9.64), (9.64, 24.88) $\cdot 10^{-3}$ m_0c for W), which are often used for the study of metal. This does not substantially change the S and W values of any of the samples. All the data analyses reported in this chapter are based on the results obtained with the first set of windows.

4.2.2 Positron lifetimes of UO_{2+x}

In addition to the Doppler broadening spectroscopy, we also determined positron lifetime characteristics at 300 K of several oxidized samples. The lifetime spectra of UO_2 (GA16), $UO_{2.002}$, $UO_{2.042}$, $UO_{2.16}$, $UO_{2.21}$ were analysed with the Posfit software, the principles of which are presented in section 2.5.4. The analysis results can be found in Table 4.1.

Table 4.1: Positron lifetimes resolved from the spectra for $UO_{2.002}$, $UO_{2.042}$, $UO_{2.16}$, $UO_{2.21}$ and UO_2 (Ga16) samples measured at 300 K.

Sample	FWHM	τ_{avg} (ps)	τ_1 (ps)	I_1 (%)	τ_2 (ps)	I_2 (%)
UO_2 (GA16)	227.3	170.6	170.6 ±0.2	100	/	/
$UO_{2.002}$	230.4	167.4	167.4 ±0.4	100	/	/
$UO_{2.042}$	226.6	265.2	170 ±0.1	35.0±0.78	316.5 ±1.5	64.7±0.78
$UO_{2.16}$	228.4	256.5	170 ±0.1	40.6±0.78	315.6 ±1.6	59.4±0.78
$UO_{2.21}$	229.1	171.3	171.3 ±0.4	100	/	/

As Table 4.1 shows, only one (short) lifetime component is resolved for UO_2, $UO_{2.002}$, and $UO_{2.21}$. The reference sample has a lifetime component of 170.6 ±0.2 ps, which compares favourably to the lattice lifetime component (169 ±1 ps) reported for UO_2 (Barthe et al., 2007). The average lifetimes of $UO_{2.002}$ and $UO_{2.21}$ are quite close to that of UO_2.

The average lifetimes for $UO_{2.042}$ and $UO_{2.16}$ are close and notably higher than for other samples. Both samples show two lifetime components. The short component (170 ps) corresponds to the expected value for the UO_2 lattice. The long components for $UO_{2.042}$ and $UO_{2.16}$, although quite close (approximately 316 ps), are much higher than the lattice lifetime. This suggest that positrons are trapped in a localised state which is different from that of lattice, indicating the presence of a particular type of defect. This observation is consistent with the Doppler broadening spectroscopy result for $UO_{2.042}$ and $UO_{2.16}$ which indicates that the low (resp. high) momentum fraction is greater (resp. smaller) than for the other three samples (UO_2, $UO_{2.002}$, $UO_{2.21}$).

In addition, the $UO_{2.042}$ sample was further characterized at low temperature. As Table 4.2 shows, we have checked that the cryostat environment does not substantially change the measured average lifetimes. However, the spectra are slightly different which leads to a slightly different long-lifetime component when the cryostat is used (324.3 ps vs. 316.3 ps). The spectrum is modified at 35 K which leads to a lower average lifetime (236.5 ps). The actual lifetime components are identical but the intensities of both components change at 35 K. From section 2.5.4.3, this could indicate the presence of negatively charged defects.

Table 4.2: Positron lifetimes resolved from the spectra of $UO_{2.042}$, measured at 300 K and 35 K in / out of the cryogenic environment with liquid Helium cooling, using two-component model.

In/Out cryo-environment	**T (K)**	**FWHM**	τ_{avg} **(ps)**	τ_1 **(ps)**	I_1 **(%)**	τ_2 **(ps)**	I_2 **(%)**
Out	300	232.0	260.1	**170**	38.4 ±1.1	**316.3 ±2.2**	61.6± 1.1
In	300	234.1	260.0	**170**	41.7±1.0	**324.3 ±2.3**	58.3±1.0
In	35	231.9	236.5	**170**	57.0 ±1.0	**324.5 ±3.0**	43.0± 1.0

4.2.3 Conclusions

In summary, we have determined annihilation characteristics of samples with different levels of hyper-stoichiometry. The results indicate a homogenous microstructure. The lifetime determined for the UO_2 lattice is approximately 170 ps and compares well to the literature. Also, characteristic slopes for UO_{2+x} samples in the (W,S) representation are identified. The positron lifetime and Doppler broadening spectroscopy results are consistent. In particular, the $UO_{2.042}$ and $UO_{2.16}$ samples have a short lifetime component corresponding to annihilation in the lattice and a long lifetime component which could correspond to the presence of a vacancy defect. They also have one of the highest (resp. lowest) low (resp. high) momentum fractions. The $UO_{2.21}$ sample stands out as having the highest deviation from stoichiometry but the lowest S and highest W of all samples. In the next section, we shall attempt to interpret these results.

4.3 Discussion

4.3.1 Effect of sample preparation and experimental conditions

4.3.1.1 General features of Doppler broadening results obtained on as-prepared samples

Prior to studying the defects induced by oxidizing conditions, we are going to discuss results relative to two as-prepared UO_2 disks. One was subjected to the whole preparation sequence (UO_2_PFEM), and the second disk (REF_OPU) was simply polished and was not annealed at 1700 ℃. Figure 4.4 shows the low and high momentum distribution fractions (S and W) derived from the spectra obtained at 300 K for samples UO_2_PEFM and REF_OPU. A third sample (UO_2_GA16) is shown in Figure 4.4. This sample has been used as reference in past PAS studies of UO_2 at CEMHTI. S (resp. W) decreases (resp. increases) with positron energy from 0.3 keV to 5 keV first, and then remains constant between 5 and

25 keV. This indicates the samples are homogenous beyond a depth between 100 and 200 nm (see Figure 2.19).

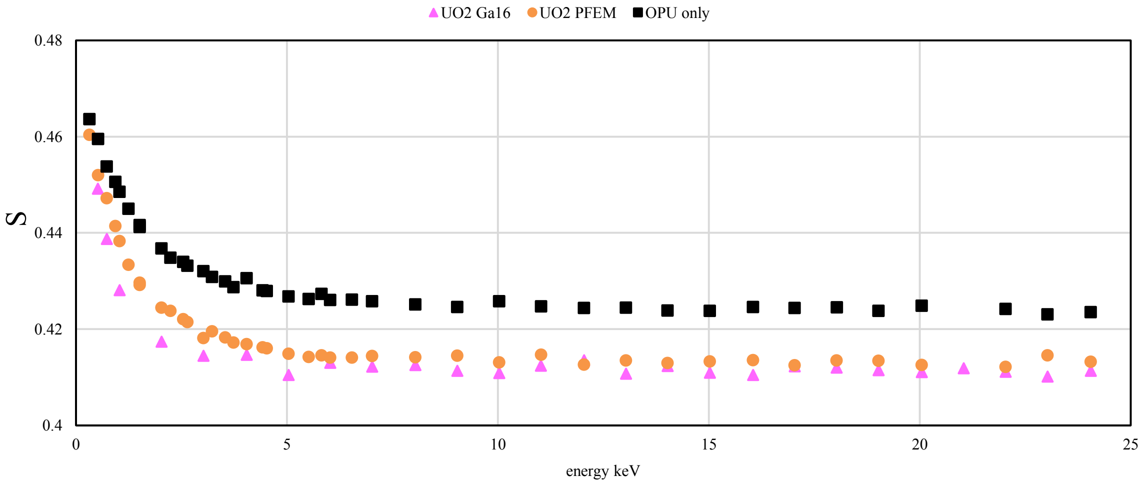

a) S as a function of E

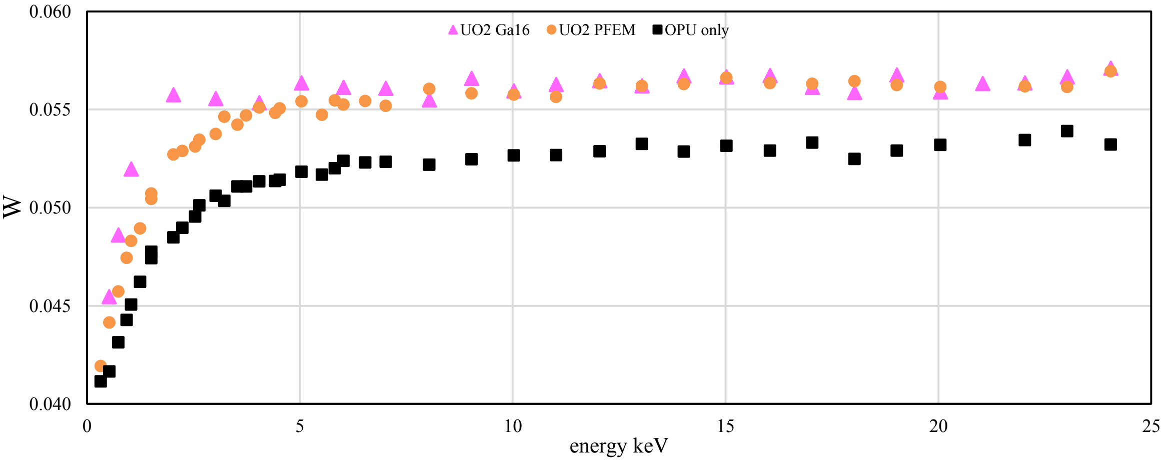

b) W as a function of E

Figure 4.4: Low and high momentum distribution fractions of UO_2 samples at 300 K as a function of positron beam energy; Squares represent as-polished UO_2; the triangles represent the polished and subsequently annealed sample in a humidified Ar/H_2 gas mixture; and the circles represent the polished and subsequently annealed sample in a dry Ar/H_2 gas mixture.

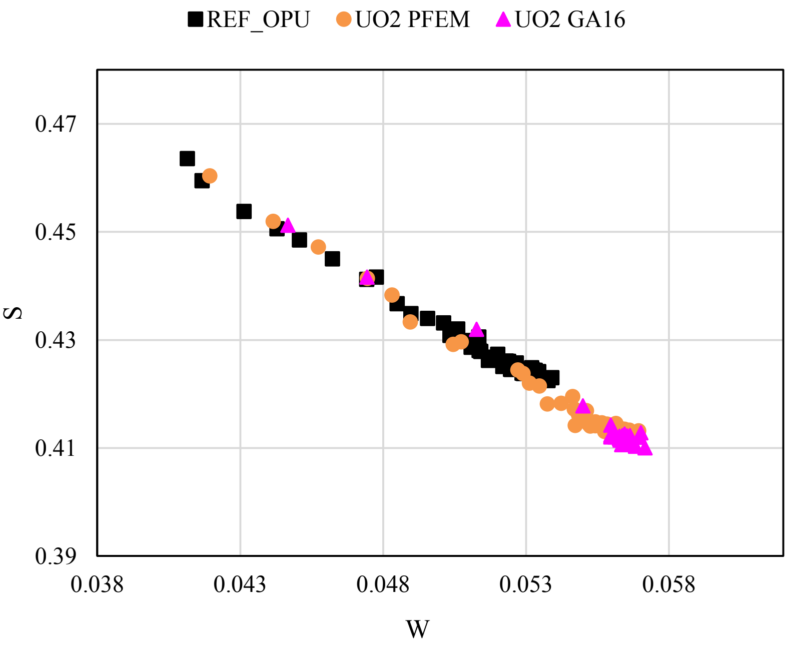

Figure 4.5: Low momentum fraction (S) as a function of high momentum fraction (W) for all energies (0.3 keV to 25 keV).

Figure 4.5 shows S as a function of W at all positron energies. For all three samples, the data points line up on a straight line indicating that positrons annihilate in one of two states. Based on Figure 4.5, the two annihilation states may be thought as corresponding to the bulk and the surface of the material. We have modelled using VEPFIT the experimental data with two homogeneous layers. The effective positron diffusion lengths derived from this analysis are as follows: 6.23±1.4 nm for UO_2_GA16, 9.26 ±0.2 nm for UO_2_PFEM, and 17.38 ±0.2 nm for REF_OPU.

4.3.1.2 Effect of humidification during annealing

Figure 4.4 shows the low and high momentum fractions as a function of energy for the reference sample we prepared and that used as reference in previous studies (Barthe et al., 2004; Labrim et al., 2006), and indicates that the former (UO_2_PFEM) has characteristics that are slightly but detectably different from the latter (UO_2_GA16). One should note that the reference sample in this study was annealed in a dry mixture of argon and 5% hydrogen whereas the reference sample from previous studies was annealed in a humidified mixture. The obvious conclusion is that the oxygen partial pressures which prevailed during annealing of both these reference samples were sufficient to induce the microstructural changes picked up by PAS.

One can estimate the relative oxygen interstitial concentrations from annealing conditions. Ideally, annealing would be carried out with an *in situ* measurement of the oxygen partial pressure. Failing this, we can estimate the thermodynamic conditions hence the expected deviations-from-stoichiometry both conditions led to.

In Labrim's study, annealing was carried out with a water vapour pressure of approximately 10^{-3} atm (Labrim, 2006; Labrim et al., 2006). In our case, typical water vapour pressure values for Ar 5%H_2 mixtures are in the region of $2 \cdot 10^{-5}$ atm. The final deviation from stoichiometry of the sample is fixed during the cooling stage and is determined by the temperature at which the material effectively "freezes out", i.e. when the temperature is low enough for solid-gas exchanges to cease. That temperature is probably in the region of 1300 ℃ but we do not need to know it for the ratio of interstitial concentrations corresponding to the two annealing conditions to be estimated. The ratio of oxygen partial pressures at which the samples freeze out is given by the square of the water vapour pressure ratios ($(10^{-3}/2 \cdot 10^{-5})^2 \approx 2500$). Now the interstitial concentration can be estimated from the following relationship (Garcia et al., 2017):

$$\frac{[O_i''] \cdot h^{\circ 2}}{\sqrt{p_{O_2}}} = K(T) \tag{4.1}$$

Where $[O_i'']$ is the oxygen interstitial concentration, h° is the hole concentration, p_{O_2} is the oxygen partial pressure, and K(T) is the temperature-dependent equilibrium constant for oxidation at low oxygen content.

Because both types of samples contain very low impurity concentrations, the hole concentrations can be regarded as a thermodynamic temperature-dependent function. Equation (4.1) shows therefore that the ratio of oxygen interstitial concentrations following annealing is **proportional to the ratio of water vapour pressures *i.e.* 50 (square root of 2500). So the differences observed in Figure 4.4 between our reference sample and that of previous studies could correspond to the latter sample being more oxidised. Deviation from stoichiometry in the latter is expected to be greater than in the former by a factor of 50**.

4.3.1.3 Effect of gas mixture used

Regarding annealing conditions, the question has arisen in the past about the effect hydrogen (used during annealing) could have on positron annihilation characteristics (Barthe et al., 2004). The authors compared the effect of annealing at 400 ℃ in vacuum and in hydrogen and concluded, based on high/low momentum annihilation fractions that hydrogen could permeate through the material and end up being trapped in vacancy defects effectively making PAS oblivious to them. In order to check that there was no such effect in our study, we annealed samples using both H_2O/H_2 and CO/CO_2 equilibria but under identical oxygen partial pressures leading to an oxygen to metal ratio of 2.042. The S and W results are indicated in Figure 4.6, and show that S and W fractions for these two samples at all energies are identical. **This suggests that we are characterizing annihilation characteristics that are only dependent upon extensive thermodynamic quantities**.

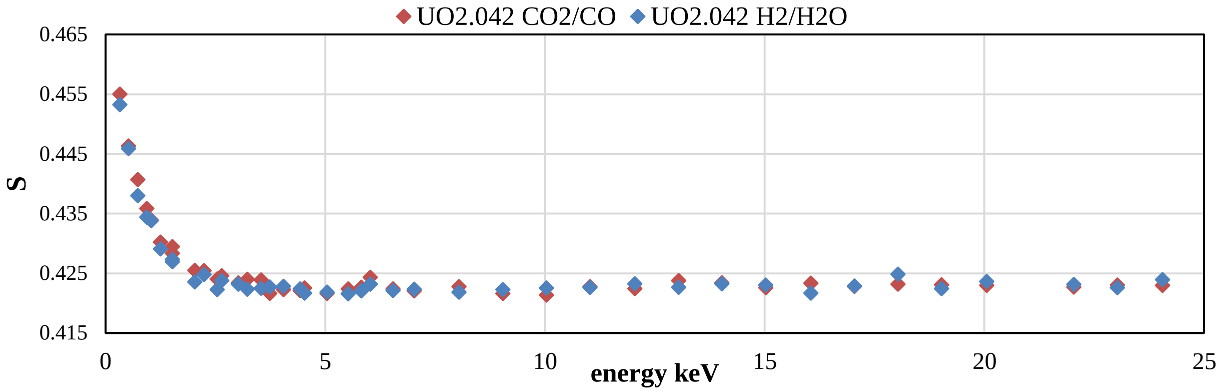

a) S(E) of two UO$_{2.042}$ measured at 300 K

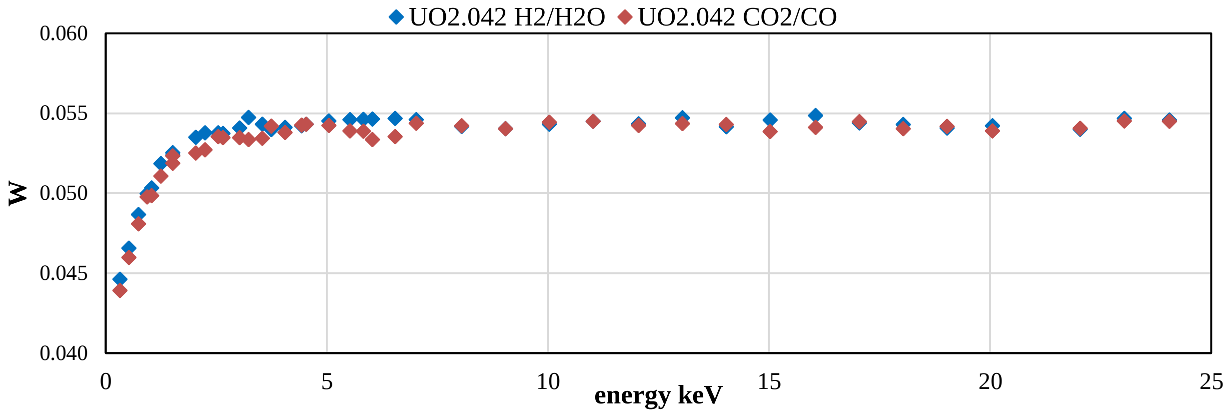

a) W(E) of UO$_{2.042}$ measured at 300 K

Figure 4.6: Positron momentum distribution fractions of two UO$_{2.042}$ prepared under different gas equilibria

4.3.1.4 Polishing induced damage and annealing thereof

Figure 4.4 also shows that the as-polished material has a higher value of S in the bulk and at the surface than the annealed samples indicating that polishing damage extends into the bulk to at least 1.3 µm (see Figure 2.19, section 2.5.3.2). This damage is probably in part due to dislocations that form below the surface. We have seen in section 1.3.3 that dislocations constitute regions of the material where tensile areas develop of low electronic density that PAS can detect. Labrim and co-workers have shown that annealing at 1700 ℃ is sufficient to eliminate this damage (Labrim, 2006).

4.3.1.5 Conclusions

In conclusion, we can state that although our sample preparation protocol is slightly different from the one used previously, it leads to microstructures or at least annihilation characteristics that are similar to those of samples used as reference in previous work. In order to be able to compare our high and low momentum fractions to those of previous studies, we have chosen to normalise all values to reference UO$_2$_GA16.

Having looked into the effect of sample preparation and experimental conditions, we now turn to the relationship between positron annihilation characteristics and how they are influenced by the presence of oxygen or uranium defects

4.3.2 Effect of oxygen interstitial ions in UO_{2+x}

The $UO_{2.042}$ sample was characterized by Doppler broadening spectroscopy before, during and following annealing at 750 K in high vacuum (roughly 10^{-7} Pa). Figure 4.7.a shows the low and high momentum fractions as a function of positron energy (0.5 keV to 25 keV). The (W,S) plot is shown in Figure 4.7.b. There are definite differences between the low momentum annihilation fractions before, during and following annealing. The higher value determined at high temperature is no doubt related to a thermal expansion effect. As will be seen later, this particular sample is proven to contain a uranium vacancy-type defect. Thermal expansion will lead positrons trapped in those vacancies to sample a greater volume at high temperature than they would at low temperature. Hence an increase in S is expected as it is less probable that they will annihilate with core electrons (Tuomisto and Makkonen, 2013).

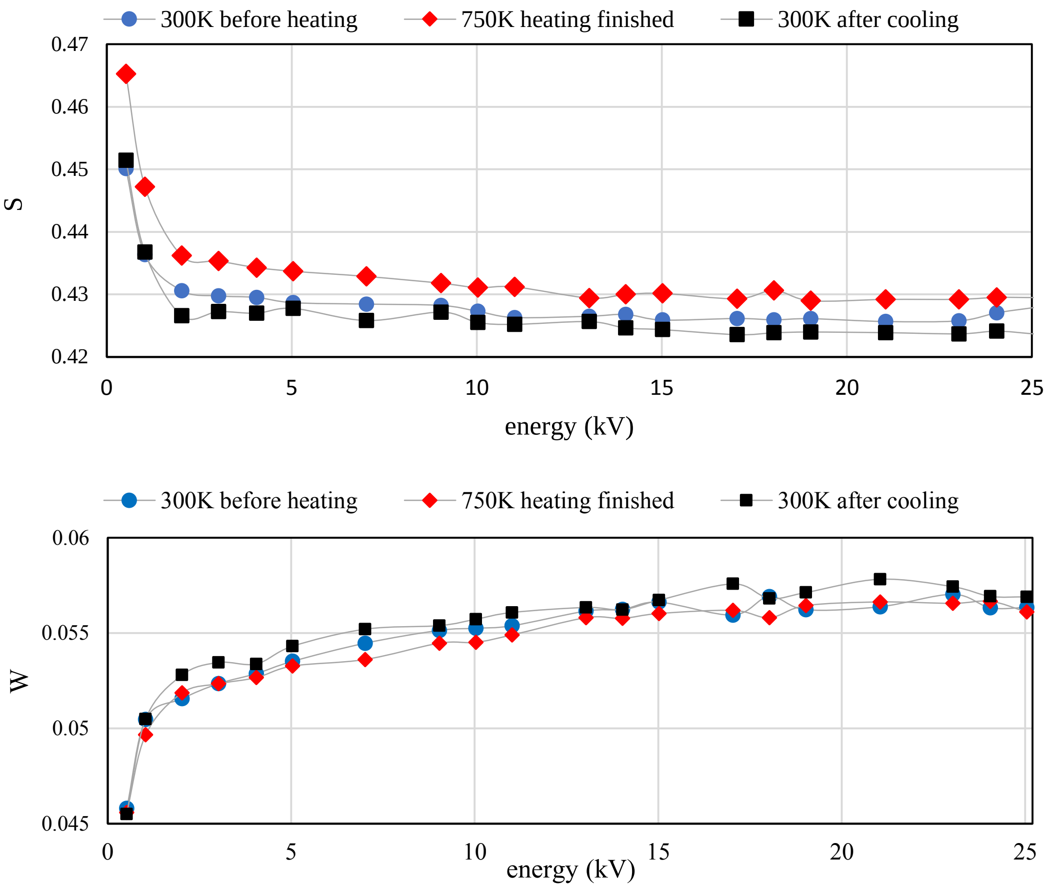

a) S(E) and W(E) of $UO_{2.042}$ measured at 300 K, then heated to 750 K and then cooled to 300 K again.

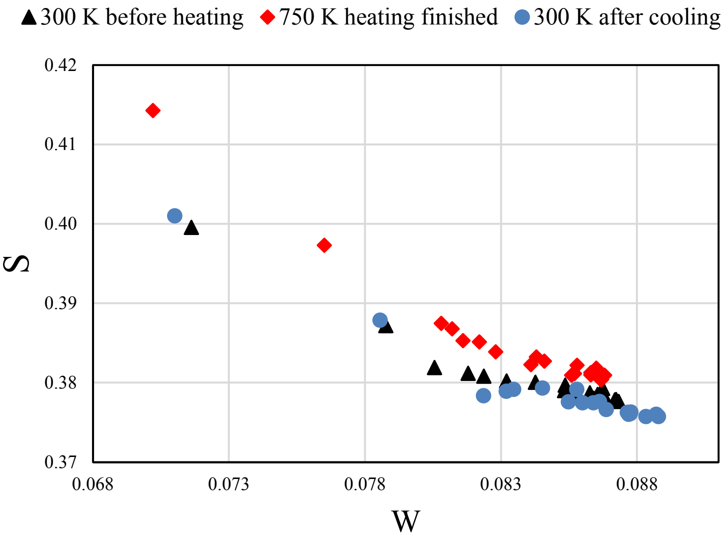

b) S(W) of $UO_{2.042}$ at 300 K before heating, 750 K and 300 K after cooling.

Figure 4.7: Temperature-dependent annihilation characteristics of $UO_{2.042}$

However, in addition to this effect, S values measured at room temperature following annealing, lie below the corresponding values prior to annealing, indicating a possible change in the microstructure. Indeed, the residual oxygen pressure in vacuum could be sufficient to slightly oxidize the sample. It is worth drawing a parallel between this observation and the fact that, as Figure 4.3 shows, the S values (resp. W) for UO_{2+x} (UO_2_GA16), $UO_{2.002}$, $UO_{2.007}$, $UO_{2.012}$, $UO_{2.21}$, are lower (resp. higher) than that of our reference sample (UO_2_PFEM). As seen in section 4.3.1.2, our reference sample would appear therefore to contain the lowest oxygen interstitial concentration. This is also reflected in the effective positron diffusion lengths provided in 4.3.1.1. The value determined for UO_2_PFEM is consistent with the literature (Barthe et al., 2007). Positrons diffuse over a smaller distance in UO_2_Ga16 than in UO_2_PFEM as the former one is expected to contain negative interstitial ions that positron can easily trap and annihilate with.

Although all samples have not been characterized with lifetime spectroscopy, the $UO_{2.002}$ (167.4 ±0.4 ps) and $UO_{2.21}$ (171.3 ±0.4 ps) samples show only a single lifetime component similar to the lifetime corresponding to the UO_2 lattice (169 ±1 ps) (see section 4.2.2). This indicates these samples contain a single type of defect related to oxygen interstitials. Recently, Wiktor and co-workers calculated the effect on the momentum distribution of the presence of negatively-charged oxygen interstitials. Although they encountered difficulties relating to non-physical localization effects they found qualitatively that **the annihilation fraction with valence electrons goes down slightly whereas the annihilation fraction with core electrons goes up substantially**. This theoretical result corroborates our observations.

Note also that for the lower deviation-from-stoichiometry values (e.g. 0.002, 0.007, 0.012), interstitial oxygen ions may remain isolated as suggested by neutron diffraction studies in Chapter 3, and electrical conductivity measurements (Garcia et al., 2017). Thus, when positrons are trapped in these low energy (Rydberg) states, they are still interacting with the electronic density of the lattice (Tuomisto and Makkonen, 2013), and their annihilation characteristics are similar to that of the lattice. This does not apply to the low-temperature-annealed (900 ℃) $UO_{2.21}$ sample, which shows a substantially different momentum distribution. In this case, oxygen defects tend to form large, regularly-spaced clusters. As a result, the core electron density increases substantially, and this feature stands out in the momentum distribution.

In relation to this issue, two additional points may be made:

- It is actually a very general rule that the high momentum distribution changes reflect the change in chemical environment (Tuomisto and Makkonen, 2013). Wiktor's work (Wiktor et al., 2017) shows this indeed applies to UO_2 (see above comment about effect of oxygen interstitials on S and W). **It is not surprising therefore that oxidation translates as a low S(W) slope in Figure 4.3**.
- The lifetime component of the three samples, UO_2, $UO_{2.002}$, and $UO_{2.21}$ are quite similar, because lifetime is much less sensitive to the chemical environment than to the volume of vacancy defects (Puska and Nieminen, 1994; Tuomisto and Makkonen, 2013).

Oxidation modifies Doppler broadening characteristics but less so in the low-deviation from stoichiometry region than in the high. We also confirm that chemical effects are indeed better characterised by Doppler broadening spectroscopy (Tuomisto and Makkonen, 2013). In the next section, we focus more on lifetime measurements which are more explicitly correlated to the presence of vacancy defects.

4.3.3 Effect of vacancy-type defects in UO_{2+x}

Samples with deviations-from-stoichiometry between 0.002 and 0.16 were annealed at the same temperature (1623 K) and so are expected to contain an increasing quantity of uranium vacancies (see chapter 1). Beyond an x value of 0.012, the low momentum fraction increases substantially as seen in Figure 4.8. An increase in S is expected when vacancy-type defects are present because positrons are trapped over longer periods in these defects and this reduces the probability of them annihilating with core electrons. The reason why the $UO_{2.002}$ sample appears to contain such small quantities of uranium vacancies could be due to the fact that a change in stoichiometry from 2.002 to 2.03 at 1350 ℃ corresponds to a six order of magnitude increase in oxygen partial pressure. Assuming the uranium vacancy concentration is proportional to the oxygen partial pressure (Dorado et al., 2012), this change in conditions would lead to a six order of magnitude increase in the vacancy concentration. It should also be noted that the positron lifetime spectroscopy is only sensitive to vacancies in a narrow range of concentrations spanning one or two orders of magnitude at the most. According to Tuomisto (Tuomisto and Makkonen, 2013), in semi-conductors this range is between 10^{16} and 10^{18} vacancies/cm^3 and is dependent upon whether vacancies are charge or not.

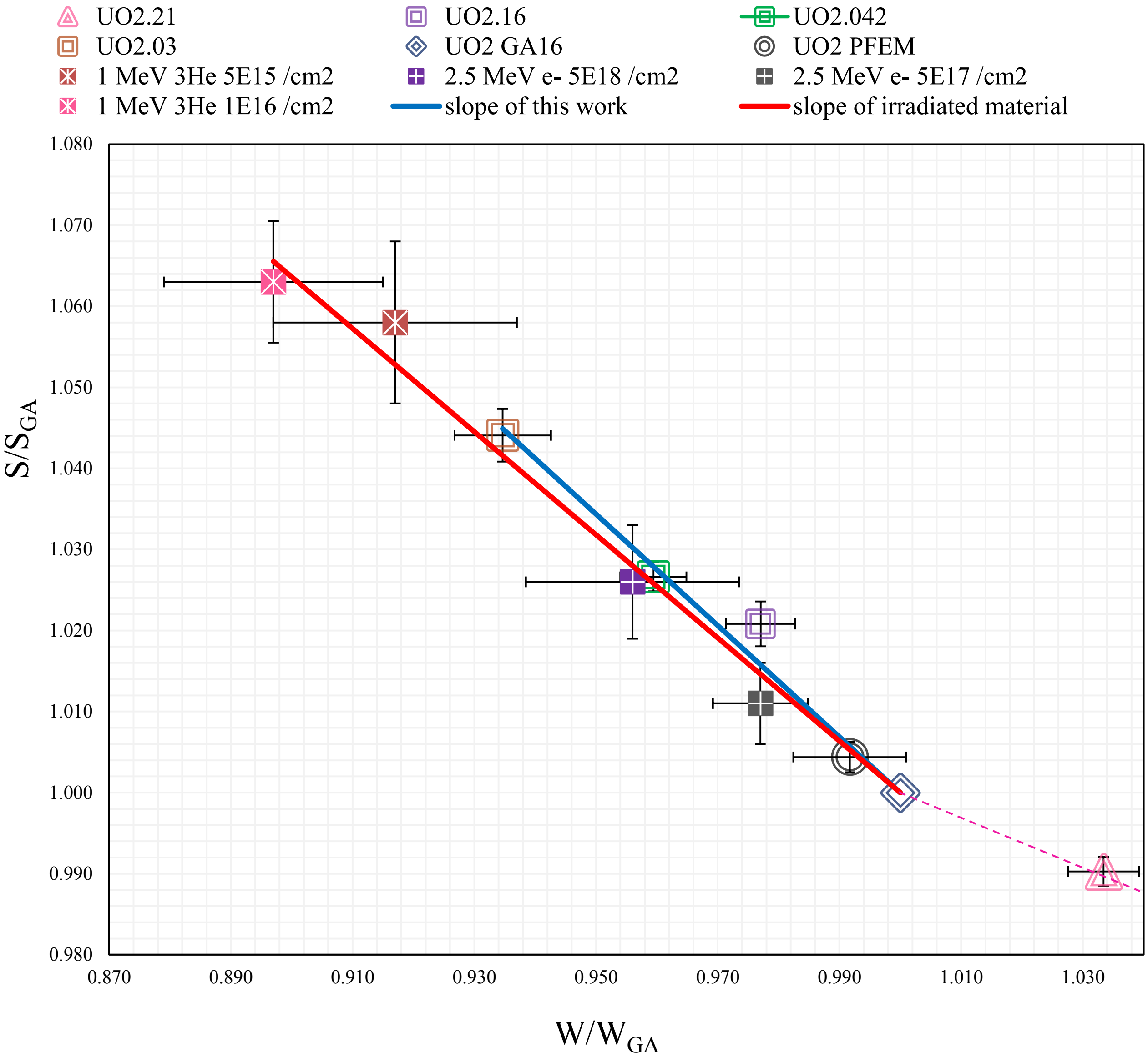

Figure 4.8: S(W) of UO_{2+x} normalised to UO_2 in comparison to the reported S(W) slope in relation to vacancy defects in irradiated material (Labrim, 2006).

Figure 4.8 shows our high deviation-from-stoichiometry data points along with data points corresponding to materials irradiated with ions or electrons reported in (Labrim, 2006). We have also plotted the lines that supposedly characterize the defects these materials contain. **Both slopes, for our equilibrated material and for irradiated material, are very similar** (resp. 0.69±0.03, 0.64±0.03). Amongst the higher deviation-from-stoichiometry samples, i.e. above $UO_{2.012}$, the lifetime spectra were characterized in $UO_{2.042}$ and $UO_{2.16}$. In both these samples (see Table 4.1), two components were resolved: one short lifetime component corresponding to the lattice (170 ±0.1 ps), and one long lifetime component presumably corresponding to a vacancy defect (316.5 ±1.5 ps, and 315.6 ±1.6 ps). As seen in Chapter 1 section 1.3.3, from a combination of experimental and theoretical considerations, the authors concluded that the defects they were dealing with in irradiated samples were neutral Schottky trios characterized by a long lifetime component of 317 ±2 ps. Figure 4.9 shows a comparison of the lifetime spectra of the 45 MeV α-irradiated sample (Labrim, 2006) and our $UO_{2.042}$ sample, indicating defects of similar nature are present in similar quantities.

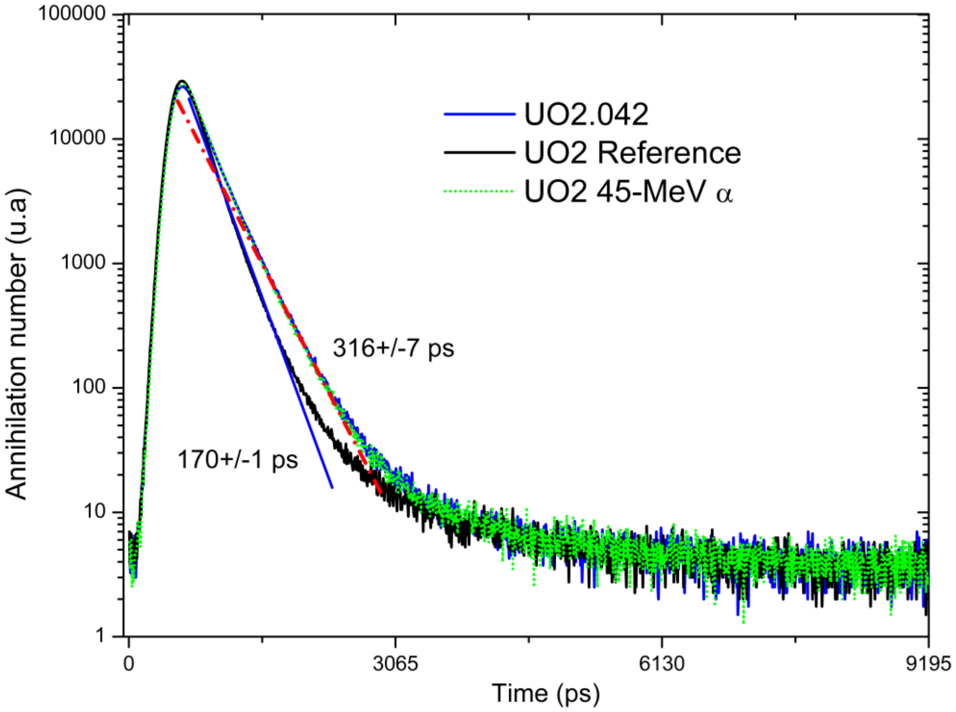

Figure 4.9: Lifetime spectra of UO_2 (solid black line), $UO_{2.042}$ (solid blue line), and 45 MeV α-particle irradiated UO_2 (dotted green line). The straight lines represent the lifetime components resolved from the spectra.

Although the similarities between the two samples are striking, we believe that the vacancy-type defects in the irradiated and oxidized sample could be different. Firstly, the fact that the second, long lifetime component is similar does not constitute a proof in itself that we are dealing with identical defects. Wiktor has shown (Wiktor et al., 2014) that irrespective of the complexity of the defect, when the defect contains a single uranium vacancy, positrons localise there. As a result, it is difficult to discriminate amongst defects, e.g. mono or tri-vacancies, based solely on the long lifetime component value.

There are two particular features which we would like to discuss in relation to lifetime and Doppler broadening spectroscopy results. The first concerns the fact that the average lifetime of sample $UO_{2.16}$ is less than the lifetime of sample $UO_{2.042}$ as a result of the intensity of the second lifetime component, which presumably corresponds to the presence of uranium vacancies (both neutral and negatively charged), being less in the higher deviation from stoichiometry sample. This would seem to contradict the fact that the vacancy concentration is an increasing function of non-stoichiometry. Indeed when a single vacancy type defect exists, the average lifetime is expected to change monotonously over a limited vacancy concentration range, from that of the lattice to a higher value intermediate between the vacancy type defect lifetime component and that of the lattice (Krause-Rehberg and Leipner, 1999b;

Tuomisto and Makkonen, 2013). Our observation may be rationalised using a three-component trapping model in Chapter 2 section 2.5.5. In this model (see equation (2.63) in section 2.5.5), the average lifetime may be expressed as the weighted lifetimes of the lattice, vacancy (uranium vacancy in our case) and shallow traps / Rydberg states (negatively charged excess oxygen ions). The weights are the respective fractions I_i of positrons annihilating in those three different states. Further, it is reasonable to assume that the lifetime corresponding to shallow traps is very close to that of the lattice (as the lifetime for sample $UO_{2.21}$ is virtually identical to that of UO_2). So the average lifetime for the $UO_{2.04}$ or $UO_{2.16}$ samples may be written as:

$$\tau_{avg} = (1 - I_V)\tau_L + I_V \tau_V \tag{4.2}$$

Our lifetime spectrum analysis indicates that both samples ($UO_{2.042}$ and $UO_{2.16}$) have identical lifetime components so that a decrease in τ_{avg} must stem from a decrease in I_V. I_V is proportional to the vacancy trapping rates κ_V (that appear in equations (2.51) and (2.52) in section 2.5.5), which is the product of the vacancy concentration c_V and trapping coefficient μ_V (see equation (2.54) in section 2.5.5). This must still hold albeit with average values when different vacancies, e.g. with different charge states, coexist. Because lifetime is not strongly dependent upon charge state, the difference in I_V must come from a difference in trapping coefficients μ_V. This could indeed be the case. As deviation from stoichiometry increases, the charge of vacancies is expected to change from their value expected in a purely ionic model (-4) to -3, -2 or possibly 0 (Crocombette, 2012). We also know from Puska (Puska et al., 1990) that the trapping coefficient of vacancies is strongly dependent upon charge state (much less for neutral vacancies than for negatively-charged vacancies). In conclusion, it is reasonable to think that the observed decrease in average lifetime with increased deviation from stoichiometry reflects an increase in the proportion of neutral vacancies to the detriment of charged vacancies.

The second observation concerns the gradual decrease in S (respectively increase in W) as the stoichiometry of the material goes from 2.03 to 2.16 and finally 2.21. We wish to understand why this quantity decreases. Applying the three-state trapping model again, this time to the low S and high W momentum fractions yields:

$$S|W = f_L S_L|W_L + f_{V_{-}^{*}} S_{V_{-}^{*}}\big|W_{V_{-}^{*}} + f_{V_0} S_{V_0}\big|W_{V_0} + f_{ST} S_{ST}|W_{ST} \tag{4.3}$$

One can assume that f_L is proportional to the volume fraction of non-oxygen-defective material so that as the stoichiometry increases (since the material is characterised at room temperature) this volume fraction is equivalent to that of UO_2 with the complementary fraction corresponding to the volume fraction of U_4O_9. Equation (4.3) becomes:

$$S|W = \alpha\, f_{UO2} S_L|W_L + f_{V_{-}^{*}} S_{V_{-}^{*}}\big|W_{V_{-}^{*}} + f_{V_0} S_{V_0}\big|W_{V_0} + \beta(1 - f_{UO2}) S_{ST}|W_{ST} \tag{4.4}$$

, where α and β are stoichiometry independent constants and f_{UO2} is the volume fraction of UO_2 at room temperature for the given deviation from stoichiometry of the sample.

Note there is no reason why S_L or W_L should change or indeed why S_{ST} or W_{ST} should change either with increasing deviation from stoichiometry. Regarding S_{V-} and S_{V0}, Wiktor's calculations indicate that the momentum distribution ratio curves assuming neutral and -4 charged uranium vacancies are identical (Wiktor et al., 2017). Equation (4.4) may be simplified further:

$$S,W = \alpha\, f_{UO2}S_L,W_L + (f_{V_{-}^{*}}+f_{V_0})\, S_V,W_V + \beta(1-f_{UO2})S_{ST},W_{ST} \qquad (4.5)$$

f_V may decrease a little with increasing deviation-from-stoichiometry in proportion to the intensity changes highlighted from the average lifetime changes previously alluded to.

f_{ST} will rise with increasing deviation from stoichiometry but the value of S obtained for the highest deviation-from-stoichiometry sample ($UO_{2.21}$) which contains no detectable uranium vacancies can be regarded as reflecting the presence of ordered cuboctahedra (Bevan et al., 1986). These cuboctahedra correspond to oxygen chemical environments that are substantially different from those encountered in the low deviation from stoichiometry material.

In conclusion one can say, based on equation (4.5), that the decrease in S and corresponding increase in W at high deviation from stoichiometry results from momentum distribution modifications characteristic of oxygen defect clusters. It would further greatly advance the interpretation of these experimental data if momentum distribution ratios of these cluster types were modelled from first principles.

4.3.4 Consistency between positron trapping model and estimated defect concentration

4.3.4.1 Introduction

The aim of this section is not to determine accurate values for defect concentrations but to check whether we can estimate defect concentrations using reasonable parameters for the three-state trapping model (see section 2.5.5). To this end, we are going to use the lifetime measurements obtained at 35 K and 300 K for $UO_{2.042}$ and $UO_{2.16}$ (see section 4.2.2).

4.3.4.2 Estimates of characteristics positron /material- related parameters

The model covers essentially three types of defects: negatively charged oxygen interstitials, neutral and negatively charged uranium vacancies. Note that the long-range Coulomb potential sensed by positrons at negatively charged defects is assumed to induce Rydberg states. A fully quantitative approach may not be adopted here because the trapping coefficients for our material are not known from lack of both theoretical and experimental studies, but we assume for all negatively charged defects a $T^{-\frac{1}{2}}$ dependence of the trapping coefficients. The trapping coefficients for shallow traps, e.g. oxygen interstitials, provided in literature are in the following range: $7{\cdot}10^{15}$ to $1{\cdot}10^{18}$ s^{-1} at 20 K (Krause-Rehberg and Leipner, 1999b). The trapping coefficients reported for neutral and negatively charged vacancies range from 10^{14} to 10^{17} s^{-1} at 20 K (Krause-Rehberg and Leipner, 1999b; Puska et al., 1990; Tuomisto and Makkonen, 2013). The trapping coefficient estimated from theory and widely used for a neutral vacancy defect is 10^{15} s^{-1}. We consider the binding energy of positrons to interstitial defects is at least 0.3 eV, and the binding energy at Rydberg states is approximately 10 meV (Krause-Rehberg and Leipner, 1999b). The positron lifetimes for the lattice and the oxygen interstitial are approximately 170 ps as seen in section 4.2.2. For vacancy-type defects, we use the experimental values derived from the lifetime spectra, i.e. the long lifetime component. In addition, the oxygen interstitial concentration assumed is based on the fact that the basic oxygen cluster at the temperatures studied is the cuboctahedron cluster as described in Chapter 3 (Bevan et al., 1986).

4.3.4.3 Temperature dependence

We have two sets of lifetime data for $UO_{2.042}$ obtained at two extreme temperatures (35 K and 300 K). Figure 4.10 shows the average, long and short lifetime components and the long lifetime intensity calculated using the three-state trapping model in comparison to the experimental data. These model results were obtained with the physical quantities presented in Table 4.3.

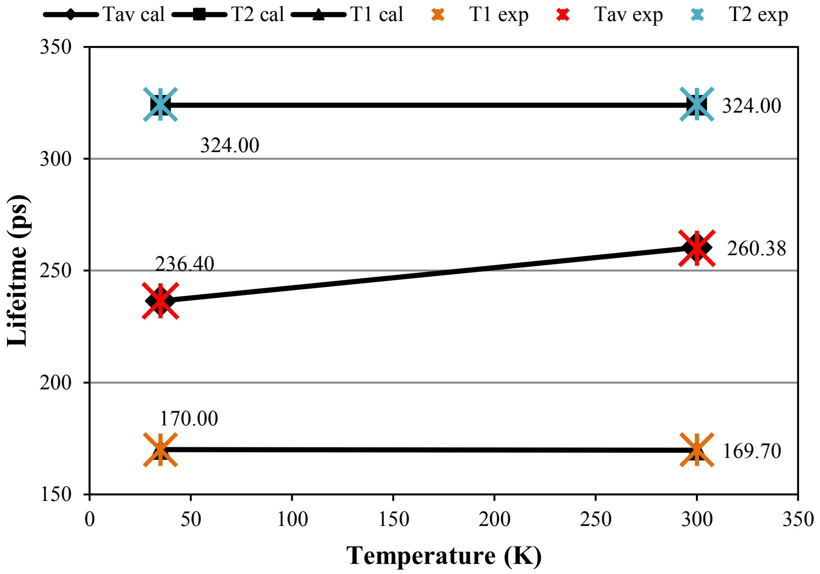

a) Positron lifetimes measured for $UO_{2.042}$ (coloured symbols) and calculated using a positron trapping model at 35 K and 300 K (black symbols and lines). Tav: average positron lifetimes; T1: short lifetime components; T2: long lifetime components. The figures next to the symbols are the calculated values of positron lifetime.

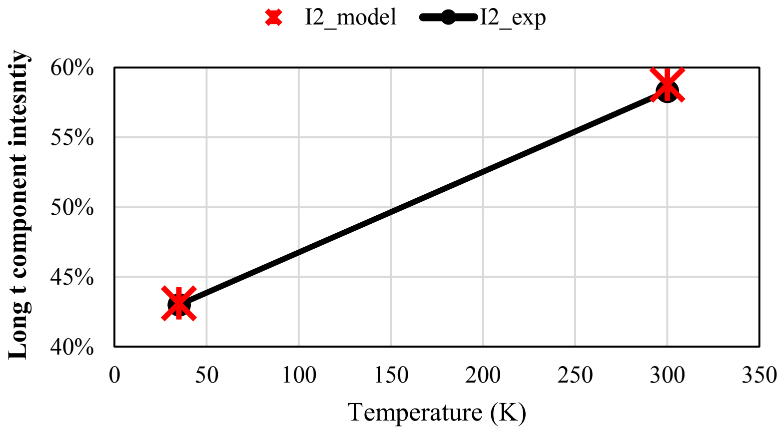

b) Intensity for the positron long lifetime component. Red symbols are the experimental value; black symbols and line is the model.

Figure 4.10: Positron lifetime measured at 300 and 35 K for $UO_{2.042}$ and fitted using the positron trapping model presented in section 2.5.5.

Table 4.3: Trapping coefficients μ at 20 K and estimated defect concentrations c for $UO_{2.042}$ at 35 K and 300 K. The density of $UO_{2.042}$ is $7.43 \cdot 10^{22.}$ atm/cm^3. V_0 represents neutral vacancy, V_-^* represents negatively charged vacancy, and ST represents oxygen interstitial defects. R, V^- represents the Rydberg state for negatively charged vacancy defects.

μ_{V_0} (s^{-1})	$\mu_{V_-^*}$ (s^{-1})	μ_{ST} (s^{-1})	35 K	c_{V_0}(cm^{-3})	$c_{V_-^*}$(cm^{-3})	c_{ST}(cm^{-3})
$1 \cdot 10^{15}$	$4 \cdot 10^{17}$	$4 \cdot 10^{16}$		$5.0 \cdot 10^{19}$	$1.2 \cdot 10^{19}$	$1.6 \cdot 10^{20}$
μ_{R,V^-} (s^{-1})	$\tau_{V_-^*} \vert \tau_{V_0}$ (ps)	ϑ (s^{-1})	300 K	c_{V_0}(cm^{-3})	$c_{V_-^*}$(cm^{-3})	c_{ST}(cm^{-3})
$3 \cdot 10^{15}$	324	$1 \cdot 10^{11}$		$4.0 \cdot 10^{19}$	$2.2 \cdot 10^{19}$	$1.6 \cdot 10^{20}$

This set of parameters provides values for the total uranium vacancy concentration that does not depend upon temperature. The trapping coefficients for oxygen interstitials and neutral uranium vacancies at 20 K are the same as in Wiktor's study (Wiktor et al., 2014). One must point out that the trapping coefficient for negatively charged vacancies at 20 K is one order of magnitude above the value used by Wiktor. However, this value is in the range of recommended values for semi-conductors (Puska et al., 1990). This highlights the need for some independent evaluation of this quantity if PAS is to be used to estimate defect concentrations.

4.3.4.4 Stoichiometry dependence

We also applied the trapping model to interpret the lifetime data for $UO_{2.042}$ and $UO_{2.16}$ obtained at 300 K. Figure 4.11 shows the average, long and short lifetime components and the long lifetime intensity calculated using the three-state trapping model in comparison to the experimental data. These model results were obtained with the physical quantities presented in Table 4.4.

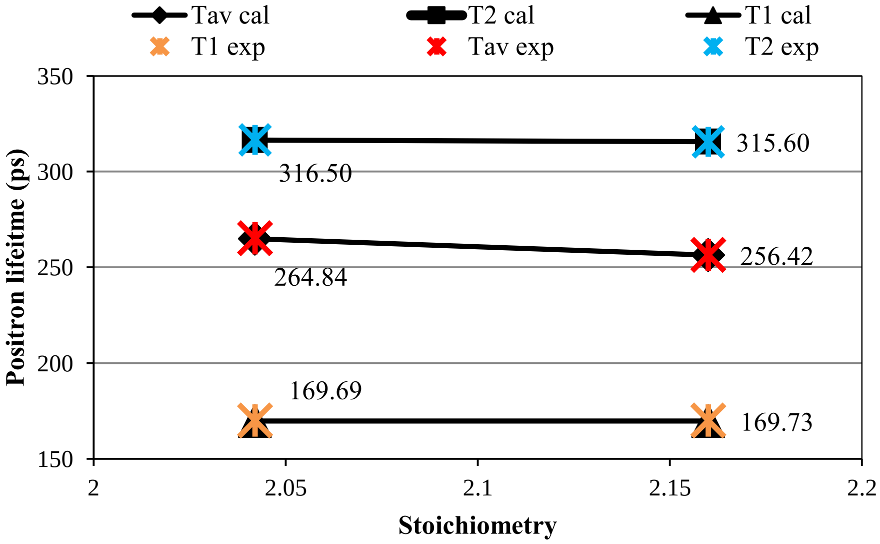

a) Positron lifetimes measured for $UO_{2.042}$ (colour dots) and calculated using a positron trapping model at 35 K and 300 K (black line). Tav: average positron lifetimes; T1: short lifetime components; T2: long lifetime components. The figures next to the symbols are the calculated values of positron lifetime.

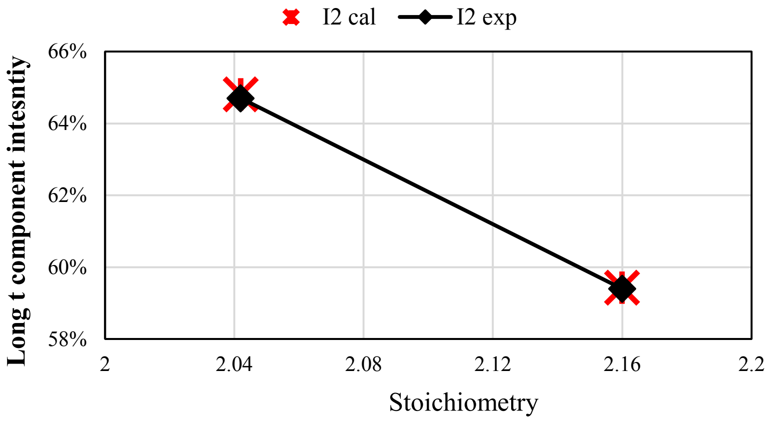

b) Intensity for the positron long lifetime component. Red symbols correspond to the experimental value; black line and symbols is the model.

Figure 4.11: Positron lifetime measured for $UO_{2.042}$ and $UO_{2.16}$ at 300 K using the three-state positron trapping model

Table 4.4: Trapping coefficients μ at 20 K and estimated defect concentrations c for $UO_{2.042}$ and $UO_{2.16}$ at 300 K. The densities of $UO_{2.042}$ and $UO_{2.16}$ are $7.43 \cdot 10^{22}$. and $7.72 \cdot 10^{22}$ atm/cm^3. V_0 represents neutral vacancy, V_-^* represents negatively charged vacancy, and ST represents oxygen interstitial defects. R, V^- represents the Rydberg state for negatively charged vacancy defects.

μ_{V_0} (s^{-1})	$\mu_{V_-^*}$ (s^{-1})	μ_{ST} (s^{-1})	2.042	c_{V_0}(cm^{-3})	$c_{V_-^*}$(cm^{-3})	c_{ST}(cm^{-3})
$1 \cdot 10^{15}$	$4 \cdot 10^{17}$	$4 \cdot 10^{16}$		$2.8 \cdot 10^{19}$	$2.7 \cdot 10^{19}$	$1.5 \cdot 10^{20}$
μ_{R,V^-} (s^{-1})	$\tau_{V_-} \vert \tau_{V_0}$ (ps)	ϑ (s^{-1})	2.16	c_{V_0}(cm^{-3})	$c_{V_-^*}$(cm^{-3})	c_{ST}(cm^{-3})
$3 \cdot 10^{15}$	316	$1 \cdot 10^{11}$		$1.0 \cdot 10^{20}$	$6.7 \cdot 10^{19}$	$4.7 \cdot 10^{20}$

The positron trapping coefficients used for various states at 20 K are the same as in the previous model. The estimated total vacancy and interstitial concentrations for $UO_{2.042}$ at 300 K are consistent with the estimates in the previous application. As the stoichiometry increases to 2.16, the population of both oxygen interstitials and total vacancies rises.

4.4 Conclusion and prospects

We have carried out Doppler broadening and lifetime spectroscopy measurements on UO_2 and UO_{2+x} samples, mainly at 300 K but also at 35 K and 750 K, to study both uranium and oxygen defects. The hyper-stoichiometric samples were obtained from high-temperature controlled oxidation experiments and were quenched from a temperature at which the uranium sublattice is expected to be sensitive to thermodynamic conditions.

The Doppler broadening spectroscopy results show that the (W, S) data points are on a line which is very similar to that determined for irradiated UO_2 and which was interpreted as being characteristic of a neutral Schottky trio (Wiktor et al., 2014). These results are also consistent with the positron lifetime measurements at 300 K as the long lifetime component which appears in samples with deviations from stoichiometry above 2.03-2.04 is equivalent to that observed in irradiated material, i.e. roughly 316 ps. Despite the similarities between equilibrated and irradiated samples, there is still doubt as to whether the detected uranium vacancy defects are indeed neutral Schottky trios since their concentration is expected not to be deviation from stoichiometry dependent.

Amongst the more striking results in this study is the fact that increasing stoichiometry appears to induce a decrease in the low momentum annihilation fraction S and an increase in the high momentum annihilation fraction W in line with preliminary results from first principles calculations. The study of a sample oxidised at a temperature below which the cation sublattice is expected to be insensitive to temperature and oxygen activity, confirms that Doppler broadening spectroscopy is more sensitive to chemical environment around oxygen defects. By chemical environment one is specifically alluding to the typical oxygen clusters that are known to appear in hyper-stoichiometric material and discussed in chapter 3.

For samples in which a uranium type vacancy defect is detected, we have applied the so-called three-state trapping model. It is possible to interpret the results using trapping coefficient values that are consistent with values obtained in other semiconductors. This analysis enables estimates to be made of defect concentrations that suggest that although constituting the minority cation defect, negative uranium vacancies are present in addition to neutral vacancies. This analysis is also consistent with the fact that the fraction of neutral vacancies increases with increasing deviation from stoichiometry.

The overall picture that emerges from this PAS study confirms the expected complexity of a material in which defect charge states and compositions are very much dependent upon temperature and non-stoichiometry. The additional difficulty encountered in interpreting the Doppler broadening data for instance, lies in that uranium vacancy and oxygen clusters affect the low (resp. high) momentum annihilation fractions in opposite ways with different sensitivities (at different defect concentrations). As an example, the presence of uranium vacancies will have a tendency to increase S and that of oxygen clusters to decrease this quantity. Positron lifetime on the other hand appears to be insensitive to the presence of oxygen clusters but very sensitive to uranium vacancies. A number of different areas are now identified for future investigation which we organise in the following paragraph in different categories: further analysis of existing data, generation of new data, theoretical studies to complement this experimental approach.

Regarding the first category, one must note that the three-state model approach requires physical quantities, notably trapping coefficients that of the utmost importance and can be obtained from theory or experiment. The idea would be to analyse the Doppler broadening data at different deviations from stoichiometry in a way that is consistent with the trapping model, in order to determine annihilation fractions corresponding either to delocalised or localised states. These fractions could then be used in the lifetime analysis to limit the number of unknown quantities and could potentially provide improved estimates of defect concentrations. The second category of studies would first involve further characterisation of existing samples such as a systematic lifetime characterisation of all samples at 300 K, and a more systematic temperature dependent lifetime spectroscopy characterisation of samples in which a second lifetime component is detected. It is also clear that a systematic PAS characterisation of samples oxidised at lower temperatures is necessary as it would enable Doppler broadening of oxygen rich defects to be clearly separated from the signature of uranium vacancies.

Finally, regarding theoretical approaches, a number of suggestions can be made. The most significant should involve applying Fermi’s golden rule to the study of trapping mechanisms hence coefficients associated with different types of charged defects (Puska et al., 1990). This would greatly reduce the uncertainties relating to trapping coefficients and, assuming the experimental approach is successful, would provide a counterpart to it. Other efforts should also be made with regard to the effect of oxygen defects and clusters upon the annihilating electron-positron pair momentum distribution. Even the study of neutral oxygen interstitials would be enlightening.

Chapter 5 A study of uranium self-diffusion

5.1 Introduction

Characterising cation defect properties is a complicated task because it involves much slower processes but also because the choice of property has to fall upon a physical quantity which is directly dependent upon the nature of cation defects (see Chapter 1). Uranium self-diffusion is one such property.

Although uranium diffusion involves defects in much smaller concentrations than those responsible for oxygen diffusion, it is essential to characterise this property because it is the rate-determining step for a variety of essential microstructural changes covering the whole range of the nuclear fuel cycle. Grain growth, sintering, dislocation movement as observed during stress and temperature induced deformation are examples of these. In fact it is thought that cation defect mobility is also key to understanding radiation induced changes in the fuel microstructure (Andersson et al., 2011). The uranium self-diffusion coefficient is a quantity implemented in fuel behaviour applications which enters into a number of physical models such as fission gas swelling. Using accurate values for it should be of invaluable help to make current applications such as ALCYONE more reliable and increase their predictive capability when used outside their validation domain.

The characterization of cation self-diffusion usually relies on the isotopic exchange methods in the solid-state with isotopic tracers such as ^{233}U, ^{235}U, ^{237}U for UO_2, and ^{238}Pu for $(U, Pu)O_2$ (Noyau, 2012; Noyau et al., 2012), *etc*. Isotopic tracer layers are first deposited at the surface of the sample which are then subjected to diffusion annealing. A variation on this method involves annealing diffusion couples made up of a depleted uranium oxide sinter and ^{235}U enriched powder. Two studies can be found in which this strategy is adopted (Nagels et al., 1966; Sabioni et al., 1998). Following diffusion annealing, the depth profile is normally obtained by techniques such as non-destructive α-particle counting, α- or γ- spectrometry when unstable isotopes are involved, and secondary ion mass spectrometry (SIMS) in the case of long-lived isotopes. Diffusion coefficients of cations are then derived from solving an *ad hoc* diffusion equation.

In this study, we aim to establish a method for determining uranium self-diffusion coefficients which we could further apply to measuring this quantity as a function of temperature and oxygen partial pressure. Ultimately, we aim to correlate cation self-diffusion to defect equilibria. Another issue of which little is known, is the role of grain boundaries in general and in the self-diffusion process in particular. To this end, it is essential to study poly-crystalline samples. We have also prepared poly-crystalline UO_{2+x} samples doped with trivalent additives (Cr_2O_3) in order to understand how dopants can modify defect equilibria and hence uranium self-diffusion.

Section 5.2 concerns the depth profiling procedures and how the depth resolution is determined. Section 5.3 reports the various depth profiles and associated sputtering rates obtained. In section 5.4 we model the depth profiles and discuss the diffusion coefficients derived therefrom in the light of previously published data.

5.2 Crater depth profiling and depth resolution

The uranium tracer (^{235}U) self-diffusion coefficient for a given sample is obtained by comparing the experimental depth profile to a model calculation involving the resolution of Fick's second law. The uncertainty associated with a diffusion coefficient will come from uncertainties in ^{235}U concentrations and the uncertainty related to depth. We have seen in the Chapter 2, section 2.6 that the former uncertainty was very small (around 0.1%). A special attention must therefore be paid to the depth resolution which constitutes the main source of error. During the experiment, the ^{235}U concentration profile of each crater is obtained from SIMS time-dependent signals. To correlate the depth with sputtering time, one needs to determine the sputtering rate (v_p) for each depth-profile analysis.

Assuming that the sputtering rate is constant in the sample, the relationship between crater depth (z) and sputtering time (t_s) may be expressed as follows:

$$z = v_p \cdot t_s \tag{5.1}$$

During the depth-profiling process, roughness develops at the bottom of the crater so that although the average sputtering rate remains constant it fluctuates locally from one analysis point at surface to the other. These variations have to be quantified so that the depth resolution may be estimated for each data point of the profile, which represents an average value. The depth resolution is obtained from an analysis of the crater images taken with the chromatic confocal microscope using a Monte-Carlo method.

As Figure 5.1 illustrates, two types of regions are selected to generate altitude distributions in regions located at the bottom and at the surface of the craters. Altitude data collected from four rectangular areas represent the surface of the sample. For the crater depth, a circular zone roughly 50 µm in diameter is selected in the centre of the crater (150 µm x 150 µm). This guaranteed a conservative estimate of the resolution to be derived as this area necessarily includes the central area where the SIMS signals originate (i.e. a 30 µm circular zone).

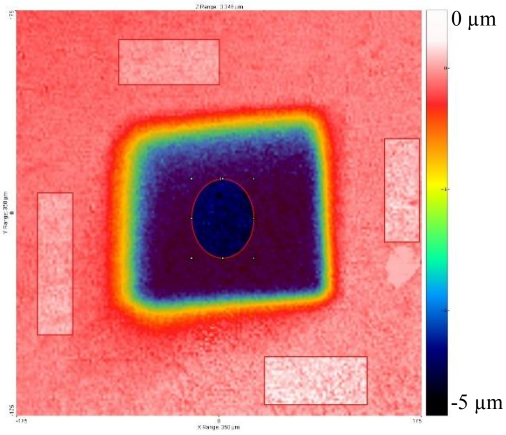

a) Colour coded image of one crater on a single-crystal sample

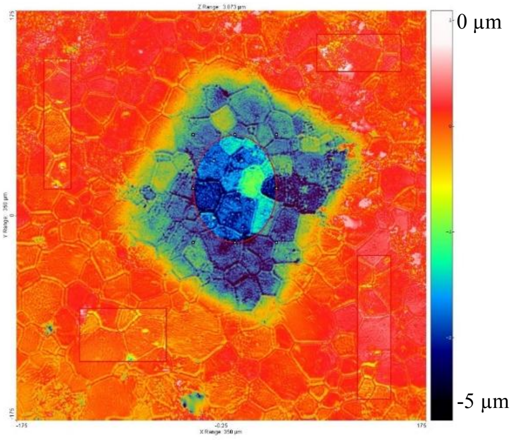

b) Colour coded image of one crater on a small-grain poly-crystalline sample

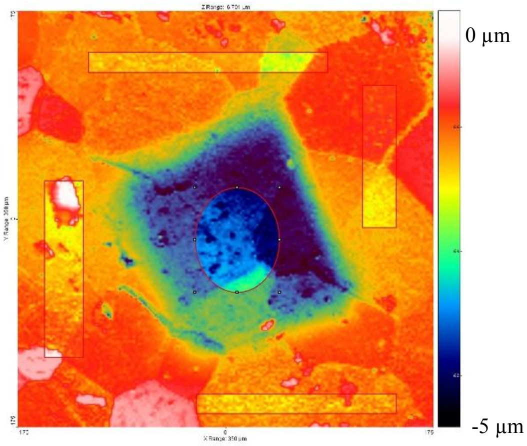

c) Colour coded image of one crater on a Chromium-doped UO_2

Figure 5.1: Altitude maps of typical craters in both a) single-crystal and b) poly- crystalline undoped specimens and c) Chromium-doped UO_2 using the chromatic confocal microscope.

Blue points shown in Figure 5.2 correspond to points collected from the circular zone at the crater bottom. Only the depth distribution of a single-crystal sample can be satisfactorily fitted with a single

Gaussian function. The width of the fitted Gaussian distribution function for the single-crystal UO_2 is much narrower than that for poly-crystalline samples, which confirms the crater bottom roughness is less significant as revealed in Figure 5.1.a). This is no doubt due to a slightly inhomogeneous primary beam. However, the depth variation it induces is taken into account in the data analysis. This phenomenon can further be minimised by using smaller primary beam currents which is also conducive to smaller more homogeneous beam sizes (Garcia et al., 2010).

For poly-crystalline samples, the depth distributions may be fitted by summing several Gaussian functions. In poly-crystalline samples, the circular zone selected at the bottom of the crater covers several grains as illustrated in Figure 5.1.b) and c, and all the more so if the grain size is small. The main difficulty here therefore comes from the fact that sputtering rates are highly grain-orientation dependent (Pizzi et al., 2012). This is also illustrated in Figure 5.3. In the corresponding line scan on the right-hand side, one can follow the altitude change from one grain to the next.

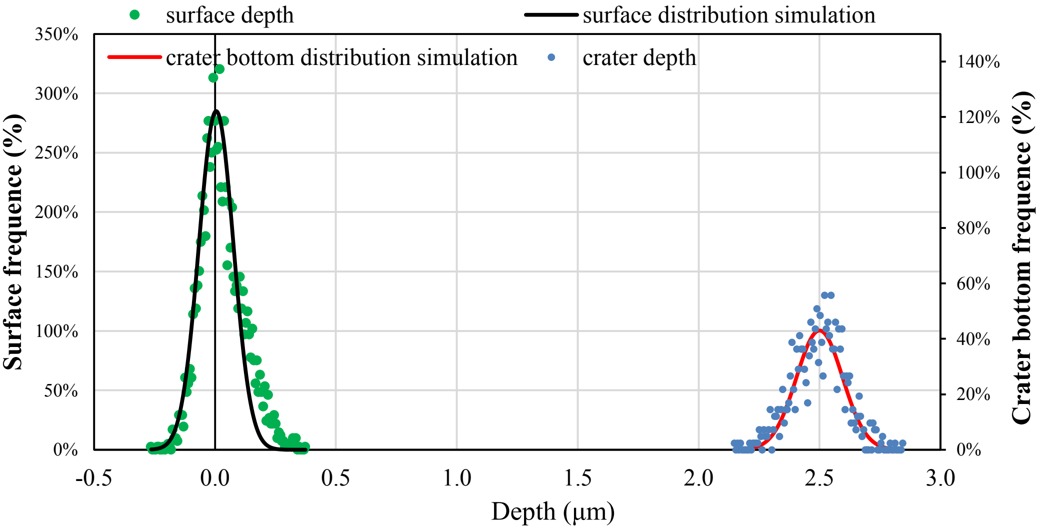

a) Depth distribution of a single-crystal sample

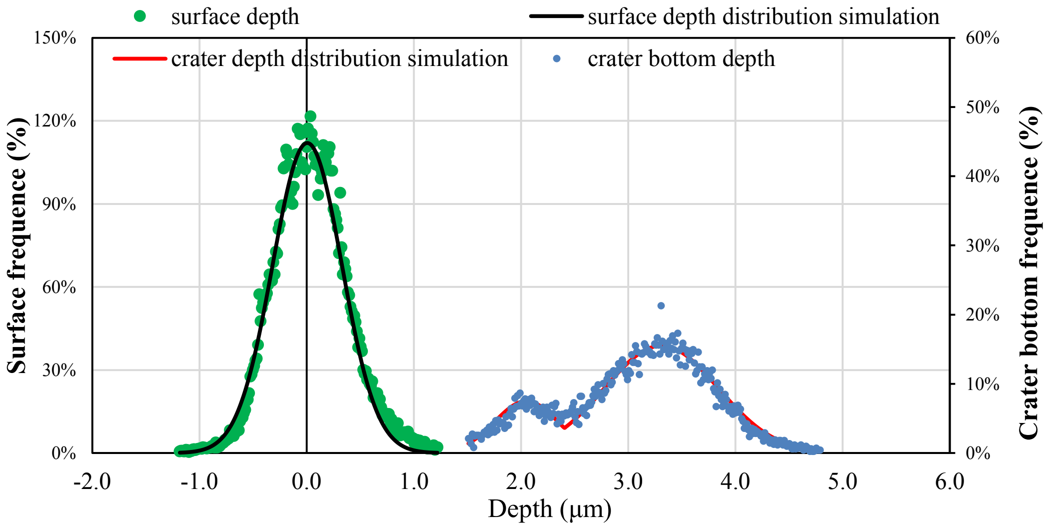

b) Depth distribution of a Chromium-doped UO_2

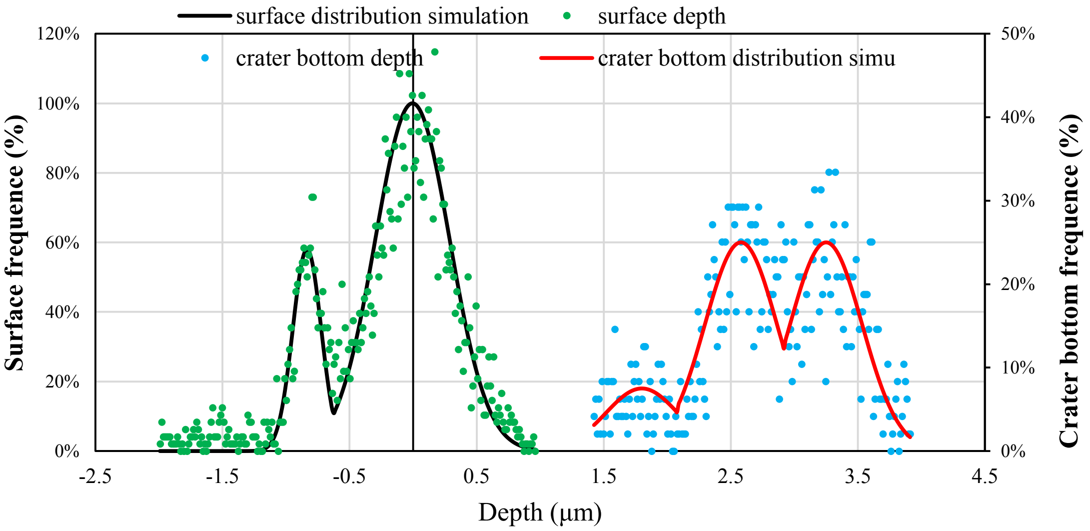

c) Depth distribution of an undoped poly-crystal sample

Figure 5.2: Examples of altitude distributions at the bottom and surface of craters a) undoped single-crystal, b) Chromium-doped poly- crystal and c) undoped poly-crystal; blue full circles correspond to the crater bottom and green circles correspond to the sample surface; black and red lines are their respective analytical Gaussian distributions.

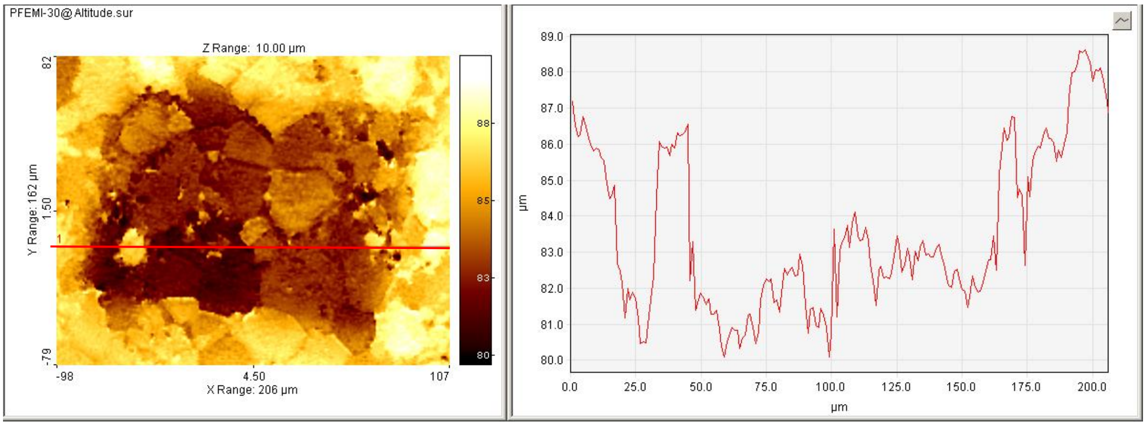

Figure 5.3: Chromatic confocal image of a poly-crystalline UO_2 sample; Left: “grey” level coded crater bottom; right: altitude linescan corresponding to red line in left-hand-side image.

Green points in Figure 5.2 correspond to the altitude distributions of the surface of the samples and which we have grossly approximated using a Gaussian distribution. The distributions relative to the surface of both poly-crystalline and single-crystal UO_2 are broad in comparison to other similar SIMS works (Garcia, et al., 2010). This could be the result of an initially heterogeneous deposit.

From the altitude distributions, it is possible to derive the distribution function for the overall depth distribution:

$$f(z) = \int_{x_{bott,min}}^{x_{surf,max}} f_{crater}(x+z) \cdot f_{surface}(x) dx \tag{5.2}$$

where z is the crater depth, $x_{surf,max}$ and $x_{bot,min}$ are the lowest and highest altitudes. $f_{crater}(x+z)$ and $f_{surface}(x)$ are normalised Gaussian distribution functions relative to the crater bottom and sample surface respectively. This derived overall depth distribution (equation (5.2)) allows us determining the average depth $\langle z \rangle$ and its standard deviation. As a result, the average sputtering rate $\langle v_p \rangle$ is defined as the ratio of the average crater depth to the total sputtering time:

$$\langle v_p \rangle = \langle z \rangle / t_s \tag{5.3}$$

The great advantage of this procedure is that the depth resolution for each data point in the profile can be determined by the standard deviation obtained from a set of sputtering rates. Similar to equation (5.3), the spatial resolution for a data point in the concentration profile obtained at time t is given by:

$$\delta z = \varepsilon(v_p) \cdot t \tag{5.4}$$

This analysis is essential as it enables us to determine the standard deviation associated with the sputtering rates generated when analysing a crater, which will ultimately provide a standard deviation for the diffusion coefficient derived from the corresponding depth profile.

5.3 UO_{2+x} samples depth profiles

5.3.1 Crater depth and profile characterizations

From the average crater depth obtained using chromatic confocal microscopy, one can determine the average sputtering rate for each crater. Table 5.1 shows the average sputtering rates and associated uncertainties for individual craters in our single crystal and poly- crystalline sample.

Table 5.1: Average depth and corresponding sputtering rate v_p determined for each crater in the single- and poly- crystalline UO_2, and Cr-doped UO_2 samples. In this table SC, PC and CrPC stand for single crystal, polycrystalline and chromium doped samples respectively.

Sample	**Profile #**	**T (°C)**	**pO_2 (atm)**	**Primary beam I (nA)**	**Sputtering time (s)**	**Average crater depth (µm)**	**Average sputtering rate (nm/s)**
SC-1 L2_MR_23	1	1350	8.5×10^{-12}	11.0	7298	3.3 ±0.6	0.49 ±0.09
	2			11.4	7298	3.3 ±0.7	0.50 ±0.10
	3			11.1	2432	1.5 ±1.0	0.62 ±0.20
SC-2 L2_MR_19	1	1500	9.4×10^{-13}	22.2	4914	2.5 ±0.4	0.51 ±0.04
	2			23.2	4914	2.9 ±0.5	0.59 ±0.05
	3			22.0	3694	1.6 ±0.1	0.43 ±0.03
	4			21.5	3694	1.9 ±0.1	0.51 ±0.04
	5			21.2	3694	2.8 ±0.4	0.75 ±0.05
SC-3 L2_MR_28	1	1500	5.0×10^{-12}	20.5	3694	2.5 ±1.0	0.69 ±0.03
	2			19.5	3694	3.8 ±0.1	1.00 ±0.02
	3			19.5	4908	2.6 ±0.1	0.53 ±0.02
SC-4 L2_MR_17	1	1500	4.7×10^{-11}	19.2	3694	1.8 ±0.1	0.49 ±0.02
	2			18.7	3694	1.9 ±0.1	0.50 ±0.02
SC-5 L2_MR_21	1	1600	4.7×10^{-12}	18.4	3694	2.0 ±0.1	0.54 ±0.03
	2			18.2	3694	2.6 ±0.1	0.71 ±0.09
	3			22.3	3694	2.0 ±0.1	0.55 ±0.03
PC-1 P_EFM_30	1	1350	8.5×10^{-12}	11.7	7298	3.9 ±2.0	0.59 ±0.30
	2			11.7	7298	0.5 ±0.3	0.07 ±0.04
	3			9.5	4853	0.4 ±0.3	0.06 ±0.05
	4			9.6	4853	0.4 ±0.3	0.07 ±0.04

	5			9.5	4853	0.5 ±0.3	0.08 ±0.04
PC-2 pc_du_4	1	1500	9.4×10^{-13}	17.3	3694	3.3 ±0.5	0.89 ±0.10
	2			16.9	3694	1.9 ±0.5	0.53 ±0.10
	3			24.0	3694	1.8 ±0.4	0.49 ±0.10
PC-3 pc-du-8	1	1500	5.0×10^{-12}	16.1	3694	1.9 ±0.4	0.51 ±0.10
	2			16.1	3694	1.9 ±0.4	0.52 ±0.10
CrPc J73	1	1500	9.4×10^{-13}	16.5	3694	2.7 ±0.5	0.74 ±0.10

The average sputtering rates indicated in Table 5.1 for a given sample but different craters are different despite the fact that the experimental conditions (mainly the primary beam current) are identical. These discrepancies can be largely explained by the effect of grain-orientations. The standard deviation associated with sputtering rates for the two types of poly-crystals are much greater than those for single crystals. With the determined average sputtering rate, one may obtain the depth profiles for all the craters. Figure 5.4, Figure 5.5 and Figure 5.6 present examples of depth profiles for single-crystals, undoped and doped poly-crystals.

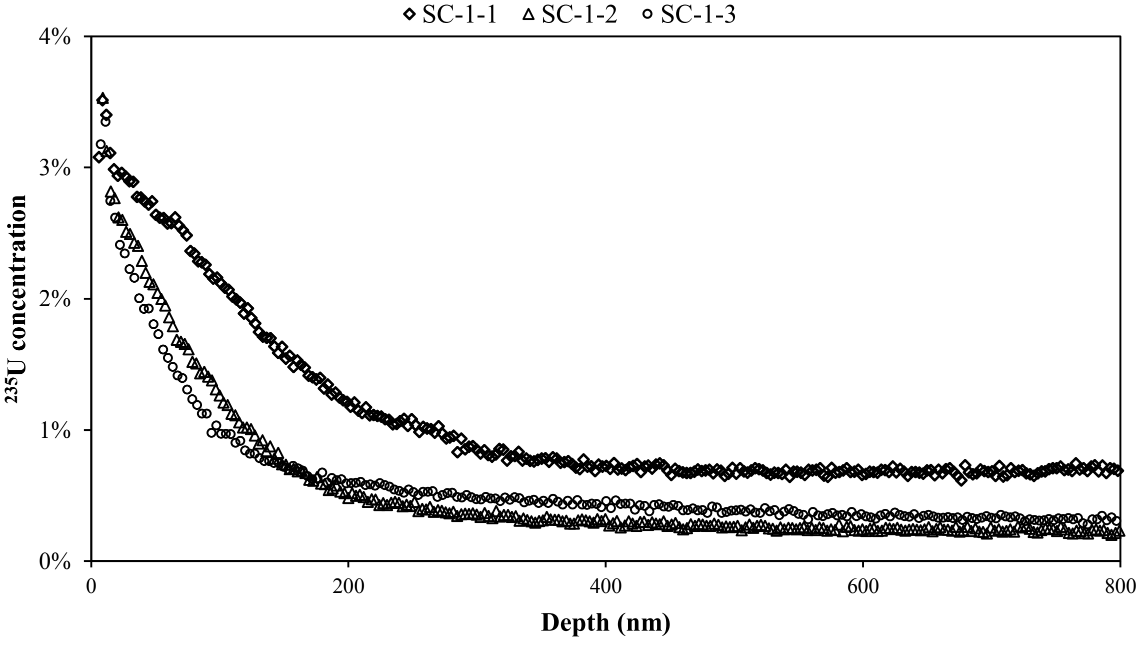

a) SC-1

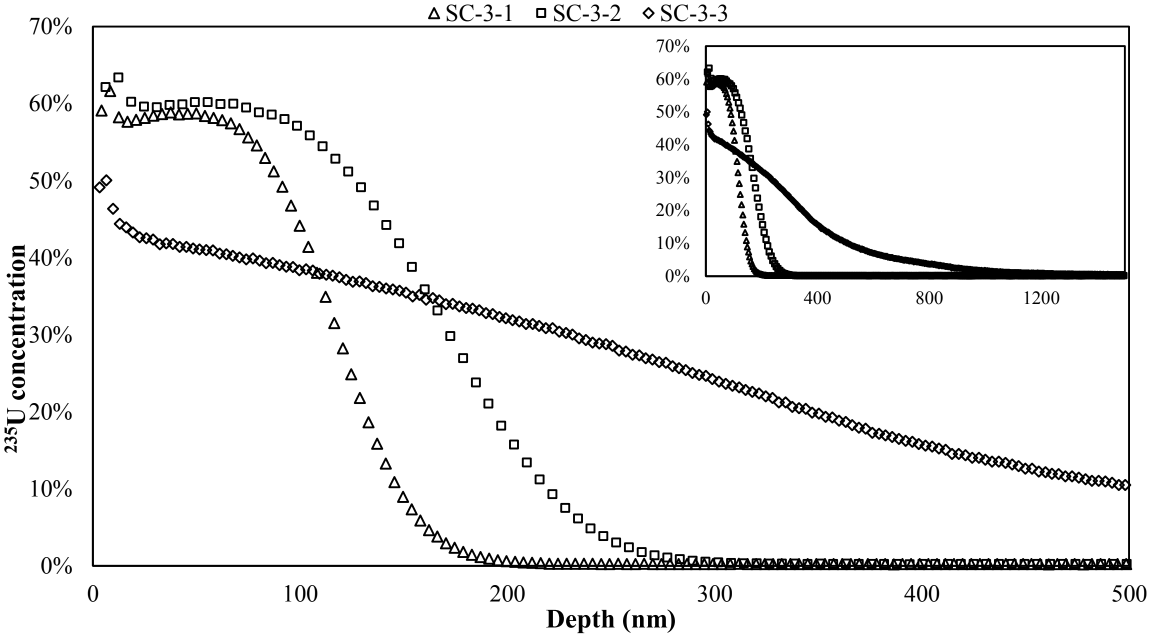

b) SC-3

Figure 5.4: Average depth profiles for two single-crystal samples: a) SC-1 is annealed in a small diameter tube-type alumina furnace in which the gas is renewed at a fast rate (every 5 minutes), for 18.5 hrs at 1350 ℃, p_{O_2} =8.5×10^{-12} atm; b) SC-3 is annealed in a large size tungsten furnace with a low renewal rate of the gaseous atmosphere (every 2 hours) for 24 hours at 1500 ℃. p_{O_2} =5.0×10^{-12} atm.

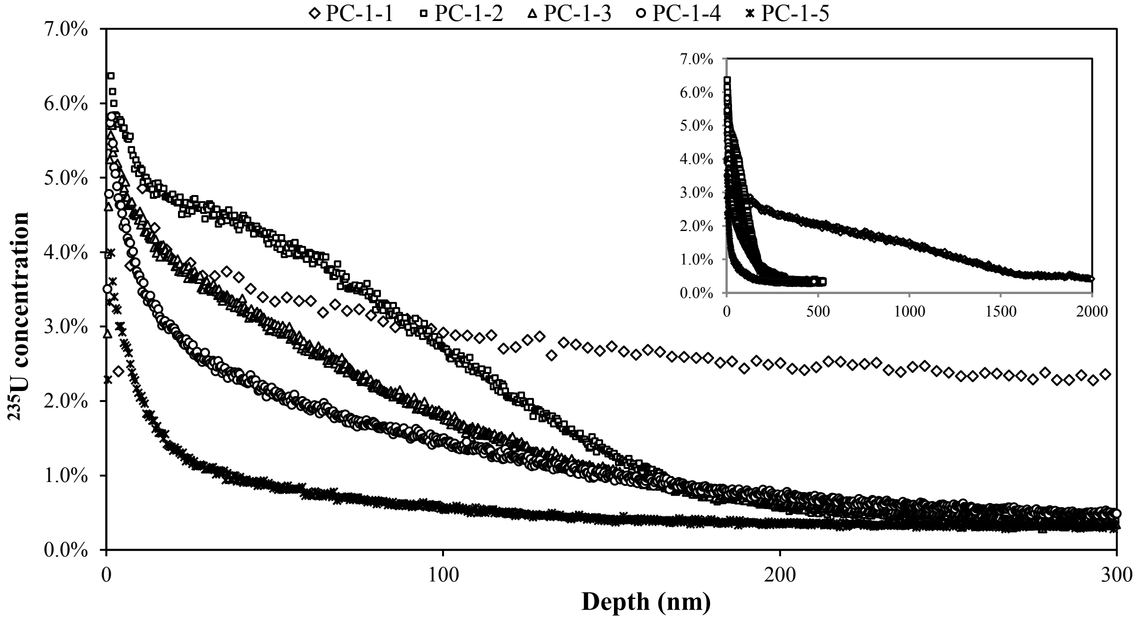

a) PC-1

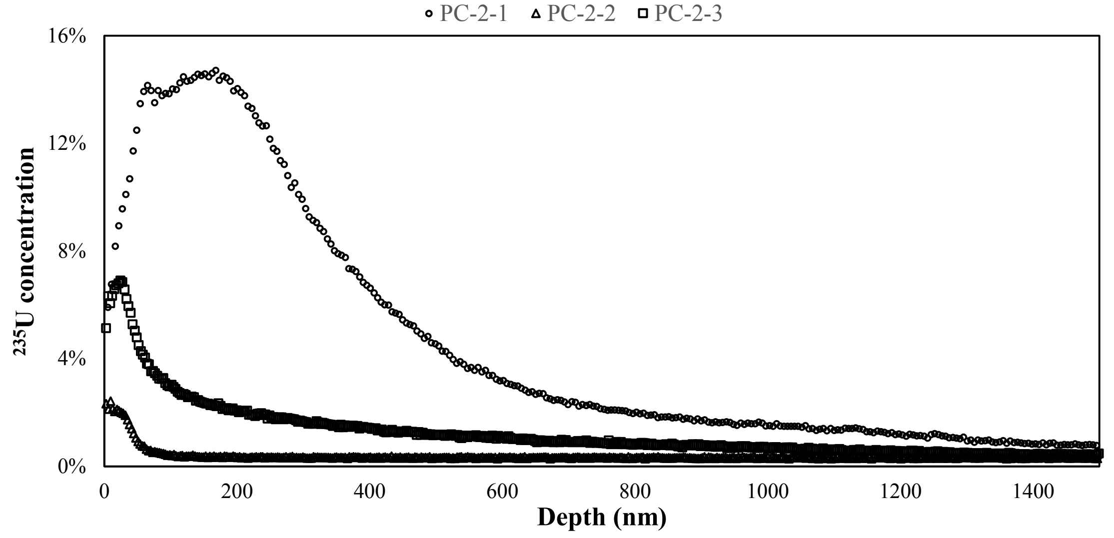

b) PC-2

Figure 5.5: Average depth profiles for two poly-crystalline specimens: a) PC-1 is annealed in a small diameter tube-type alumina furnace in which the gas is renewed at a fast rate (every 5 minutes), for 18.5 hrs at 1350 ℃, p_{O_2} =8.5×10^{-12} atm; b) PC-2 is annealed in a large size tungsten furnace with a low renewal rate of the gaseous atmosphere (every 2 hours) for 24 hours at 1500 ℃. p_{O_2} =9.4×10^{-13} atm.

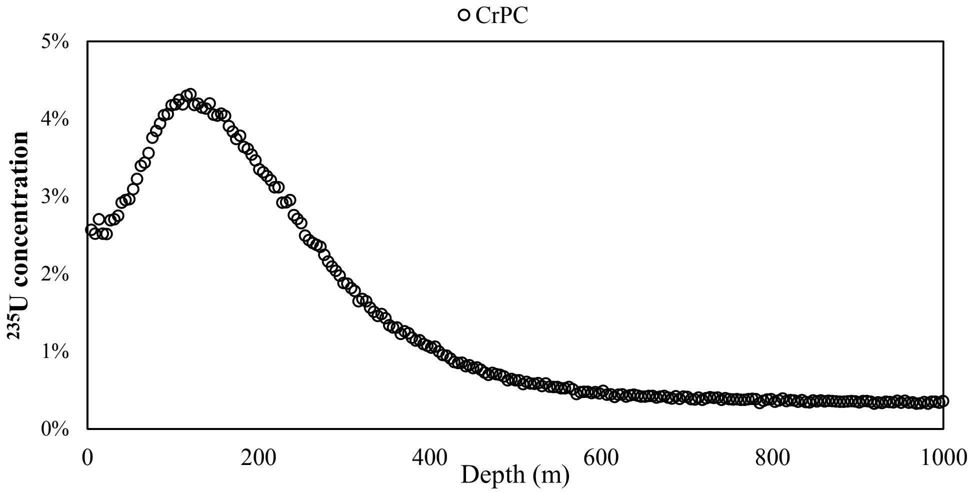

Figure 5.6: Depth profiles obtained using an average sputtering rate for Cr-doped poly-crystal specimens annealed for 24 hours at 1500 ℃. p_{O_2} =9.4×10^{-13} atm.

A comparison of the depth profiles presented above leads to a number of comments:

1- Very few depth profiles show ^{235}U concentrations in excess of 10% which is much smaller than the initial ^{235}U enrichment in the nitrate solution, which is about 97.7%. Integration of the ^{235}U concentration over depth, for example for profile SC-1-1 given in Figure 5.1.a), yields an initial thickness of enriched oxide of about 10 nm for an expected thickness between 46 nm and 127 nm estimated from the size and the number of drops deposited prior to the annealing. This is an indication that a fraction of the initial deposit has been lost because evaporation of the surface layer is occurring.

2- The concentration of ^{235}U in depth profiles of poly-crystals PC-2 and CrPC (chromium doped) increases first to a peak value then decreases with increasing depth. For the single-crystal SC-3 the ^{235}U concentration remains high for the first 80 to 100 nm.

3- For PC-2, the integration of the absolute concentration of ^{235}U varies substantially from one profile to the other. The Cr-doped poly-crystal also has a very low initial concentration. This is counter-intuitive to the fact that this sample was annealed in a cylindrical furnace, where no significant evaporation would occur.

4- As Figure 5.1.b and Figure 5.2.a illustrate, two profiles SC-3-3 and PC-1-1 have much longer tails as the inset shows.

5- For Cr-doped UO_2, only a single crater could be characterised using confocal microscopy. This is because other craters were too shallow to be found at the surface of the samples.

5.3.2 Depth profiles analyses

Before, further analysing the depth profiles, it is worth mentioning that one single-crystal and one poly-crystalline samples (SC-1 and PC-1) were prepared in a tubular alumina furnace of small volume (roughly 1 litre). Because the flow rates were generally limited to 200 mL/min, this means that the renewal rate of the gas surrounding the samples was very high (roughly every 5 minutes). All the other samples presented in the following sections were annealed in a large volume tungsten furnace (roughly 20 litres). The gas renewal rate was consequently of the order of every two hours.

Based on SIMS depth profiling results as well as the SEM images of the material microstructure prior to, following the uranyl nitrate deposit and after diffusion annealing, we can identify five reasons for the observations listed in section 5.3.1:

1- **The effect of evaporation and condensation**

As we stated before, samples SC-1 and PC-1 are diffusion-annealed in a small volume alumina type furnace whilst all other samples were annealed in a much larger volume furnace (see Chapter 2 section 2.3.5). It appears therefore that prior to, following or in the course of the diffusion annealing in the small furnace, a substantial amount of ^{235}U is lost which implies that **evaporation occurs** during diffusion annealing.

The rise first and then the drop of ^{235}U concentration in the profiles PC-2-1 and CrPC has been observed before in the literature (*i.e.* the deposited ^{235}U-enriched layer) (Matzke, 1983) and could indicate a shift in the interface. This may be an indication of a **condensation** phenomenon. This may also be case for the single-crystal SC-3.

2- **The heterogeneous distribution of the uranyl nitrate deposit**

The third phenomenon concerns the deposit of the nitrate solution. When depositing the liquid uranyl nitrate on the solid substrate, the surface tension forces between liquid and solid are such that spherical shaped droplets form at the surface of the sample. As the liquid dries, an uneven and brittle nitrate layer forms at the surface.

For poly-crystal PC-2, the differences in concentration profiles we have characterised could have their origin in the heterogenous distribution of the deposit, i.e. an uneven layer thickness across the surface of the samples. Our Cr-doped poly-crystalline samples are small semi-circular disks, so that the droplet did not spread across the entire face of the sample. The initial thickness of $^{235}UO_2$ layer may be very small at the place where the crater is located.

3- **The roughness induced during preparation and annealing**

Both the third phenomena observed in the depth profiles, and the fact that the standard deviations associated with the depth measured for poly-crystalline materials are very large, is correlated with the roughness induced in the various stages prior to the SIMS characterization.

The as-fabricated disks were annealed at 1700 ℃ for 24 hours. After annealing, **deep furrows** may be formed at the boundaries between the different grains (See chapter 2 section 2.3.1). The low-temperature annealing (following the deposit and before diffusion-annealing) does not alter this. But is worth mentioning that the surface roughness measured following the nitrate deposit and low temperature annealing, although not negligible, is substantially less than the actual depth at which the isotope diffuses. This means that despite the roughness effects alluded to above, it is reasonable to attempt to derive a diffusion coefficient from such profiles.

4- The dependence of the sputtering rate upon grain orientation

The plateau observed in profile PC-1-2 could possibly be explained from the grain-orientation dependence of the sputtering rate mentioned in section 5.3.1. The very broad range of sputtering rates may lead certain grains to sputter very slowly. Consequently, a grain may still be providing a contribution to the overall signal at long sputtering times despite representing a small surface fraction. This will lead to an overestimation of the ^{235}U concentration at large depths.

It has to be noticed that the depth resolution for this crater is as expected much lower than for our single-crystals. Figure 5.7 shows the associated error bars for all data points. This is likely to induce a high uncertainty upon any uranium diffusion coefficient derived.

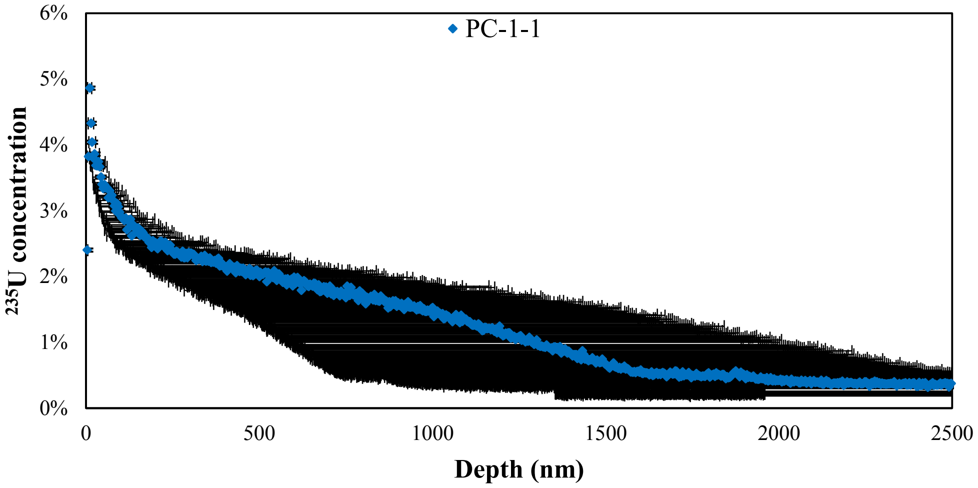

Figure 5.7: Depth profile of one crater in poly-crystalline sample annealed at 1350 ℃ with error bars for each data point.

5- Possible short-circuit diffusion mechanisms

The long tails identified in certain depth profiles (see SC-3-3 and PC-1-1), could be interpreted as an indication that ^{235}U ions have diffused much further into sample than at other locations at the sample surface. The SIMS conditions for all the characterizations are identical and therefore, some accelerating mechanism may be active.

Accelerated grain-boundary diffusion has often been considered very relevant to uranium dioxide. Sabioni e*t al.* (Sabioni et al., 2000) obtained very large values for uranium self-diffusion coefficients in poly-crystals, and regarded these high values as evidence of grain-boundary diffusion. The authors based their conclusions on the analysis of concentration profiles similar to that shown in Figure 5.8. The grain-boundary diffusion coefficient was five orders of magnitude greater than the volume diffusion coefficient obtained from depth profiling a single-crystal annealed under identical conditions.

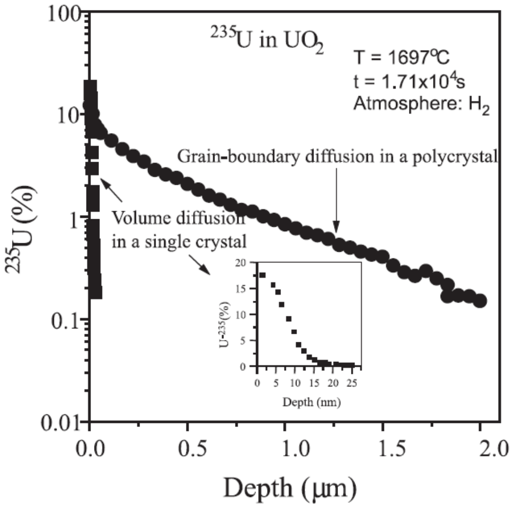

Figure 5.8: Depth profiles of single- and poly- crystal UO$_2$ by Sabioni et al (Sabioni et al., 2000).

This could constitute an interpretation for the long tails in depth profiles observed in some of our samples, as would be expected in B-type intergranular diffusion (Philibert, 1991). This type of diffusion is thought to occur under the condition that:

$$\delta \ll \sqrt{Dt} < \Phi/2 \tag{5.5}$$

, where D is the diffusion coefficient, t: diffusion time, δ grain-boundary width, Φ is the grain size.

B-type intergranular diffusion is defined as one dimensional diffusion from a surface, assuming either a constant surface concentration, or, a thin-layer source which corresponds to our case. We will further investigate this point in the following sections in which we attempt to model the measured depth profiles.

For the single-crystal, accelerated diffusion may occur near a surface when a network of **dislocations** is present (Philibert, 1991). UO$_2$ may also form **shear structures** which little knowledge is provided related to its impact on self-diffusivities (Matzke, 1983). Also, it is reported that **initial surface roughness** induced for example by mechanical polishing will ‘increase’ the derived diffusion coefficient.

In summary, we have determined crater depths with their associated standard deviations as well as sputtering rates. This has enabled us to determine ^{235}U concentration profiles. By analysing

and comparing the sputtering rates and respective depth profiles for each sample, we have identified several important points which must be borne in mind in the interpretations formulated in the following sections.

First, it appears that evaporation or condensation of species occurs at the surface of the sample and that the extent to which this happens depends upon the furnace in which annealing has taken place and conditions the samples were subjected to.

Secondly several factors combine and contribute to deteriorating the depth resolution: the formation of an ^{235}U enriched layer of uneven thickness and the initial surface roughness of the samples. Thirdly, there are signs of what could be interpreted as short-circuit mechanisms in both single- and poly- crystalline materials. This will be further discussed in the subsequent section.

5.4 Modelling the ^{235}U depth profile and discussion

5.4.1 Diffusion model

The uranium self-diffusion coefficient, as reviewed in Chapter 1, is obtained from fitting the experimental depth profiles to the result of a model calculation with appropriate boundary and initial conditions. In this experiment, a thin layer of uranyl nitrate containing the ^{235}U tracer isotopes, is deposited in the form of **a thin layer** onto the surface of the samples. The corresponding diffusion equation to be solved is:

$$\frac{\partial c(x,t)}{\partial t} = \frac{\partial}{\partial z}\left(D\frac{\partial c(x,t)}{\partial z}\right) \tag{5.6}$$

In the thin layer approximation, the initial and boundary conditions are as follows (Philibert, 1991):

$$\begin{gathered} t = 0,\ \ c(x,0) = Q\delta(x) \text{ at } x = 0 \\ c(\infty,t) = c_0, \text{ at all times} \end{gathered} \tag{5.7}$$

$\delta(x)$ is the Dirac delta function. The integral is chosen depending on whether the sample is semi-infinite or infinite. Parameter $\boldsymbol{Q}$ represents the initial surface concentration of ^{235}U on the substrate prior to diffusion annealing. An analytical solution to this problem (Philibert, 1991) is:

$$c(x,t) = c_0 + \frac{Q}{2\sqrt{\pi D t}}\exp\left(-\frac{x^2}{4Dt}\right) \tag{5.8}$$

The quantity $\sqrt{2Dt}$ is an estimate of the penetration depth and represents the half-width of the Gaussian distribution.

One can estimate the value of $\boldsymbol{Q}$ in this solution based on the initial thickness of the $^{235}UO_2$ layer, which can be determined by the number and size/shape of the drops deposited assuming no solution is lost. It is worth noting that $\boldsymbol{Q}$ is probably not identical for all the craters on a single sample since the uranyl nitrate deposit was shown to be heterogeneous. Based on the number and volume of drops deposited at the surface, the average thickness of the surface layer is estimated at 46 nm to 127 nm for single- crystals, and 88 nm to 294 nm for poly crystalline samples from the drops of uranyl nitrate deposit.

Also, when samples are placed in the sample holder during diffusion annealing, either the deposited layer is directly exposed to the flowing gas, or samples are placed as pairs with deposited layers facing each other. No weight is added in this case. One of the observations that emerges from the previous section is that surface evaporation may occur during diffusion annealing which is something reported in the literature (Sabioni et al., 1998). The Diffusion equation may be modified to take into account an average surface evaporating denoted $\langle v \rangle$:

$$\frac{\partial C}{\partial t} = \frac{\partial}{\partial z}\left(D\frac{\partial C}{\partial z}\right) - v\frac{\partial C}{\partial z} \tag{5.9}$$

An analytical solution for this equation with identical initial and boundary conditions as (5.7) is given by:

$$c(x,t) = c_0 + \frac{Q}{2\sqrt{\pi D t}}\exp\left(-\frac{(x-\langle v\rangle t)^2}{4Dt}\right) \tag{5.10}$$

In principle, the velocity $\langle v \rangle$ should be constant and the same for all samples and depth profiles, but may be slightly affected by the fact that the surface of the sample is directly exposed to the gas phase or facing another sample. It is also possible that this evaporation rate, which is determined by the temperature and oxygen partial pressure during diffusion annealing, may be affected by grain orientation as well. So in the case of polycrystalline samples, the evaporation rate may actually be different from one grain to the next.

A temperature dependent expression as well as actual values for $\langle v \rangle$ are reported in the literature (Sabioni et al., 1998) for an atmosphere involving pure hydrogen. At 1350 ℃, this evaporation rate is reported as being $8 \cdot 10^{-16}$ m/s. The lowest oxygen partial pressure that samples were subjected to in one of our diffusion annealing is $9.4 \cdot 10^{-13}$ atm. The oxygen partial pressure in the gas phase in reference (Sabioni et al., 1998) is not specified, but samples were annealed under pure H_2, and the corresponding equilibrium oxygen partial pressure is much lower than ours. As a result, it is reasonable to assume a higher evaporation rate in our case. Also, the evaporation rate is also dependent on the grain-orientation. Therefore, the value used in modelling can be slightly adjusted from one profile to the next. Our analysis of a given data therefore provides three physical parameters:

1- The diffusion coefficient
2- The effective thickness of $^{235}UO_2$ layer at the sample surface which may vary from one sample to the next and even from one crater to the next as a result of possible inhomogeneities in the surface layer at the surface of samples

3- The evaporation rate which appears to be sensitive to temperature, oxygen partial pressure and gas flow conditions.

5.4.2 Modelling depth profiles

We show examples of typical depth profiles in Figure 5.9, Figure 5.10 and Figure 5.11 using the model above. Several important points emerge from this effort to model the depth profiles:

1- Ideal solutions to diffusion equations

As Figure 5.9.a) demonstrates, the analytical solution to the diffusion equation 6.6 well reproduces some single-crystal and poly-crystalline depth profiles. The relevance of such modelling as well as the values derived for self-diffusion coefficients is based primarily on the ability of the model to reproduce the experimental data points but this does not constitute the only criterion. Results are also analysed critically based on the fact that we expect to derive a consistent, physical set of data which include: the effective initial thickness of the ^{235}U-enriched layer $\boldsymbol{Q}$, the evaporation/condensation rate $\langle \boldsymbol{v} \rangle$ and the diffusion coefficient of course. For example, for profile SC-1-1 shown in Figure 5.9.a), the determined uranium self-diffusion coefficient is 2.0×10^{-19} m^2/s, using a $\boldsymbol{Q}$ of 10 nm and a $\langle \boldsymbol{v} \rangle$ of 1.8×10^{-12} m/s in the model which are reasonable values.

2- The near surface effect

In the modelling, two or three regions are usually observed in the majority of depth profiles such as is illustrated in Figure 5.9.b) and d), and Figure 5.10.a) and d). Near surface data points corresponding to region I have a steep slope, and the diffusion coefficient derived D_U is small. Region II extends generally over a restricted range of depths, and region III corresponds to profile tails which extend much deeper into the sample and yields much greater diffusion coefficient values. For example, the uranium self-diffusion coefficients determined by model 1, 2 and 3 in Figure 5.9.d) are 1.5×10^{-19} m^2/s, 6.7×10^{-19} m^2/s, and 1.2×10^{-18} m^2/s respectively.

Matzke considered that D_U determined from region I is the true volume diffusion coefficient, while that derived from modelling region III reveals some high-diffusivity paths (Matzke, 1983). For a single-crystal, the paths can be the induced dislocations or shear structures following the nitrate deposition and low-temperature annealing. For the poly-crystalline material, this could correspond to the specific behaviour of grain-boundaries. It may also be related to the temperature induced interface shift due to the mobility of isotope-enriched layer. In this work, we consider the uranium self-diffusion coefficient determined from the near-surface points in one depth profile as the bulk diffusion coefficient.

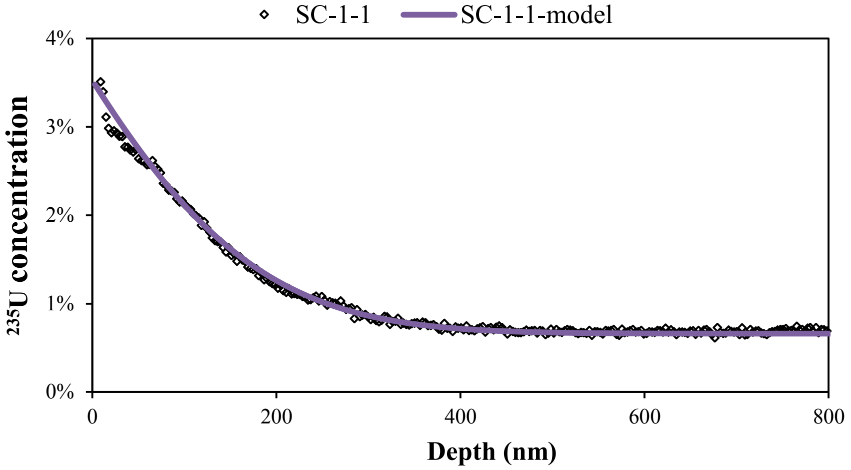

a) SC-1-1 depth profile and model result

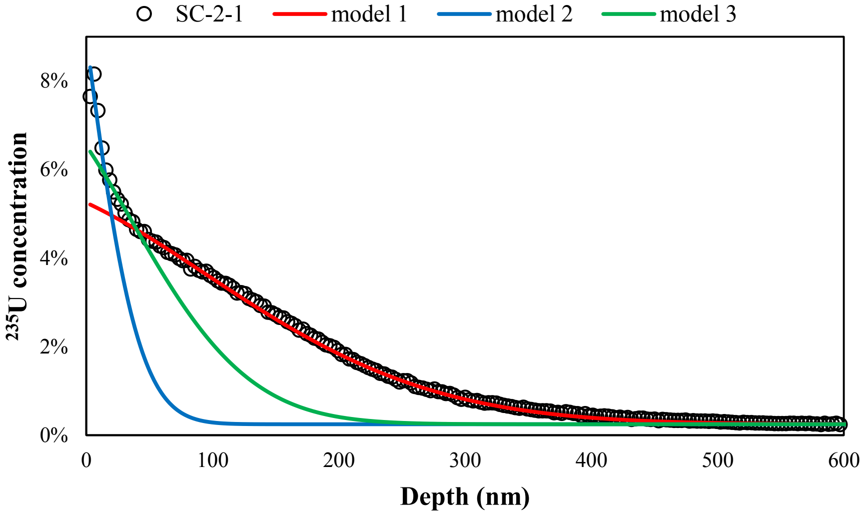

b) SC-2-1 depth profile and model results

c)

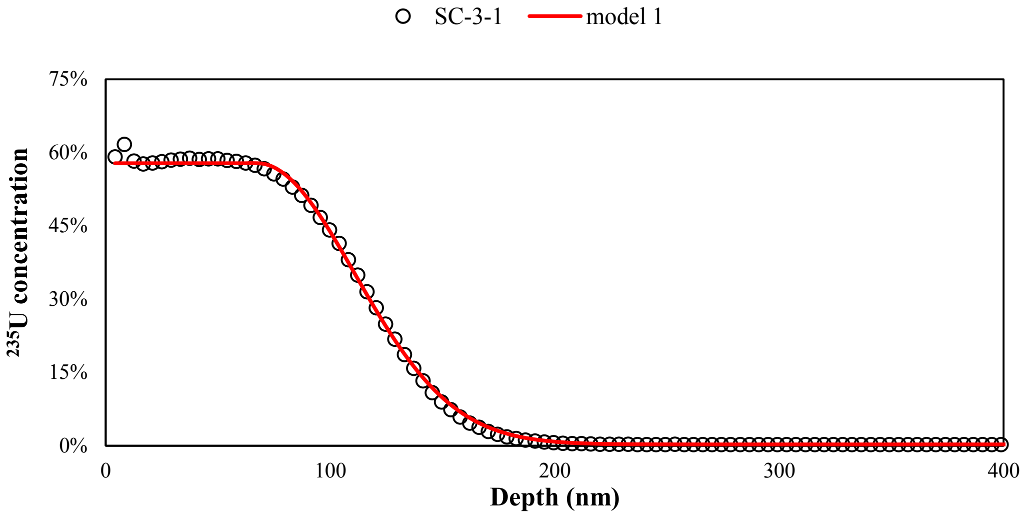

c) SC-3-1 depth profile and model result

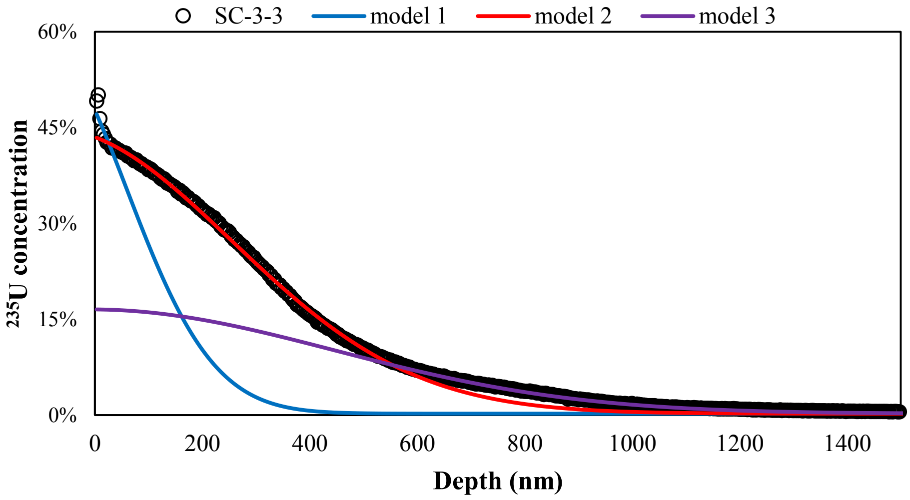

d) SC-3-3 depth profile and model results

Figure 5.9: Four typical depth profiles for craters on the single-crystals annealed at 1350 ℃, 1500 ℃ and 1600 ℃ and in different oxidizing equilibria and corresponding modelling results in colour.

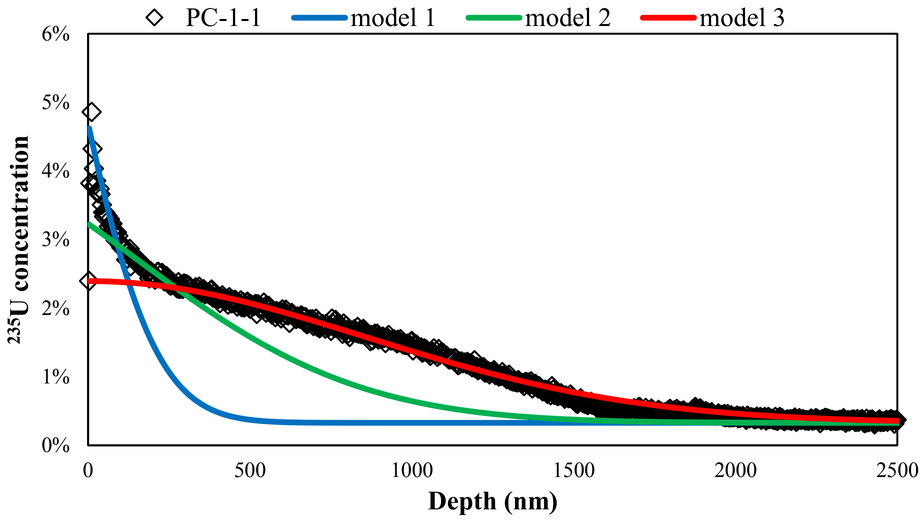

a) PC-1-1 depth profile and model results

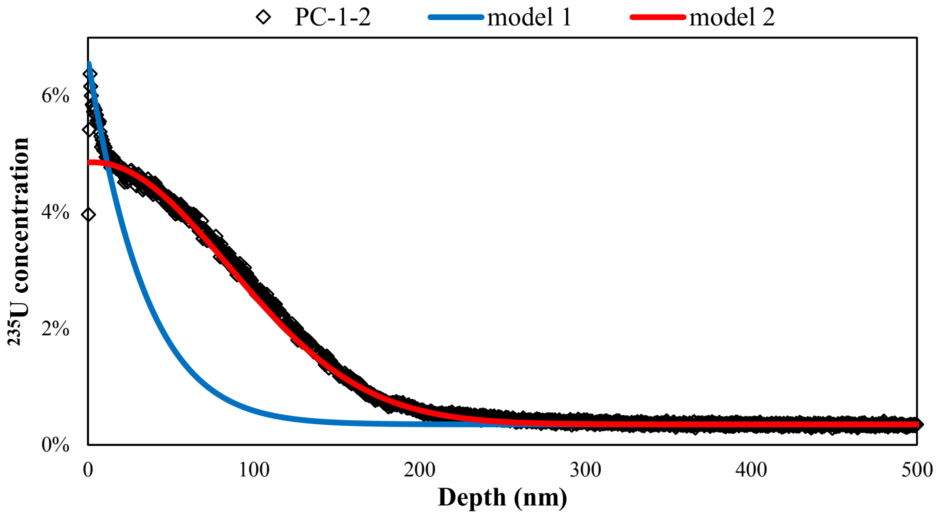

b) PC-1 depth profile and model results

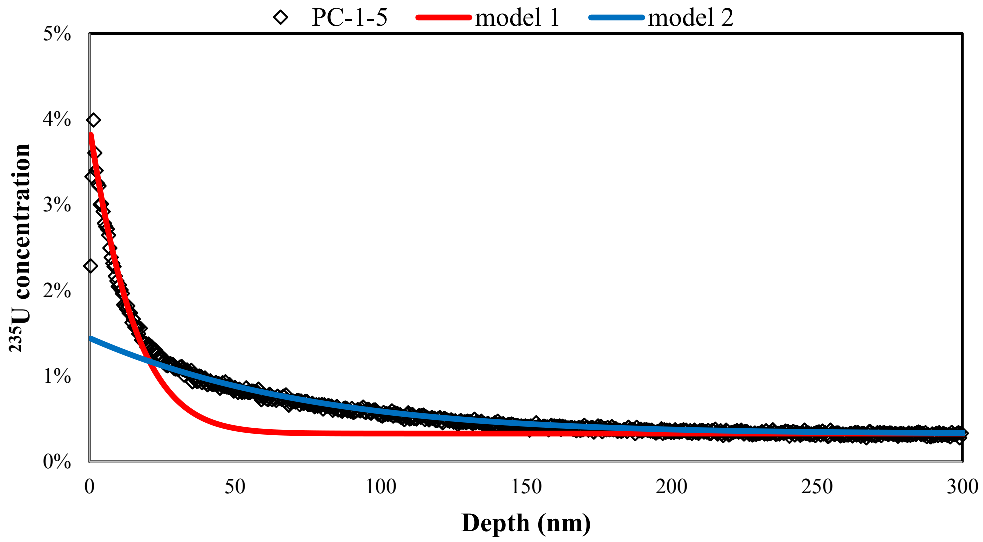

c) PC-1-5 depth profile and model results

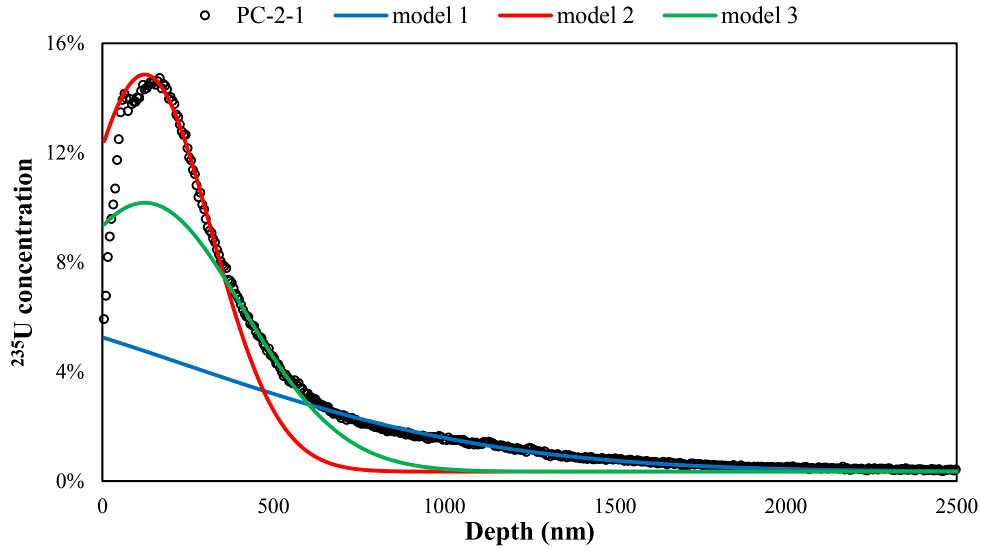

d) PC-2-1 depth profile and model results

Figure 5.10: Four typical depth profiles for craters on the undoped poly-crystals annealed at 1350 ℃, 1500 ℃ and in different oxidizing equilibria and corresponding modelling results in colour.

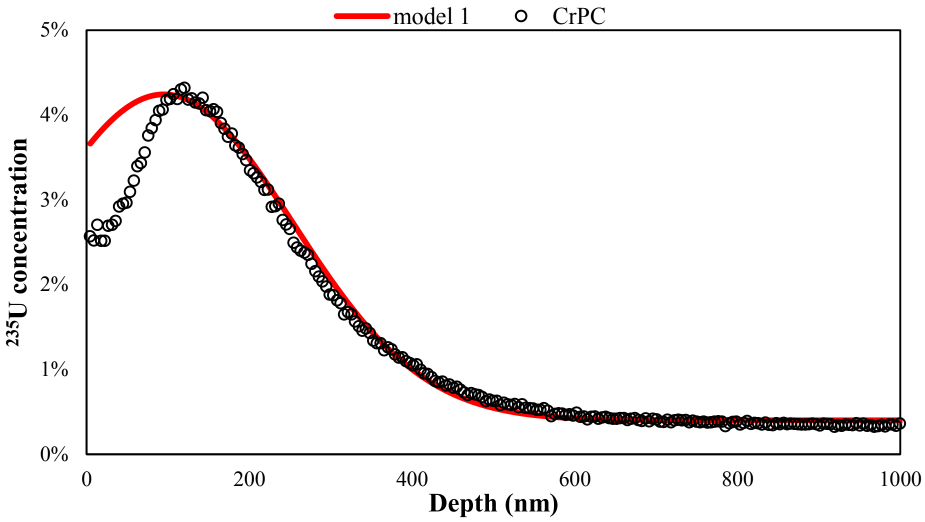

Figure 5.11: Depth profile for the Cr-doped poly-crystal annealed at 1500 ℃ and slightly oxidizing environment and corresponding modelling results in colour.

3- The grain-orientation effect

The shoulder region in Figure 5.10.b) is mainly a result of low-sputtering rates resulting from certain grain orientations. Both two regions may be fitted with **an** ideal diffusion solution with specified $\boldsymbol{Q}$ and $\langle \boldsymbol{v} \rangle$. The determined uranium self-diffusion coefficients, for instance, for two regions in Figure 5.10.b) are 8×10^{-20} m^2/s and 5×10^{-20} m^2/s. **This indicates that the grain-orientation effects do not in general significantly modify the diffusivity derived from our analysis.**

This grain orientation effect can be demonstrated from SIMS ionic images at various distances from the sample surface, hence corresponding to certain depths in the concentration profile. Figure 5.12.a) and b) correspond to ionic images taken from the surface of the poly-crystalline sample (prior to rastering). The dark regions in Figure 5.12.(a) and (b) correspond to grains that are sputtering at lower rates and hence have a lower sputtering yield since the dark regions of the ^{235}U image correspond relatively well to dark regions in the ^{238}U image (Pizzi et al., 2012).

We surmise therefore that the apparent shoulders observed in these depth profiles are due to very poor depth resolutions which result from these different sputtering yields. Grains that sputter at much slower rates can under certain conditions, contribute in a much higher proportion to the overall concentration profile than the grains which sputter at a higher rate.

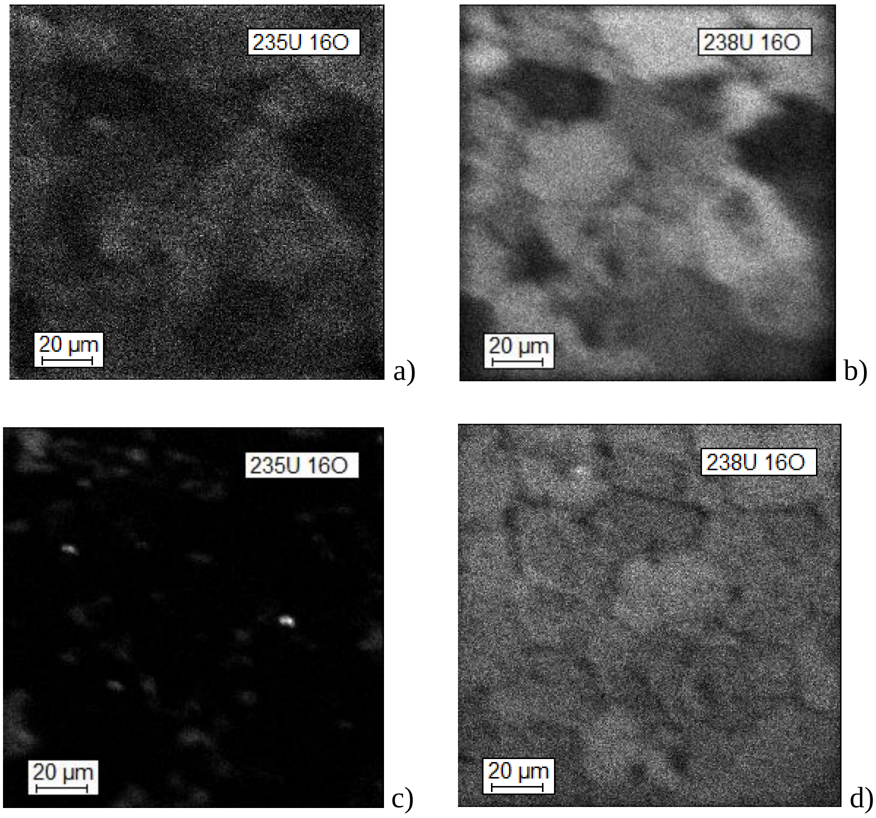

Figure 5.12: Secondary ion images of $^{235}UO_2$ and $^{238}UO_2$ taken a) and b) at the surface of a polycrystalline sample before raster, and c) and d) in the middle of raster.

4- Modelling the condensation process

We have interpreted certain observations as a contribution of surface condensation on the depth profiles. These observations concern all types of samples and is illustrated in Figure 5.10.d. To reproduce the depth profile a simple diffusion solution is applied with a negative $\langle \boldsymbol{v} \rangle$ which corresponds to the model in red in three graphs.

5- Modelling the thick $^{235}UO_2$ layer

As Figure 5.9.c shows, the ^{235}U concentration remains at 60% over the first 60 nm, which is consistent with the expected thickness of the $^{235}UO_2$ layer. The diffusion model given in section 5.3 assumes a thin enriched layer at the sample surface. This is not the case in Figure 5.9.c. To model the profile we assume a constant concentration at the interface between the enriched layer and the depleted substrate. We instead only simulate a proportion of experimental data corresponding to the diffusion process in the substrate.

6- Modelling uranium inter-diffusion in the doped material

With the first method, no combination of model parameters is capable of reproducing the rise in the ^{235}U concentration up to approximate 120 nm in profile CrPC in Figure 5.12. The observation may be more related with an inter-diffusion process. It is expected that there is a gradient in the uranium self-diffusion coefficient as the $^{235}UO_2$ layer contains no Chromium whereas the substrate does. Notwithstanding, the uranium self-diffusion coefficient determined by applying the same diffusion model is $1.5 \cdot 10^{-20}$ m^2/s.

7- The grain-boundary diffusion

If considering the near-surface effect, by assuming reliable values for $\boldsymbol{Q}$ and $\langle \boldsymbol{v} \rangle$, the uranium self-diffusion coefficient given by model PC-1-1, however, is still much higher than all the other depth profiles. The yellow curve (model 3) in Figure 5.10.a) that reproduces well the very long tail-end of the profile provides a much higher uranium self-diffusion coefficient ($5.5 \cdot 10^{-18}$ m^2/s) than the values derived from all the other crater depth profiles. The red curve (model-1), which corresponds to a diffusion coefficient of $4.6 \cdot 10^{-19}$ m^2/s reproduces the near-surface data, but is still roughly one order of magnitude higher than the average diffusion coefficient from other crater profiles ($5.2 \cdot 10^{-20}$ m^2/s).

The diffusion coefficient obtained and the characteristics of our poly-crystalline sample satisfy the conditions in equation (5.10) ($\sqrt{Dt}$ is approximate 0.5 μm, $\Phi/2$ in our case is approximate 5 μm and the grain-boundary width is a few nanometres at the most. So if grain-boundary diffusion of ^{235}U occurs in our experiment either exclusively, or in conjunction with volume diffusion, one should observe decorated grain boundaries in the ionic images. As Figure 5.12.a and d suggest, grain boundaries **do not** show any particular contrast as would be expected if grain-boundary diffusion was active. Therefore, this profile is considered as an artefact.

In summary, we applied a solution of Fick's second law, which is suitable for the case of a thin source layer on the surface of a semi-infinite sample. Analysing depth profiles with such a model has enabled us to identify a number of issues related to this technique: the near-surface effects (Matzke, 1983), grain-orientation effects for poly-crystalline materials, evaporation and condensation effects, and several short-circuit diffusion mechanisms including grain-boundary diffusion. The uranium self-diffusion coefficients for three types of materials and given in the following sections and correspond to the volume self-diffusion coefficient determined from the near-surface region.

5.5 Self-diffusion coefficients and discussion

We present in Table 5.2 the uranium self-diffusion coefficients determined for the three types of materials we have studied: single-crystal, undoped and Cr-doped poly-crystalline uranium dioxide. All the values presented here are considered to be volume-diffusion coefficients.

Table 5.2: Bulk diffusion coefficient D_U and associated uncertainties, with corresponding values of ^{235}U-enriched effective oxide layer thickness $\boldsymbol{Q}$ and evaporation / condensation rate $\langle \boldsymbol{v} \rangle$ used in the depth profile modelling. The colour code in Table 6.1 is indicative of annealing conditions.

Sample	**T (℃) / pO_2 (atm)**	**Estimated x**	**Profile #**	$\boldsymbol{Q}$ (nm)	$\langle \boldsymbol{v} \rangle$ (m/s)	**D_U (m^2/s)**	**Average D_U (m^2/s)**
SC-1 L2_MR_23	1350 8.5×10^{-12}	2.004 $\pm10^{-4}$	1	5.0	6.0×10^{-13}	1.5×10^{-19}	7.3×10^{-20} $\pm10^{-20}$
			2	13.5	2.3×10^{-12}	**8.0×10^{-20}**	
			3	5.2	1.1×10^{-12}	**6.5×10^{-20}**	
SC-2 L2_MR_19	1500 9.4×10^{-13}	2.001 $\pm10^{-4}$	1	8.8	5.0×10^{-13}	1.0×10^{-20}	1.1×10^{-20} $\pm1\times10^{-21}$
			2	15.4	-2.8×10^{-13}	**1.1×10^{-20}**	
			3	220	1.7×10^{-12}	3.0×10^{-20}	
			4	40	1.0×10^{-12}	4.0×10^{-20}	
			5	75	0.9×10^{-12}	5.0×10^{-20}	
SC-3 L2_MR_28	1500 5.0×10^{-12}	2.002 $\pm10^{-4}$	1	3.8	-7.8×10^{-13}	**1.4×10^{-20}**	2.0×10^{-20} $\pm1\times10^{-20}$
			2	6.0	-6.3×10^{-13}	**3.0×10^{-20}**	
			3	132	1.2×10^{-12}	1.5×10^{-19}	
SC-4 L2_MR_17	1500 4.7×10^{-11}	2.004 $\pm10^{-4}$	1	4.8	2.5×10^{-13}	**9.8×10^{-20}**	8.9×10^{-20} $\pm5\times10^{-20}$
			2	6.8	3.0×10^{-13}	**8.0×10^{-20}**	
SC-5 L2_MR_21	1600 4.7×10^{-12}	2.001 $\pm10^{-4}$	1	800	1.9×10^{-12}	2.0×10^{-20}	2.1×10^{-20} $\pm3\times10^{-21}$
			2	210	1.8×10^{-12}	2.5×10^{-20}	
			3	420	1.8×10^{-12}	1.8×10^{-20}	
PC-1 PEFM_30	1350 8.5×10^{-12}	2.004 $\pm10^{-4}$	1	32	4.5×10^{-12}	4.5×10^{-19}	4.7×10^{-20} $\pm1\times10^{-20}$
			2	620	4.5×10^{-12}	8.0×10^{-20}	
			3	70	3.0×10^{-12}	6.4×10^{-20}	
			4	680	3.2×10^{-12}	3.5×10^{-20}	
			5	23	1.3×10^{-12}	1.0×10^{-20}	
PC-2 pc_du_4	1500 9.4×10^{-13}	2.001 $\pm10^{-4}$	1	40	-1.4×10^{-12}	2.2×10^{-19}	$1.0\times10^{-20}\pm1\times10^{-20}$
			2	0.6	-1.4×10^{-13}	3.6×10^{-21}	
			3	22	-1.4×10^{-13}	8.0×10^{-21}	
PC-3 pc-du-8	1500 5.0×10^{-12}	2.002 $\pm10^{-4}$	1	105	3.0×10^{-12}	1.7×10^{-19}	$2.1\times10^{-19}\pm5\times10^{-20}$
			2	160	3.2×10^{-12}	2.5×10^{-19}	
CrPc J73	1500 9.4×10^{-13}	2.001 $\pm10^{-4}$	1	8.6	-1.1×10^{-12}	**1.5×10^{-19}**	$1.5\times10^{-19}\pm2\times10^{-20}$

5.5.1 Comparison of bulk diffusion coefficients for different materials

The bulk diffusion coefficients of pure single- and poly-crystalline samples oxidized at 1350 ℃ at an oxygen partial pressure of 8.5×10^{-12} atm are roughly equivalent. However, the bulk diffusion coefficients for pure poly-crystals (annealed at 1500 ℃ and for oxygen pressures in the region of $9.4\times10^{-}$

^{13} atm and 5×10^{-12} atm) are approximately a half-order of magnitude higher than those of single-crystals. The differences between the bulk diffusion coefficients determined in single- and poly- crystalline materials may be a combined result of multiple factors which are foreign to the bulk properties of the material such as surface roughness, temperature gradient induced enriched-layer mobility (Matzke, 1983) as well as the effect of evaporation / condensation and their correlation to grain-orientation.

The uranium self-diffusion coefficient determined in the chromium-doped material (1.5×10^{-19} m^2/s) at 1500 ℃ is slightly higher than the diffusion coefficient determined for undoped poly-crystalline material (0.8×10^{-19} m^2/s). This value is nearly one order of magnitude larger than that of the single-crystal which was annealed simultaneously, hence under identical thermodynamic conditions. High temperature uranium diffusivity measurements under controlled atmosphere relating to UO_2 containing Cr_2O_3 additives do not exist. However, there are two sets of results relating to chromium doped UO_2 that provide circumstantial evidence of its effect on bulk diffusion. Previous work by Peres *et al.* (Peres et al., 2012; Peres and Dehaudt, 2002) suggests that chromium additives may enhance cation diffusivities. It is indeed known that additional of Cr enhances grain growth during sintering. The main explanation put forward for this has been the formation of a liquid CrO phase at the grain boundaries under certain favourable conditions. However, when Cr oxide is present even below its solubility level, so that no separate phases are formed, grain growth in Cr containing UO_2 is enhanced and this requires enhanced volume diffusion coefficients. Also, creep tests carried out on Cr_2O_3-doped UO_2 fuel by Dugay *et al.* (Dugay et al., 1998) at 1500 ℃ in a H_2 rich environment show that the fuel creep rate is greater under similar conditions than that of undoped UO_2. Although the exact oxygen partial pressure is unknown in these experiments, the results tend to indicate that the rate-controlling phenomenon which is cation self-diffusion coefficient is accelerated (Philibert, 1984). Kashibe *et al.* (Kashibe and Une, 1998) also observed that the Xenon diffusion coefficient in Cr_2O_3-doped UO_2 fuel (measured between 1500 ℃ and 1600 ℃ in a He + 8% H_2 gas equilibrium) is nearly three order of magnitude higher than in an undoped material.

Our experimental result on Cr-doped material is more consistent with Kashibe and Dugay's observations. However, no definite conclusion can be drawn regarding the effect of additives on uranium diffusivities due to the lack of additional data. More experiments are quite obviously required to clarify this point.

5.5.2 Effect of thermodynamic conditions on the uranium volume diffusion coefficient

a) D_U versus the deviation-from-stoichiometry

As shown in Table 5.2, we prepared single-crystal samples and annealed them under different conditions. The corresponding O/M ratio for each sample can be estimated based on the temperature and oxygen partial pressure. We present our uranium self-diffusion coefficients (volume diffusion) for $UO_{2.001}$, $UO_{2.002}$, and $UO_{2.004}$ in Figure 5.13 (orange squares) in comparison with results from the literature. Our results appear to be consistent with those of Marin and Contamin (Marin and Contamin, 1969) but are slightly lower than those provided by Matzke (Matzke, 1973) and Hawkins and Alcock (Hawkins and Alcock, 1968). One possible reason is that the annealing conditions for their experiments are different (*i.e.* more oxidizing than ours). It also maybe they have focussed on the depth profile relative to region II or III away which would provide higher diffusion coefficients.

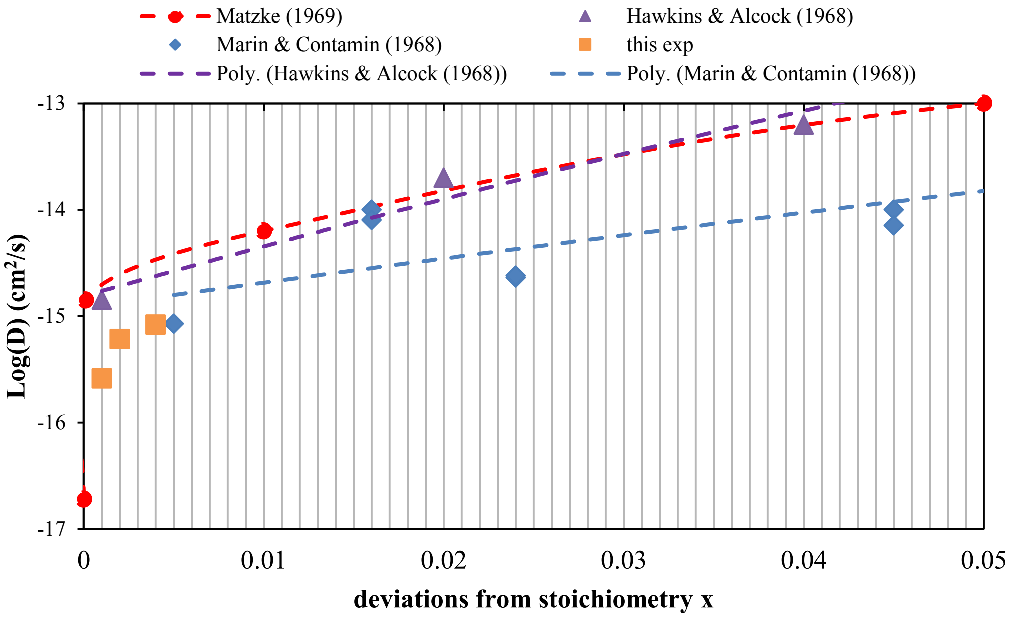

Figure 5.13: Our uranium self-diffusion coefficients for $UO_{2.001}$, $UO_{2.002}$, and $UO_{2.004}$ (orange square) in comparison to previously published results at 1500 ℃.

Since the deviation-from-stoichiometry is relatively small, it is also interesting to compare our results to reported self-diffusion coefficients of nominally stoichiometric material. An extrapolation of Sabioni's volume diffusion data (the red square on the blue dash line from reference (Sabioni et al., 1998)) to 1500 ℃ ($10^4/T = 5.75\ K^{-1}$) provides an approximate value of $2.3 \cdot 10^{-23}\ m^2/s$. Our uranium bulk diffusion coefficient of undoped single-crystal $UO_{2.001}$ (in blue), shown in Figure 5.14, is roughly three-orders of magnitude higher than the values derived from Sabioni's single-crystal data.

The reason for this, we believe, are the different oxygen partial pressures under which both experiments were carried out. Sabioni *et al.* carried out the diffusion experiment in pure H_2, so that the oxygen partial pressure in this case was much lower than in our experiment. The partial pressure measured at 650 ℃ would be expected to be in the region of 10^{-30} atm. which is about four or five orders of magnitude below the oxygen partial pressure of our experiment. The difference in diffusion coefficients could therefore be explained through the possibly linear dependence upon partial pressure in this region of the uranium vacancy concentration (Garcia et al., 2017).

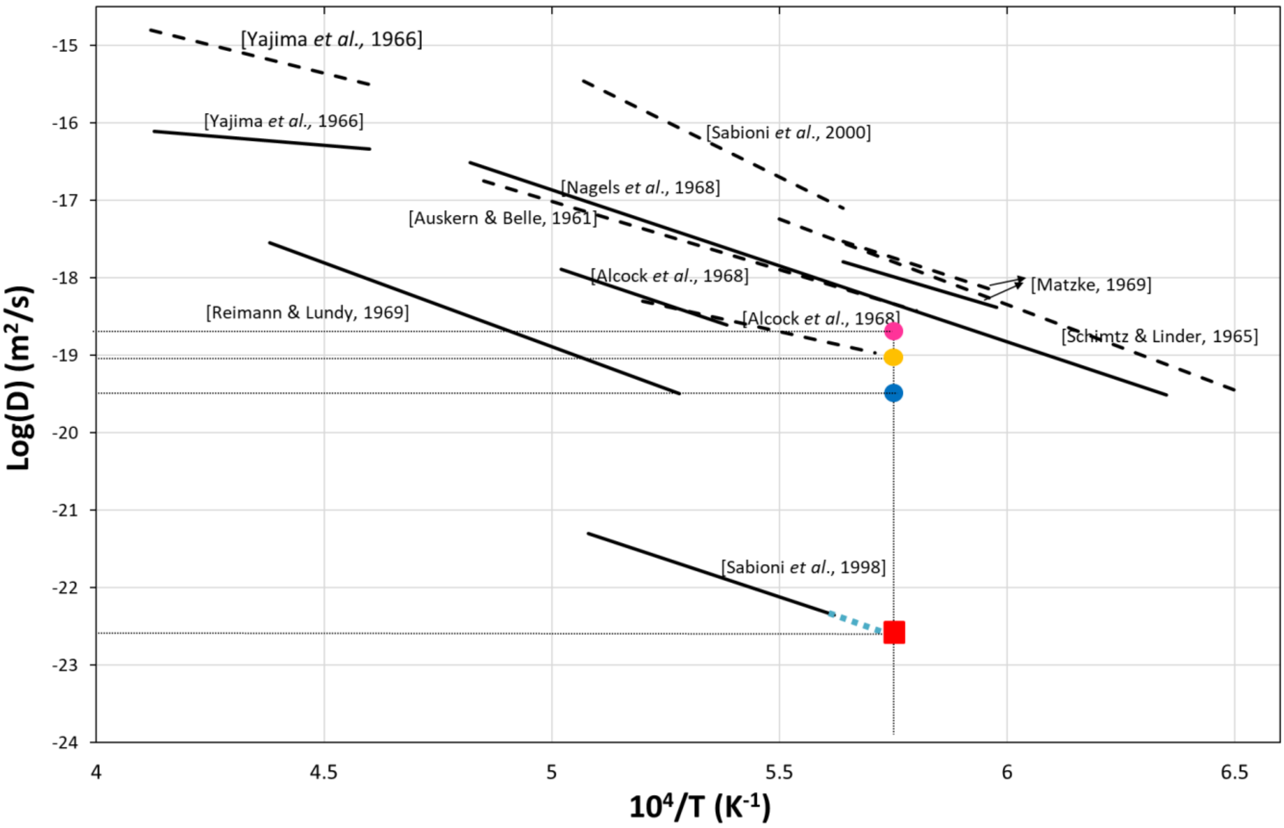

Figure 5.14: The uranium self-diffusion coefficients of $UO_{2.001}$ obtained in this work from single-crystal samples (blue), poly-crystalline (yellow), and Cr-doped (pink) materials annealed at 1500 ℃ and an oxygen partial pressure of $9.43 \cdot 10^{-13}$ atm compared to literature relating to nominally stoichiometric UO_2. The blue dotted line extrapolates Sabioni's single-crystal data (Sabioni et al., 1998) at a temperature of 1500 ℃; the red square is Sabioni's predicted value at 1500 ℃. Black solid lines are D_U results measured for single-crystals and dashed lines are D_U results measured for poly-crystals.

We also present here the bulk diffusion coefficients measured in undoped and Cr-doped poly-crystal $UO_{2.001}$ (the yellow and pink dots in Figure 5.14). Our bulk diffusion coefficient in poly-crystalline $UO_{2.001}$ is consistent with the extrapolation of Alcock's results at our experimental temperature (Alcock et al., 1966) which could suggest, although he does not quote the gas composition under which he carried out his experiment, a similar mechanism for uranium diffusion in single- and poly-crystalline UO_2.

5.6 Conclusion and prospects

Uranium self-diffusion was characterised in single- and poly- crystalline UO_{2+x} as well as chromium doped materials. Experiments were carried out at 1350 °C, 1500 °C and 1600 °C under different oxidizing conditions (between $9.4 \cdot 10^{-13}$ and $4.7 \cdot 10^{-11}$ atm oxygen partial pressure). A ^{235}U-enriched uranyl nitrate solution was first deposited at the surface of samples, which further transformed into a $^{235}UO_2$ layer following low temperature annealing. Diffusion of the isotopic tracer ^{235}U was characterized by Secondary Ion Mass Spectrometry. The depths corresponding to all SIMS craters on the surface of the samples were characterised with a chromatic confocal microscope. This enables us to have a concentration profile for each crater. The depth resolution for each profile, which in part determines the error associated with uranium self-diffusion coefficient, is obtained using a Monte Carlo method.

For each crater, the average depth profile was modelled using an analytical solution to the diffusion equation. The solution assumes the surface material is evaporating or condensing at a certain rate. We obtained uranium self-diffusion coefficients for the poly-crystalline samples, which in general are half-order of magnitude higher than those of the single-crystal materials annealed at the same condition, which is approximately three orders of magnitude higher than the reported volume diffusion coefficient for nominally stoichiometric UO_2. This difference is ascribed to oxygen partial pressure effects. We have shown that the method of depositing uranyl nitrate for the isotopic $^{235}UO_2$ layers at the sample surfaces leads to a layer thickness which can be estimated from the amount of uranyl nitrate initially deposited. However, it is evident that this enriched layer is very unevenly deposited and this induces roughness. A model analysis provides estimates of the bulk diffusion coefficient and the effective thickness of the enriched oxide layer prior to rastering, which is consistent with the experimental roughness determined by the chromatic confocal microscopy. However, there are a number of complicating factors which make these experiments difficult to interpret unequivocally; some which could be avoided in future experiments, but others which are inherent to the method. These complicating factors lead to depth profiles which are not systematically reproducible from one point of the surface to another of a given sample. Amongst these factors we have identified:

- The initial surface roughness of the material.
- The roughness induced by the deposit and the heterogenous distribution of this deposit.
- Evaporation phenomena which appear to be dependent upon the thermohydraulic conditions in which samples are annealed.
- The sputtering rate variations from one grain to another in polycrystalline samples.

Despite this, a number of additional conclusions may be drawn. Ionic images of polycrystalline samples collected by SIMS at different depths do not show the expected contrast if accelerated grain boundary diffusion was operative. This is consistent with the comment made above about diffusion coefficients in single and poly crystals. The bulk diffusion coefficient obtained for a Cr-doped sample appears to be higher than in the undoped material. However, this result needs to be further validated by performing additional diffusion experiments in different conditions. Also in order to precisely determine the uranium self-diffusion coefficient in Cr-doped materials, raster time for future SIMS characterization should be longer so that the crater is deep enough to be identified under the confocal microscope.

To further investigate the uranium diffusion mechanisms in UO_{2+x}, we have designed several other diffusion experiments to be carried out at various temperatures and oxygen partial pressures. Also, the surface preparation of poly-crystalline samples leads to a level of roughness which substantially deteriorates the depth resolution. This issue has to be addressed by improved experimental design, for example, by means of preparing samples in sandwich form and characterizing them with the nano-SIMS.

Chapter 6 Overall discussion, conclusions and prospects

Thesis objective and scope

Uranium dioxide is an oxygen excess, non-stoichiometric fuel material which exists over a wide range of compositions. Both stoichiometric and hyper-stoichiometric fuels have been studied over several decades, the latter of which is more relevant to the technological and industrial applications of nuclear power generation. In the hyper-stoichiometric domain, excess oxygen ions absorbed from the gas phase are incorporated within the lattice at interstitial sites and this leads to the oxidation of uranium ions (Willis, 1964). A great effort has been devoted to understanding the oxygen defects behaviour and corresponding induced changes in important fuel properties such as deviation-from-stoichiometry (Perron, 1968), oxygen activity (Ruello et al., 2004) and diffusivity (Garcia et al., 2010). However, the picture of oxygen defect structures or clusters, for example in a range between 0 and 0.25, is still not clear, which in result leads to a lack of knowledge in proper defect models at given compositions for interpreting fuel properties in the corresponding phase domain.

Understanding and predicting fuel behaviour at all stages of the fuel cycle requires measuring and controlling their basic engineering properties, the majority of which are governed by the nature and behaviour of point defects existing not only on anion sublattice, but more importantly on the cation sublattice. For example, the cation transport property is known as a rate-determining step for diffusion-controlled mass transport such as grain-growth, sintering, creep, etc. The prerequisite for these microstructure deformations is the migration of fuel cations and anions which is proved by experimental studies and first-principles calculations occurring via a vacancy mechanism (Dorado et al., 2012; Matzke, 1973). However, characterising cation defect (mainly uranium vacancy) in UO_{2+x} and its corresponding properties, cation diffusion for instance, is a complicated task as it involves a much slower process than oxygen diffusion and occurring at higher temperature. Diffusion mechanism is also complicated to understand as it may involve grain-boundaries regarding poly-crystalline material and also effect of additives.

In addition to the difficulties mentioned above, prior to this work, although abundant experimental and computational data regarding defect dependent properties, for instance uranium self-diffusion or fuel creep, were available, results were quite scattered. Contradictory and less reproducible results are thought to mainly be due to insufficient control and monitoring of all the thermodynamics variables, i.e. temperature and oxygen partial pressure, that the samples were subjected to.

Therefore, this work has been dedicated to study both cation and anion point defects, and their behaviours in UO_2 and UO_{2+x}. Two strategies have been adopted: The first one is to have direct characterizations via advanced diffraction or spectroscopic techniques; The second one is to measure important macroscopic fuel properties to understand the correlations related to microscopic defects behaviour. A comprehensive and systematic research was made possible in this work by adopting an original and trusted experimental strategy, i.e. measuring fuel properties as function of all the physical variables which determine them – temperature and composition. The latter quantity is determined, depending on the temperature range of interest, by the equilibrium oxygen partial pressure and the concentrations of bi- or tri-valent impurities presented on the uranium sub-lattice.

To characterize the point defects in UO_2 and UO_{2+x}, two advanced experimental techniques were implemented in this thesis: 1) neutron scattering followed with the pair distribution function (PDF) analysis to probe the atomic local arrangements; 2) Positron annihilation spectroscopy (PAS) for defects study (vacancy-type defects mainly), including positron annihilation Doppler broadening and lifetime spectroscopy. Poly-crystalline samples were prepared from sintered pellets and oxidized under well controlled thermodynamic conditions in terms of temperature and oxygen partial pressure for these two studies. Samples were quenched at the end of oxidation sequence to 'freeze' the oxygen distributions and corresponding deviations-from-stoichiometry, in which case the nature of the defects and populations in one sample may be directly correlated with its corresponding annealing conditions.

Summary of neutron scattering results and defect clustering

Neutron scattering experiments were carried out on UO_2 and UO_{2+x} ($x \approx 0.007$, and $x \approx 0.16$) at D4c diffractometer ILL Grenoble. D4c is equipped with a monoenergetic neutron beam of a small wavelength (~0.5 Å) in order to explore a large range in the reciprocal space and thus to benefit from a high real-space resolution in the Pair distribution function analysis. This latter has allowed a study of the local disorder in the oxygen sub-lattice by picking up the diffuse scattering intensities between the Bragg peaks.

Results related to thermal expansion and lattice parameters for stoichiometric UO_2 have confirmed the experiment and data processing. In addition, we have have further shown from the PDF analysis that oxygen ions are displaced in such a way that the local distortions responsible for their anharmonic thermal motions are locally consistent with the $Pa\bar{3}$ symmetry. This has been considered in the PDF and Rietveld refinements of hyper-stoichiometric UO_{2+x} as well which further shed a light upon the defect structures in the single phase, high-temperature region (900°C).

We have compared the experimental PDF data of UO_{2+x} to those calculated from either the conventional fourfold cell, or the supercells up to a size of 4×4×4. The PDF analysis of two UO_{2+x} samples suggests that interstitial oxygen ions can be displaced along either <110> or <111> directions. The refinement for the $UO_{2.007}$ sample indicates the system is too dilute to differentiate between isolated or di-interstitial clusters. The weak contribution from the low concentration defects to the PDF could be in part hidden by the oxygen Frenkel defects which are not taken into account in the cell model. For the higher deviation from stoichiometry material, i.e. $UO_{2.16}$, several defect structures are tested. Site occupancies determined from fourfold cell analysis compare well with those determined by Willis (Willis, 1978) although our refinements lead to centre occupied cuboctahedron clusters rather than 2:2:2 clusters.

As discussed in Chapter 3, the PDF analysis results suggests that increasing non-stoichiometry favours both anion clustering and a decrease in the charge state of the most stable clusters. An *ab initio* theoretical study of the electronic structure of Uranium L_3 near edge Xray absorption fine structure, NEXAFS, of different oxidation states of U in UO_x by Nelin et al. has come to the same idea (Nelin et al., 2014). Literature studies by electrical conductivity measurements (Garcia et al., 2017) have also shown that as deviation from stoichiometry increases doubly charged isolated interstitials give way to single charged di-interstitials. The overall charge of the cluster tends to be neutral and their concentration increases as deviation from stoichiometry rises.

Oxygen centre occupied cuboctahedra are the elemental constituents of U_4O_9 (Cooper and Willis, 2004; Desgranges et al., 2016). They precipitate in UO_2 as a secondary β-U_4O_9 phase as UO_{2+x} solid solution becomes saturated with them. Such a precipitation appears to occur along specific crystal directions with, according to literature, platelets observed under the SEM, parallel to {111} planes thus drawing the so-called Widmanstätten features. Recent molecular dynamic calculations by Aidhy et al. simulated a defect clustering process in Urania and Ceria under irradiation (Aidhy et al., 2011). The results suggested that Frenkel pairs forming first <111> Schottky defects then clustering into a cuboctahedron cluster with a uranium at the centre during the kinetic phase of thermal annealing both in stoichiometric UO_2 at 1000K and CeO_2 at 300K. At high enough temperatures clusters tend to evolve toward dislocation loops lying in the {111} planes with Burger vector in the <111> direction.

Another aspect of the clustering phenomenon is that as oxygen anions move, U-O distances change as well as the relative directions of U-O bonds around U cations. This would lead to a change in the bonding to be partially covalent. This may explain the asymmetric structure of the cuboctahedra cluster we determined from the PDF analysis, as not all the bonds have shown the same degree of covalence.

Summary of defect characterizations by positron annihilation spectroscopy

Neutron scattering experiment and the PDF analysis have demonstrated their capacity to identify mainly the nature of oxygen defects and clusters. The second method implemented in this thesis, positron annihilation spectroscopy, has shown its superiority at studying both cation and anion defects in UO_{2+x}. This method, which has rarely been applied in actinide oxides, was designed to characterize microscopic vacancy-type defects (Labrim et al., 2006), dislocations (Trumpy, 1994) or open volumes (Barthe et al., 2004). To this end, poly-crystalline UO_{2+x} samples annealed at high temperature under oxidizing equilibria were studied, and we may draw two fundamental conclusions about the phenomena involved:

- Positron lifetime in UO_{2+x} increases when vacancy defects are present. However, positron lifetime determined for oxygen defects is the same as for the lattice since positrons are sampling the same electronic density of the lattice.
- Doppler broadening spectroscopy however, is very sensitive to the chemical environment, therefore to the presence of oxygen clusters. The increasing quantity of oxygen defects leads to a decrease in low momentum fraction while the emergence of uranium vacancy tends to increase the low momentum distribution.

Also, we have developed a three-state trapping model that has taken into account positron annihilation in the major point defects in UO_{2+x}, i.e. negatively charged oxygen interstitials (shallow traps), negatively charged uranium vacancies and neutral uranium vacancies. Positron detrapping from the Rydberg states of shallow traps and even trapping again in deep traps have all been considered. By using this trapping model, uranium vacancy concentrations at two different compositions – 2.042 and 2.16, and at different temperatures – 35 K and 300K, have been estimated. In this work, trapping coefficients in various localised states were unknown, and were simply estimated from reference values suggested by literature (Krause-Rehberg and Leipner, 1999b; Puska et al., 1990). Still, the uranium vacancy concentrations reported in Chapter 4 are considered reliable because the derived oxygen defect concentrations in two samples are consistent with our knowledge of oxygen defects nature and amounts. Therefore one significance of this work is to provide a reference for determining positron trapping coefficients for various types of defects, and also for understanding the future positron trapping mechanisms.

Summary of uranium self-diffusion study and its correlations with defect study in this work

The fuel property focused in this thesis is uranium self-diffusion. To understand the effect of microstructure (e.g. grain-boundary) and additives, three kinds of material were looked into: single-crystals, small grain-size poly-crystalline and Cr-doped poly-crystalline materials. Characterization of cation self-diffusion usually relies on the isotopic exchange methods in the solid-state with isotopic tracers of ^{235}U. Therefore, samples to be used to study uranium diffusion are prepared as follows: 1) sample being fully equilibrated under certain oxygen partial pressure and temperature, 2) sample being deposited with a ^{235}U enriched uranyl nitrate layer, 3) sample being low-temperature annealed to transform nitrate layer into oxide, and 4) sample being diffusion annealed at the same conditions as in stage 1. Diffusion of the ^{235}U tracer in each sample was characterized by the SIMS.

A thorough examination of the crater depth profile has identified several factors that increase the complexity of the analysis, which are a) surface roughness prior to the deposit and induced by the deposit, b) grain-orientation effect, and c) evaporations of the solid matter occurring in diffusion annealing. Uranium self-diffusion coefficients have been obtained for different micro-structures and annealing conditions. This was done by modelling the depth profiles using an ideal solution of the Fick’s second law which have account the factors described above. Uranium bulk self-diffusion coefficients determined from single-crystal and poly-crystalline samples are very close at 1350 ℃ and 1500 ℃, and there is no evidence of grain-boundary diffusion in the poly-crystalline material. The analysis of depth profiles has indicated that the chromium additive appears to accelerate the diffusivity of uranium.

As presented in Chapter 2, we have systematically prepared three microstructures, three temperatures (1350 ℃, 1500 ℃, and 1600 ℃) at the same oxygen partial pressure, and three oxygen partial pressure at the same temperature. However, only a proportion of the samples we prepared are characterized by SIMS. Characterizations on the rest of samples in the future would improve the understanding of uranium self-diffusion mechanisms.

With the diffusion coefficients obtained so far, we have estimated the dependence of bulk diffusion coefficient D_U upon oxygen partial pressure, which at 1500 ℃ is a power law function of the oxygen partial pressure, with an exponent of **0.34**. As demonstrated in Chapter 1, section 1.3.2, the uranium vacancy concentration is a power law function of the oxygen partial pressure. The exponent upon the pre-exponential factor $A{\cdot}p_{O_2}^{\alpha}$ derived from the estimated uranium vacancy populations in $UO_{2.042}$ and $UO_{2.16}$ by positron annihilation spectroscopy (see section 4.3.4 Chapter 4) at room temperature is **0.22**. These results are also consistent with the correlation determined from the latest creep tests on poly-crystalline pellets performed in identical conditions. It is also consistent with the following hypotheses:

1- That oxygen interstitials remain isolated;
2- The electroneutrality equation is given by a balance between the U^{5+} ion concentration and negatively charged anion interstitials;
3- Presence of chottky and oxygen Frenkel disorder;

Indeed from the above hypotheses which are reasonable considering the levels of deviation from stoichiometry, **an exponent of 1/3** is expected.

Uranium diffusion is the time limiting phenomenon leading under some assumptions to the creep of UO_2 material (diffusional creep in particular). Therefore, this study is quite useful because the understanding it gives of the diffusion phenomena could help modelling the pellet-cladding interaction and also optimizing the fuel to limit creep under irradiation.

Prospects

Our work has no doubt provided some essential insights into cation vacancies and anion cluster behaviour, and corresponding macroscopic properties. It has allowed a thorough comprehension of point defects in hyper-stoichiometric fuel and their impact on cation diffusion property. But deepening the understanding is still necessary. For this purpose, several recommendations are proposed:

In the future, as it is suggested in Chapter 3, it appears diffraction and PDF data of different samples with intermediated compositions, or at different temperatures would be interesting to look into. Also, other novel methods may be attempted to study the local disorder induced by the presence of anion defects. For example, instead of applying Placzek's corrections, the inelastic neutron scattering intensities may be retained to extract information of local dynamics in our UO_{2+x} material by means of a complementary analysis to the PDF method – the Dynamic atomic Pair Density Function analysis (Egami and Dmowski, 2012). Another approach that could be worth investigating would be to interpret both elastic and diffuse scattering simultaneously in order to further understand the relationship between long- and short- range ordering.

Positron annihilation spectroscopy has been proved to be a well-developed method for defects study in fuel material. On the basis of this work, more efforts should be devoted to obtaining the annihilation fractions of positrons in various traps. Future work may be also dedicated to improving the understanding of trapping mechanisms and obtaining the trapping coefficients by both experimental and computational research. Complementary lifetime experiments at various temperatures on samples annealed at different oxidation conditions may be interesting as well to understand the evolution of vacancy defects charges and concentrations as a function of stoichiometry. Samples prepared following the low-temperature oxidation, i.e. containing no uranium vacancy defects, can be characterized by Doppler broadening spectroscopy to see how the charge state and concentrations modify as function of deviations-from-stoichiometry.

In current self-diffusion experiments the major problem is the surface roughness which further complicates the depth profile analysis and induces substantial uncertainties in the determined uranium self-diffusion coefficients. One of the solution to this problem is to prepare ‘sandwich couples’ of depleted and ^{235}U enriched disks cut from sintered poly-crystalline pellets. The sandwich couple after diffusion annealing may be characterized by means of the nano-SIMS technique.

References

Aidhy, D.S., Wolf, D., El-Azab, A., 2011. Comparison of point-defect clustering in irradiated CeO2 and UO2: A unified view from molecular dynamics simulations and experiments. Scr. Mater. 65, 867–870. doi:10.1016/j.scriptamat.2011.07.051

Alatalo, M., Barbiellini, B., Hakala, M., Kauppinen, H., Korhonen, T., Puska, M.J., Saarinen, K., Hautojärvi, P., Nieminen, R.M., 1996. Theoretical and experimental study of positron annihilation with core electrons in solids. Phys. Rev. B Condens. Matter 54, 2397–2409.

Alcock, C.B., Hawkins, R.J., Hills, A.W.D., McNamara, P., 1966. A Study of Cation Diffusion in Stoichiometric UO_2 Using α-Ray Spectrometry.

Allen, G.C., Tempest, P.A., 1983. The accommodation of oxygen clusters in hyperstoicheiometric uranium dioxide and its effects on crystal structure. J. Chem. Soc. Dalton Trans. 0, 2673–2677. doi:10.1039/DT9830002673

Ambler, J.F.R., Slattery, G.F., 1961. New metallographic techniques for the examination of uranium, uranium alloys and uranium dioxide. J. Nucl. Mater. 4, 90–99. doi:10.1016/0022-3115(61)90153-2

Andersson, D.A., Espinosa-Faller, F.J., Uberuaga, B.P., Conradson, S.D., 2012. Stability and migration of large oxygen clusters in UO2+x: Density functional theory calculations. J. Chem. Phys. 136, 234702. doi:10.1063/1.4729842

Andersson, D.A., Garcia, P., Liu, X.-Y., Pastore, G., Tonks, M., Millett, P., Dorado, B., Gaston, D.R., Andrs, D., Williamson, R.L., Martineau, R.C., Uberuaga, B.P., Stanek, C.R., 2014. Atomistic modeling of intrinsic and radiation-enhanced fission gas (Xe) diffusion in UO2±x: Implications for nuclear fuel performance modeling. J. Nucl. Mater. 451, 225–242. doi:10.1016/j.jnucmat.2014.03.041

Andersson, D.A., Uberuaga, B.P., Nerikar, P.V., Unal, C., Stanek, C.R., 2011. U and Xe transport in UO2±x: Density functional theory calculations. Phys. Rev. B 84, 054105. doi:10.1103/PhysRevB.84.054105

Andersson, D.A., Watanabe, T., Deo, C., Uberuaga, B.P., 2009. Role of di-interstitial clusters in oxygen transport in UO2+x from first principles. Phys. Rev. B 80, 060101. doi:10.1103/PhysRevB.80.060101

Armstrong, W.M., Irvine, W.R., 1963. Creep deformation of non-stoichiometric uranium dioxide. J. Nucl. Mater. 9, 121–127. doi:10.1016/0022-3115(63)90127-2

Ashby, M.F., Verrall, R.A., 1973. Diffusion-accommodated flow and superplasticity. Acta Metall. 21, 149–163. doi:10.1016/0001-6160(73)90057-6

Ashcroft, N.W., Mermin, N.D., 1976. Solid state physics. Saunders College.

Aucouturier, M., Blaise, G., Darque-Ceretti, E., 1989. La micro-analyse ionique (SIMS) aspects fondamentaux, in: Ammou, M. (Ed.), Microcaractérisation Des Solides. Sophia Antipolis, p. 67.

Auskern, A.B., Belle, J., 1961. Uranium ion self diffusion in UO2. J. Nucl. Mater. 3, 311–319. doi:10.1016/0022-3115(61)90199-4

Bagus, P.S., Nelin, C.J., 2014. Covalent interactions in oxides. J. Electron Spectrosc. Relat. Phenom., Core-Level Spectroscopies of Actinides 194, 37–44. doi:10.1016/j.elspec.2013.11.004

Bai, X.-M., El-Azab, A., Yu, J., Allen, T.R., 2013. Migration mechanisms of oxygen interstitial clusters in UO 2. J. Phys. Condens. Matter 25, 015003. doi:10.1088/0953-8984/25/1/015003

Baichi, M., Chatillon, C., Ducros, G., Froment, K., 2006. Thermodynamics of the O–U system. IV – Critical assessment of chemical potentials in the U–UO2.01 composition range. J. Nucl. Mater. 1–2, 17–56. doi:10.1016/j.jnucmat.2005.09.001

Barthe, M.-F., Corbel, C., Blondiaux, G., 2003. Caractérisation de défauts lacunaires par annihilation de positons. Tech. Ing. Méthodes Nucl. Anal. base documentaire : TIB389DUO.

Barthe, M.F., Guilbert, S., Labrim, H., Desgardin, P., Sauvage, T., Blondiaux, G., Carlot, G., Garcia, P., Piron, J.P., 2004. Near Surface Vacancy Defects in Sintered Polished UO2 Disks. Mater. Sci. Forum 445–446, 48–50. doi:10.4028/www.scientific.net/MSF.445-446.48

Barthe, M.-F., Labrim, H., Gentils, A., Desgardin, P., Corbel, C., Esnouf, S., Piron, J.P., 2007. Positron annihilation characteristics in UO2: for lattice and vacancy defects induced by electron irradiation. Phys. Status Solidi C 4, 3627–3632. doi:10.1002/pssc.200675752

Belle, J., 1969. Oxygen and uranium diffusion in uranium dioxide (a review). J. Nucl. Mater. 30, 3–15. doi:10.1016/0022-3115(69)90163-9

Bergersen, B., Pajanne, E., Kubica, P., Stott, M.J., Hodges, C.H., 1974. Positron diffusion in metals. Solid State Commun. 15, 1377–1380. doi:10.1016/0038-1098(74)91384-2

Bès, R., Martin, P., Vathonne, E., Delorme, R., Sabathier, C., Freyss, M., Bertolus, M., Glatzel, P., 2015. Experimental evidence of Xe incorporation in Schottky defects in UO2. Appl. Phys. Lett. 106, 114102. doi:10.1063/1.4914300

Bevan, D.J.M., Grey, I.E., Willis, B.T.M., 1986. The crystal structure of β-U4O9−y. J. Solid State Chem. 61, 1–7. doi:10.1016/0022-4596(86)90002-2

Bohaboy, P.E., Asamoto, R.R., Conti, A.E., 1969. Compressive creep characteristics of stoichiometric uranium dioxide (No. GEAP-10054), AEC Research and Development report. U.S. Atomic Energy Commision, Sunnyvale, California, USA.

Bourdineaud-Bordere, S., 1989. Etude de la thermolyse du nitrate d’uranyle hexahydrate en vue de l’obtention d’oxydes poreux et divises (PhD Thesis). Universite de Aix-Marseille, Marseille.

Brandt, O.G., Walker, C.T., 1967. Temperature Dependence of Elastic Constants and Thermal Expansion for UO2. Phys. Rev. Lett. 18, 11–13. doi:10.1103/PhysRevLett.18.11

Brandt, W., Arista, N., 1982. Thermalization and diffusion of positrons in solids. Phys. Rev. B 26, 4229–4238.

Brauer, G., Anwand, W., Nicht, E.-M., Kuriplach, J., Šob, M., Wagner, N., Coleman, P.G., Puska, M.J., Korhonen, T., 1996. Evaluation of some basic positron-related characteristics of SiC. Phys. Rev. B 54, 2512–2517. doi:10.1103/PhysRevB.54.2512

Breitung, W., 1978. Oxygen self and chemical diffusion coefficients in UO2±x. J. Nucl. Mater. 74, 10–18. doi:10.1016/0022-3115(78)90527-5

Brillant, G., Gupta, F., Pasturel, A., 2011. Fission products stability in uranium dioxide. J. Nucl. Mater. 412, 170–176. doi:10.1016/j.jnucmat.2011.02.054

Brincat, N.A., Molinari, M., Parker, S.C., Allen, G.C., Storr, M.T., 2015. Computer simulation of defect clusters in UO2 and their dependence on composition. J. Nucl. Mater. 456, 329–333. doi:10.1016/j.jnucmat.2014.10.001

Brutzel, L.V., Delaye, J.-M., Ghaleb, D., Rarivomanantsoa, M., 2003. Molecular dynamics studies of displacement cascades in the uranium dioxide matrix. Philos. Mag. 83, 4083–4101. doi:10.1080/14786430310001616081

Burton, B., Reynolds, G.L., 1973a. The diffusional creep of uranium dioxide: its limitation by interfacial processes. Acta Metall. 21, 1073–1078. doi:10.1016/0001-6160(73)90023-0

Burton, B., Reynolds, G.L., 1973b. The influence of deviations from stoichiometric composition on the diffusional creep of uranium dioxide. Acta Metall. 21, 1641–1647. doi:10.1016/0001-6160(73)90107-7

Caneiro, A., Bonnat, M., Fouletier, J., 1981. Measurement and regulation of oxygen content in selected gases using solid electrolyte cells. IV. Accurate preparation of CO2-CO and H2O-H2 mixtures. J. Appl. Electrochem. 11, 83–90. doi:10.1007/BF00615326

Catlow, C.R.A., 1978. Fission gas diffusion in uranium dioxide. Proc R Soc Lond A 364, 473–497. doi:10.1098/rspa.1978.0213

Catlow, C.R.A., 1977. Point defect and electronic properties of uranium dioxide. Proc R Soc Lond A 353, 533–561. doi:10.1098/rspa.1977.0049

Catlow, C.R.A., 1976a. The defect properties of anion-excess alkaline-earth fluorides. II. Intermediate and high dopant concentrations. J. Phys. C Solid State Phys. 9, 1859. doi:10.1088/0022-3719/9/10/006

Catlow, C.R.A., 1976b. The defect properties of anion-excess alkaline-earth fluorides. I. Low defect concentrations. J. Phys. C Solid State Phys. 9, 1845. doi:10.1088/0022-3719/9/10/005

Cheetham, A.K., Fender, B.E.F., Cooper, M.J., 1971. Defect structure of calcium fluoride containing excess anions I. Bragg scattering. J. Phys. C Solid State Phys. 4, 3107. doi:10.1088/0022-3719/4/18/016

Chung, T.E., Davies, T.J., 1979. The low-stress creep of fine-grain uranium dioxide. Acta Metall. 27, 627–635. doi:10.1016/0001-6160(79)90014-2

Coble, R.L., 1963. A Model for Boundary Diffusion Controlled Creep in Polycrystalline Materials. J. Appl. Phys. 34, 1679–1682. doi:10.1063/1.1702656

Contamin, P., Bacmann, J.J., Marin, J.F., 1972. Autodiffusion de l'oxygene dans le dioxyde d'uranium surstoechiometrique. J. Nucl. Mater. 42, 54–64. doi:10.1016/0022-3115(72)90007-4

Cooper, R.I., Willis, B.T.M., 2004. Refinement of the structure of β-U4O9. Acta Crystallogr. A 60, 322–325. doi:10.1107/S010876730401219X

Crocombette, J.-P., 2012. Influence of charge states on energies of point defects and clusters in uranium dioxide. Phys. Rev. B 85, 144101. doi:10.1103/PhysRevB.85.144101

Crocombette, J.-P., Torumba, D., Chartier, A., 2011. Charge states of point defects in uranium oxide calculated with a local hybrid functional for correlated electrons. Phys. Rev. B 83, 184107. doi:10.1103/PhysRevB.83.184107

Croff, A.G., 1980. ORIGEN2: a revised and updated version of the Oak Ridge isotope generation and depletion code (No. ORNL--5621). Oak Ridge National Lab.

Desgranges, L., Baldinozzi, G., Fischer, H.E., Garcia, P., Simeone, D., Ma, Y., 2014. Characterisation of cuboctahedra in UO2+x as function of temperature (No. DOI:10.5291/ILL-DATA.6-06-453). Institut Laue-Langevin (ILL), Grenoble, France.

Desgranges, L., Baldinozzi, G., Simeone, D., Fischer, H.E., 2016. Structural Changes in the Local Environment of Uranium Atoms in the Three Phases of U4O9. Inorg. Chem. 55, 7485–7491. doi:10.1021/acs.inorgchem.6b00654

Desgranges, L., Baldinozzi, G., Siméone, D., Fischer, H.E., 2011. Refinement of the α-U4O9 Crystalline Structure: New Insight into the U4O9 → U3O8 Transformation. Inorg. Chem. 50, 6146–6151. doi:10.1021/ic200316b

Desgranges, L., Ma, Y., Garcia, P., Baldinozzi, G., Siméone, D., Fischer, H.E., 2017. What Is the Actual Local Crystalline Structure of Uranium Dioxide, UO2? A New Perspective for the Most Used Nuclear Fuel. Inorg. Chem. 56, 321–326. doi:10.1021/acs.inorgchem.6b02111

Dherbey, F., Louchet, F., Mocellin, A., Leclercq, S., 2002. Elevated temperature creep of polycrystalline uranium dioxide: from microscopic mechanisms to macroscopic behaviour. Acta Mater. 50, 1495–1505. doi:10.1016/S1359-6454(02)00007-1

Dieckmann, R., 1984. Point defects and transport properties of binary and ternary oxides. Solid State Ion. 12, 1–22. doi:10.1016/0167-2738(84)90126-7

Dorado, B., Andersson, D.A., Stanek, C.R., Bertolus, M., Uberuaga, B.P., Martin, G., Freyss, M., Garcia, P., 2012. First-principles calculations of uranium diffusion in uranium dioxide. Phys. Rev. B 86, 035110. doi:10.1103/PhysRevB.86.035110

Dorado, B., Freyss, M., Martin, G., 2009. GGA+U study of the incorporation of iodine in uranium dioxide. Eur. Phys. J. B 69, 203–209. doi:10.1140/epjb/e2009-00145-0

Dorado, B., Jomard, G., Freyss, M., Bertolus, M., 2010. Stability of oxygen point defects in ${\text{UO}}_{2}$ by first-principles $\text{DFT}+U$ calculations: Occupation matrix control and Jahn-Teller distortion. Phys. Rev. B 82, 035114. doi:10.1103/PhysRevB.82.035114

Dugay, C., Mocellin, A., Dehaudt, P., Sladkoff, M., 1998. High temperature mechanical tests performed on doped fuels.

Dupasquier, A., Mills, J.A.P. (Eds.), 1997. Positron Spectroscopy of Solids.

Egami, T., Billinge, S., 2012. Underneath the Bragg Peaks, 2. Pergamon.

Egami, T., Dmowski, W., 2012. Dynamic pair-density function method for neutron and X-ray inelastic scattering. Z. Für Krist. Cryst. Mater. 227, 233–237. doi:10.1524/zkri.2012.1500

Eldrup, M., Singh, B.N., 2003. Accumulation of point defects and their complexes in irradiated metals as studied by the use of positron annihilation spectroscopy – a brief review. J. Nucl. Mater., Proceedings of the Second IEA Fusion Materials Agreement Workshop on Modeling and Experimental Validation 323, 346–353. doi:10.1016/j.jnucmat.2003.08.011

Ewing, R.C., 2015. Long-term storage of spent nuclear fuel. Nat. Mater. 14, 252–257. doi:10.1038/nmat4226

Farrow, C.J., Juhas, P., Liu, J.W., Bryndin, D., Božin, E.S., Bloch, J., Proffen, T., Billinge, S.J.L., 2016. PDFgui User Guide (No. DMR-0520547).

Farrow, C.L., Juhas, P., Liu, J.W., Bryndin, D., Božin, E.S., Bloch, J., Proffen, T., Billinge, S.J.L., 2007. PDFfit2 and PDFgui: computer programs for studying nanostructure in crystals. J. Phys. Condens. Matter 19, 335219. doi:10.1088/0953-8984/19/33/335219

Farrow, C.L., Shaw, M., Kim, H., Juhas, P., Billinge, S.J.L., 2011. The Nyquist-Shannon sampling theorem and the atomic pair distribution function. Phys. Rev. B 84. doi:10.1103/PhysRevB.84.134105

Fischer, H.E., 2016. Introduction to Neutron Powder Diffraction and PDF-analysis.

Fischer, H.E., 2013. Techniques in Diffraction (X or N): S(q), PDF analysis, Deconvolution.

Fischer, H.E., Cuello, G.J., Palleau, P., Feltin, D., Barnes, A.C., Badyal, Y.S., Simonson, J.M., 2002. D4c: A very high precision diffractometer for disordered materials. Appl. Phys. A 74, s160–s162. doi:10.1007/s003390101087

Fouletier, J., Seinera, H., Kleitz, M., 1975. Measurement and regulation of oxygen content in selected gases using solid electrolyte cells. II. Differential gauge. J. Appl. Electrochem. 5, 177–185. doi:10.1007/BF01637267

Frandsen, B., Yang, X., Billinge, S.J.L., 2014. Magnetic pair distribution function analysis of local magnetic correlations. Acta Crystallogr. Sect. Found. Adv. 70, 3–11. doi:10.1107/S2053273313033081

Frandsen, B.A., Billinge, S.J.L., 2015. Magnetic structure determination from the magnetic pair distribution function (mPDF): ground state of MnO. Acta Crystallogr. Sect. Found. Adv. 71, 325–334. doi:10.1107/S205327331500306X

Frazer, B.C., Shirane, G., Cox, D.E., Olsen, C.E., 1965. Neutron-Diffraction Study of Antiferromagnetism in UO2. Phys. Rev. 140, 1448–1452. doi:10.1103/PhysRev.140.A1448

Garcia, P., 2011. Cahier des charges : fourniture d'une installation de recuit thermique et de mesure de propriétés de transport dans les systèmes oxydes (Note Technique No. NT 11-007). DEC/SESC/LLCC, CEA Cadarache.

Garcia, P., Fraczkiewicz, M., Davoisne, C., Carlot, G., Pasquet, B., Baldinozzi, G., Siméone, D., Petot, C., 2010. Oxygen diffusion in relation to p-type doping in uranium dioxide. J. Nucl. Mater. 400, 112–118. doi:10.1016/j.jnucmat.2010.02.019

Garcia, P., Pizzi, E., Dorado, B., Andersson, D.A., Crocombette, J.-P., Martial, C., Baldinozzi, G., Simeone, D., Maillard, S., Martin, G., 2017. A defect model for UO2+x based on electrical conductivity and deviation from stoichiometry measurements. J. Nucl. Mater. 494, 461–478.

Geng, H.Y., Chen, Y., Kaneta, Y., Iwasawa, M., Ohnuma, T., Kinoshita, M., 2008. Point defects and clustering in uranium dioxide by LSDA+U calculations. Phys. Rev. B 77. doi:10.1103/PhysRevB.77.104120

Gracia, L., Beltrán, A., Andrés, J., 2007. Characterization of the High-Pressure Structures and Phase Transformations in SnO2. A Density Functional Theory Study. J. Phys. Chem. B 111, 6479–6485. doi:10.1021/jp067443v

Grimes, R.W., Catlow, C.R.A., 1991. The stability of fission products in uranium dioxide. Phil Trans R Soc Lond A 335, 609–634. doi:10.1098/rsta.1991.0062

Grønvold, F., 1955. High-temperature X-ray study of uranium oxides in the UO2-U3O8 region. J. Inorg. Nucl. Chem. 1, 357–370. doi:10.1016/0022-1902(55)80046-2

Guéneau, C., Baichi, M., Labroche, D., Chatillon, C., Sundman, B., 2002. Thermodynamic assessment of the uranium–oxygen system. J. Nucl. Mater. 304, 161–175. doi:10.1016/S0022-3115(02)00878-4

Hakala, M., Puska, M.J., Nieminen, R.M., 1998. Momentum distributions of electron-positron pairs annihilating at vacancy clusters in Si. Phys. Rev. B 57, 7621. doi:10.1103/physrevb.57.7621

Harada, Y., 1997. UO2 sintering in controlled oxygen atmospheres of three-stage process. J. Nucl. Mater. 245, 217–223. doi:10.1016/S0022-3115(96)00755-6

Harper, J., Dorn, J.E., 1957. Viscous creep of aluminum near its melting temperature. Acta Metall. 5, 654–665. doi:10.1016/0001-6160(57)90112-8

Hawkins, R.J., Alcock, C.B., 1968. A study of cation diffusion in UO2 + x and ThO2 using α-ray spectrometry. J. Nucl. Mater. 26, 112–122. doi:10.1016/0022-3115(68)90162-1

He, H., Shoesmith, D., 2010. Raman spectroscopic studies of defect structures and phase transition in hyper-stoichiometric UO2+x. Phys. Chem. Chem. Phys. 12, 8109–8118. doi:10.1039/B925495A

Helfer, T., Michel, B., Proix, J.-M., Salvo, M., Sercombe, J., Casella, M., 2015. Introducing the open-source mfront code generator: Application to mechanical behaviours and material knowledge management within the PLEIADES fuel element modelling platform. Comput. Math. Appl. 70, 994–1023. doi:10.1016/j.camwa.2015.06.027

Higgs, J.D., Lewis, B.J., Thompson, W.T., He, Z., 2007. A conceptual model for the fuel oxidation of defective fuel. J. Nucl. Mater. 366, 99–128. doi:10.1016/j.jnucmat.2006.12.050

Howell, R.H., Colmenares, C., McCreary, T., 1984. Oxidation and hydriding of uranium studied by positron annihilation. J. Common Met. 98, 267–278. doi:10.1016/0022-5088(84)90299-6

Hutchings, M.T., 1987. High-temperature studies of UO2 and ThO2 using neutron scattering techniques. J. Chem. Soc. Faraday Trans. 2 Mol. Chem. Phys. 83, 1083–1103. doi:10.1039/F29878301083

IAEA, 1962. Thermodynamics of Nuclear Materials - 1962.

Iwai, T., Tsuchida, H., Awano, M., 2007. Application of positron beam Doppler broadening technique to ion beam irradiation in nickel. J. Nucl. Mater., Proceedings of the Twelfth International Conference on Fusion Reactor Materials (ICFRM-12) 367, 372–376. doi:10.1016/j.jnucmat.2007.03.126

Jackson, R.A., Murray, A.D., Harding, J.H., Catlow, C.R.A., 1986. The calculation of defect parameters in UO2. Philos. Mag. A 53, 27–50. doi:10.1080/01418618608242805

Janot, C., 1976. Étude des solides par annihilation de positons. Rev. Phys. Appliquée 11, 89–100. doi:10.1051/rphysap:0197600110108900

Kapshukov, I., Lyalyushkin, N., Sudakov, L., Bevz, A., Skiba, O., 1990. Preparation of hypostoichiometric UO2-x at low temperatures and study of some properties. J. Radioanal. Nucl. Chem. 143, 213–220. doi:10.1007/BF02117563

Kashibe, S., Une, K., 1998. Effect of additives (Cr2O3, A12O3, SiO2, MgO) on diffusional release of 133Xe from UO2 fuels. J. Nucl. Mater. 254, 234–242.

Kim, K.C., Olander, D.R., 1981. Oxygen diffusion in UO2−x. J. Nucl. Mater. 102, 192–199. doi:10.1016/0022-3115(81)90559-6

Kirkegaard, P., Eldrup, M., 1972. POSITRONFIT: A versatile program for analysing positron lifetime spectra. Comput. Phys. Commun. 3, 240–255. doi:10.1016/0010-4655(72)90070-7

Knorr, D.B., Cannon, R.M., Coble, R.L., 1989. An analysis of diffusion and diffusional creep in stoichiometric and hyperstoichiometric uranium dioxide. Acta Metall. 37, 2103–2123.

Kofstad, P., 1995. Defects and transport properties of metal oxides. Oxid. Met. 44, 3–27. doi:10.1007/BF01046721

Kozlova, R.D., Matyukha, V.A., Dedov, N.V., 2007. Mechanism and kinetics of thermal decomposition of uranyl nitrate hexahydrate under the nonisothermal conditions. Radiochemistry 49, 130–134. doi:10.1134/S1066362207020063

Krause-Rehberg, R., Leipner, H., S., 1999a. Positron Annihilation in Semiconductors - Defect, Springer Series in Solid-State Sciences. Springer-Verlag Berlin Heidelberg.

Krause-Rehberg, R., Leipner, H.S., 1999b. Positron Annihilation in Semiconductors: Defect Studies. Springer Science & Business Media.

Kröger, F.A., Vink, H.J., 1956. Relations between the Concentrations of Imperfections in Crystalline Solids. Solid State Phys. 3, 307–435. doi:10.1016/S0081-1947(08)60135-6

Labrim, H., 2006. Properietes des defauts lacunnaires natifs par irradiation et implantation dans le oxide d'uranium determinees par spectroscopy de positons (PhD Thesis). Universite de Orleans, Orleans, France.

Labrim, H., Barthe, M.-F., Desgardin, P., Sauvage, T., Blondiaux, G., Corbel, C., Piron, J.P., 2006. Vacancy defects induced in sintered polished UO2 disks by helium implantation. Appl. Surf. Sci., Proceedings of the Tenth International Workshop on Slow Positron Beam Techniques for Solids and Surfaces 252, 3256–3261. doi:10.1016/j.apsusc.2005.08.045

Labrim, H., Barthe, M.-F., Desgardin, P., Sauvage, T., Corbel, C., Blondiaux, G., Piron, J.P., 2007. Thermal evolution of the vacancy defects distribution in 1MeV helium implanted sintered UO2. Nucl. Instrum. Methods Phys. Res. Sect. B Beam Interact. Mater. At., The Application of Accelerators in Research and Industry 261, 883–887. doi:10.1016/j.nimb.2007.04.059

Langdon, T.G., Yavari, P., 1982. An investigation of Harper-Dorn creep—II. The flow process. Acta Metall. 30, 881–887. doi:10.1016/0001-6160(82)90086-4

Leinders, G., Pakarinen, J., Delville, R., Cardinaels, T., Binnemans, K., Verwerft, M., 2016. Low-Temperature Oxidation of Fine UO2 Powders: A Process of Nanosized Domain Development. Inorg. Chem. 55, 3915–3927. doi:10.1021/acs.inorgchem.6b00127

Lewis, B.J., Thompson, W.T., Akbari, F., Thompson, D.M., Thurgood, C., Higgs, J., 2004. Thermodynamic and kinetic modelling of fuel oxidation behaviour in operating defective fuel. J. Nucl. Mater. 328, 180–196. doi:10.1016/j.jnucmat.2004.04.336

Lidiard, A.B., 1966. Self-diffusion of uranium in UO2. J. Nucl. Mater. 19, 106–108. doi:10.1016/0022-3115(66)90138-3

Magee, C.W., Honig, R.E., Evans, C.A., 1982. Depth Profiling by SIMS: Depth Resolution, Dynamic Range and Sensitivity, in: Secondary Ion Mass Spectrometry SIMS III, Springer Series in Chemical Physics. Springer, Berlin, Heidelberg, pp. 172–185. doi:10.1007/978-3-642-88152-7_27

Makinen, J., Palko, S., Martikainen, J., Hautojarvi, P., 1992. Positron backscattering probabilities from solid surfaces at 2-30 keV. J. Phys. Condens. Matter 4, L503–L508. doi:10.1088/0953-8984/4/36/006

Mamontov, E., Egami, T., 2000. Structural defects in a nano-scale powder of CeO2 studied by pulsed neutron diffraction. J. Phys. Chem. Solids 61, 1345–1356. doi:10.1016/S0022-3697(00)00003-2

Manninen, M., Nieminen, R.M., 1981. Positron detrapping from defects: A thermodynamic approach. Appl. Phys. A 26, 93–100. doi:10.1007/BF00616655

Marin, J.F., Contamin, P., 1969. Uranium and oxygen self-diffusion in UO2. J. Nucl. Mater. 30, 16–25. doi:10.1016/0022-3115(69)90164-0

Marin, J.F., Michaud, H., Contamin, P., 1967. Self-diffusion of uranium in uranium dioxide - Role of deviations from stoichiometry and grain joints. Comptes Rendus Académie Sci. Sér. C - Sci. Chim. 264, 1633.

Martin, D.G., 1988. The thermal expansion of solid UO2 and (U, Pu) mixed oxides — a review and recommendations. J. Nucl. Mater. 152, 94–101. doi:10.1016/0022-3115(88)90315-7

Martin, G., Garcia, P., Sabathier, C., Palancher, H., Maillard, S., 2014. Molecular dynamics simulation of displacement cascades in UO2. Presented at the Joint International Conference on Supercomputing in Nuclear Applications + Monte Carlo, held 27-31 October, 2013 in Paris, France. Edited by D. Caruge, C. Calvin, C.M. Diop, F. Malvagi, and J.-C. Trama. EDP Sciences, 2014, id.01310, 2 pp., p. 01310. doi:10.1051/snamc/201401310

Martin, P.M., Vathonne, E., Carlot, G., Delorme, R., Sabathier, C., Freyss, M., Garcia, P., Bertolus, M., Glatzel, P., Proux, O., 2015. Behavior of fission gases in nuclear fuel: XAS characterization of Kr in UO2. J. Nucl. Mater. 466, 379–392. doi:10.1016/j.jnucmat.2015.08.019

Matzke, H., 1995. Oxygen potential measurements in high burnup LWR UO2 fuel. J. Nucl. Mater. 223, 1–5.

Matzke, H., 1987. Atomic transport properties in UO2 and mixed oxides (U, Pu)O2. J. Chem. Soc. Faraday Trans. 2 Mol. Chem. Phys. 83, 1121–1142. doi:10.1039/F29878301121

Matzke, H., 1983. Diffusion processes and surface effects in non-stoichiometric nuclear fuel oxides UO2+x, and (U, Pu)O2±x. J. Nucl. Mater. 114, 121–135. doi:10.1016/0022-3115(83)90249-0

Matzke, H., 1973. Lattice disorder and metal self-diffusion in non-stoichiometric UO2 and (U, Pu)O2. J. Phys. Colloq. 34, C9-317-C9-325. doi:10.1051/jphyscol:1973956

Matzke, H., 1969. On uranium self-diffusion in UO2 and UO2+x. J. Nucl. Mater. 30, 26–35. doi:10.1016/0022-3115(69)90165-2

McEachern, R.J., Taylor, P., 1998. A review of the oxidation of uranium dioxide at temperatures below 400°C. J. Nucl. Mater. 254, 87–121. doi:10.1016/S0022-3115(97)00343-7

Mermin, N.D., 1966. A Short Simple Evaluation of Expressions of the Debye- Waller Form. J. Math. Phys. 7, 1038–1038. doi:10.1063/1.1704995

Mohamed, F.A., Soliman, M.S., 1982. On the creep behavior of uranium dioxide. Mater. Sci. Eng. 53, 185–190. doi:10.1016/0025-5416(82)90051-9

Murray, A.D., Willis, B.T.M., 1990. A neutron diffraction study of anion clusters in nonstoichiometric uranium dioxide. J. Solid State Chem. 84, 52–57. doi:10.1016/0022-4596(90)90183-X

Nabarro, F.R.N., 2002. Creep at very low rates. Metall. Mater. Trans. A 33, 213–218. doi:10.1007/s11661-002-0083-8

Nagels, P., Van Lierde, W., De Batist, R., Denayer, M., De Jonghe, L., Gevers, R., 1966. Migration and re-Orientation of Oxygen Interstitials, and Migration and Self-Diffusion of Uranium in UO_2.

Nelin, C.J., Bagus, P.S., Ilton, E.S., 2014. Theoretical analysis of the U L3-edge NEXAFS in U oxides. RSC Adv. 4, 7148–7153. doi:10.1039/C3RA46738D

Noyau, S., 2012. Etude des phenomenes d’autodiffusion et d’interdiffusion du plutonium dans des ceramiques de type U1-yPuyO2±x (PhD Thesis). Docteur de l’Universite de Limoges, CEA Cadarache.

Noyau, S., Garcia, P., Pasquet, B., Roure, I., Audubert, F., Maître, A., 2012. Towards Measuring the Pu Self-Diffusion Coefficient in Polycrystalline U0.55Pu0.45O2±x. Defect Diffus. Forum 323–325, 203–208. doi:10.4028/www.scientific.net/DDF.323-325.203

OECD NEA/NSC, 2014. Thermodynamics of Advanced Fuels – International Database (TAF-ID) [WWW Document]. URL https://www.oecd-nea.org/science/taf-id/taf-id-public/ (accessed 9.26.17).

OECD NEA/NSC, 2009. Nuclear Fuel Behaviour in Loss-of-coolant Accident (LOCA) Conditions (No. No. 6846). NUCLEAR ENERGY AGENCY ORGANISATION FOR ECONOMIC CO-OPERATION AND DEVELOPMENT.

Olander, D., 2009. Nuclear fuels – Present and future. J. Nucl. Mater., Thermochemistry and Thermophysics of Nuclear Materials 389, 1–22. doi:10.1016/j.jnucmat.2009.01.297

Park, K., Yang, M.-S., Park, H.-S., 1997. The stoichiometry and the oxygen potential change of urania fuels during irradiation. J. Nucl. Mater., Thermodynamics of Nuclear Materials 247, 116–120. doi:10.1016/S0022-3115(97)00068-8

Paulin, R., Ripon, R., Brandt, W., 1974. Diffusion constant and surface states of positrons in metals. Appl. Phys. 4, 343–347. doi:10.1007/BF00928390

Peres, V., Dehaudt, P., 2002. Application de la Maturation d’ostwald a la croissance de precipites de Cr2O3 in l’UO2 polycristallin (No. CEA-CONF-11379, FR9302946). CEA, Grenoble, France.

Peres, V., Favergeon, L., Andrieu, M., Palussière, J.-C., Balland, J., Delafoy, C., Pijolat, M., 2012. High temperature chromium volatilization from Cr2O3 powder and Cr2O3-doped UO2 pellets in reducing atmospheres. J. Nucl. Mater. 423, 93–101. doi:10.1016/j.jnucmat.2012.01.001

Perron, P.O., 1968. Thermodynamics of Nonstoichiometric Uranium Dioxide. (No. AECL--3072). Atomic Energy of Canada Ltd., Chalk River (Ontario).

Philibert, J., 1991. Atom Movements: Diffusion and Mass Transport in Solids. Editions de Physique.

Philibert, J., 1984. Creep and diffusion. Solid State Ion. 12, 321–336. doi:10.1016/0167-2738(84)90161-9

Pizzi, E., Garcia, P., Carlot, G., Palancher, H., Maillard, S., Pasquet, B., Roure, I., Pozo, C., Maurice, C., 2012. Iodine volume diffusion measurements in uranium dioxide. Defect Diffus. Forum Online 323–325, 197–202. doi:10.4028/www.scientific.net/DDF.323-325.197

Poteat, L., Yust, C., 1968. Grain Boundary Reactions During Deformation, in: Ceramic Micro-Structure. Wiley Press, New York, U.S.A., p. 646.

Prince, E., 1981. Comparison of profile and integrated-intensity methods in powder refinement. J. Appl. Crystallogr. 14, 157–159. doi:10.1107/S0021889881009059

Prodan, I.D., Scuseria, G.E., Martin, R.L., 2007. Covalency in the actinide dioxides: Systematic study of the electronic properties using screened hybrid density functional theory. Phys. Rev. B 76, 033101. doi:10.1103/PhysRevB.76.033101

Proffen, T., Billinge, S., 2003. PDFFIT 1.2 [WWW Document]. URL https://web.pa.msu.edu/cmp/billinge-group/programs/discus/pdf_man.pdf

Puska, M.J., Corbel, C., Nieminen, R.M., 1990. Positron trapping in semiconductors. Phys. Rev. B 41, 9980–9993. doi:10.1103/PhysRevB.41.9980

Puska, M.J., Nieminen, R.M., 1994. Theory of positrons in solids and on solid surfaces. doi:10.1103/revmodphys.66.841

Puska, M.J., Nieminen, R.M., 1983. Defect spectroscopy with positrons: a general calculational method. J. Phys. F Met. Phys. 13, 333. doi:10.1088/0305-4608/13/2/009

Raj, R., Ashby, M.F., 1971. On grain boundary sliding and diffusional creep. Metall. Trans. 2, 1113–1127. doi:10.1007/BF02664244

Reimann, D.K., Lundy, T.S., 1969. Diffusion of 233U in UO2. J. Am. Ceram. Soc. 52, 511–512. doi:10.1111/j.1151-2916.1969.tb09206.x

Roudil, D., Barthe, M.F., Jégou, C., Gavazzi, A., Vella, F., 2012. Investigation of defects in actinide-doped UO2 by positron annihilation spectroscopy. J. Nucl. Mater. 420, 63–68. doi:10.1016/j.jnucmat.2011.08.011

Rouse, K.D., Willis, B.T.M., Pryor, A.W., 1968. Anharmonic contributions to the Debye–Waller factors of UO2. Acta Crystallogr. B 24, 117–122. doi:10.1107/S0567740868001779

Rousseau, G., Desgranges, L., Charlot, F., Millot, N., Nièpce, J.C., Pijolat, M., Valdivieso, F., Baldinozzi, G., Bérar, J.F., 2006. A detailed study of UO2 to U3O8 oxidation phases and the associated rate-limiting steps. J. Nucl. Mater. 355, 10–20. doi:10.1016/j.jnucmat.2006.03.015

Ruello, P., 2001. Étude du changement de comportement du dioxyde d'uranium au voisinage de 1300K : propriétés électriques, optiques et structurales. École Centrale Paris.

Ruello, P., Chirlesan, G., Petot-Ervas, G., Petot, C., Desgranges, L., 2004. Chemical diffusion in uranium dioxide – influence of defect interactions. J. Nucl. Mater. 325, 202–209. doi:10.1016/j.jnucmat.2003.12.007

Ruello, P., Desgranges, L., Baldinozzi, G., Calvarin, G., Hansen, T., Petot-Ervas, G., Petot, C., 2005. Heat capacity anomaly in UO2 in the vicinity of 1300K: an improved description based on high resolution X-ray and neutron powder diffraction studies. J. Phys. Chem. Solids 66, 823–831. doi:10.1016/j.jpcs.2004.10.009

Sabioni, A.C.S., Ferraz, W.B., Millot, F., 2000. Effect of grain-boundaries on uranium and oxygen diffusion in polycrystalline UO2. J. Nucl. Mater. 278, 364–369. doi:10.1016/S0022-3115(99)00250-0

Sabioni, A.C.S., Ferraz, W.B., Millot, F., 1998. First study of uranium self-diffusion in UO2 by SIMS. J. Nucl. Mater. 257, 180–184. doi:10.1016/S0022-3115(98)00482-6

Salvo, M., Sercombe, J., Ménard, J.-C., Julien, J., Helfer, T., Désoyer, T., 2015. Experimental characterization and modelling of UO2 behavior at high temperatures and high strain rates. J. Nucl. Mater. 456, 54–67. doi:10.1016/j.jnucmat.2014.09.024

Schmitz, F., Lindner, R., 1965. Diffusion of heavy elements in nuclear fuels: actinides in UO2. J. Nucl. Mater. 17, 259–269. doi:10.1016/0022-3115(65)90169-8

Scott, R., Hall, A.R., Williams, J., 1959. The plastic deformation of uranium oxides above 800° C. J. Nucl. Mater. 1, 39–48. doi:10.1016/0022-3115(59)90009-1

Sears, V.F., 1992. Neutron scattering lengths and cross sections. Neutron News 3, 26–37. doi:10.1080/10448639208218770

Seltzer, M.S., Clauer, A.H., Wilcox, B.A., 1972. The influence of stoichiometry on compression creep of polycrystalline UO2+x. J. Nucl. Mater. 44, 331–336. doi:10.1016/0022-3115(72)90044-X

Skinner, L.B., Benmore, C.J., Weber, J.K.R., Williamson, M.A., Tamalonis, A., Hebden, A., Wiencek, T., Alderman, O.L.G., Guthrie, M., Leibowitz, L., Parise, J.B., 2014. Molten uranium dioxide structure and dynamics. Science 346, 984–987. doi:10.1126/science.1259709

Skomurski, F.N., Wang, J.W., Ewing, R.C., Becker, U., 2013. Charge distribution and oxygen diffusion in hyperstoichiometric uranium dioxide UO2+x (x ⩽ 0.25). J. Nucl. Mater. 434, 422–433. doi:10.1016/j.jnucmat.2011.09.003

Skorek, R., 2013. Étude par Dynamique d'Amas de l'influence des défauts d'irradiation sur la migration des gaz de fission dans le dioxyde d'uranium (PhD Thesis). Universite de Aix-Marseille, CEA Cadarache.

Soininen, E., Mäkinen, J., Beyer, D., Hautojärvi, P., 1992. High-temperature positron diffusion in Si, GaAs, and Ge. Phys. Rev. B 46, 13104–13118. doi:10.1103/PhysRevB.46.13104

Soullard, J., 1985. High voltage electron microscope observations of UO2. J. Nucl. Mater. 135, 190–196. doi:10.1016/0022-3115(85)90077-7

SPIP, C., 2011. Image Metrology [WWW Document]. URL https://www.imagemet.com/ (accessed 9.2.17).

Thomas, L.E., Einziger, R.E., Woodley, R.E., 1989. Microstructural examination of oxidized spent PWR fuel by transmission electron microscopy. J. Nucl. Mater. 166, 243–251. doi:10.1016/0022-3115(89)90221-3

Toby, B.H., Egami, T., 1992. Accuracy of pair distribution function analysis applied to crystalline and non-crystalline materials. Acta Crystallogr. A 48, 336–346. doi:10.1107/S0108767391011327

Trumpy, G., 1994. Observation of dislocations by the positron annihilation method. Phys. Lett. A 192, 261–264. doi:10.1016/0375-9601(94)90254-2

Tuomisto, F., Makkonen, I., 2013. Defect identification in semiconductors with positron annihilation: Experiment and theory. doi:10.1103/revmodphys.85.1583

Tuxworth, R.H., Evans, W., 1959. Habit planes for U 4O 9 precipitation in uranium dioxide. J. Nucl. Mater. 1, 302–303. doi:10.1016/0022-3115(59)90027-3

Upadhyaya, D.D., Muraleedharan, R.V., Sharma, B.D., 1982. Study of positron lifetime spectra in UO2 powders. J. Nucl. Mater. 105, 219–222. doi:10.1016/0022-3115(82)90377-4

Vathonne, E., Wiktor, J., Freyss, M., Jomard, G., Bertolus, M., 2014. DFT + U investigation of charged point defects and clusters in UO 2. J. Phys. Condens. Matter 26, 325501. doi:10.1088/0953-8984/26/32/325501

Wang, J., Ewing, R.C., Becker, U., 2014. Average structure and local configuration of excess oxygen in UO_{2+x}. Sci. Rep. 4, srep04216. doi:10.1038/srep04216

Wang, J.N., Nieh, T.G., 1996. A new interpretation of the mechanisms in Newtonian creep of uranium dioxides. J. Nucl. Mater. 228, 141–147. doi:10.1016/0022-3115(95)00200-6

Warren, B.E., 1969. X-ray Diffraction. Courier Corporation.

Weertman, J., 1957. Steady- State Creep through Dislocation Climb. J. Appl. Phys. 28, 362–364. doi:10.1063/1.1722747

Weertman, J., 1955. Theory of Steady- State Creep Based on Dislocation Climb. J. Appl. Phys. 26, 1213–1217. doi:10.1063/1.1721875

White, J.T., Nelson, A.T., 2013. Thermal conductivity of UO2+x and U4O9−y. J. Nucl. Mater. 443, 342–350. doi:10.1016/j.jnucmat.2013.07.063

White, R.J., Tucker, M.O., 1983. A new fission-gas release model. J. Nucl. Mater. 118, 1–38. doi:10.1016/0022-3115(83)90176-9

Wiktor, J., Barthe, M.-F., Jomard, G., Torrent, M., Freyss, M., Bertolus, M., 2014. Coupled experimental and DFT +U investigation of positron lifetimes in UO2. Phys. Rev. B 90, 184101. doi:10.1103/PhysRevB.90.184101

Wiktor, J., Jomard, G., Torrent, M., Bertolus, M., 2017. First-principles calculations of momentum distributions of annihilating electron–positron pairs in defects in UO 2. J. Phys. Condens. Matter 29, 035503. doi:10.1088/1361-648X/29/3/035503

Willis, B.T.M., 1978. The defect structure of hyper-stoichiometric uranium dioxide. Acta Crystallogr. A 34, 88–90. doi:10.1107/S0567739478000157

Willis, B.T.M., 1964. Structures of UO2, UO2+x andU4O9 by neutron diffraction. J. Phys. 25, 431–439. doi:10.1051/jphys:01964002505043100

Willis, B.T.M., 1963a. Neutron diffraction studies of the actinide oxides II. Thermal motions of the atoms in uranium dioxide and thorium dioxide between room temperature and 1100 °C. Proc R Soc Lond A 274, 134–144. doi:10.1098/rspa.1963.0118

Willis, B.T.M., 1963b. Neutron diffraction studies of the actinide oxides I. Uranium dioxide and thorium dioxide at room temperature. Proc R Soc Lond A 274, 122–133. doi:10.1098/rspa.1963.0117

Wolfe, R.A., Kaufman, S.F., 1967. Mechanical Properties of Oxide Fuels (lsbr/Lwb Development Program). (No. WAPD-TM--587). Bettis Atomic Power Lab., Pittsburgh, Pa. (US). doi:10.2172/4511674

Yajima, S., Furuya, H., Hirai, T., 1966. Lattice and grain-boundary diffusion of uranium in UO2. J. Nucl. Mater. 20, 162–170. doi:10.1016/0022-3115(66)90004-3

List of Figures

List of Tables

Appendix: Résumé étendu

Le dioxyde d'uranium est un matériau de type fluorite, non stœchiométrique, présentant un excès d'oxygène qui existe sur une large gamme de composition. À des températures et des activités d'oxygène qui sont pertinentes vis-à-vis de son comportement en réacteur, la littérature fait état de divers types de défauts ponctuels et de leurs clusters avec différents états de charge et différentes compositions sur les sous-réseaux anionique et cationique. Ces défauts ont une influence majeure sur certaines propriétés d'usage clés telles que l'auto-diffusion des cations ou le fluage. C'est le but de ce travail à la fois de caractériser les défauts majoritaires présents à l'équilibre thermodynamique et d'approfondir notre compréhension de leur impact sur l'autodiffusion de l'uranium. A cette fin, trois types d'expériences ont été réalisés. La diffraction neutronique a été utilisée, car les neutrons sont sensibles aux ions oxygène, afin de caractériser des échantillons avec différents rapports oxygène-métal et à différentes températures. Ce travail a été réalisé à l'Institut Laüe Langevin à Grenoble sur le diffractomètre D4c qui permet la détermination des arrangements atomiques locaux au moyen de l'analyse de la fonction de distribution de paires. Les fonctions de distribution radiale ont été modélisées et comparées aux données expérimentales. Il est difficile de tirer des conclusions définitives quant à savoir si les interstitiels d'oxygène demeurent isolés ou forment des amas d'ions aux faibles écarts à la stœchiométrie car le système est extrêmement dilué. Cependant, dans les échantillons contenant beaucoup plus d'oxygène, les résultats sont compatible avec lla formation de clusters, soit dans une configuration de type 2: 2: 2 ou sous la forme de clusters dit « cuboctaèdres », semblables à ceux observés dans U_4O_9.

La spectroscopie d'annihilation des positons a également été réalisée au CEMHTI, Orléans sur des échantillons à l'origine équilibrés à haute température mais sous différentes pressions partielles d'oxygène et ensuite trempés. À des pressions d'oxygène assez élevées, l'élargissement Doppler et la spectroscopie de temps de vie prouvent l'émergence d'un défaut spécifique contenant de l'uranium, avec des caractéristiques similaires à celles observées dans le matériau irradié. Nos résultats mettent également en évidence l'effet spécifique de la présence d'interstitiels d'oxygène sur les caractéristiques d'élargissement Doppler et confirment que leurs propriétés de durée de vie sont similaires à celles du réseau. Les concentrations en uranium et en oxygène sont déduites de l'interprétation les données en utilisant un modèle de piégeage. Enfin, ces résultats sont complétés par des expériences de diffusion avec un traceur d'uranium et une tentative est faite pour interpréter les changements dans les coefficients d'autodiffusion de l'uranium sur la base de notre connaissance de la compréhension de comportement des défauts ponctuels.

Chapitre 1. Etude bibliographique

Le système U-O est rendu complexe par la variété de défauts cristallographiques possibles, il peut accommoder des défauts électroniques ou ponctuels avec différents états de charge, à la fois sur les sous-réseaux anioniques et cationiques. Les populations de défauts dans UO_{2+x} ont plusieurs caractéristiques générales :

1- Les défauts électroniques constituent la majorité des défauts ponctuels, et la concentration de défauts sur le sous-réseau anionique est supérieure à celle du sous-réseau cationique. Leur mobilité suit le même ordre décroissant.
2- La sur-stœchiométrie produit une augmentation concomitante des interstitiels d'oxygène et des lacunes d'uranium.
3- La sur-stœchiométrie éloigne le matériau d’un comportement purement ionique. Les défauts anioniques ont tendance à se regrouper dans le but de réduire l'énergie globale du système.
4- Les défauts auront tendance à prendre un état de charge neutre avec un écart croissant par rapport à la stœchiométrie pour la même raison que mentionné ci-dessus.

Il est rapporté que les amas d'oxygène di-interstitiels présentent une charge apparente de -1 au lieu de -4 attendue si le comportement ionique était pertinent. Les lacunes d'uranium ont un état de charge -4 pour une composition stœchiométrique, mais il y a des preuves qu'ils deviennent neutres à des écarts à la stœchiométrie plus élevés. Ces changements dans les populations de défauts induisent des changements dans les propriétés correspondantes. La formation de clusters anioniques peut être corrélée à une réduction de la diffusion chimique de l'oxygène avec un écart croissant à la stœchiométrie. Cependant, il y a beaucoup d'incertitudes sur la nature détaillée des défauts mis en jeu. La diffusion des neutrons est une technique puissante pour étudier de tels défauts anioniques et ce point est développé au chapitre 3 dans lequel nous décrivons l’analyse d’un certain nombre de fonctions de distribution de paires. Parce que l'écart à la stœchiométrie devrait également induire une augmentation de la concentration en lacunes d'uranium, il s'accompagne d'une augmentation correspondante du coefficient d'auto-diffusion de l'uranium et d'autres propriétés étroitement liées au comportement des défauts lacunaires d'uranium (diffusion des produits de fission, fluage, etc.). Parmi les méthodes spectroscopiques envisageables pour caractériser les lacunes d'uranium, la Spectroscopie d’Annihilation de Positons (PAS) s'est avérée être une technique très prometteuse. Au chapitre 4 de ce document, nous décrivons un ensemble d’expériences de PAS effectuées sur plusieurs échantillons stœchiométriques et non-stœchiométriques pour essayer de déterminer :

1- si les lacunes d'uranium induites thermodynamiquement peuvent être détectées en utilisant cette méthode et si oui,
2- comment leurs caractéristiques d'annihilation se comparent à celles rencontrées dans les études sur UO_2.

Au chapitre 5, nous tentons de développer une méthode de traceur isotopique utilisant le SIMS pour caractériser l'auto-diffusion de l'uranium. Cette méthode est appliquée à des échantillons mono et polycristallins. Le but est ici de mesurer cette propriété en fonction de la température et de la pression partielle d'oxygène dans un effort pour obtenir des informations quantitatives sur les défauts lacunaires d'uranium et les équilibres de défauts associés.

Les principaux résultats qui ont émergé au cours de ce travail sont mis en évidence et résumés dans le chapitre 6 dans lequel nous soulignons également un certain nombre de domaines dans lesquels les progrès expérimentaux ou théoriques pourraient être faite sur ces points.

Chapitre 2 - Matériaux et techniques expérimentales : principes et applications

Ce chapitre constitue une toile de fond pour le reste du travail effectué dans cette étude. En particulier, nous décrivons :

1- Les matériaux que nous avons étudiés et leur microstructure
2- Les méthodes utilisées pour les expériences d'oxydation contrôlée
3- Le protocole adopté pour le dépôt d'une couche d'oxyde enrichie en ^{235}U pour les expériences d'auto-diffusion.

Nous sommes confiants sur le fait que les écarts à la stœchiométrie des échantillons sont relativement bien estimés du fait des conditions thermodynamiques étant bien contrôlées. Les principales techniques expérimentales utilisées dans cette thèse en termes de théorie et d'applications sont également décrites y compris :

1- la diffraction neutronique pour l'étude du désordre structural dans UO_{2+x} et les défauts d'oxygène en particulier (chapitre 3) ;
2- la Spectroscopie d'annihilation de positons à la fois en élargissement Doppler et en configuration durée de vie, la première étant bien adaptée à la caractérisation des lacunes d'uranium (chapitre 4) ;

et

3- la spectrométrie de masse des ions secondaires qui est essentielle à la mesure de coefficients de diffusion à l'aide d'un traceur (chapitre 5).

Chapitre 3 Caractéristiques des défauts d'oxygène dans UO_{2+x} en utilisant la diffusion des neutrons et l'analyse PDF

Trois types d'échantillons UO_{2+x} ont été fabriqués avec des stœchiométries proches de 2, 2.007 et 2.16. Les échantillons ont été caractérisés en utilisant la microscopie électronique à balayage. Nous avons effectué des expériences de diffusion de neutrons in situ sur le diffractomètre D4c à l'ILL avec une longueur d'onde neutronique courte pour disposer d'une haute résolution dans l'espace réel. L'UO_2 stœchiométrique a été utilisé comme matériau modèle pour confirmer la qualité de l'acquisition et du traitement des données. La dilatation thermique du réseau a été caractérisée par une analyse Rietveld et comparée favorablement à la littérature. La fonction de distribution de paires (PDF) de des échantillons a ensuite été déterminée. Les résultats des mesures sont rapportés pour une température de 900°C. La comparaison des PDF indique un niveau croissant de désordre à mesure que la teneur en oxygène des échantillons augmente. Les changements des spectres dans l'espace réciproque à mesure que la stœchiométrie augmente peuvent être observés et consistent essentiellement en une diminution des hauteurs de pics et une augmentation du signal entre les pics signe d'un désordre croissant.

En ce qui concerne la PDF de l'UO_2, il est intéressant de noter que les données recueillies constituent par elles-mêmes des résultats. Nous avons vu que la longueur de liaison la plus courte est une fonction décroissante de la température. Aucun modèle n'est nécessaire pour arriver à cette conclusion car elle découle directement de la PDF (RDF). Cette observation est liée à la distorsion de l'oxygène déduite par Willis d'une interprétation par un modèle des expériences de diffraction neutronique sur UO_2 monocristallin.

Les données PDF ont été interprétées sur la base de différents types de clusters qui ont été obtenus par des études expérimentales ou sur la base de calculs ab initio. Le modèle de maille moyenne (d'ordre quatre) indique que les données expérimentales entre 1 et 6 Å sont mieux reproduites lorsque les atomes d'oxygène du réseau sont autorisés à se déplacer le long des directions <111> à haute température reflétant ainsi le comportement thermique anharmonique des ions d'oxygène. L'étude de $UO_{2.007}$ et $UO_{2.16}$ suggère également que les deux types d'ions d'oxygène interstitiels devraient être considérés : les ions O 'et O" sont déplacés des sites octaédriques le long respectivement des directions <110> et <111>. Les données expérimentales sont en fait bien décrites en utilisant cette approche mais une approche de maille moyenne fournit seulement un aperçu limité de l'arrangement réel à l'échelle atomique. Les données ont également été interprétées en utilisant une approche super cellulaire. Nous avons étendu la maille d'ordre 4 de la fluorine cubique en modèles à 96 atomes (2x2x2, $U_{32}O_{64}$), à 324 atomes (3x3x3, $U_{108}O_{216}$) et à 768 atomes (4x4x4, $U_{225}O_{512}$). Les résultats à faible écart à la stœchiométrie (x = 0,007), suggèrent que le système est trop dilué pour qu'un choix soit fait entre des amas isolés ou des di-interstitiels. À fort écart à la stœchiométrie (x = 0,16) plusieurs les modèles structuraux ont été testés. Le cluster cuboctaèdrique occupé en son centre fournit le meilleur facteur de qualité de raffinement bien que les différences avec les clusters 2: 2: 2 soient faibles. Les caractéristiques du cuboctaèdre dérivé de l'analyse sont assez similaires à celles de Cooper et Willis. L'image qui émerge pourrait donc être qu'à mesure que la température augmente, l'arrangement des cuboctaèdres qui forment la phase U_4O_9 dans le matériau biphasé est perdu mais les cuboctaèdres restent la population de défauts de base.

Pour compléter ce travail, l'effet de la température serait notamment à étudier. Des améliorations à la modélisation des données pourraient également être faites. En particulier, il ressort du modèle de maille moyenne que le matériau peut contenir une quantité significative de désordres de Frenkel. Ce désordre de Frenkel pourrait être approfondi dans le cadre d'un modèle super cellulaire. Enfin, corréler ces résultats à ceux de la dynamique moléculaire ab initio fourniraient sans aucun doute un aperçu essentiel du comportement des cluster d'anions et mériterait de faire l'objet d'investigations complémentaires.

Chapitre 4 Une étude des défauts ponctuels dans UO_{2+x} par spectroscopie d'annihilation de positrons

Nous avons réalisé des mesures d'élargissement Doppler et de spectroscopie de temps de vie sur des échantillons de UO_2 et UO_{2+x}, principalement à 300 K mais aussi à 35 K et 750 K, pour étudier les défauts d'uranium et d'oxygène. Les échantillons sur-stœchiométriques ont été obtenus à partir d'expériences d'oxydation contrôlée à haute température et ont été trempés à partir d'une température à laquelle le sous-réseau d'uranium devrait être sensible aux conditions thermodynamiques. Les résultats de spectroscopie d'élargissement Doppler montrent que les points de données (W, S) sont sur une ligne qui est très similaire à celle déterminée pour UO_2 irradié et qui a été interprétée comme étant caractéristique de trios de Schottky neutres (Wiktor et al., 2014). Ces résultats sont également en accord avec la durée de vie du positron, mesures à 300 K, comme la composante à longue durée de vie qui apparaît dans les échantillons avec des écarts de la stœchiométrie supérieurs à 2,03-2,04 est équivalente à celle observée dans le matériau irradié, c'est-à-dire environ 316 ps.

Malgré les similitudes entre les échantillons équilibrés et irradiés, il subsiste des doutes quant à savoir si les lacunes d'uranium détectées sont en effet des trios Schottky neutres puisque leur concentration ne devrait pas dépendre de l'écart à la stœchiométrie.

Parmi les résultats les plus frappants de cette étude, le fait qu'une augmentation de la stœchiométrie semble induire une diminution de la fraction d'annihilation à faible moment cinétique et une augmentation du de la fraction de moment est conforme aux résultats préliminaires des calculs ab initio. L'étude d'un échantillon oxydé à une température inférieure à laquelle le sous-réseau cationique devrait être insensible à la température et l'activité de l'oxygène, confirme que la spectroscopie d'élargissement Doppler est plus sensible à l'environnement chimique. Par environnement chimique on fait spécifiquement allusion à l'oxygène typique des amas qui sont connus pour apparaître dans le matériau sur-stœchiométrique et discutés au chapitre 3.

Pour les échantillons dans lesquels un défaut de type lacune d'uranium est détecté, nous avons appliqué ce que l'on appelle modèle de piégeage à plusieurs états. Il est possible d'interpréter les résultats en utilisant des valeurs de coefficient de piégeage compatibles avec les valeurs obtenues dans d'autres semi-conducteurs. Cette analyse permet de faire des estimations de concentrations de défauts qui suggèrent que, bien que constituant le défaut cationique minoritaire, négatif des lacunes d'uranium sont présentes en plus des lacunes neutres. Cette analyse est également compatible avec fait que la fraction des lacunes neutres augmente avec l'écart croissant à la stoechiométrie.

L'image globale qui ressort de cette étude PAS confirme la complexité attendue du matériau ; les états de charge et les compositions en défauts dépendent beaucoup de la température et de stoechiométrie. La difficulté supplémentaire rencontrée dans l'interprétation des données d'élargissement Doppler par exemple, réside dans le fait que les lacunes d'uranium et les clusters d'oxygène affectent la fraction de faible moment cinétique (ou fort) de façon opposée et avec différentes sensibilités (à différentes concentrations de défauts).

A titre d'exemple, la présence de lacunes d'uranium aura tendance à augmenter S et celle des clusters d'oxygène à diminuer cette quantité. D'autre part, la durée de vie du positron semble insensible à la présence de clusters d'oxygène mais très sensible aux lacunes d'uranium. Un certain nombre de domaines différents sont maintenant identifiés pour de futures recherches que nous présentons dans le chapitre suivant en différentes catégories : poursuite de l'analyse des données existantes, acquisition de nouvelles données, études théoriques. En ce qui concerne la première catégorie, il faut noter que l'approche du modèle à trois états exige de connaître des grandeurs, notamment des coefficients de piégeage de la plus haute importance et peuvent être obtenus à partir de la théorie ou de manière expérimentale. L'idée serait d'analyser les données d'élargissement Doppler à différents écarts à la stœchiométrie d'une manière compatible avec le modèle de piégeage, afin de déterminer les fractions d'annihilation correspondant à des états délocalisés ou localisés. Ces fractions pourraient ensuite être utilisées à l'analyse du temps de vie pour limiter le nombre de quantités inconnues et pourrait potentiellement améliorer l'estimation des concentrations en défauts. La deuxième catégorie d'études impliquerait d'abord de caractériser des échantillons existants, comme une caractérisation systématique en durée de vie de tous les échantillons à 300 K, et une caractérisation plus systématique de la spectroscopie de durée de vie en fonction de la température des échantillons pour lesquels une deuxième composante de durée de vie est détectée. Il est également clair qu'une caractérisation systématique en PAS des échantillons oxydés à des températures plus basses sont nécessaires car ils permettraient un élargissement Doppler pour lequel les défauts riches en oxygène doivent être clairement séparés de la signature des lacunes d'uranium. Enfin, en ce qui concerne les approches théoriques, un certain nombre de suggestions peuvent être faites. La plus significative devrait impliquer l'application de la règle d'or de Fermi à l'étude des mécanismes de piégeage, donc des coefficients associés à différents types de défauts chargés (Puska et al., 1990). Cela réduirait considérablement les incertitudes liées aux coefficients de piégeage. D'autres efforts devraient également être faits en ce qui concerne l'effet des défauts et des amas d'oxygène sur la distribution du moment des paires électrons-positrons. L'étude des interstitiels d'oxygène neutres serait aussi nécessaire.

Chapitre 5 Une étude de l'auto-diffusion de l'uranium

L'autodiffusion de l'uranium a été caractérisée sur des échantillons de UO_{2+x} monocristallin et polycristallins ainsi que dopés en chrome. Des expériences ont été réalisées à 1350°C, 1500°C et 1600°C sous différentes conditions oxydantes (entre $9{,}4\times10^{-13}$ et $4{,}7\times10^{-11}$ atm de pression partielle d'oxygène). Une solution de nitrate d'uranyle enrichi en ^{235}U a d'abord été déposée à la surface des échantillons, qui a ensuite été transformée en une couche de $^{235}UO_2$ après un recuit à basse température. La diffusion du traceur isotopique ^{235}U a été caractérisée par spectrométrie de masse d'ions secondaires. Les profondeurs correspondant à tous les cratères SIMS à la surface des échantillons ont été caractérisées avec un microscope confocal chromatique. Cela nous permet d’obtenir un profil de concentration pour chacun des cratères. La résolution en profondeur pour chaque profil, qui détermine en partie l’erreur associée au coefficient d'auto-diffusion de l'uranium, est obtenue par une méthode de Monte Carlo.

Pour chaque cratère, le profil de profondeur moyen a été modélisé à l'aide d'une solution analytique à l’équation de diffusion. La solution suppose que le matériau en surface s'évapore ou se condense à une certaine vitesse. Les coefficients d'autodiffusion de l'uranium obtenus pour les échantillons polycristallins, qui sont un ordre de grandeur supérieur à ceux des matériaux monocristallins recuits dans les mêmes conditions, qui est environ trois ordres de grandeur plus élevé que le coefficient de diffusion de volume rapporté pour UO_2 nominalement stœchiométrique. Cette différence est attribuée aux effets de la pression partielle de l'oxygène. Nous avons montré que la méthode de dépôt de nitrate d'uranyle pour les couches enrichies en isotope $^{235}UO_2$ à la surface des échantillons conduit à une épaisseur de couche qui peut être estimée à partir de la quantité de nitrate d'uranyle initialement déposée. Cependant, il est évident que cette couche enrichie est très inégalement déposée et cela induit une rugosité. Une analyse du modèle fournit des estimations du coefficient de diffusion en volume et de l'épaisseur de la couche d'oxyde enrichie avant le balayage SIMS, ce qui est cohérent avec la rugosité déterminée par la microscopie confocale chromatique. Cependant, il y a un certain nombre de des facteurs de complication qui rendent ces expériences difficiles à interpréter sans équivoque ; certains qui pourraient être évités dans de futures expériences, mais d'autres qui sont inhérents à la méthode.

Ces complications conduisent à des profils de profondeur qui ne sont pas systématiquement reproductibles d'un point de la surface à un autre pour un échantillon donné. Parmi ces facteurs, nous avons identifié:

1- La rugosité de surface initiale du matériau.
2- La rugosité induite par le dépôt et la distribution hétérogène de ce dépôt.
3- Les phénomènes d'évaporation qui semblent dépendre des conditions thermodynamiques dans lesquelles les échantillons sont recuits.

4- La vitesse de pulvérisation varie d'un grain à l'autre dans les échantillons polycristallins.

Malgré cela, un certain nombre de conclusions supplémentaires peuvent être tirées. Des images ioniques d'échantillons polycristallins recueillies par SIMS à différentes profondeurs ne montrent pas le contraste attendu si la diffusion accélérée par les grain joints de grains était opérationnelle. Ceci est cohérent avec le commentaire ci-dessus sur les coefficients de diffusion sur mono et poly cristaux. Le coefficient de diffusion global obtenu pour un échantillon dopé au Cr semble être plus élevé que dans le matériau non dopé. Cependant, ce résultat doit être validé plus avant en effectuant des expériences de diffusion supplémentaires dans différentes conditions. Aussi, afin de déterminer avec précision le coefficient d'auto-diffusion de l'uranium dans un matériau dopé au Cr, la durée de balayage pour la caractérisation SIMS future devrait être plus longue pour que le cratère soit assez profond pour être identifié sous le microscope confocal.

Pour mieux étudier les mécanismes de diffusion de l'uranium dans UO_{2+x}, nous avons conçu plusieurs autres expériences de diffusion à effectuer à diverses températures et pressions partielles d'oxygène. Également la préparation de surface d'échantillons polycristallins conduit à un niveau de rugosité qui détériore sensiblement la résolution en profondeur. Ce problème doit être résolu par une conception expérimentale améliorée, par exemple, en préparant des échantillons sous forme de sandwich et en les caractérisant par nano-SIMS.

Chapitre 6 Perspectives

Notre travail a sans aucun doute fourni des informations essentielles sur les lacunes cationiques et le comportement des clusters d'anions, ainsi que sur les propriétés macroscopiques correspondantes. Il a permis une compréhension approfondie des défauts ponctuels du combustible sur-stœchiométrique et leur impact sur la propriété de diffusion des cations. Mais un approfondissement de cette compréhension est toujours nécessaire. A cet effet, plusieurs recommandations sont proposées :

À l'avenir, comme il est suggéré dans le chapitre 3, il ressort qu’il serait intéressant d’étudier des données de diffraction et de PDF de différents échantillons avec des compositions intermédiaires, ou à différentes températures. Aussi, d'autres nouvelles méthodes peuvent être tentées pour étudier le désordre local induit par la présence de défauts anioniques. Par exemple, au lieu d'appliquer les corrections de Placzek, la diffusion inélastique des neutrons pourrait être utilisée pour extraire des informations sur la dynamique locale dans notre matériau UO_{2+x} au moyen d’une analyse complémentaire à la méthode PDF - l'analyse dynamique de la densité de la paire atomique (Egami et Dmowski, 2012). Une autre approche qui mériterait d'être étudiée serait d'interpréter la diffraction et l’intensité diffuse simultanément afin de mieux comprendre la relation entre ordre à court et à longue distance. La spectroscopie d'annihilation des positrons s'est révélée être une méthode bien adaptée pour l'étude des matériaux combustible. Sur la base de ce travail, plus d'efforts devraient être consacrés à l'obtention des fractions d'annihilation de positrons dans divers pièges. Des travaux futurs pourraient également être consacrés à la compréhension des mécanismes de piégeage et à l’obtention des coefficients de piégeage ainsi qu’aux calculs numériques. Des expériences complémentaires de durée de vie à différentes températures sur des échantillons recuits sous différentes conditions d'oxydation peuvent être intéressantes aussi bien pour comprendre l'évolution des charges des lacunes et leur concentration en fonction de l’écart à la stœchiométrie. Des échantillons préparés après oxydation à basse température, c'est-à-dire ne contenant pas de défauts lacunaires d'uranium, peuvent être caractérisés par Spectroscopie d'élargissement Doppler pour voir comment l'état de charge et les concentrations changent en fonction des écarts à la stoechiométrie. Dans les expériences actuelles d'auto-diffusion, le problème majeur est la rugosité de surface qui complique l'analyse du profil de profondeur et induit des incertitudes importantes dans la détermination des coefficients d'auto-diffusion de l'uranium. Une des solutions à ce problème consisterait à préparer des "couples sandwich" de UO_2 appauvri et des disques enrichis en ^{235}U coupés à partir de pastilles polycristallines frittées. Le couple sandwich après le recuit de diffusion peut être caractérisé au moyen de la technique nano SIMS.